

AD-A110 291

WRIGHT STATE UNIV DAYTON OHIO  
PROBLEMS IN FORCED UNSTEADY FLUID MECHANICS. (U)  
NOV 81 H VIETS, M PIATT, M BALL, R J BETHKE

F/G 20/4

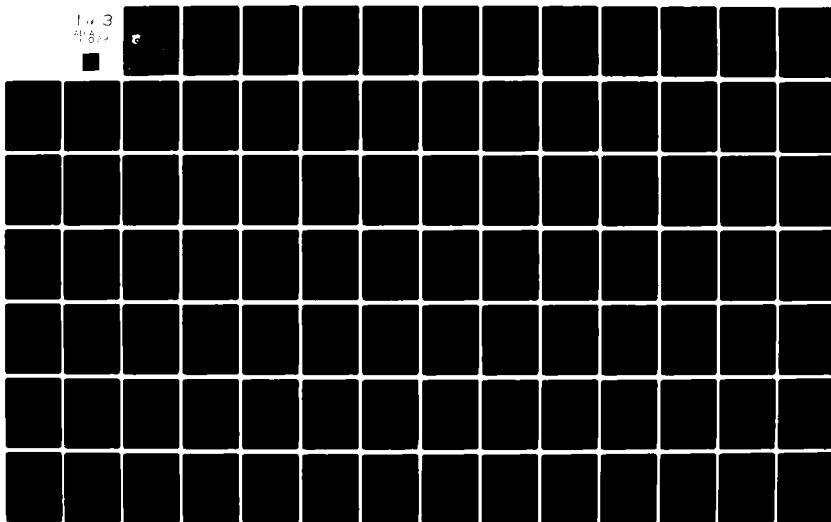
AFOSR-78-3525

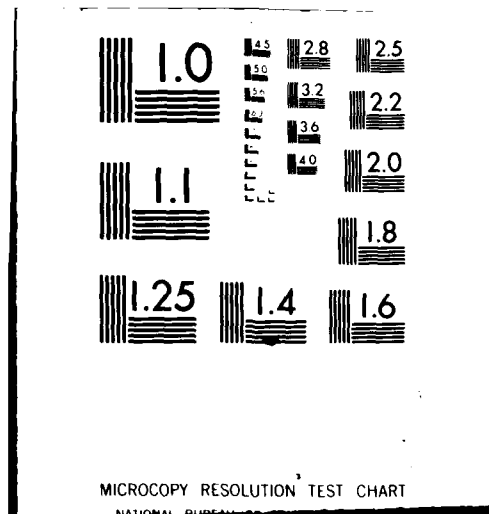
UNCLASSIFIED

AFWAL-TM-81-148-FINM

NL

1 of 3  
4/8/82





AFWAL TM-81-148-FIMM

② LEVEL II

AD A110291



## PROBLEMS IN FORCED, UNSTEADY FLUID MECHANICS

BY

HERMAN VIETS  
MICHAEL PIATT  
MONT BALL  
RICHARD J. BETHKE  
DAVID BOUGINE

WRIGHT STATE UNIVERSITY  
DAYTON, OH 45435

NOVEMBER 1981

DTIC  
ELECTE  
JAN 29 1982  
S B

APPROVED FOR PUBLIC RELEASE; DISTRIBUTION UNLIMITED.

DTIC FILE COPY

FLIGHT DYNAMICS LABORATORY  
AIR FORCE WRIGHT AERONAUTICAL LABORATORIES  
WRIGHT-PATTERSON AIR FORCE BASE, OHIO 45433


82 01 29 021

## FOREWARD

This report was prepared by Herman Viets, Michael Piatt, Mont Ball, Richard Bethke and David Bougine of Wright State University. The work was performed at Wright State University under AFOSR Contract #78-3525. The project engineer was Capt George Catalano with his work performed under work unit #2307N417 and covers the period from November 1977 to October 1980.

This Technical Memorandum has been reviewed and is approved for publication.

  
Aerospace Engineer  
Project Engineer

  
LOWELL C. KEEL, Maj USAF  
Chief, Aerodynamics and  
Airframe Branch

SECURITY CLASSIFICATION OF THIS PAGE (When Data Entered)

REPORT DOCUMENTATION PAGE		READ INSTRUCTIONS BEFORE COMPLETING FORM	
1. REPORT NUMBER		2. GOVT ACCESSION NO. <b>AD-A110291</b>	
4. TITLE (and Subtitle) <b>Problems in Forced Unsteady Fluid Mechanics,</b>		3. RECIPIENT'S CATALOG NUMBER	
		5. TYPE OF REPORT & PERIOD COVERED <b>Technical Final</b> <b>1 Nov 1977-31 Oct 1980</b>	
7. AUTHOR(s) <b>Hermann Viets</b> <b>Michael Piatt</b> <b>Mont Ball</b> <b>Richard J. Bethke</b> <b>David Bouginé</b>		6. PERFORMING ORG. REPORT NUMBER	
9. PERFORMING ORGANIZATION NAME AND ADDRESS <b>Wright State University</b> <b>Dayton, Ohio 45435</b>		8. CONTRACT OR GRANT NUMBER(s) <b>AFOSR-78-3525</b>	
11. CONTROLLING OFFICE NAME AND ADDRESS <b>Air Force Office of Scientific Research</b> <b>Bolling Air Force Base, DC 20332</b>		10. PROGRAM ELEMENT, PROJECT, TASK AREA & WORK UNIT NUMBERS	
14. MONITORING AGENCY NAME & ADDRESS (if different from Controlling Office) <b>Flight Dynamics Laboratory/FXM</b> <b>Wright-Patterson AFB, Ohio 45433</b>		12. REPORT DATE <b>Nov 1981</b>	
		13. NUMBER OF PAGES <b>231</b>	
		15. SECURITY CLASS. (of this report) <b>Unclassified</b>	
		15a. DECLASSIFICATION/DOWNGRADING SCHEDULE	
16. DISTRIBUTION STATEMENT (of this Report)  <b>Approved for public release; distribution unlimited</b>			
17. DISTRIBUTION STATEMENT (of the abstract entered in Block 20, if different from Report)			
18. SUPPLEMENTARY NOTES			
19. KEY WORDS (Continue on reverse side if necessary and identify by block number) <b>unsteady flow</b> <b>time dependent flow</b> <b>wing</b> <b>rotor</b> <b>jets</b> <b>fluidics</b> <b>ramp</b> <b>vortex</b> <b>forced flow</b> <b>flow structure</b> <b>diffuser</b> <b>dump combustor</b>			
20. ABSTRACT (Continue on reverse side if necessary and identify by block number) <b>Forced unsteady fluid flows are examined from the point of view of positive implications of the time dependency. Particular problems examined in a forced unsteady mode are jets, wind tunnels, wings, ramps and diffusers, dump combustors and vortex structure. Two methods of forcing the flow are studied in detail, fluidic feedback and a cam-shaped rotor. The fluidic method produces an unsteady jet while the rotor acts as a time dependent vortex generator. Potential performance improvements with unsteady flow are evident in all of the flows examined.</b>			

DD FORM 1 JAN 73 1473

EDITION OF 1 NOV 68 IS OBSOLETE

SECURITY CLASSIFICATION OF THIS PAGE (When Data Entered)

iii/iv

24-201

JEH

PROBLEMS IN  
FORCED UNSTEADY FLUID MECHANICS

Hermann Viets\*  
Michael Piatt\*\*  
Mont Ball\*\*\*  
Richard J. Bethke†  
David Bouginett††

Wright State University  
Dayton, Ohio 45435

---

\*Professor

\*\*Research Assistant (presently with Systems and Applied Sciences,  
Hampton, Va.)

\*\*\*Senior Research Technician

†Associate Professor

††Research Assistant

v/vi

# TABLE OF CONTENTS

<u>Section</u>		<u>Page</u>
I	Introduction .....	1
II	Flowfield of an Unsteady Jet ..... by M. Piatt and H. Viets	2
III	Large Scale Structure in an Unsteady Jet ..... by H. Viets	9
IV	Multijet Flowfield as a Gust Tunnel ..... by H. Viets; M. Ball and M. Piatt	16
V	Linearized Unsteady Jet Analysis ..... by H. Viets and M. Piatt	23
VI	Forced Unsteady Flow Over a Wing ..... by H. Viets; M. Ball and M. Piatt	33
VII	Unsteady Flow Over a Rearward Facing Ramp ..... by H. Viets; M. Ball and M. Piatt	37
VIII	Induced Unsteady Flow in a Dump Combustor Geometry ..... by H. Viets and M. Piatt	45
IX	Performance Potential of Unsteady Diffusers ..... by H. Viets; M. Ball and D. Bougine	51
X	Details of the Flow Produced by the Rotor Vortex Generator . by H. Viets; M. Piatt and M. Ball	57
XI	Data Analysis to Identify Large Scale Vortex Structures .... by R.J. Bethke and H. Viets	64
XII	References .....	71
XIII	Tables .....	78
XIV	Figures .....	87



Accession For	
NTIS GRA&I	<input checked="" type="checkbox"/>
DTIC TAB	<input type="checkbox"/>
Unannounced	<input type="checkbox"/>
Justification	
Distribution/	
Availability Codes	
Avail and/or	
Dist	Special
A	

# LIST OF ILLUSTRATIONS

FIGURE		PAGE
1	Schematic of a fluidically oscillating jet	87
2	Smoke flow visualization of the oscillating jet in a coflowing stream of 45.8% of the jet velocity	88
3	Smoke flow visualization of the oscillating jet in a coflowing stream of 28% of the jet velocity	89
4	Experimental setup	90
5a	Time averaged velocity measurements in the oscillating jet, $U_0=43$ m/sec, $\omega=12$ Hz	91
5b	Continued	92
5c	Continued	93
5d	Continued	94
5e	Continued	95
6	Composite view of the time average oscillating jet	96
7	Centerline and peak velocity decay for various frequencies in the time averaged oscillating jet	97
8	Half width growth in the time averaged oscillating jet for various frequencies	98
9	Schematic of the electronic circuitry employed to conditionally sample the unsteady jet flowfield	99
10	Definition of the jet phase angle in terms of jet orientation	100
11a	Instantaneous velocity profiles in the oscillating jet at a frequency $f=12$ Hz and a phase angle $\theta=90^\circ$	101
11b	Continued	102
11c	Continued	103
11d	Continued	104

FIGURE	PAGE
12a Composite of the instantaneous streamwise velocity profiles for $f=12$ Hz, $\theta=90^\circ$	105
12b Transverse location of the maximum streamwise velocity with distance downstream, $\theta=90^\circ$	106
13a Instantaneous velocity profiles in the oscillating jet at a frequency $f=12$ Hz and a phase angle $\theta=180^\circ$	107
13b Continued	108
13c Continued	109
14a Composite of the instantaneous velocity profiles for $f=12$ Hz, $\theta=180^\circ$	110
14b Transverse location of the maximum streamwise velocity with distance downstream, $\theta=180^\circ$	111
15a Composite of the instantaneous velocity profiles for $f=12$ Hz, $\theta=270^\circ$	112
16a Instantaneous velocity decay for various phase angles and a frequency $f=12$ Hz	113
17 Typical velocity profiles from Simmons, Platzer and Smith, Reference 5	114
18 Smoke flow visualization of the oscillating jet in a coflowing stream of 28% of the jet velocity	115
19 Evolution of the jet surface waves	116
20a Jet velocity field at a frequency $\omega=18$ Hz and phase angle $\theta=270^\circ$	117
20b Coherent structure of the jet seen in a moving coordinate system	118
21 Anticipated vortex locations based on flow visualization results	119
22a Jet velocity field at a frequency of $\omega=12$ Hz and phase angle $\theta=90^\circ$	120
22b Coherent structure of Vortex B in a moving coordinate system	121

FIGURE	PAGE
23a Jet velocity field at a frequency of $\omega=12$ Hz and a phase angle $\theta=180^\circ$	122
23b Coherent structure of Vortex D in a moving coordinate system	123
24a Jet velocity field at a frequency of $\omega=12$ Hz and a phase angle of $\theta=270^\circ$	124
24b Coherent structure of Vortex F in a moving coordinate system	125
25 Effect of the vortex structure on the instantaneous jet velocity decay	126
26 Schematic of mechanically controlled, fluidically activated nozzle	127
27 Schematic of jet controlled gust tunnel	127
28 Geometry of the experimental subscale pilot gust tunnel	128
29 Flow visualization of the in-phase configuration in the up and down orientations	129
30 Schematic of conditional sampling electronics	130
31 Flowfield at $\bar{X} = 20$ for the in phase configuration in the upward orientation	131
32 Flowfield at $\bar{X} = 20$ for the in phase configuration in the downward orientation	131
33 Decay of the velocity non-uniformity in the flowfield	132
34 Variation of the centerline transverse velocities with time at several streamwise positions	133
35 Flowfield at $\bar{X} = 20$ for the out of phase configuration and an inward orientation	134
36 Flowfield at $\bar{X} = 20$ for the out of phase configuration and an outward orientation	134
37 Variation of the centerline streamwise velocities with time at several streamwise positions	135
38 Streamwise velocities at various positions with a $45^\circ$ phase between the nozzles and the upper nozzle in the upward orientation	136

FIGURE	PAGE
39 Same nozzle configuration as Figure 13 but with the upper nozzle in the downward orientation.	137
40 Flow visualization of the in-phase gust flow over an airfoil at various phase angles.	138
40 Continued	139
41 Schematic of the vibrated jet studied by McCromack, Cochran and Crane. <sup>29</sup>	140
42 Flapping jet with angular time variation at the exit studied by Viets et al. <sup>3</sup> , A <sup>5</sup> and Platzer et al. <sup>10</sup>	140
43 Jet with time dependent mass flow studied by Binder and Favre-marinet and Curtet and Girad. <sup>2</sup>	141
44 Initial and downstream velocity profiles	141
45 Fluidically Controlled Jet Nozzle Design	142
46 Half width growth dependent upon oscillation frequency	143
47 Flow over a wavy wall	144
48 Geometry and Flowfield of an Oscillating Airfoil	145
49 Hydrogen Bubble Flow Visualization of the Field Around an Oscillating Airfoil (from McAllister and Carr, Ref. 37A)	146
50 Vortex Generation by an Embedded Rotor	147
51 Airfoil and Rotor Geometry	148
52 Airfoil Mounted for Low Speed Wind Tunnel	149
53 Vortex Structure Behind the Rotor on a Flat Plate	150
54 Flow Visualization of the Flow Structure at $\alpha = 20^\circ$ .	151
55 Effect of the Rotor Speed on the Streamline pattern over the Airfoil	152
56 Instantaneous Vortex Structure on the Airfoil for $\alpha = 20^\circ$ , $\omega = 1000$ rpm.	153
57 Pressure Variation with Rotor Speed for Three Angles of Attack	154

FIGURE	PAGE
58 Pressure Variation with Angle of Attack with/without Activated Rotor	155
59a Unsteady Ramp Flow Configuration	156
59b Tunnel Geometry	156
60 Pressure Distribution on the Ramp for $\theta = 20^\circ$	157
61 Pressure Distribution on the Ramp for $\theta = 28^\circ$	158
62 Pressure Distribution on the Ramp for $\theta = 30^\circ$	159
63 Time averaged Flow for $\theta = 28^\circ$	160
64 Instantaneous Streakline Photographs for Various Rotor Speeds at $\theta = 28^\circ$	161
64 Continued	162
65 Schematic of a three dimensional rotor geometry (Tapered rotor)	163
66 Comparison between rotor motion in the upstream (+) and downstream (-) directions for $\omega = 1000$ and $2500$ rpm, and a tapered rotor	164
67 Same as Figure 66 for $\omega = 4000$ and $5000$ rpm	165
68 Pressure rise down the ramp for $\pm 1000$ rpm and a tapered rotor	166
69 Pressure rise down the ramp for $\pm 5000$ rpm and a tapered rotor	167
70 Streaklines in the ramp flowfield for a tapered rotor moving in the counter-clockwise (+) and clockwise (-) directions	168
71 Same as Figure 70 for higher rotor speeds	169
72 Ramjet Combustor Flowfield	170
73 Experimental Geometry and Rotor Flowfield	171
74 Streamline Shapes for Various Rotor Speeds, $\bar{h} = 1/3$	172
75 Instantaneous Streaklines for $\omega = 0$ , $\bar{h} = 1/3$	173
76 Streaklines at Three Different Instants, $\omega = 2500$ rpm, $\bar{h} = 1/3$	174
77 Streaklines for $\omega = 5000$ rpm, $\bar{h} = 1/3$	175
78 Streamline Shapes for Various Rotor Speeds, $\bar{h} = 1$	176

FIGURE	PAGE
79 Streaklines for Various Rotor Speeds, $\bar{h} = 1$	177
80 Pressure Distribution Downstream of the Dump Station; $\bar{h} = 1/3$ , Various Rotor Speeds	178
81 Pressure Distributions Downstream of the Dump Station; $\bar{h} = 2/3$ , Various Rotor Speeds	179
82 Pressure Distributions Downstream of the Dump Station; $\bar{h} = 1$ , Various Rotor Speeds	180
83 Effect of Rotation Direction on Pressure Distributions	181
84 Effect of Rotor Geometry as a Passive Trip	182
85 In phase and out of phase rotor orientation	183
86 Vortex produced near the corner of the diffuser	184
87 Multiple vortices produced in the diffuser by increasing the speed of the rotor	185
88 Streaklines produced for $\theta = 8^\circ$ and $12^\circ$ showing separation at $12^\circ$ and time averaged velocity profiles taken at the diffuser exit verify the separation	186
89 Longer exposure streamline photographs for $2\theta = 30^\circ$ . (a). Separation at the bottom for $\bar{\omega} = 0$ (b). Weaker separation at the top for $\bar{\omega} = 11.84$ (both in phase)	187
90 Pressure rise through the diffuser for $2\theta = 16$ and various rotor speeds, out of phase	188
91 Pressure rise for larger angle diffuser, $2\theta = 24^\circ$ , out of phase	189
92 Pressure rise for $2\theta = 30^\circ$ , out of phase	190
93 Diffuser performance for rotors set in phase and $2\theta = 24^\circ$ , in phase rotors	191
94 In phase pressure rise for $2\theta = 30^\circ$ , and rotors in phase	192
95 Streakline photographs of the diffuser flow at different phase positions with superimposed instantaneous velocity profiles	193

FIGURE	PAGE
96 Streakline photographs for a larger diffuser angle and for the out of phase rotor orientation	194
97 The presence of a counter-clockwise vortex near the upper wall or a clockwise vortex near the lower wall leads to instantaneous velocity changes in the streamwise ( $u'$ ) and transverse ( $v'$ ) directions	195
98 Velocity difference between the presence of a vortex pair ( $\phi = 180^\circ$ ) and no vortex ( $\phi = 90^\circ$ )	196
99 The velocity changes due to the presence of a single vortex in the out of phase condition. The profiles are those in Figure 96 (b) and (d)	197
100 Schematic of the vortex flow generated by a cam shaped rotor	198
101 Flow visualization of vortex structure produced by the vortex generator with $\omega = 3000$ rpm	199
102 Flow visualization of vortex structure produced by the vortex generator with $\omega = -3000$ rpm	200
103 Flow visualization of vortex structure produced by the vortex generator with $\omega = 2000$ rpm	201
104 Flow visualization of vortex structure produced by the vortex generator with $\omega = -2000$ rpm	202
105 Flow visualization of vortex structure produced by the vortex generator with $\omega = 1000$ rpm	203
106 Flow visualization of vortex structure produced by the vortex generator with $\omega = -1000$ rpm	204
107 Schematic of conditioned sampling apparatus	205
108a Instantaneous velocity field with the rotor fully extended in the $\theta = 0^\circ$ position	206
108b Identification of a vortex structure in a reference frame moving at 11.5 m/sec	207
109a Instantaneous velocity field with the rotor in the $\theta = 120^\circ$ position	208
109b Identification of a vortex structure in a reference frame moving at 11.8 m/sec	209

FIGURE	PAGE
109c More detail of the flow near the rotor with $\theta = 120^\circ$	210
109d Identification of a vortex structure in the flowfield of Figure 109c	211
110a Instantaneous velocity field with the rotor in the $\theta = 240^\circ$ orientation	212
110b Identification of a vortex structure in the flowfield of Figure 110a at $\bar{x} = 4.5$ , $\bar{y} = 2.0$	213
110c Identification of a vortex structure in the flowfield of Figure 110a at $\bar{x} = 13.0$ , $\bar{y} = 5.75$ .	214
111 Trajectory of the vortex center as it moves downstream	215
112 Influence of the vortex on the streamwise velocity profile	216
113a Spatial vortex existing on the axis	217
113b Transformation of the vortex of Figure 113a	218
114a Vortex shifted to an off axis location. Center shifted down by 50 units and right by 64 units from the upper left data point.	219
114b Schematic of phase angle shift	220
115 Rotational flow with a constant magnitude velocity	221
116a Superimposed vortex on a parabolic translational flow	222
116b Translational velocity component of the flowfield of Figure 5a	222
116c Flowfield in the moving coordinate system	223
117 Instantaneous velocity structure of an oscillating jet	224
118 Flow structure in a reference frame moving with the velocity at the point identified as the vortex center	225
119 Generated velocity field containing two vortices	226
120a Schematic of two vortices in the physical plane	227
120b Schematic of the transformed plane of vortex number 1 in Figure 120a showing magnitudes and phase angle changes due to shift of vortex center location	228

FIGURE	PAGE
120c Schematic of the transformed plane of vortex number 2 in Figure 120a, showing magnitudes and phase angle changes due to shift of vortex center location	228
121 Instantaneous velocity field generated by the rotor	229
122a The upstream vortex in a coordinate frame moving with its center	230
122b The downstream vortex in a coordinate frame moving with its center	231

## SECTION I

### INTRODUCTION

The historical evolution of fluid mechanics has generally emphasized the elimination of unsteady flows as undesirable. Two examples are the attempts to eliminate inlet buzz and wing flutter. There are, however, situations in which unsteady flows can have performance advantages and some have led to application as in the case of pulsed combustion "buzz bombs" of the 1940's.

More recently, the potential advantages of unsteady flow have been pursued in a variety of applications. The rates at which jets mix with their surroundings have been increased by introducing a time dependency into the jets by acoustic,<sup>1</sup> mechanical<sup>2</sup> or fluidic<sup>3</sup> means. In the boundary layer, mechanically activated unsteady wall jets have been shown to achieve the same performance as steady jets with only one half the mass flow required.<sup>4</sup> Pulsed combustion gas furnaces are currently being investigated<sup>5</sup> with an eye to improving efficiency.

In the animal world, unsteady flow is rather common and its advantages are chronicled by Lighthill.<sup>6</sup> The question of flapping wing flight is currently being investigated to determine performance effects of the time dependency<sup>7</sup> while in the boundary layer the moving surface waves on porpoises may lead to drag reduction.<sup>8</sup>

The above examples, as well as many others, indicate that unsteady flow is not always detrimental to performance but is actually advantageous in particular cases. Thus, the objective of the present investigation is to examine unsteady flow from a positive point of view and to identify situations where the time dependency is an asset.

The earlier sections deal with unsteady flow in jets and the resulting large scale flow structures. Later sections are concerned with unsteady flowfields produced by a mechanical rotor which creates transverse vortices. In each case some potential advantages are discussed.

## SECTION II

### FLOWFIELD OF AN UNSTEADY JET

#### 1. Background

Various methods have been proposed to induce unsteady flow in jets.<sup>1-4,9,10</sup> In general, the objective is to affect the rate at which the jet mixes with its surroundings. The particular jet nozzle design employed in the present study is described in Reference 3 and consists of a modified fluidic element with a feedback mechanism.

The nozzle design and the jet it produces are shown in Figure 1. In this case the feedback loop is built around the nozzle body in order to minimize its influence on any external flow. The jet oscillates from side to side in a quasi-sinusoidal fashion and rapidly mixes with the coflowing stream or the ambient fluid. The oscillation is produced without the need for moving parts.

#### 2. Flow Visualization

The fluidic nozzle shown in Figure 1 is mounted in a smoke tunnel to illustrate the dynamic interaction between the jet and the surrounding fluid. The smoke is produced by allowing kerosene to drip on an inclined resistance heater. The kerosene vapor is forced out through tubes and then entrained into the open circuit smoke tunnel inlet. The instantaneous streakline pattern is shown in Figure 2 for a coflowing stream to jet velocity ratio of .46 and a frequency of 30.5 Hz. A sinusoidal-like structure may be seen, but the interaction between the jet and coflowing stream is rather weak.

Reducing the coflowing stream to 28% of the jet velocity while holding the jet velocity (and hence the frequency) constant results in a greatly increased interaction between the jet and external flow as may be seen in Figure 3. The shear forces between the two flows have increased and produce an apparent vortex structure which is swept downstream. The vortex formation enhances the mixing due to the presence of the large scale structures.

#### 3. Time Average Measurements

The fluidic nozzle is mounted between two Plexiglas sheets to minimize the three dimensional effects, as shown in Figure 4. A hot wire probe is mounted on a motorized traversing mechanism which also drives a potentiometer to indicate the position of the probe. A Flow Corporation (now Datametrics, Inc.) Model 900

two channel constant temperature hot wire anemometer is employed along with an X probe geometry. A pair of Thermo Systems, Inc., model 1072 linearizers multiply the signal from each wire by a fourth order polynomial whose required coefficients have been determined by calibration. Thus the output voltage of each varies linearly with velocity. The appropriate geometrical relationships (based on the orientation of wires) then yield the x and y velocity components which are then simply filtered to eliminate the A.C. and leave only the D.C. or time average signal. The velocity and the probe position are then plotted on a Hewlett-Packard Model 2FA X-Y plotter. The circuitry required to obtain the instantaneous velocity distribution will be discussed in the following subsection.

A series of velocity profiles depicting the time averaged flowfield structure is shown in Figure 5. The velocity distribution at a point close to the nozzle exit ( $\bar{x} = .20$ ) is presented in Figure 5a, both for the streamwise (u) and transverse (v) components. The frequency is 12 Hz and the velocity profiles are similar to those found in steady jets. The transverse velocity (v) indicates that far from the jet, entrainment causes an inflow toward the jet which increases as the jet is approached. The inflow goes to zero at the jet's edge and within the jet the transverse flow is outward due to the spreading of the jet itself.

Farther downstream at  $\bar{x} = 6$ . ( $\bar{x} = x/D$  where D is the nozzle throat dimension) the character of the average flow changes considerably as shown in Figure 5b. The streamwise profile has developed a double peak. It appears that this phenomenon is due to the quasi-sinusoidal oscillation characteristic of the particular nozzle design. The jet spends more time in the extreme angular positions than it does making the transition from side to side. Examination of the transverse velocity profile shows that flow is moving from the center valley toward the peaks, with additional entrainment of ambient fluid from outside the jet.

At the streamwise distance 10 diameters downstream the u velocity profile still exhibits a double peak as shown in Figure 5c. An indication of the interaction between the two peaks is given by the corresponding transverse velocity profile which has an extensive flat region in the center. Thus the transverse velocity between the peaks is very small. If the two peaks are considered to be individual steady jets for the sake of analysis, their effect

on each other is simply to limit the entrainment on their common side. Each jet would then behave as though there were an inviscid wall on that side.

Still farther downstream at  $\bar{x} = 14$ , the transverse velocity profile shows that now flow is moving from the peaks into the center valley filling that valley as shown in Figure 5d. Figure 5e shows the time averaged  $u$  and  $v$  velocity profiles at 22 diameters downstream. The streamwise velocity has returned to a single peak profile. The transverse velocity has also returned to a form typical of a steady jet which is not rapidly growing. That is, the flow within the jet itself is roughly parallel so no outflow appears but only inflow produced by entrainment.

A composite picture of the streamwise velocity profiles at their relative downstream positions for a frequency of 12Hz is shown in Figure 6. The behavior of the time averaged velocity distribution can be described in a three step process. Near the nozzle exit the double peak profiles are formed and diverge from each other, entraining fluid from outside the jet and from the center valley. Farther downstream, the velocity in the valley reaches a minimum. The transverse flow begins to move toward the jet centerline, filling the valley while entraining fluid from outside the jet. The final process is the development of a typical two dimensional jet velocity profile with a single peak on the centerline.

This behavior was observed at four different frequencies from 4 Hz to 18 Hz. Figure 7 depicts the time averaged centerline velocity decay for frequencies of 4, 8, 12 and 18 Hz respectively. Their corresponding half width growths are shown in Figure 8. The centerline velocity is nondimensionalized with respect to the time averaged exit velocity. The half width, defined as the distance between the centerline and the position of half the reference velocity, is nondimensionalized with half the nozzle exit dimension.

As shown in Figures 5 and 6, the maximum velocity is not always at the jet centerline. In steady jet problems, the centerline velocity is generally used as the reference velocity for the half width growth and velocity decay determination. However, the peak velocity may be more indicative of the mixing rate so both are shown. For the same reason, both the values of half widths based on the peak and valley velocities are presented in Figure 8. Of course, the two sets of curves coalesce when the double peak disappears.

The time averaged velocity decays (Figure 7) and half width growths (Figure 8) are rather weak functions of frequency, if they are based on the peak velocity

at each streamwise position. However, based on the centerline velocity, both the velocity decay and the jet growth are strong functions of oscillation frequency. At low frequencies, the centerline velocity decays very rapidly and then rises somewhat under the influence of the double jet peaks. At higher frequencies, the decay is much weaker and leads to the conclusion that at very high frequencies, it is possible that only a single velocity peak appears.

The use of the centerline velocity as a reference also leads to a frequency variation in the half width growth. The difference between the two computed half widths is greatest at low frequencies and has almost disappeared at a frequency of 18 Hz.

#### 4. Instantaneous Velocity Measurements

##### a. Experimental Apparatus

The objective of this portion of the experiment is to produce velocity profiles to indicate the unsteady flowfield at a single instant. In order to achieve this, the hot wire must sample at precise times and these samples must be taken when the jet itself is in a known orientation. Thus the sampling of the hot wire circuit must be conditioned by the knowledge of the overall jet orientation. The jet orientation is determined by an additional hot wire probe referred to as a trigger. A schematic of the circuitry is shown in Figure 9.

The triggering probe employs the simplest hot wire circuit, a power supply in series with a large resistor and the wire. The hot wire resistance is relatively small so that the current passing through it is essentially constant. The wire is placed in a fixed orientation near the jet exit so that it is periodically exposed to the jet flow. The periodic signal is amplified and band pass filtered so that only the fundamental jet frequency is present. The resulting signal is passed through a zero crossing detector which then produces a square wave which is correlated with the jet orientation.

Since one wishes to sample the flowfield with the jet in several different (but fixed) orientations, a variable phase shifter is employed. The signal then can be used as a trigger for the jet in various fixed positions. After suppressing the D.C. voltage produced by the phase shifter, the signal is amplified and fed to a Schmitt trigger which again

produces a square wave. The square wave is differentiated and clipped to yield a spike of 50  $\mu$ s width. Finally, this spike is the input to a sample and hold amplifier along with the analog signal from the hot wire anemometer. The output is the conditionally sampled hot wire data where the timing of the sample is determined by the triggering circuit. Thus the circuit only samples when the jet is in a given fixed position and the signal is output on an X-Y plotter versus the vertical position determined from a potentiometer. The result then is a velocity profile at an instant when the jet is in a given orientation.

b. Orientation 90°

A sketch of the jet orientations defined in the present case is shown in Figure 10. The first orientation to be discussed here is the 90° case where the jet at the origin is instantaneously pointing straight downstream and moving down between an upward and downward orientation. The frequency is 12 Hz.

The instantaneous velocity distributions at  $\bar{x} = .20$  is shown in Figure 11a. The streamwise component is a single peak as might be expected and is almost symmetrically oriented with respect to the streamwise axis. The instantaneous  $v$  velocity component is not at all symmetrical, however, and gives the first indication of the time dependency involved in the flow. Approaching the jet from below, there is an upward component due to the entrainment into the jet. Within the lower part of the jet,  $v$  is downward because the lower part of the jet is spreading in that direction. The upper half of the jet has a rather large upward velocity component which is probably due partly to spreading in that direction and partly to a small asymmetry which can also be seen in the  $u$  component (with some difficulty).

At a streamwise position  $\bar{x} = 6$ , (see Figure 11b) the asymmetry of the time dependency is clear. Here even the  $u$  velocity is asymmetrical with respect to the centerline and within the jet the  $v$  velocity is strongly upward. The reason for this may be seen in the schematic of Figure 12 showing the jet in the instantaneous 90° position and the quasi-sinusoidal wave downstream. At  $\bar{x} = 14$ , the asymmetry in the  $u$  velocity is rather strong (Figure 11c) and the position of the jet can be determined almost as well by the maximum  $v$  velocity as the maximum  $u$  component. The slower decay of the  $u$  component below the jet (as opposed to above) is due to the

setting up a significant entrainment flow as may be seen in the strong upward flow of the  $v$  component below the jet.

The effect gets even stronger by  $\bar{x} = 22$ , but by  $\bar{x} = 30$  the flow is rather diffuse, Figure 11d. The fact that the  $u$  component reaches its maximum below the nominal centerline may be seen and is borne out by the fact that the  $v$  component is downward. A plot of the lateral position of maximum streamwise velocity is presented in Figure 12b and confirms the schematic of Figure 12a.

c. Orientation  $180^\circ$

At an orientation of  $180^\circ$ , the jet is in the extreme downward position, as seen in Figure 10. This is evident in Figure 13a where the  $u$  component is skewed to a position below the centerline and the  $v$  component indicates entrainment into the jet from above and below while the  $v$  velocity within the jet is in a downward direction.

By  $\bar{x} = 6$  (Figure 13b), the streamwise flow is highly asymmetric and, except for some entrained flow rather far below the jet, in a very strongly downward orientation. At an  $\bar{x} = 18$ , the jet orientation is upward as may be seen in the  $u$  component peak above the axis and the upward component in  $v$  (Figure 13c). The full flowfield at the instant the exit jet is in the down position is shown in Figure 14, along with the plot of the maximum velocity position as a function of streamwise distance. The position of the unsteady jet may still be clearly seen at  $\bar{x} = 30$  and to some extent at  $\bar{x} = 40$ .

d. Orientation  $270^\circ$

At an orientation of  $270^\circ$  the jet is in a horizontal position, moving up between a downward and upward orientation. Similar behavior is observed and in fact the velocity profiles are almost the same as an inverted version of those obtained at the  $90^\circ$  orientation. The composite picture of the streamwise velocity profiles and the corresponding plot of the transverse coordinate of maximum streamwise velocity are shown in Figure 15.

The downstream velocity distribution at any instant reflects, of course, the past history of the jet. At an oscillation frequency of 12 Hz it appears that approximately  $3/4$  of a wave has traveled downstream in 30 jet diameters. Each of the phase angles investigated show the maximum

streamwise velocity at  $\bar{x} = 30$  to be located at a  $y$  coordinate corresponding to a phase shift of roughly  $270^\circ$  from the jet orientation at the nozzle exit.

#### e. Velocity Decay

The time averaged jet velocity decay has been discussed in relation to Figure 7 for various oscillation frequencies. The corresponding instantaneous streamwise velocity decays are shown in Figure 16 for both the 12 and 18 Hz frequencies. Thus the data represents the spacial decay of streamwise velocity within an existing jet at a single instant of time. The velocities are all nondimensionalized with respect to the instantaneous exit velocity.

The velocity decay rates are much greater than the decay rate for a steady two dimensional jet, also shown in Figure 16. However, by comparison with Figure 7, it may be seen that the instantaneous jet decays more slowly than the time averaged unsteady jet. This is to be expected since the time averaged jet mixes very rapidly in part by the actual distribution of the flow by the flapping process.

The streamwise velocity decay for both a steady and a time average jet is a monotonically decreasing function. However, for the instantaneous jet, it is evident that there exists a small peak in the otherwise generally decaying function. Recent evidence leads to the conclusion that these peaks are associated with a large scale unsteady structure in the oscillating jet. This structure will be discussed in the following section.

### 5. Discussion

The most relevant comparison with existing experimental data is with that due to Simmons, Platzer and Smith<sup>5</sup> who studied a mechanically oscillating plane jet. The oscillation was forced by actually rotating the nozzle exit through small angles.

A basic result of the Simmons, et al.<sup>5</sup> paper is that the low frequency unsteady jet may be treated in a quasi-steady manner. That is, the velocity profiles shown in Figure 17 (from Ref. 5) are essentially symmetrical about their maximum velocity positions and the unsteady jet flap structure is similar to a plane jet issuing into a coflowing stream. Thus the time dependency is overpowered by the quasi-steady structure set up so quickly about the jet (relative to the oscillation) that the jet acts as though it were a steady jet in that orientation. The present results do not indicate such a situation. The dynamics of the jet motion are clearly important in the instantaneous structure since there is no

similarity in the streamwise velocity profiles and indeed a very strong change in the character of the transverse velocities (which were not measured in Ref. 5).

At least two reasons for the discrepancy can be advanced. The first is the difference in the reduced frequency of the oscillations; that is, the speed of the oscillation relative to the experimental parameters, specifically the jet velocity and a scale length. If the reduced frequency is defined as

$$\frac{\omega}{U_{\text{jet}}/D}$$

where  $\omega$  = forcing frequency,  $U_{\text{jet}}$  is the jet exit velocity and  $D$  the jet exit scale, then in the Simmons, et al.<sup>5</sup> results, this parameter has a value of from .00824 to .0058. In the present experiments the values are an order of magnitude higher, ranging from .0081 to .0363. The effect is primarily due to a reduction of the jet velocity and an increase in the jet exit scale.

An even stronger effect on the importance of unsteady flow in the jet mixing is the presence of a coflowing external stream. It can be clearly seen in Figures 2 and 3 that the presence of a coflowing stream can have a substantial influence on not only the rate of jet spread but also on the scale of the time dependency. Therefore, it appears likely that a reduction of coflowing stream speed will result in an increased mixing rate due to the unsteadiness of the flow.

### SECTION III

#### LARGE SCALE STRUCTURE IN AN UNSTEADY JET

##### 1. Background

The existence of coherent structures in turbulent shear flows<sup>11</sup> has greatly complicated the task of modelling these flows. Since the use of local transport properties does not appear to be adequate, future descriptions of turbulent flows will probably rely more heavily on phenomenological models. The flow may then be based on some observations of its structure. A very simple example would be to model the coherent large scale structure of a free jet by a number of vortices being convected downstream in a jet without a large scale structure. Of course, other difficulties arise; in particular, the questions of how this structure is initially formed<sup>12</sup> and the geometrical relationships involved.<sup>13</sup>

The motivation, then, for studying unsteady flows is not only due to their own usefulness but also as a guide to the modelling of "steady" flows. In particular,

the purpose of the present section is twofold:

1. Demonstrate some positive aspects of unsteady flow.
2. Produce flows in which the origin of the coherent structure is readily identifiable, thereby perhaps simplifying the modelling task.

## 2. Qualitative Structure

The introduction of a time dependency into free jet flows has been accomplished by various methods including mechanical,<sup>2</sup> acoustic<sup>1</sup> and fluidic<sup>3</sup> means. The fluidic method is considered here and consists of a feedback circuit which produces a jet which flaps from side to side.<sup>3</sup> The main advantage of this system (as with all the unsteady jets) is a more rapid mixing of the jet with the surrounding fluid. The unsteady jet nozzle employed here is shown in Figure 1 and described in detail in Ref. 3. The feedback loop is incorporated into the nozzle body to minimize the interference with the coflowing stream.

The large scale coherent structure in free shear layers, as demonstrated by Roshko and Brown<sup>14</sup> (see also Ref. 11), is difficult to model due to the lack of detailed understanding of its origin. Although it is clear that the large scale structure is born in the turbulent shear layer, its growth and geometrical spacing have not been predicted analytically. However, it has been shown that the scale must increase with streamwise distance<sup>12</sup> and that the spacing also increases by the amalgamation of adjoining structures.<sup>13</sup> A simpler problem, from the modelling point of view, is the unsteady flow in which the origin of the largest scale structure is more evident.

The large scale structure in the oscillating free turbulent jet is shown in Figure 2. The flow structure is visualized by entraining kerosine smoke into the open circuit low speed wind tunnel. The nozzle exit is at the left and the flow is from left to right. The ratio of the coflowing stream to nozzle exit velocity is .458. Although the jet is highly turbulent, the coflowing stream turbulence is low enough to produce a visible study of the entrainment into a unsteady jet. With such a relatively high coflowing stream, the amplitude of the jet oscillation is not large but the appearance of the large scale structure is evident at various streamwise positions. At position A the large scale structure can only be seen with some difficulty. By position B, the structure is a clearly defined mass of fluid which is rotating in the clockwise sense. The disturbance has grown quite large by streamwise position C.

If the coflowing stream velocity is reduced to 28% of the jet exit velocity, the magnitude of the large scale structure is increased significantly as shown in Figure 3. Now the large scale structure is very evident at position A and the structure at position C has grown to the extent that it dominates the jet flow. Perhaps even more interesting is the structure at position B where the turbulent flow is clearly rotating in a clockwise sense. Since the flow is unsteady, the smokelines are not streamlines but streaklines so the interpretation is less straight forward. However it appears that of the two streaklines at position B, the lower one is deflected around the large scale structure while the upper streakline is being entrained into the turbulent large scale structure which is the jet. This interpretation is verified by observing the oscillation with a strobe light which is tuned so that there is a small frequency difference between the strobe frequency and the jet oscillation frequency. Then the jet appears to flap in slow motion and the rotational motion may be clearly seen. Thus, the large scale unsteady structure behaves in the same way as the large scale undriven flow structure described by Roshko<sup>11</sup> and entrains fluid on the upstream side. A similar entrainment pattern for the turbulent wake has been found by Bevilaqua and Lykoudis.<sup>15</sup> The effect may be seen for the larger structure at position C in Figure 18 where the turbulent flow is entraining the coflowing stream on the upstream side of the large scale structure.

Returning now to Figure 2, it may be seen that the turbulent jet produces a large scale structure of its own in addition to that produced by the time dependency. The peaks of smoke on the streaklines closest to the nominal jet centerline all point in a downstream sense, in the same way as those produced by the time dependent structure (position C of Figure 18). Thus, the turbulent unsteady jet produces a "steady" and an unsteady large scale structure but the unsteady portion appears to dominate the flowfield. This may be somewhat analogous to the domination of the large scale structure over the fine scale turbulence in the "steady" jet. Here "steady" is employed to indicate that the jet is steady in the gross view, while there is unsteadiness associated with the turbulence structure.

Both the "steady" and unsteady large scale structures appear to arise through the same, or at least a similar, mechanism. The jet produces a perturbation on its surface. This bulge in the surface grows into a rotating mass of fluid with a vortex-like structure. In the "steady" case the origin and spacing of the structure is not fully understood. In the unsteady case, the

bulges are produced at a known position and frequency and therefore may be easier to analyze.

### 3. Modelling the unsteady jet

To understand the production of the large scale unsteady structure in the unsteady jet, it is useful to construct a very simple phenomenological model of the process. It appears that the growth of the unsteady structure greatly resembles the growth and subsequent breaking of a water wave. This may be seen by examining three positions of the developing large scale structure shown schematically in Figure 19a, where  $u_j(x)$  and  $u_c$  are the jet and coflowing stream velocities, respectively. The original deformation of the free jet surface is a relatively small amplitude wave. This wave travels downstream (left to right) at a velocity  $u_{\text{wave}}$  such that  $u_c < u_{\text{wave}} < u_j$ . Therefore the wave is in a shear flow which causes it to curl in a counter-clockwise direction and entrain fluid into itself. Even without shear, it can be shown that the top of the wave outruns the bottom and curling results.<sup>16</sup> After the curling up is completed, the vortex-like structure continues to entrain fluid. The photographs of Figure 19b are taken from positions A, B & C of Figure 3, where position B has been printed as it would appear on the upper surface of the jet. They clearly verify the schematics of Figure 19a.

If one considers a breaking water wave, the schematic of Figure 19a corresponds to the wave shape at three instants of time, however with the wave traveling from right to left. Position A is the earliest swelling of wave. As the wave travels to the left, its forward face steepens and finally breaks as shown at position B. By position C the wave has broken and resembles a vortex like structure. The energy of the breaking wave is transformed partially into turbulence, which is eventually dissipated as heat, and partially serves to energize the undertow<sup>16</sup> which is the jet velocity itself in the present analogy. The analogy is incomplete, however, because the water wave is driven by gravity and somewhat by viscous effects while the jet structure is entirely a viscous phenomenon. In spite of this, once the viscosity has created a vortex sheet at the interface, the deformation of this sheet may be modelled inviscidly<sup>12,13</sup> with considerable success.

The main point then is not that the steady and unsteady flow structures are the same but rather that they may have similar origins. As the unsteady structure grows from a large amplitude surface wave, so that steady structure may grow from a small amplitude surface wave.

#### 4. Quantitative Confirmation

The unsteady fluidically controlled jet was examined in some detail by employing a hot wire anemometer along with conditioned sampling of the data to reveal the time dependent character of the flowfield. The jet was positioned between two Plexiglas sheets to attempt to minimize the three dimensionality of the field, as shown in Figure 4. The hot wire anemometer was driven through the flowfield by a motorized traversing mechanism which also turns a potentiometer, so the probe position is known at any time.

The data required are the velocities in the jet at a specific instant of time (or alternately, at a specific point in the oscillation cycle, since the oscillation is repeatable). The conditioned sampling method is shown schematically in Figure 9. A third hot wire anemometer is employed to indicate the position of the jet since its signal is maximized when the jet is in the upward orientation. As discussed in Section II, the velocity data is only accepted and recorded when the third hot wire indicates the jet is in the required instantaneous orientation.

The data obtained by the above technique have been reported in some detail in Reference 17. The aim here is to investigate quantitatively the existence of large scale coherent structure in the jet as appears to be evident in the flow visualization experiments described above. Looking back at the schematic of the unsteady jet field in Figure 1, a growing sinusoidal wave traveling downstream, where should one look for the existence of the vortex structure observed in the smoke photographs? The question is answered by another look at the model of Figure 19. As the bulge of the jet flow curls up to create a vortex structure, it necessarily does so by breaking toward the upstream direction (as driven by the slower coflowing stream or ambient fluid). Thus the vortex produced would be expected to exist at a position somewhat upstream of the initial jet bulge, which in this case is the extreme off axis position of the instantaneous jet centerline.

A portion of the jet flowfield, for the case of a frequency of 18 Hz and an extreme downward orientation of the jet at the nozzle exit, is shown in Figure 20a. The lengths of the arrows are proportion to the local velocity and the angles are determined from the measured axial and transverse velocities. The instantaneous jet centerline is also shown, from which it may be estimated that if a vortex is present, it should be centered roughly between 16 and 22 jet diameters downstream. No vortex-like structure is evident in this region.

Several investigators have shown, however, that in order to see the coherent motion of a group of particles, the observer must be travelling with the velocity of the center of mass of those particles. Probably the first examination of this effect was made by Prandtl<sup>18</sup> who photographed a boundary layer by travelling at various speeds relative to the flow. Each photograph then revealed a different coherent structure.

In order to see the structure in the flowfield of Figure 20a., a nominal velocity of the vortex center is assumed and that streamwise velocity subtracted from each of the data points in the field. The result is shown in Figure 20b and clearly shows a vortex located in the very region where one would expect it based on the flow visualization results presented above.

Based on the phenomenological model of Figure 19 and the quantitative results of Figure 20 one can then make more predictions of the location of large coherent vortices in a family of instantaneous jets as shown in Figure 21. The 12 Hz frequency jet is shown for three phase angles, 90°, 180° and 270° or horizontal (sweeping top to bottom), extreme downward or horizontal (sweeping bottom to top) orientation, respectively. The centerline positions of the jets are based on quantitative results. The vortices are drawn in the positions where they might be expected to be found based on the previous results.

Searching at the three positions closest to the nozzle exit, A, C and E leads to the conclusion that coherent vortices do not exist at those positions. This is, however, entirely consistent with the model proposed in Figure 5. It is clear from the flow visualization experiments that it takes some time (or equivalently, distance) for the bulge on the jet to curl up into a coherent structure. The positions near the jet exit simply have not allowed enough time (or distance) for this process to take place.

Looking for the vortex B, the local jet velocity field is shown in Figure 22a. Assuming the vortex center to exist at roughly  $\bar{x} = 22$  and subtracting the streamwise velocity at that point results in the Figure 22b where the vortex structure is evident. It should be emphasized, of course, that the local structure depends upon the velocity of the observer, so subtracting a somewhat different velocity will result in a somewhat different appearance of the vortex. However, the important fact that the vortex is there is clear in any case.

The local velocity field for a phase angle of  $\theta = 180^\circ$  is shown in Figure 23a. Again no vortex structure is seen until the flow is observed from a moving coordinate system as shown in Figure 23b. The vortex appears to be centered

approximately at  $\bar{x} = 10$ . Looking back at the schematic of Figure 21, it may be seen that vortices A, D and F are really one and the same vortex at successive times. Thus an indication of the translational speed of the vortex can be obtained by locating the vortex F, having already found vortex D.

The jet flowfield in the region where vortex F is expected is shown in Figure 24a. In a moving coordinate system the coherent structure of the jet may be seen in Figure 24b. The vortex center is located at approximately  $\bar{x} = 22$ . Then the translational velocity of the vortex between the positions D and F of Figure 21 is

$$V = \frac{\Delta x}{\text{time}} = \frac{(22-10) \frac{1}{24} \text{ ft}}{(1/12 \text{ sec/cycle}) (1/4 \text{ cycle})} = 24 \text{ ft/sec.} = 7.3 \text{ m/sec}$$

The instantaneous centerline velocities corresponding to the locations of vortices D and F are 11.5 m/sec and 10.8 m/sec, respectively. It should be noted, however, that the vortex translational velocity is only an approximate value because the determination of the vortex locations is not precise. A composite view of the streamwise velocity distribution corresponding to the jet in Figures 24a and b is shown in Figure 15a.

Further evidence of the existence of a large scale vortex structure in the unsteady jet may be found in the instantaneous decay of the jet centerline velocity. In the case of steady jets, the centerline velocity decay is a monotonically decreasing function of streamwise distance. In the unsteady jet case, the centerline velocity decay (where the centerline is a quasi-sinusoidal shape) has a typical behavior<sup>17</sup> shown in Figure 25. The velocity decays with streamwise distance, reaches a local minimum and starts to increase again. A peak is reached, where upon the decay begins anew. The location of the peak corresponds to the existence of a vortex at that position, as illustrated in the inset to Figure 25.

Considering the induced velocity distribution due to the vortex and superimposing that velocity on a monotonically decaying centerline velocity results in the typical distribution of Figure 25. Thus the visual observation of a vortex structure in the unsteady jet is consistent with the quantitative measurements, specifically the instantaneous velocity structure and its centerline decay.

## 5. Discussion

The qualitative similarities between the vortex structure in a forced unsteady jet and the vortex structure in a quasi-steady jet (at least one that is

not driven) suggest the possibility of understanding more of the latter by studying the vortex dynamics of the former. This may be true not only for jets but also for the structure of boundary layer flows, particularly those near transition.

## SECTION IV

### MULTIJET FLOWFIELD AS A GUST TUNNEL

#### 1. Background

The development of a time dependent flow test facility has been attempted by a variety of methods. Mitchell<sup>19</sup> employed a technique in which the model was moved in relation to the flow, passing orthogonally through an open jet wind tunnel. Gillman and Bennett<sup>20</sup> studied gusts produced by a set of airfoils mounted in a biplane arrangement on the opposite walls of a wind tunnel. As these airfoils were oscillated in a sinusoidal fashion, they induced an oscillating flow between them. Other methods include employing moving sinusoidal waves in the test section walls,<sup>21</sup> oscillating the inlet section of an open circuit tunnel,<sup>22</sup> an oscillating array of airfoils<sup>23</sup> and circulation control on a set of elliptical airfoils.<sup>24</sup>

The method which is probably the closest to that of the present investigation is due to Simmons and Platzer<sup>25</sup> who employed a pair of jet flaps. Each of the jet flaps is a fluidically oscillating jet driven by a pair of control jets, one on either side.

#### 2. Operation of the Jets

As a consequence of an effort to develop fluidically controlled time dependent jets for application to several diverse problems,<sup>3,9</sup> a new technique was proposed for the construction of a high frequency gust tunnel.<sup>26</sup> A single nozzle was constructed and tested and is shown schematically in Figure 26.

The method of operation of the nozzle is as follows:

The flow passes through the throat of the jet nozzle (Fig. 26) and into a rapid expansion region. Because of the relative proximity of the walls, the flow must attach to one side of the expanded region or the other. This bistable condition can be strongly influenced by a small pressure difference between the two sides of the expanded channel. In a normal fluidic oscillator or a fluidically oscillating jet,<sup>3</sup> this pressure difference is supplied by a feedback system

between the two sides. In the present case, this pressure difference is created by the rotating valves shown on each side of the jet. The valves are rotated out of phase with each other, so that one is open when the other is closed. The resulting flow always attaches to the closed side and thus produces a jet which oscillates from side to side.

### 3. Tunnel Concept

The actual gust tunnel design involves a number of these nozzles and is shown schematically in Figure 27. The tunnel flow passes between the individual nozzles so that the flow actually guides the tunnel flow from side to side.

Some of the potential advantages of this method of gust generation are as follows:

1. High frequency capability
2. Low torque motors required
3. Capable of producing transverse or longitudinal gusts
4. Capable of producing various wave forms
5. Capable of producing programmed transverse disturbances
6. Capable of various phase relationships between components
7. Capable of uniform flow across tunnel

It is the purpose of this paper to present the first results of a subscale multi-jet model of such a gust tunnel and to verify some of the advantages cited above.

### 4. Tunnel Geometry

The actual tunnel geometry is shown in Figure 28, along with the details of the nozzle construction employed here. It may be seen that the scale is rather small, the nozzles having exit sizes of .508 cm. and being 2.54 cm. apart. In addition, the depth of the tunnel is only 2.5 cm. The limited scale leads to some problems because the control valving is not as easily reduced in size as the remainder of the geometry. There is, for example, separation of the tunnel flow from the nozzle body just before the nozzle exit, if the exit velocity is very low.

In spite of the scale problems the nozzles oscillate well and control the tunnel flow as shown in Figure 29 for the case of all nozzles in phase. The flow visualization is accomplished by means of kerosine vapor produced by dripping the kerosine on an inclined resistance heater and entraining the

resulting vapor into the tunnel, between the oscillating nozzles.

The jet exit velocity is 108 m./sec. while the tunnel velocity is 26 m./sec. The resulting Jet Reynolds Number based on nozzle velocity and exit size is  $Re = 3.8 \times 10^4$ . At an oscillation frequency of 60 Hz, the reduced frequency is  $k = .055$  based on the nozzle spacing and an average velocity of 40 m/sec.

#### 5. Hot Wire Surveys

A constant temperature hot wire anemometer is employed to survey the instantaneous velocity field. The particular instrument is a Flow Corporation (now Datametrics) Model 900 anemometer used in conjunction with a pair of Thermo Systems, Inc. linearizers. In order to obtain instantaneous velocity profiles, a triggering system of some sort must be applied to condition the hot wire signal by deciding when to record the time varying data. In previous jet measurements<sup>17</sup> a third hot wire has been employed as the trigger. Although such a method could also be employed here, there is yet a simpler technique. A magnetic pickup is used on one of the rotating slot valves so that the position of the valve (and hence the position of the corresponding jet) is known as a function of time. As shown schematically in Figure 30, the triggering signal from the magnetic pickup is electronically manipulated and used to arm a Schmitt trigger which in turn controls a sample and hold circuit. Thus the hot wire continuously samples the flow velocity, but the signals are only recorded when the flow is in a specified orientation as determined by the rotating valve position. Then all data recorded with the sampling electronics at a given setting apply to the same instant in the oscillation cycle and effectively, the data is instantaneous (as long as the cycles are sufficiently repeatable).

#### 6. Jets in Phase

As discussed in Reference 26, the multi-jet tunnel is conceptually capable of producing both lateral and longitudinal gusts depending on the phase relationship between the various nozzles. If the nozzle flows are all oscillated in phase, they produce a rather large oscillation in transverse velocity (orthogonal to the mean tunnel direction). This may be seen in Figure 31 and 32.

Figure 31 shows the instantaneous velocity distribution produced by the nozzles at the instant the nozzle flow is in the extreme upward position. Since the distance from the nozzle exits is not large (20 nozzle exit sizes), there is still the evidence of the jet nozzles in the streamwise velocity profiles. However, even this close to the exits, the velocity ratio between the peaks and valleys has

been reduced from more than four at the nozzle exits to less than two. Perhaps more important is the existence of a strong lateral velocity, equal to more than 3% of the jet exit velocity or almost 10% of the local average streamwise velocity. The dashed line on the velocity profiles is the zero value before correction for a bias in the mean tunnel direction.

For comparison, the streamwise and transverse velocities for the case of the jets in the instantaneous downward position are shown in Figure 32. Thus Figure 31 and 32 are the same flowfields with a  $180^\circ$  difference in phase. There is some shift in the streamwise velocity but an even larger effect may be seen in the transverse velocity. Thus the difference in the velocity component between these two particular points in the cycle, is roughly 15-20% of the mean streamwise velocity.

If the test section is moved to a position farther downstream relative to the nozzle exits, then the non-uniformity in the streamwise velocity will be rapidly reduced while the transverse oscillations with time will likewise decrease. The position of the test section is dictated, to some extent, by the fluid dynamic problem to be simulated. Farther downstream is probably best for application to aircraft gust response studies while the conditions reflected by Figures 31 and 32 are perhaps more appropriate to the study of cascade wakes. The decay of the jet's velocity and its mixing with the coflowing tunnel stream is shown in Figure 33 for the case of all jets in phase. Thus by 50 jet widths downstream, the velocity non-uniformity is only about 7% based on the jet exit velocity.

An important potential of the present gust tunnel concept is the ability to create a transverse disturbance which passes across the tunnel. As discussed in Reference 26, such a disturbance can be generated by designing the rotating control valves in such a way as to cause the jets to periodically skip an oscillation. That is, a jet remains attached to one side while the remainder of the jets proceed through another cycle. This skipping occurs in successive nozzles on successive cycles, so the disturbance marches across the tunnel test section. This effect can then be examined as an analogue to rotating stall. However, in order to include the required changes in the control valves, the scale of the experiment must be considerably increased and thus cannot be examined with the existing apparatus. An alternate method of achieving this effect is discussed below in relation to a phase lag between the jet oscillations.

One difficulty which appears in Figures 31 and 32, and will also be obvious in the out of phase results, is the end effect of the set of nozzles. These are a finite number of nozzles in the tunnel and since the nozzle exit velocities are larger than the tunnel velocity, the tunnel stream is really entrained by the nozzle flow. Thus the entire set of nozzles entrains the entire tunnel flow, producing an in flow at the ends of the nozzle bank (i.e., a flow toward the center of the tunnel). The effect may be seen in the upper portion of Figure 31 when the expected upflow is not seen but is countered by the entrained flow leading to a very small downward flow. Likewise, in the results of Figure 32, the expected downflow at the lowest nozzle is countered by an entrained velocity (producing an upflow) and the result is practically a zero transverse velocity. It is therefore clear that for application this effect may be minimized by employing a larger number of nozzles and then making use of the more central portions of the velocity field.

An alternate point of view is to place the hot wire probe in the flow at a certain position and then examine the change of velocity at that position as a function of time (or perhaps more accurately, as a function of phase angle). If the time varying velocities at various streamwise positions are then plotted on the same time (or phase angle) scale, the gusts traveling downstream will be clear. This is the effect seen in Figure 34, where the transverse velocities on the tunnel centerline at four streamwise positions are plotted as functions of phase angle. It may be clearly seen that the waves of transverse velocity (or gusts) travel downstream and that there is the expected phase lag between their appearance at various positions. The arrows indicate the progression of the same wave downstream.

#### 7. Jets Out of Phase

In an attempt to produce longitudinal gusts, the relative phases of the four jets are set such that the two upper jets are  $180^\circ$  out of phase with the two lower jets. The two sets of jets are then alternately aimed toward and away from each other. The flowfield corresponding to these two situations measured at a position twenty jet thicknesses downstream, are shown in Figures 35 and 36 respectively. It may be seen that in each case the transverse velocity is roughly zero at the tunnel centerline (after being corrected for the tunnel bias) and consistent with the jet orientations for positions off the tunnel axis.

Especially interesting is the possibility of using the tunnel centerline position as a test section. Comparing the centerline velocities of Figure 35 and 36, it is clear that a longitudinal gust of roughly 25% of the local velocity is produced.

The effect of the entrainment of the tunnel flow by the unsteady jets themselves is again evident, especially in the upper portion of Figure 36. There the  $v$  velocity component is expected to be positive (upward) but in fact is somewhat downward (negative) reflecting the presence of the entrainment velocity. As discussed above, this effect can be minimized by including more nozzles in the gust tunnel design, or contouring the tunnel walls.

Taking a more detailed look at the centerline velocity change with time, the results are shown in Figure 37 for various streamwise positions from  $\bar{x} = 15$  to  $\bar{x} = 30$ . The existence of a wavelike structure at any instant may be seen by looking at the velocities at the various positions at a particular time. In addition, the time lag as the wave travels downstream is evident as well as a distinct change in the shape of the wave. As it moves downstream, the high velocity portion of the wave expands, probably due to the mixing of the jet itself.

#### 8. Phase Lag Between the Jets

Consider an alternate phase relationship between the various nozzles as shown in Figure 38 and 39. There is a phase lag of  $45^\circ$  between each of the nozzle flow orientations, starting from the top. In Figure 38, the top nozzle is in the extreme upward orientation, the second nozzle lags it by  $45^\circ$  phase while the third lags it by  $90^\circ$  phase and is therefore horizontal at the instant shown. The fourth nozzle is instantaneously oriented at  $45^\circ$  phase below the horizontal,  $135^\circ$  behind the top nozzle. The phase angles do not, of course, correspond exactly to the physical angles. The arrows on the flow vectors indicate the direction in which the exit flow orientation is progressing. Thus the top jet is in the extreme position and stationary while the rest of the jets are moving toward the top.

The phase positions shown indicate the mechanical position of the control valves. The actual position of the jets can be somewhat different because there is some hysteresis in the attachment of the jets. Thus, in the results of Figure 38, the third nozzle is really inclined somewhat more upward resulting in a wider angle between the flow from the third and fourth nozzles. This appears as a widening between the velocity peaks formed by these jets, as they move downstream.

If the upper nozzle is in the extreme downward orientation and the same  $45^\circ$  phase lag is specified, the velocity profiles are shown in Figure 39. In this case, it again appears that jet produced by nozzle number three is somewhat ahead of the phase position indicated by the mechanical positions of the control valves. Thus the instantaneous orientation of the jet emitted by nozzles 3 and 4 is toward each other and they produce the double peak shown in Figure 39. This double peak eventually merges into a single peak farther downstream, as was also the case in the results of Figure 38 where the top two jets merged into a single peak. However, if there is a phase lag between the jets, even though the upper jets are  $180^\circ$  out of phase between Figures 38 and 39, the instantaneous flowfields have no such relationship.

A method was proposed above to produce a disturbance marching transversely across the wind tunnel. The results in Figures 38 and 39 suggest an alternate method which will not require more intricate control by means of the rotating valves on either side of the nozzles. The mechanism is simply to run one of the jets at a different frequency from the other nozzles which may be in phase with each other. Thus, the out of phase jet will periodically reinforce one of the others and this reinforcing will run transversely across the tunnel. It will, however, run back and forth and therefore requires more adaptation to be useful for a rotating stall analog.

#### 9. Preliminary Airfoil Tests

In order to have some indication of the interaction of the multi-jet gust tunnel flow with a body in the test section, preliminary tests are performed with a simple cambered airfoil at an angle of attack of  $18^\circ$ . The jet frequency is 60 Hz and the flow visualization is again accomplished by vaporizing kerosene. The results are shown in Figure 40 for every  $60^\circ$  of phase angle.

In Figure 40a, the nozzle flow is in its extreme upward position, although the phase lag of the flow farther downstream shows a portion of the flow in a downward motion almost following the shape of the airfoil. With a  $60^\circ$  phase angle, Figure 40b, the time history of the flow may be clearly seen as it travels downstream. The jets are in an orientation which is almost horizontal. Farther downstream, the prior upward orientation of the jet is evident in the curling of the streakline over the airfoil. It should be noted here that the smokelines are streaklines, not streamlines. Thus they do not particle trajectories but rather the position of a group of particles which have all passed through the same point at various times.

The phase lag between the orientation of the jets at the nozzle exits and the direction of the flow over the airfoil surface appears to be approximately  $180^\circ$ . This may be seen in the cases of  $0^\circ$  and  $360^\circ$  phase angle (both the same orientation, of course). In each case the nozzle exit flow is in the extreme upward position while the flow over the airfoil (and even farther away), is in the downward orientation.

In these preliminary tests, employing this particular airfoil at  $18^\circ$  angle of attack, there appears to be no unsteady separation. With the phase lag discussed above, it might be expected that separation be most likely at a phase angle of  $180^\circ$ , since the flow over the airfoil will then be in the upward orientation. No separation is evident at  $180^\circ$  and in fact the flow is clearly attached at angles to either side of that value,  $120^\circ$  and  $240^\circ$ . Further tests will be required to see if the gust flow can lead to intermittent separation and thereby a decrease in the mean lift coefficient.

#### 10. Discussion

Subscale experiments with a gust tunnel driven by a bank of unsteady oscillating nozzles operating in a fixed phase relationship indicate that such a device can be employed as a means to generate both lateral and longitudinal gusts. The percentage gust can be rather large, approaching 20% of the mean flow value. For smaller percentage gusts, small spacial deviations in the streamwise velocity can also be produced. No unsteady separation was found in preliminary airfoil tests but it is expected that this will occur under some circumstances.

### SECTION V

#### LINEARIZED UNSTEADY JET ANALYSIS

##### 1. Background

The objective of this section is to propose a method of analysis which may be applied to the unsteady jet flowfields discussed in the previous section.

Examples of the types of jets which may be treated by the present analysis are shown in Figures 41-43. The jet exit position of Figure 41 oscillates from side to side and produces a relatively constant magnitude streamwise wave. In Figure 42 the velocity vector at the jet exit oscillates in direction and produces a growing streamwise wave. The unsteadiness of Figure 43 consists of

a sinusoidal change with time of the mass flow at the jet exit and thus produces a nominally constant amplitude wave pattern.

The mathematical complexity of time dependent flows is such that one usually is forced to resort to one of three possible attacks:

1. A fully numerical solution of the governing equations
2. A phenomenological model
3. The use of limiting assumptions which simplify the governing equations.

A fully numerical solution is possible but requires the dedication of very significant amounts of time and effort. A recent interesting example of a phenomenological model is presented by Simmons, Platzner and Smith,<sup>27</sup> who assume that the unsteady jet may be decomposed into a number of steady jets which exist during short intervals at the nozzle exit and produce short bursts along the steady jet trajectories.

Much of the unsteady flow work employing limiting assumptions is based in principle on the celebrated work of Lin,<sup>28</sup> who analyzed the boundary layer beneath a time dependent external flow. Lin's technique is limited to high frequencies and benefits from the fact that the particular problem allows the specification of an unsteady static pressure distribution within the boundary layer. The extension of Lin's analysis to the jet case is hampered by the fact that the time dependent pressure distribution is unknown and there is no comparable technique to Lin's use of the unsteady Bernoulli equation.

The application of Lin's technique to unsteady jets was carried out by McCormack, Cochran and Crane<sup>29</sup> for the case of a jet vibrated from side to side at high frequency (see Figure 41). However, the strict application of the Lin analysis leads to the conclusion that the convective term in the momentum equation is negligibly small. This result is not acceptable to McCormack, et al., since it is clear that the convective term is of importance as in the steady flow case. Thus, McCormack et al.<sup>29</sup> present a phenomenological argument that the convective term must be included (in spite of the fact that the analysis excludes the term) and proceed to assume a linear form for it which then results in a linear equation. The analysis, therefore, is a mixture of types 2 and 3 above.

The present analysis follows the spirit of the linearized jet analyses due to Pai.<sup>30</sup> The linearization of the equations is achieved by an order of magnitude analysis which is rigorous and removes the need for a phenomenological argument. The requirement of high frequency is also removed and a technique described for including a time dependent pressure distribution which is produced by the motion of the jet.

## 2. Relationship Between Steady and Time Averaged Flows

The objective of this study is to determine the effect of the unsteady flow components on the time averaged flow. That is, what advantages does the unsteady flow hold in terms of steady state mass and momentum transfer? The answer should appear in a steady flow relation including time averaged effects of the unsteady components.

The two-dimensional boundary layer equations are

$$\frac{\delta u}{\delta t} + u \frac{\delta u}{\delta x} + v \frac{\delta u}{\delta y} = -\frac{1}{\rho} \frac{\delta p}{\delta x} + \frac{1}{R} \frac{\delta^2 u}{\delta y^2} \quad (1)$$

$$\frac{\delta u}{\delta x} + \frac{\delta v}{\delta y} = 0 \quad (2)$$

where each term is non-dimensionalized so  $R$  = Reynolds Number.

Consider the velocity profiles shown in Figure 44. The initial jet velocity is a function of time while the coflowing stream velocity is steady. The independent variables can then be separated into time averaged (  $\bar{\phantom{x}}$  ) and time dependent (  $\prime$  ) quantities with  $U$  = coflowing stream velocity.

$$\begin{aligned} u(x, y, t) &= U + \bar{u}(x, y) + u'(x, y, t) \\ v(x, y, t) &= \bar{v}(x, y) + v'(x, y, t) \\ p(x, y, t) &= \bar{p}(x, y) + p'(x, y, t) \end{aligned} \quad (3)$$

Substituting the expansions of the independent variables into the momentum equation and taking the time average of each term results in

$$(U + \bar{u}) \frac{\delta \bar{u}}{\delta x} + \bar{v} \frac{\delta \bar{u}}{\delta y} = \frac{\delta \bar{p}}{\delta x} - \left[ \overline{u' \frac{\delta u'}{\delta x}} + \overline{v' \frac{\delta u'}{\delta y}} \right] + \frac{1}{R} \frac{\delta^2 \bar{u}}{\delta y^2} \quad (4)$$

It may be seen that the effect of the unsteady terms on the average velocity is the same as an additional (or artificial) pressure gradient. Thus, if the time dependent velocities are known, the bracketed term can be evaluated and the effect of the unsteadiness on the mean flow determined (See Ref. 31).

## 3. Determination of Time Dependent Velocities

The objective is, therefore, to determine the unsteady velocity components  $u'$  and  $v'$ , to evaluate the bracketed term in Eqn. 4 and thereby to find the average velocity distribution  $U + \bar{u}$ ,  $\bar{v}$ . Approximate solutions for  $u'$  and  $v'$  can be found

by the following order of magnitude analysis.

Consider the case where the steady state jet velocity deviates only slightly from the coflowing stream velocity and, as well, the unsteady velocity components are small compared to the coflowing stream velocity.

Mathematically -

$$\bar{u}, \bar{v}, u', v', \ll U \quad (5)$$

Expanding the momentum equation (1) by the steady and unsteady velocity components (Eqn. (3)) results in

$$\begin{aligned} \frac{\delta u'}{\delta t} + (U + \bar{u} + u') \frac{\delta}{\delta x} (U + \bar{u} + u') + (\bar{v} + v') \frac{\delta}{\delta y} (U + \bar{u} + u') \\ = \frac{\delta}{\delta x} (\bar{p} + p') + \frac{1}{R} \frac{\delta^2}{\delta y^2} (U + \bar{u} + u') \end{aligned} \quad (6)$$

In view of the assumptions (5), all products of small variables in Eqn. (6) are neglected and only terms up to first order in the small variables are retained.

(Note also that  $U = \text{constant}$ )

$$\frac{\delta u'}{\delta t} + U \frac{\delta \bar{u}}{\delta x} + U \frac{\delta u'}{\delta x} = - \frac{\delta p}{\delta x} - \frac{\delta p'}{\delta x} + \frac{1}{R} \left( \frac{\delta^2 \bar{u}}{\delta y^2} + \frac{\delta^2 u'}{\delta y^2} \right) \quad (7)$$

The steady and unsteady portions of Eqn. (7) may be separated by taking the time average of (7):

$$U \frac{\delta \bar{u}}{\delta x} = - \frac{\delta p}{\delta x} + \frac{1}{R} \frac{\delta^2 \bar{u}}{\delta y^2} \quad (8)$$

and subtracting this from (7) to yield

$$\frac{\delta u'}{\delta t} + U \frac{\delta u'}{\delta x} = - \frac{\delta p'}{\delta x} + \frac{1}{R} \frac{\delta^2 u'}{\delta y^2} \quad (9)$$

This, then, is the governing equation for the unsteady velocity distribution for the jet in Figure 44 with the small perturbation assumptions of equation (5). The initial condition may be seen from Figure 44 to be a top hat velocity profile whose magnitude is a function of time. The lateral boundary conditions are that

$$\lim_{y \rightarrow \pm \infty} u' = 0 \quad (10)$$

The unsteady pressure gradient may, in general, be a function of position and time,

$$\frac{\delta p'}{\delta x} = f(x, y, t), \quad (11)$$

but is not known directly in the jet case. In a later section a technique is described which allows an approximation to the unsteady pressure distribution. For the present, the pressure will be neglected and thus the governing equation reduces to

$$\frac{\delta u'}{\delta t} + U \frac{\delta u'}{\delta x} = \frac{1}{R} \frac{\delta^2 u'}{\delta y^2} \quad (12)$$

This equation is similar to that developed in Reference 29 but in this case it is not limited to high frequencies and requires no phenomenological arguments. The initial and boundary conditions are the same as those for Equation (9). The solution to the linear Equation (12) is

$$u' = \frac{\alpha U}{2} e^{(wT - wX)} \left[ \operatorname{erf} \left( \frac{1-y}{2\sqrt{X}} \right) + \operatorname{erf} \left( \frac{1+y}{2\sqrt{X}} \right) \right] \quad (13)$$

where

$$T = t/R, \quad X = x/RU, \quad \alpha = \left. \frac{u'}{U} \right|_{x=0}$$

and the error function is defined as

$$\operatorname{erf} \eta = \frac{2}{\sqrt{\pi}} \int_0^\eta e^{-\eta^2} d\eta \quad (14)$$

The actual form of the exponential depends upon the initial condition on the jet. If the initial condition is that the unsteady flow varies about some mean as a cosine function, then the solution is -

$$u' = \frac{\alpha U}{2} \cos(wT - wX) \left[ \operatorname{erf} \left( \frac{1-y}{2\sqrt{X}} \right) + \operatorname{erf} \left( \frac{1+y}{2\sqrt{X}} \right) \right] \quad (15)$$

#### 4. Determination of the Steady Artificial Pressure Gradient

The overall continuity Equation (2) can be expanded by the velocity definitions, Eqn. (3), and then split into steady and unsteady forms,

$$\frac{\delta \bar{u}}{\delta x} + \frac{\delta \bar{v}}{\delta y} = 0 \quad \text{and} \quad \frac{\delta u'}{\delta x} + \frac{\delta v'}{\delta y} = 0 \quad (16)$$

from which it follows that

$$v' = - \int_0^y \frac{\delta u'}{\delta x} dy \quad (17)$$

Then from Eqn. (15) and (17)

$$\begin{aligned} v' = & -\frac{\alpha w}{2} \sin(wT - wX) \int_0^y \left[ \operatorname{erf}\left(\frac{1-y}{2\sqrt{X}}\right) + \operatorname{erf}\left(\frac{1+y}{2\sqrt{X}}\right) \right] dy \\ & \frac{\alpha \cos(wT - wX)}{4\sqrt{\pi} X^{3/2}} \int_0^y \left[ \exp\left(-\left(\frac{1-y}{2\sqrt{X}}\right)^2\right) (1-y) \right. \\ & \left. + \exp\left(-\left(\frac{1+y}{2\sqrt{X}}\right)^2\right) (1+y) \right] dy \end{aligned} \quad (18)$$

The resulting artificial pressure gradient term is

$$\begin{aligned}
 & \left[ \overline{u' \frac{\delta u'}{\delta x}} + \overline{v' \frac{\delta u'}{\delta y}} \right] \\
 &= F_1 F_3 \overline{\cos(wT - wX) \sin(wT - wX)} \\
 &+ F_1 F_4 \overline{\cos^2(wT - wX)} \\
 &+ F_6 F_9 \overline{\sin(wT - wX) \cos(wT - wX)} \\
 &+ F_7 F_9 \overline{\cos^2(wT - wX)} \quad (19)
 \end{aligned}$$

where the  $F_i$  terms are independent of time. The averaging of the trigonometric terms over one cycle results in

$$\begin{aligned}
 \overline{\cos^2(wT - wX)} &= \frac{1}{2} \\
 \overline{\sin(wT - wX) \cos(wT - wX)} &= 0 \quad (20)
 \end{aligned}$$

so -

$$\left[ \overline{u' \frac{\delta u'}{\delta x}} + \overline{v' \frac{\delta u'}{\delta y}} \right] = \frac{1}{2} F_1 F_4 + \frac{1}{2} F_7 F_9 \quad (21)$$

where

$$\begin{aligned}
 F_1 &= \frac{\alpha U}{2} \left[ \operatorname{erf} \left( \frac{1-y}{2\sqrt{X}} \right) + \operatorname{erf} \left( \frac{1+y}{2\sqrt{X}} \right) \right] \\
 F_4 &= \frac{-\alpha}{4\sqrt{\pi}} X^{3/2} \left\{ \exp \left[ -\left( \frac{1-y}{2\sqrt{X}} \right)^2 \right] (1-y) + \exp \left[ -\left( \frac{1+y}{2\sqrt{X}} \right)^2 \right] (1+y) \right\} \\
 F_7 &= \frac{\alpha}{2\sqrt{\pi}} X^{1/2} \left\{ \exp \left[ -\left( \frac{1-y}{2\sqrt{X}} \right)^2 \right] + \exp \left[ -\left( \frac{1+y}{2\sqrt{X}} \right)^2 \right] \right\} \\
 F_9 &= -U F_7
 \end{aligned} \tag{22}$$

With the artificial pressure gradient known, the steady state velocity distribution may be found numerically from Eqn. (4).

It should be noted that the final solution of Eqn. (4) cannot be a function of magnitude of the jet frequency since none of the terms in Eqn. (22) depend on frequency. The importance of this fact will become apparent in the next section.

##### 5. Experimental Observations

The jet flow illustrated in Figure 42 has been investigated experimentally, as shown schematically in Figure 4, to determine the unsteady inputs into the time averaged jet behavior. The data are taken by a two channel hot wire anemometer probe, linearized, averaged, and read out on a set of digital voltmeters. The average is found by an electronic filter designed for this experiment by McCormick.<sup>32</sup> The jet nozzle is fluidically controlled, as shown in Figure 45, and is based on a design by Viets.<sup>3</sup>

A set of time averaged velocity profiles showing the typical development of the jet in the streamwise direction was shown in Figure 6. The double peaked profiles are caused by the time dependent flow inclination at the nozzle exit and disappear as the mixing progresses downstream.

The most important data from the point of view of the present analysis is shown in Figure 46; the comparison of steady half width growth rates for the

same jet at various oscillation frequencies. The half width is defined here as the distance from the jet centerline to the position on the profile where the velocity is half the maximum velocity found on the profile. It may be seen that there is an appreciable effect of frequency on the jet half width growth, with the minimum growth at a frequency of zero, i.e. the steady two dimensional jet.

If one examines the time averaged term which reflects the effect of unsteadiness on the mean velocity distribution, Equation (21), it can be seen that this term is not a function of frequency. This is true since none of its components [Eqn. (22)] depend on frequency. There are three strong possibilities for this discrepancy.

- a. The analysis is linear while the jet is non-linear. ———
- b. The analysis is applicable but the eddy viscosity is not the same as the steady state (a very likely situation) and is, in particular, a function of frequency. ———
- c. The time dependent pressure distribution in Equation (9) is not zero as was assumed earlier in the analysis but is really a function of frequency. ———

This possibility is examined in the following section.

#### 6. Effect of a Time Dependent Pressure Variation

The basis for an unsteady pressure distribution is the interaction between the unsteady jet and the coflowing stream. If one considers the simplest case of a jet which does not mix with the ambient fluid, then the jet surface appears as a traveling sinusoidal wave to the coflowing stream. The inclusion of mixing modifies the shape of this wave but near the jet exit the shape is still very nearly sinusoidal.

The simplest model for the pressure variation produced by a wave pattern is that produced by the inviscid flow over a wavy wall, shown in Figure 47. A linearized treatment of this problem is given by Liepmann and Roshko<sup>33</sup> and results in the pressure distribution

$$P = P_{\infty} (1 - B \epsilon \alpha \sin \alpha x) \quad (23)$$

where B depends upon the freestream conditions,  $P_{\infty}$  is the freestream pressure and the other variables are defined in Figure 47. It may be seen that the pressure variation is in phase with the wall shape.

The real jet case is, of course, a viscous problem (as is the real wavy wall

case). Thus, the pressure dependence is not as straightforward as indicated above. This has been demonstrated experimentally by Kendall,<sup>34</sup> who studied a mechanical wave traveling relative to a freestream. Kendall's results indicate a phase shift between the wall shape and the pressure distribution. The magnitude of the phase shift depends upon the ratio of the wave speed to the coflowing stream velocity. For a wave speed approximately equal to the coflowing stream velocity, the phase shift is approximately 10° downstream.

With the velocity varying as a cosine function as in Eqn. (15), the static pressure should vary as a sine function. In addition there must be a phase shift and the boundary conditions require that the pressure approach the limit of the freestream pressure as the distance from the jet increases. The pressure dependence satisfying these conditions as well as the requirement that the pressure be proportional to the square of the velocity difference between the coflowing stream and wave speed is

$$p' = - \frac{C_p \rho (U - c)^2}{2} e^{-\sqrt{R} |y|} \sin \left[ w(T - T_0) - wX \right] \quad (24)$$

where  $C_p$  may be obtained from Kendall.<sup>34</sup> Including this term in the governing differential Equation (9) gives rise to another term in the solution for  $u'$  in order to balance the  $\frac{dp}{dx}$  term.

Then

$$u' = u'_{p'=0} - \frac{C_p \rho (U - C)^2}{U/w} e^{-\sqrt{R} |y|} \cos \left[ w(T - T_0) - wX \right] \quad (25)$$

The main point here is that  $u'$  now is a function of frequency and therefore the bracketed term in Eqn. (4) is also a function of frequency. Thus the inclusion of the time dependent pressure allows the prediction of an average velocity  $\bar{u}$  which depends upon frequency.

Thus the unsteady flowfield generated by a time dependent jet can be treated by a linearized attack which is not limited by frequency constraints and evolves through a rigorous simplification of the equations of motion.

## SECTION VI

### FORCED UNSTEADY FLOW OVER A WING

#### 1. Background

The unsteady jet methods discussed in the previous sections lead to performance improvements which are due to the increased mixing rate between the jet and the surroundings. In the present section, a mechanical device will be examined which drives the flow near a wall to be unsteady. The origin of the present mechanical system lies in experiments on oscillating airfoil sections. The airfoil, shown in Figure 48a, is oscillated in a sinusoidal manner about a mean angle of attack.

As reported by McCroskey,<sup>35</sup> Kramer<sup>36</sup> was the first investigator to discover that such a dynamic arrangement delayed the onset of stall. That is, the flow remained attached to the upper surface at higher angles of attack in the dynamic case than in the static condition. Several investigators have performed flow visualization studies and found that the oscillating airfoil produces a vortex structure on the upper surface as shown in Figure 48b. Apparently the vortices act to energize the boundary layer on the airfoil and thereby delay separation. A visualization of this flowfield, due to McAllister and Carr<sup>37a</sup> is shown in Figure 49 employing hydrogen bubbles. The sense of the rotation is in the clockwise direction<sup>37b</sup> as in Figure 48b.

For most applications, the oscillation of the entire airfoil to produce the desired vortex structure is not really feasible. However, a similar vortex structure may be generated by a number of simple techniques, one of which is illustrated in Figure 50. The vortices are created by a cam shaped rotor moving in the counter-clockwise direction as shown. Each time the rotor surface discontinuity sweeps by, a vortex is generated in much the same manner as the recirculation region behind a rearward facing step but with increased strength. The vortex spacing depends upon the local velocity and the frequency of generation. The actual geometry of the airfoil used in the present experiments is shown in Figure 51. A single static pressure tap has been incorporated to allow a pressure determination of the rotor's utility in the stalled regime.

#### 2. Flow Visualization

The experimental setup, as assembled in the low speed flow visualization tunnel is shown in Figure 52. The model has a span of 12.7 cm. and since it

does not span the tunnel, end walls are added to promote the two dimensionality of the flow. The tunnel itself is a low turbulence open circuit smoke flow visualization channel with a 30.48 cm. square test section and a nominal speed of 8 m/sec. The Reynolds Number, based on the airfoil chord, is approximately 100,000. The smoke is generated by vaporizing kerosene on an inclined resistance heater and entraining the vapor into the tunnel inlet.

The flow produced by the rotor mounted in a flat plate is shown in Figure 53. The flow is from left to right and the rotor location is indicated. The vortex structure may be seen moving downstream until it appears to "burst" in a fashion reminiscent of transition. This does not mean that the vortex is destroyed but rather that the external laminar flow becomes turbulent, probably by entrainment into the vortex structure itself.

On the airfoil, separation first occurs in a limited fashion at an angle of attack of  $14^\circ$  and the flow is fully separated at  $20^\circ$ . This is determined by observation of the smoke flow structure as well as pressure measurement at the single static pressure port shown in Figure 51. The pressure measurements will be discussed in the next section.

The structure of the flow about the airfoil at an angle of attack of  $20^\circ$  and the rotor withdrawn into the body is shown in Figure 54a. In order to avoid acoustic interaction between the flow and the rotor cavity, the cavity has been covered by tape. (Although some distinguishable tones were observed at lower angles of attack, none were found in vicinity of the separation angle). Without any other changes (except removing the tape) the rotor described above is activated at a rotational frequency of 2400 rpm and the resulting flow visualization shown in Figure 54b.

For the sake of clarity, a tracing of the smoke streamline patterns is shown in Figure 55a. The effect of the active rotor is to draw the streamlines down closer to the surface of the airfoil and thereby reduce the size of the separated region. In addition, a streamline which passes below the airfoil in the case of no rotor activity ( $\omega = 0$ ), appears above the airfoil for  $\omega = 2400$  rpm. This indicates an increase in the airfoil lift and a reduction in the upper surface pressure (as will be verified below).

The effect of an intermediate rotor speed is shown in Figure 55b which compares the streamline pattern for  $\omega = 1800$  rpm to that for  $\omega = 2400$  rpm. The intermediate

frequency also produces the appearance of an additional streamline above the airfoil but the deflection of the streamlines toward the upper surface is not as pronounced as at the higher frequencies.

Thus, based on the flow visualization observations, the active rotor produces a vortex pattern above the airfoil which energizes the boundary layer and reduces the size of the recirculation region. The instantaneous flow structure at an angle of attack of  $20^\circ$  and a rotor frequency of 1000 rpm is shown in Figure 56 and compared to the oscillating airfoil at an instantaneous angle of attack of  $21^\circ$  as shown in Figure 49. The similarity between the two flow structures may be clearly seen.

### 3. Quantitative Results

A single static pressure port is built into the airfoil section at the 63% chord position as shown in Figure 51. Readings are taken at this position in order to verify the interpretation of the flow visualization results presented in the preceding section. The variation of the pressure at this point with rotor speed is shown in Figure 57 for three different angles of attack. The first,  $\alpha = 15^\circ$ , corresponds to slight separation. At  $\alpha = 18^\circ$  the flow is more completely separated and by  $\alpha = 20^\circ$  the flow is fully separated. While  $P$  is the pressure at the indicated static pressure port,  $P_{fs}$  is the freestream static pressure upstream of the airfoil location. The difference between the freestream static pressure and the pressure on the airfoil are presented versus rotor frequency. The pressure difference is non-dimensionalized with the same pressure difference at  $\omega = 0$ .

From the point of view of performance, the optimum condition is to maximize the pressure difference since this implies a minimum pressure on the airfoil (because  $P_{fs}$  is unchanged by the rotor activity). For  $\alpha = 15^\circ$ , the maximum pressure difference occurs at 500 rpm and from there the performance decreases. The reduction is expected since in the limit of very high frequency, the flow cannot react quickly enough and therefore the problem is again reduced to a steady flow as far as the fluid is concerned. A similar pressure variation is found at the intermediate angle of attack,  $\alpha = 18^\circ$ . At  $\alpha = 20^\circ$ , the flow is fully separated and the static pressure port is more deeply submerged in the separated flow. The maximum pressure difference is now at a higher value of  $\omega$ . The precise location cannot be seen due to a speed limit on the present experimental facility. The

pressure difference exceeds 35% at  $\alpha = 20^\circ$  and implies a similar increase in lift. However, in the absence of complete pressure distributions along the airfoil surface, a definitive statement on the change in lift cannot be made.

The variation of the single static pressure with angle of attack of the airfoil is presented in Figure 58. Again the pressure difference parameter between the upstream static and the airfoil static pressure is employed, this time non-dimensionalized with the same difference at  $\omega = 0$  and  $\alpha = 0$ . Considering first the inactive case ( $\omega = 0$ ), the pressure parameter initially rises with angle of attack (due to a drop in  $P$ ). A maximum is reached at about  $15^\circ$  where separation becomes evident. As the separation increases, the pressure parameter decreases (due to an increase in  $P$ ) until the flow is fully separated at approximately  $20^\circ$ . A further increase in angle of attack again increase the pressure parameter. From this point of view, the separation process can be seen as delaying the rise of this pressure parameter (or slowing the decrease of  $P$ ).

If the maximum values of the pressure parameter obtained at a given  $\alpha$  (regardless of the necessary  $\omega$ ) are plotted, they lie in roughly a straight line with the initial pressure rise before separation. Thus the rotor activity may be viewed as reducing the effect of separation, specifically on the upper surface pressure and, by implication, on the airfoil lift.

#### 4. Discussion

The purpose of the present section is not simply to propose the vortex rotor as a method to delay separation, but rather to point out the utility of a time dependent method of boundary layer control. In this regard, there is no assurance that the rotor method is superior to, say, an oscillating plate<sup>38a,b</sup> which alternately protrudes from and withdraws into the surface of the airfoil. The choice of the rotor was due to the obvious vibration advantages of a rotary motion over the reciprocating motion. This is especially true if the rotor is designed so that it is dynamically balanced. There are certainly other time dependent devices which are capable of producing the same vortex structures, such as an oscillating air brake configuration.

No attempt has been made to optimize the performance of the rotor in terms of position on the airfoil or size relative to the boundary layer thickness. The boundary layer in the present experiment is thinner than the protrusion of the

rotor. However, in other experiments related to the vortex generation upstream of a ramp, (see following section) the boundary layer was substantially thicker than the protrusion of the rotor and the boundary layer was turbulent. Neither of these conditions had any detectable negative influence on the ability of the rotor to generate vortices.

As noted in the description of the experiment, to obtain the base case of no rotor, the rotor is withdrawn into the airfoil and the cavity covered with tape. The purpose is to avoid an acoustic interaction with the cavity flow which could have a strong effect on the flow over the airfoil. Such a tunable cavity which improves the ability of the flow to remain attached has been proposed by Quinn.<sup>39</sup> The acoustic disturbance produced by the cavity appears to energize the boundary layer. The acoustical effect has been observed in the present experiment with untaped cavities at lower angles of attack. Since the present cavity is not tunable (except in the sense of a change the static position of the rotor), it would not be expected that the acoustic effect would be everywhere evident.

Both the acoustic effect and the present mechanical method are examples of employing unsteady flow in an advantageous manner. The acoustical method is attractive because of its relative simplicity since it only requires an adjustable cavity. The mechanical method reduces the complexity of the cavity but requires the additional input of energy into the rotor. It does, however, have the potential advantage of allowing a variable input of energy into the boundary layer control.

Thus the use of time dependent lateral vortices to energize the boundary layer appears to warrant further investigation in terms of more quantitative results and optimization of the configuration.

## SECTION VII

### UNSTEADY FLOW OVER A REARWARD FACING RAMP

#### 1. Background

The control of boundary layers in an adverse pressure gradient is of interest in a variety of applications where separation is to be avoided. This is, of course, especially true for transportation systems where the desire to reduce drag is driven by economic and speed objectives. In addition, aircraft need to

avoid separation in order to maintain the required lift force.

Boundary layer control has historically emphasized three methods; blowing, suction and vortex generation. The blowing method adds energy in the lower boundary layer and suction removes the low energy flow from the same region. The vortex generation method neither adds nor removes mass but rather causes an interchange of mass between the outer flow and the lower boundary layer. Thus the flow near the wall is energized and able to overcome a larger pressure gradient. The vortices are of two types, longitudinal (or streamwise) vortices which are continuously created at a streamwise position and lateral (or cross stream) vortices which are formed by some non-uniformity in the surface and swept downstream. The strength of the lateral vortices is limited by the velocity of the freestream flow while the frequency of generation is limited by rate at which the vortices are shed by the generator. The vortices thus created deform into three dimensional shapes as they are swept downstream.

In order to achieve an independent control over the strength and spacing of the lateral vortices, the present paper considers their generation by an active device and their effect on a flow geometry common to transportation systems, the rearward facing wedge or boat tail. For internal fluid dynamics, the shape also corresponds to a half diffuser and many of the results herein presented will refer to that device.

## 2. Vortex Generator

As discussed in the introduction, the field of fluid dynamics has generally avoided unsteady flows wherever possible because the unsteadiness has often been associated with undesirable consequences such as noise and material fatigue. In some cases, however, unsteady flows are unavoidable (for example in turbo-machinery) and in others desirable results are produced by the unsteadiness (for example the unsteady jet results of Sections II - V).

The time dependent vortex structure considered in this section is produced by the cam shaped rotor shown in Figure 59a. The flow is from left to right and the rotor turns in the counter-clockwise direction. The discontinuity in the rotor surface generates one lateral vortex for each turn of the rotor. The effect of the vortices is to energize the lower portion of the boundary layer and enable the flow to withstand stronger pressure gradients. The mechanism by which this is accomplished is probably the actual exchange of low energy fluid in the boundary layer for higher energy fluid from the mainstream. It

should be emphasized that the direction of rotation of the cam is such that it does not push the flow. Thus the energy put into the rotor is only the small amount required for the mass exchange, not the energy put into the boundary layer (which comes from the freestream).

Figure 59b shows the particular geometry of interest here, a half boat tail geometry (which could also be considered a half diffuser from the point of view of internal flows). Such a method is a potential way of filling the wake of a bluff body to reduce the drag. More generally, the technique is representative of a positive view of unsteady flow which searches for beneficial aspects of unsteady flows as opposed to those leading to performance degradation.

The structure of the vortex field downstream of the rotor is shown in Figure 53 for the flat plate case ( $\theta = 0$ ). The flow is made visible by the addition of smoke upstream. The location of the rotor is labeled and the approximate locations of the vortex centers are indicated by the bulges in the streamlines nearer to the wall. The vortices are swept downstream so that their spacing depends directly upon the flow velocity and inversely upon the rotor speed.

The experiments are performed in a low speed smoke tunnel. The remainder of the tunnel is constricted so that all the flow is forced through the duct and over the rearward facing ramp. The velocity produced upstream of the ramp is nominally 32 m/sec resulting in a Reynolds number of  $1.97 \times 10^6$  per meter. The distance the rotor extends into the flow is .381 cm. and the Reynolds number of the rotor, based on its height and tip speed at a rotational speed of 1000 rpm is 256. The boundary layer thickness at the rotor location is approximately .635 cm. and is turbulent due to the rough inlet extension of the plate and a trip upstream. The remainder of the flow through the device is low turbulence level, having passed through a dozen upstream screens. A smoke generator was employed to produce visible streamlines to be entrained into the tunnel inlet. In the case of unsteady flow these lines are, of course, streak-lines (as seen in Figure 53) rather than streamlines and their interpretation is less straightforward.

### 3. Quantitative Results

Two methods are employed to assess the utility of the vortex generator described above. One is to visualize the flow by the use of smoke and will be treated next. The other is to measure the pressure distribution along the ramp

and the velocity just upstream of the rotor. When the flow is attached to the ramp, the pressure distribution resembles that through a diffuser; a low pressure rising to a level higher than the upstream value. In the present experiment, the downstream pressure is relatively fixed (neglecting any fan stall) so that changes in the flow are reflected as changes in upstream static pressure.

The pressure distribution corresponding to a ramp angle of  $20^\circ$  is shown in Figure 60. The pressure levels are referred to the ambient static pressure values upstream of the ramp  $P_{f.s.}$ . The pressures are obtained by a Statham pressure transducer which is calibrated by means of a Merriam micromanometer. Pressure taps are located at various positions on the ramp and the freestream pressure and velocity are obtained by means of a pitot-static tube. The difference between the ramp pressure,  $P$ , and the upstream pressure,  $P_{f.s.}$ , is non-dimensionalized with the dynamic pressure and plotted versus the streamwise distance normalized with the upstream wall separation (Figure 1b.). It is clear from Figure 60 that the ramp flow is attached even without the rotor operational since the pressure rises along the ramp to a value above the freestream value. It should be noted that the no rotor ( $\omega = 0$ ) cases are obtained with the rotor cavity covered with tape to avoid any acoustic effects. The use of the rotor at a speed of 2500 rpm has no major effect on the flow. The rotor does appear to slightly improve the flow attachment along the ramp as evidenced by the reduced pressure distribution. Farther downstream the pressures for the two cases are indistinguishable.

The situation changes considerably when the ramp angle is increased to  $28^\circ$  as shown in Figure 61. For the case of  $\omega = 0$  (i.e. rotor unused), the pressure distribution on the ramp deviates only slightly from the freestream value. This indicates the flow is separated at the ramp and therefore the effective area that the flow experiences is nearly a constant area duct. The use of the rotor at 1000 rpm reduces the pressure distribution at the beginning of the ramp, indicating that the flow more easily negotiates the turn.

As the rotor speed increases above 1000 rpm, the static pressure on the ramp decreases, indicating improved flow performance. The performance at rotor speed of 4000 and 5000 rpm is virtually indistinguishable, suggesting that this speed range may contain the maximum performance in terms of  $\omega$  for this particular case. That question cannot be completely answered here since 5000 rpm is the upper range

of the present experimental capabilities.

As the ramp angle is increased to  $30^\circ$  (Figure 62), the separated flow (for  $\omega = 0$ ) reacts even less to the presence of the ramp; the pressure distribution deviates even less from the freestream value. The general behavior of the flowfield with increasing  $\omega$  is similar to that at  $28^\circ$ . As the rotor speed is increased, the pressure distribution on the ramp decreases. Again, the difference between the 4000 and 5000 rpm values is very small.

The main difference between the performance at  $28^\circ$  and  $30^\circ$  is in the actual level of the pressure changes. The pressure rise along the ramp at  $28^\circ$  is twice that at  $30^\circ$ . Thus it is clear that the flow at  $30^\circ$  is more difficult to control than that at  $28^\circ$ , although in each case the use of the rotor improves performance. This is not unexpected especially when one considers the additional energy involved in turning the flow an additional two degrees. The performance may perhaps be improved at  $30^\circ$  if more energy is put into the rotor, most likely by simply increasing its size. The present facility is not capable of such a change.

#### 4. Flow Visualization Results

The smoke flow photograph in Figure 53 as well as those to be presented hereafter, are obtained by the entrainment of kerosine smoke into the tunnel inlet. The smoke is produced by allowing liquid kerosine to drip slowly on an inclined plate heated by a resistance element. As the kerosine flows down the plate, it is vaporized. A fan blows over the plate and drives the kerosine vapor to the tunnel inlet where it is released at several points and entrained into the tunnel.

The photograph in Figure 53 was obtained by a single strobe flash and, therefore, is a relatively instantaneous view of the flowfield. Several longer time exposures (1/100 sec) of the flow over the ramp are shown in Figure 63. The wall angle is  $28^\circ$  and the rotor speed varies between  $\omega = 0$  in Figure 6a to  $\omega = 4000$  in Figure 63d. As the rotor speed increases, the positions of the mean streamlines move closer and closer to the ramp, indicating better flow attachment and verifying the pressure measurements of Figure 61.

Perhaps of even more interest are the high speed photographs of Figure 64 a-f for various rotor speeds at a ramp angle of  $28^\circ$ . For a zero rotor speed and the cavity taped, the flow clearly separates as shown in Figure 64a. There is some large scale structure in the separated shear layer but not enough momentum transfer to lead to reattachment. If the rotor is activated with  $\omega = 1000$  rpm (Figure 64b),

the separated flow curves down toward the ramp surface, very much in the same manner as the time averaged picture at the same rotor speed, Figure 63b.

With a rotor speed of 2500 rpm (Figure 64c), the curvature of the flow toward the ramp becomes more pronounced. In addition, the time dependent structure becomes significantly larger. A vortex may be seen in Figure 64c, with a region farther downstream which appears to be separated. The sequence of events appears to be as follows: Suppose the flow is initially separated. The rotor generates a vortex which causes the flow to attach for a moment before it is forced to detach again by the adverse pressure gradient. At this time the flow needs a new vortex to force it to attach again. If the speed (or effectively, the generation frequency) is sufficiently high, the necessary vortex is available.

The flow situation described above may be seen in Figures 64d and 64e for both of which  $\omega = 4000$  rpm. The two photographs indicate considerably different flow patterns. Actually they are examples of the same time dependent flow at two different times. These are the extreme positions of the oscillatory flow pattern at 4000 rpm. The mean pressure distribution on the ramp reflects the time average of the oscillatory flow. The instantaneous flow patterns, Figures 64d, e are fully consistent with the time average flow pattern of Figure 63d, where the apparent lack of smoke near the wall is due to the fact that the streakline is there only intermittently. It should be noted that the position of the incoming smoke is unchanged in the sets of photographs resulting in Figures 63 and 64.

The transition between the flow patterns of Figures 64d and e is shown in Figure 64f (for a speed of 5000 rpm). The flow far down the ramp is clearly separated while that nearer to the corner is relatively attached. The attached flow is produced by the vortex sweeping downstream, momentarily overcoming the adverse pressure gradient, as discussed above.

##### 5. Three Dimensional Rotor

The foregoing results employ a rotor which is uniform in cross section throughout its length. Of course, in terms of application the rotor must end at some point. In addition, there are some applications where a uniform rotor must be integrated transverse to an axisymmetric geometry (i.e. perpendicular to a round pipe). Thus the question of a three dimensional rotor is of interest.

The three dimensional rotor geometry employed here is shown in Figure 65. On the centerline of the rearward facing ramp geometry, the rotor cross section has the same shape as the uniform rotor employed in the earlier parts of this section and shown in Figure 59. However, as one moves away from the centerline (i.e. into or out of Figure 59) the size of the rotor tapers to zero at a transverse position of 3.6 cm from the centerline. Another difference is that there is no undercut in the rotor shape but the discontinuity in the rotor shape is merely a straight step. The subsequent flow visualization results and pressure measurements are all made on the centerline of the flowfield.

The effect of the magnitude and direction of the rotation speed on the ability of the flow to remain attached to a  $28^\circ$  ramp is shown in Figures 66 and 67. The detached flow for the case of no rotor is shown in Figure 63a. The flow separates immediately at the beginning of the ramp. The nominal velocity at the top of the ramp is 32 m/sec. The photographs in Figures 66 and 67 are taken with a sufficiently long time exposure so that the results are essentially a time average of the flowfield and hence are average streamlines.

In Figure 66 the comparison is made between rotation in the counter-clockwise (+) direction and the clockwise (-) direction for speed of 1000 and 2500 rpm. The direction of rotation does not appear to be a major effect, but the rotation has not yet caused the flow to turn the corner very effectively. With an increase of rotational speed to 4000 and 5000 rpm, the effect of the rotation direction becomes very pronounced. In particular, at  $\omega = \pm 5000$  rpm the effect is very strong, resulting in a fully attached flow for a counter-clockwise rotation and a fully separated flow for a clockwise rotation.

The time average pressure distribution on the ramp are shown in Figures 68 and 69 for two sets of rotational speeds,  $\pm 1000$  rpm (Figure 68) and  $\pm 5000$  rpm (Figure 69). At the lower rotational speeds, the pressure rise on the ramp is rather small and only weakly affected by the direction of rotation. This is consistent with the results of Figure 66 and indicates that the frequency of vortex generation is too low to achieve sufficient boundary layer energization to allow the flow to remain attached. Changing the direction of rotation (at the same  $\omega$ ) keeps the frequency of vortex generation unchanged but changes the strength of each vortex because the relative velocity between the stream and the rotor is changed. However, since the frequency of generation is insufficient for attachment even with the counter-clockwise rotation, the effect is minimal.

At higher rotational speed, however, the effect of rotational direction is very significant as shown in Figure 69 for the case of  $\pm 5000$  rpm. The counter-clockwise rotation (+) produces the stronger vortex and leads to a higher pressure rise on the ramp. This result is a reflection of the improved flow attachment on the ramp and verifies the flow visualization results of Figure 67.

The details of the flow structure may be seen in the streakline photographs of Figures 70 and 71. In this case, the photographs are taken with a single flash strobe and thus yield the instantaneous positions of the entrained smoke or streakline. The interpretation of streakline patterns is more difficult but can be guided by observations of their dynamic behavior as observed with a tunable strobe light. The results at the lower rotational speeds, Figure 70, verify the results of Figure 66 in that the effect of rotation direction is not very strong and indeed, the ability of the unsteady energization to cause the flow to remain attached is rather limited. However, at larger rotational speeds, Figure 71, the effect of rotor direction is very pronounced, leading to a very strong vortex structure and a successful attachment when rotated in the counter-clockwise (+) direction. When rotated in the clockwise (-) direction, the strength of the vortices produced is greatly reduced (since the relative velocity is reduced) and the resulting flow is not well attached to the ramp.

Thus the time dependent method of boundary layer energization appears to show promise from the point of view of application. Rotation in the upstream direction (+) direction is desirable to maximize the relative velocity between the rotor and freestream and thus maximize the vortex strength. Three dimensional rotors show the same promise but additional data is needed on geometrical effects.

## 6. Discussion

The results presented above indicate the usefulness of unsteady flow to control boundary layers in the face of adverse pressure gradients. In this case the unsteady structure is created by a rotating cam but the present design of the cam (or indeed the use of a cam itself) is not intended to suggest an optimum configuration. Rather, the objective of this section is merely to point out the potential advantage of unsteady flows.

The unsteady structure can also be accomplished by various other devices such as oscillating spoilers, plates or even membranes. The advantage of the rotor system is primarily that the reciprocating motion has been avoided. In addition, with the use of modern composites, the rotor could be built as designed and yet be well balanced, again avoiding troublesome vibrations.

## SECTION VIII

### INDUCED UNSTEADY FLOW IN A DUMP COMBUSTOR GEOMETRY

#### 1. Background

The dump combustor, illustrated schematically in Figure 72 (from Drewry<sup>40</sup>) involves a rapid diffusion of a duct flow by the geometrically simple device of a step enlargement in the duct diameter. The recirculation region thus produced acts as a flameholder and keeps the flame from being blown downstream by the high speed flow. Therefore, the recirculation region is designed to act as an ignition for the main flow passing through the duct. In order for ignition to be accomplished, there must be an interaction between the two flow regions. It is the purpose of this section to propose a simple mechanical method which indicates a potential performance improvement since it increases the fluid dynamic interaction between the recirculation region and the main flow.

The method proposed here is demonstrated in a two-dimensional arrangement although most dump combustor applications for ramjets are axisymmetric. This is due to the relative simplicity of the 2-D device but the same principle can be applied to the axisymmetric case, probably in the form of segmented rotors or several rotors around the periphery of the duct.

Dump combustor performance, especially as it relates to ramjets, has been studied by several investigators<sup>40-43</sup> both analytically and experimentally. The present experiment is performed at relatively low speed and aimed at a flow visualization understanding of the process, verified by time averaged pressure measurements.

The objective of an increased flow interaction which leads to improved performance is not unique. One of the more successful attempts has been by Choudhury<sup>44</sup> who introduced jets from the walls immediately upstream of the dump station. In some cases these entered at some oblique angle to the wall and thereby produced a swirling inlet flow which improved the performance of the combustor. The jets, unfortunately, require relatively high pressure gas which must be carried with the flight vehicle and included in an assessment of the overall performance. The use of swirl to increase combustion efficiency has also been investigated from the point of view of heating furnaces<sup>45</sup> and the mixing of jets.<sup>46</sup>

## 2. Experimental Apparatus

The two-dimensional half dump combustor geometry employed in the present experiment is shown in Figure 73a. Three step sizes are considered,  $\bar{h} = 1/3, 2/3, 1$ . The nominal upstream velocity is 120 ft/sec with some variation with overall performance. As in the schematic of Figure 72, the flow separates at the corner and forms a recirculation region. In order to increase the interaction with the main flow, the device illustrated in Figure 73b is proposed. It consists of a simple cam shaped rotor which turns in the counter-clockwise direction and produces a transverse clockwise vortex with each sweep of the rotor's surface "discontinuity". A rotor of this type can be shown to be a useful tool to energize the boundary layer and to reduce problems associated with separation on airfoils (Section VI) and diffusers (Section IX). It should be emphasized that these effects were obtained with rotation in the counter-clockwise direction so the rotor simply does not push the flow downstream.

In the present case the objective is not only to energize the boundary layer but to actually cause a time dependent variation in the structure of the recirculation region. That this is accomplished may be seen in the flow visualization results of the following section. The rotor method employed here is *not* expected to be the only way to generate such an unsteady flow structure. A similar effect could be obtained by the use of an oscillating plate which appears normal to the surface in a sinusoidal fashion. Another possibility is the use of an oscillating air brake (a plate in the surface hinged on the upstream side and alternately raised and lowered from the surface).

## 3. Flow Visualization Results

The flow is rendered visible by the entrainment of smoke into the inlet of the open circuit wind tunnel. The smoke is generated by vaporizing drops of kerosine on an inclined resistance heater. The resulting time averaged streamlines are shown in Figure 74a for the case of no rotor motion (i.e., the rotor withdrawn into the surface and the cavity covered). The time averaging takes place over the exposure time, 1/100 sec. The length of the recirculation region is approximately eight or nine step heights as compared to a length of eight step heights in a comparable high speed axisymmetric experiment.<sup>40</sup> That the activation of the rotor decreases the average length of the recirculation region may be seen in Figure 74b where the rotor speed is 1000 rpm. The reduced

length is approximately 7-8 step heights. Increasing the rotational speed produces yet a further reduction in the average recirculation zone length, as seen in Figure 74 c-e. Although, it is not possible to determine the length with any precision, it is clear that increasing the rotor speed decreases the average length of the recirculation zone. The difficulty in resolution is caused by the fact that the flow is not steady and thus the photograph, even using a short time exposure, is smeared due to the rapid changes in structure.

In order to show the instantaneous structure of the flow, a single flash strobe light is employed. Even with moderate camera speed, the strobe captures the time dependent motion as may be seen in Figure 75, showing the streaklines for the case of no rotor activity ( $\omega = 0$ ). The breakdown of the shear layer into a larger scale structure may be seen near the end of the separated region. The length of this recirculation region is approximately 8-9 step heights as was estimated from the time averaged photograph, Figure 74a.

The introduction of unsteady flow by means of the rotor results in very significant time dependent changes in the flow structure. Some indication of this effect is seen in Figure 74 b-e where the spreading of the streamlines indicate their extreme positions. More dramatic evidence is presented in the following set of figures for the case of  $\omega = 2500$  rpm. Figure 76a shows the structure of the flow as not much different from that of zero rotor speed, Figure 75. However, at another instant of time, Figure 76b, the structure is quite different. The tail of the recirculation region has been swept away while the upstream portion is relatively unchanged. At yet another instant, Figure 76c, the recirculation region has again attained the expected elliptical shape but with a much decreased length. The interaction of the two flow regions is very strong with the length of the recirculation (or flame holding) region effectively pulsing back and forth. In the combustion case this should lead to improved performance.

At higher frequencies, the vortices generated by the rotor are closer together and their influence on the flowfield can be even stronger. An instantaneous streakline for a rotor speed of  $\omega = 5000$  rpm is shown in Figure 77. In terms of its relation to the cyclical behavior of the recirculation region, Figure 77 is probably comparable to Figure 76b. That is, the longer recirculation region of a prior time is being shortened by the vortex structure and the end of

the region is shed. The interaction may be seen to be very strong indeed. The upsweep of the streamline at the dump position is typical of the higher rpm values of the rotor (for this step), while at lower rpm's the flow separates practically parallel to the upstream surface.

For the largest step size considered in this experiment,  $\bar{h} = 1$ , the available distance downstream is not sufficient for reattachment to take place. However, the change in character of the time average streamlines with changing rotor speed, is still evident in Figure 78. In the case of an inactive rotor ( $\omega = 0$ ), the streamlines separate at the corner and become smeared farther downstream due to the very turbulent structure developed in the shear layer. When the rotor is activated, the size of the recirculation region is reduced with increasing rotor speed. At  $\omega = 5000$  rpm, its length is estimated to be four step heights.

The instantaneous streakline structure of the flow over the  $\bar{h} = 1$  step is shown in Figure 79. For  $\omega = 0$ , the streakline shows little distinctive structure and is similar to the upstream portion of that for the smaller step height and  $\omega = 0$ , Figure 75. However, the use of the rotor produces, as in the smaller step case, a very strong vortex structure, appearing in Figure 79b at only one step height downstream. There results a clear and strong interaction between the recirculation region and the main flow. A similar structure is evident at higher rotational speed,  $\omega = 5000$  rpm, in Figure 79c. There is no indication in the large step case of the separation at an angle to the upstream surface as observed in Figure 77.

From the preceding Figures, especially Figures 76, 77 and 79, the potential advantages to a dump combustor due to the introduction of a time dependent vortex structure may be seen in a qualitative fashion. A quantitative look at the time averaged pressure distribution and the effect of the rotor is presented in the following section.

#### 4. Pressure Distribution

The streamwise pressure distribution is obtained from static pressure orifices mounted in the wall downstream of the dump corner. A Statham pressure transducer is employed along with a Daytronic Model 601B signal conditioner and a Datametrics digital readout. The static pressure transducer is used to obtain all readings and is calibrated before and after each run with a Meriam Micromanometer. The static and total pressures upstream are obtained in order to determine the upstream velocity and a base for the pressure distributions.

The static pressure downstream of the corner for a step height  $\bar{h} = 1/3$  is presented in Figure 80. The basic effect of unsteadiness on the time average flow is seen to be the shortening of the recirculation region length. That is, the pressure reaches its maximum at a streamwise distance which is inversely proportioned to rotor speed. The maximum pressure position is not the reattachment point since it has been shown,<sup>40</sup> based on flow visualization, that reattachment occurs upstream of where the maximum pressure is attained. Thus the reattachment, in the case of the withdrawn rotor ( $\omega = 0$ ) should occur before ten step heights (where the maximum pressure is attained). This is consistent with the estimate of eight or nine step heights from Figure 74a. For a high rotational speed of 5000 rpm, the average reattachment point should occur before the maximum pressure is attained at  $\bar{x} = 6$ . This, to, is consistent with an estimate of four to five step heights based on the flow visualization in Figure 74e.

With a change in step height to  $\bar{h} = 2/3$ , the results in Figure 81 are produced. At this step height, there is insufficient streamwise distance available in the present experimental setup to allow for reattachment, at least for the zero rotation case. However, the question of performance is clear since the use of the rotor allows a more rapid and substantial pressure increase. Here the rearward facing step acts more like a diffuser. That is, if the step is to act as a diffuser, then the flow should at least partially reattach to the lower wall. The more complete reattachment yields a more rapid pressure rise. The use of the rotor aids reattachment and thus results in a larger pressure rise.

The same situation is true for the case of  $\bar{h} = 1$ , Figure 82 where length of the lower plate is only on the order of three step heights. Here, too, the use of the rotor allows the rearward facing step to act as a better diffuser. The flow, however, retains its unsteady nature and thus its major advantage from the point of view of interaction of the main flow and the recirculation region.

The decision to drive the rotor in a counter-clockwise direction is motivated by three objectives. One was the aim, in an earlier experiment involving an airfoil (Section VI), to produce an unsteady vortex pattern similar to that found above an airfoil with a time varying angle of attack. The second objective is the overall one of this entire sequence of experiments; to demonstrate the advantageous use of unsteady flow. In that regard, rotating in the counter-clockwise direction clearly relies on unsteady flow to energize the boundary layer since the upper surface of the rotor is moving upstream, and therefore cannot simply push the boundary layer flow downstream.

The third objective is to produce strong and concentrated vortices. To achieve this effect, it is desirable to maximize the relative velocity between the flow and the rotor. This is, of course, attained when the flow and rotor tip are moving in opposite directions.

The effect of the direction of rotation is examined in Figure 83 for  $\bar{h} = 1$ . The positive direction is that involved in the previous results, counter-clockwise rotation. For rotational speeds of 1000 and 2500 rpm (both positive and negative), there appears to be little dependence of the streamwise pressure distribution on sign. However, for  $\omega = \pm 4000$ , the difference is significant, amounting to roughly a 10% improvement in static pressure rise for the counter-clockwise rotation. For the reasons mentioned above, this improvement was anticipated. The surprise is that the same effect did not appear at lower rpm values. The resolution between anticipation and results is shown in Table 1.

As the rotor turns, the streamwise component of its tip speed, both maximum and average, are calculated as compared to the nominal freestream velocity of 123.5 ft/sec. It may be seen that for a rotor speed of 2500 rpm, the maximum streamwise velocity of the tip is moving at a velocity less than 7% difference from the flow velocity. The average velocity difference is even smaller, being slightly over four percent.

Thus the change in vortex strength with rotor speed is not very high and does not have a significant effect until  $\omega = 4000$  rpm where the maximum change exceeds 10%.

Although the effect of direction is not very important until higher rotational speeds, it may be seen (from Figure 80-82) that the effect of speed is still very significant. Therefore the primary effect is not one of vortex strength but rather vortex spacing (or frequency of generation). The flow, then, requires the passage of a vortex with a minimum frequency in order to retain the favorable aspects of the unsteady flow.

One final point to be examined is to ensure that the rotor is not simply acting as a trip which could be replaced by a static one. A comparison is presented in Figure 84 between a dump flow without any rotor and one in which the rotor is in a fixed upward position, acting as a static trip. The rotor in such a position is even out performed by the no rotor case which leads to a higher downstream pressure and thus acts as a more effective diffuser in the steady sense.

## 5. Discussion

The use of time dependent flow to enhance the interaction between the flame holding recirculation region in a dump combustor geometry and the main flow appear to have very significant potential for performance improvement. The device proposed here is certainly not the only manner in which this potential can be realized. Numerous other techniques could be devised to employ the advantages of time dependent fluid mechanics. Further work is needed to determine the quantitative effect on a combustor system.

## SECTION IX

### PERFORMANCE POTENTIAL OF UNSTEADY DIFFUSERS

#### 1. Background

Artificially induced large scale flow structures have been employed successfully in the past to improve performance. Two examples are the common streamwise vortex generators sometimes used to control the flow over an aircraft wing and to maintain attached flow in large angle diffusers. In each case, streamwise vortices are created which cause a transfer of energy from the outer flow to the boundary layer. The large scale streamwise structures are created by the passive vortex generators simply mounted in the surfaces.

Transverse flow structures have also been examined as a method to control boundary layer separation. Quinn<sup>39</sup> employed a transverse cavity to generate an acoustic disturbance in order to keep the flow over an airfoil attached at high angles of attack. Stull et. al.<sup>47</sup> used spacers to build transverse cavities on diffuser walls. Standing vortices were produced in the cavities in an attempt to improve the diffuser performance. A transverse standing vortex, driven by a control jet at a fixed position in the diffuser was examined by Haight and O'Donnel.<sup>48</sup> The device, named the trapped vortex diffuser, led to a performance improvement.

The objective of this investigation is to examine the potential performance advantages of a diffuser in which the flow is forced to be unsteady. There are, of course, various methods which can be employed to force the flow, including adapting Quinn's acoustic method,<sup>39</sup> mechanically controlled boundary layer injection<sup>4</sup> and boundary layer blowing controlled by fluidic means.<sup>3</sup>

The question of the response of a diffuser flow to an unsteady input has been examined experimentally by Stenning and Schachenmann<sup>49</sup> and analytically by Schachenmann and Rockwell.<sup>50</sup> Their investigations had a different perspective because they recognized that diffusers often need to operate with an unsteady inlet flow and that the effect of this time dependency on the overall performance is of significant interest. In the present case, the time dependency is forced in an attempt to improve the performance of the device.

## 2. The Forced Diffuser

The method considered here is a simple mechanical device illustrated in Figure 85. A spiral shaped rotor is mounted in the wall on each side of the channel just upstream of the diffuser section. The rotor surface has a discontinuity which ends in a cusp. The rotor turns in such a direction that the motion of the portion exposed to the flow is always against the flow, i.e. the upper rotor turns in a clockwise direction while the lower rotor turns in the counter-clockwise sense.

Each time the surface discontinuity of the rotor is swept through the fluid, a vortex is formed which then is convected downstream. The rotors (and hence the vortices) can have an arbitrary phase relationship. In Figure 1a the rotors appear simultaneously and thus the vortices are formed in phase with each other and are symmetrically positioned. Figure 1b illustrates the out of phase condition where the discontinuities appear alternately and thus the vortices formed are staggered as they sweep downstream.

The experimental geometry shown in Figure 85 has the following scale:  $D = 15.2$  cm;  $L = 30.4$  cm;  $h = .38$  cm; and the nominal inlet velocity is  $V = 40$  m/sec. The resulting range for the nondimensionalized angular velocity of the rotors is approximately  $10 \leq \bar{\omega} \leq 20$  where  $\bar{\omega} = \omega D/V$ .

The rotor device in Figure 85 has been successfully applied in other flow situations, in particular on an aircraft wing (Section VI) and just upstream of a rearward facing ramp (Section VII). The ramp problem approximates a half diffuser and is therefore of particular interest here. In the ramp case it was shown that for sufficiently large angles (roughly above  $25^\circ$ ) the flow separates at the corner rather than turning through that angle. The addition of the rotating vortex generator in such a flowfield, allows the flow to turn through a larger angle.

Thus the use of the rotors is designed to allow the diffuser to operate at a larger area ratio without separation. The unsteady vortex structure energizes the boundary layer and allows it to overcome a larger pressure gradient. The vortex structure produced by the rotor is shown in Figure 86 by means of kerosine vapor streaklines. The vortex, at the instant of the photograph, is located somewhat downstream of the diffuser corner.

As the rotor speed increases with a fixed tunnel speed, the spacing of the consecutive vortices decreases, as well as the size of the vortices themselves. This effect may be seen in Figure 87 where the streamwise velocity through the diffuser has been held artificially low in order to more clearly illustrate the structure. The lowest photograph is at a rotor speed of  $\omega = 1000$  rpm with an increase of 1000 rpm to each photograph above. Thus the number of vortices seen in the photographs is proportional to the rotor speed.

The beginning of flow separation in the diffuser (without a rotor) may be seen in the  $\theta = 80^\circ$  and  $12^\circ$  cases in Figure 88, showing both flow visualization and exit velocity profiles. The separation may be clearly seen in the exit profiles, to occur at the lower wall, resulting in a profile which is skewed toward the upper wall. The velocity coordinate is nondimensionalized with the inlet velocity and the distance with the inlet dimension  $D$ . It should be noted that the exit size is larger in the  $12^\circ$  case than the  $8^\circ$  case so the separation is even more substantial than is apparent at first glance. The profiles are taken with a hot wire anemometer employing a low pass filter to produce the time average readings. The photographs are taken with a single flash strobe and thus show the streakline pattern.

A comparison of the flow patterns with and without the use of a rotor is shown in the photographs of Figure 89. In this case the exposure time of the film is much longer and the result is an effective time average resulting in a streamline pattern. In each case the diffuser angle is  $2\theta = 30^\circ$ . The upper case employs no rotor and strong separation is apparent from the lower wall of the diffuser. The lower photograph employs a rotor at a nondimensional speed of  $\bar{\omega} = 11.84$  with the rotors in phase with each other. The separated region has moved to the upper wall and has been significantly reduced in size.

### 3. Performance

The performance of the various diffuser combinations are compared by means of the nondimensional pressure rise (or pressure recovery) through the device. The

nondimensional pressure,  $\bar{P}$  is defined as the difference between the wall pressure within the diffuser and the inlet pressure, divided by the inlet dynamic pressure,

$$\bar{P} = \frac{P_{\text{wall}} - P_{\text{inlet}}}{\frac{1}{2} \rho V^2}$$

The pressure rise with nondimensional streamwise distance is shown in Figures 90-92 for the case of an out of phase orientation of the two rotors. The pressure rise is plotted for various rotor speeds including the case of  $\bar{\omega} = 0$  which corresponds to no rotor and having the rotor cavities covered to avoid acoustic interactions. The lowest angle case is shown in Figure 90,  $2\theta = 16^\circ$ . As was evident in Figure 88, there is no separation within the diffuser at this angular setting. This is also verified by the similarity in the pressure distributions on the opposite sides of the diffuser for  $\bar{\omega} = 0$  in Figure 90. Since no separation exists, the use of rotors cannot improve the performance and, in fact, results in a performance reduction.

Increasing the diffuser angle to  $2\theta = 24^\circ$  results in a separated flow, as previously seen in Figure 88 and verified by the pressure distributions of Figure 91 for  $\bar{\omega} = 0$ . In this case, the use of the rotors results in roughly the same performance although there is a positive trend with rotor speed. In addition, with the use of the rotor, the pressure distribution on both walls assumes the shape corresponding to attached flow. At the highest angular setting,  $2\theta = 30^\circ$ , the overall performance decreases. However, the use of the out of phase rotors results in a significant performance improvement compared to the no rotor condition.

The corresponding results for the in-phase orientation of two rotors are shown in Figures 93 and 94. For an angular setting of  $2\theta = 24^\circ$ , the pressure rise on the two walls of Figure 93 indicate a small performance improvement due to the use of the rotors. Perhaps even more important is the positive trend with rotor speed that is evident. For the largest diffuser angle tested  $2\theta = 30^\circ$ , the in-phase rotor results (Figure 94) indicate a very substantial performance improvement on both walls.

#### 4. Flow Structure

Instantaneous velocity profiles are taken within the diffuser by employing a hot wire anemometer along with a conditioned sampling device. The hot wire

produces a continuous signal. The conditioned sampling circuit only accepts the hot wire signal when the rotor is instantaneously in a predetermined position. A probe traverse under these conditions results in the instantaneous velocity profile which exists each time the rotor is in that particular position. The input required to define the rotor position comes from a magnetic pickup on the rotor drive shaft. A more detailed description of the data acquisition system is given in the following section. The magnetic pickup can also be used to trigger a strobe light and thereby produce streakline photographs of the diffuser flowfield with the rotors in a particular predetermined phase position.

A combination of the instantaneous flow streakline pattern produced by flow visualization and the corresponding instantaneous velocity profiles can be an aid to the identification of the large scale flow structures and are shown in Figures 95 and 96. The in-phase configuration for an angle of  $2\theta = 24^\circ$  is shown in Figure 95. It is evident that the basic flow is attached to the upper wall and that the forced unsteadiness modifies that condition. The flow visualization reveals a strong vortex near the lower wall at  $\phi = 180^\circ$ . Since the rotors are in-phase there is a corresponding mirror image vortex near the upper wall which does not appear to be as large and also is located further downstream. Both of these effects are consistent with the flowfield since the growth of the vortex is inhibited by the proximity of the wall and the vortex is convected more rapidly due to the higher velocity near the fully attached wall. The presence of the vortex at the  $180^\circ$  phase angle is verified by the superimposed streamwise velocity profile which is enhanced near the center of the channel and reduced in the region between the vortex and the wall. Both effects are caused by the induced velocity due to the presence of the vortex pair.

With the rotors in the in-phase orientation, the flowfield is expected to have a pulsating character due to the time dependent change of the blockage at the diffuser inlet. This effect is evident in the flow visualization result at  $\phi = 90^\circ$  where the pulsing appears to be almost symmetrical. The effect may also be seen by comparing the instantaneous velocity profile at  $\phi = 90^\circ$  to that at  $\phi = 180^\circ$ . The former profile is wide and relatively uniform while the latter is constricted at the edges and accelerated near the center.

Streaklines with superimposed velocity profiles are shown in Figure 96 for an out of phase rotor orientation and a larger diffuser angle  $2\theta = 30^\circ$ . In this

case the basic flow is attached to the lower wall of the diffuser. The instantaneous phase angles of the individual rotors are indicated on each side of the diffuser. Due to the out of phase orientation of the rotors, the flowfield has essentially a flapping character. This is most evident in Figure 96d. The vortices appear to be located in the vicinity of the measuring station in (b) and (d). In each case, the upper vortex in (b) and the lower vortex in (d), the presence of the vortex results in a decreased velocity near the wall and an increased value near the centerline. These velocity changes may again be attributed to the induced velocity of the vortex structure.

In order to more clearly specify the effect of a vortex on the flowfield (and thus be more capable of identifying the vortex location) consider the schematics of Figure 97. The objective is to demonstrate the local change in velocity, both streamwise ( $u'$ ) and transverse ( $v'$ ), produced by the presence of the vortices which are shown schematically as swirling fluid near each wall. The vortex near the upper wall is rotating in the counter clockwise direction while the vortex near the lower wall rotates in the clockwise direction. The qualitative transverse velocity changes,  $u'$ , (equivalent to the induced velocity) may be seen not to depend upon whether the profile is taken in front or in back of the vortex location but does depend upon the sense of rotation of the vortex. Thus the streamwise velocity profiles can be used to determine the sign of the vorticity.

The qualitative effect on the transverse velocity change ( $v'$ ) indicates that there is a sign change from the upstream to the downstream side of the vortex and also a sign change with the sign of the rotation itself. However, it is not possible to distinguish between, for example, the upstream side of a counter clockwise vortex from the downstream side of a clockwise vortex. Thus both velocity profiles are required, but knowing both can result in the identification of the vortex.

In order to verify the schematics of Figure 97, consider some data taken from the in-phase results of Figure 95. In particular, compare the velocity profiles for the case where a vortex pair is present ( $\phi = 180^\circ$ ) near the measuring plane to a case where no vortices are present ( $\phi = 90^\circ$ ). This comparison is presented in Figure 98. The difference in the streamwise velocity corresponds, for both the upper and lower vortex, to the situation of the profile being taken on the downstream side of the vortex as in Figure 97. This is certainly consistent with

the flow visualization results at  $\phi = 180^\circ$  of Figure 95. Comparison of the transverse velocity profiles verifies this conclusion since the difference qualitatively agrees with the schematic profiles downstream of the vortices in Figure 97.

Consider now the case of the out of phase results of Figure 96. A vortex is evident near the upper wall of Figure 96b while none appears near that wall in Figure 96d. A comparison of the streamwise and transverse velocity profiles of these cases is shown in Figure 99. From the streamwise comparison, it is clear that the vortex is turning in the counter clockwise direction when compared to Figure 97. The difference between transverse velocity profiles indicates that the profile containing the vortex (Figure 96b,  $\phi = 90^\circ$ ) was taken upstream of the vortex. This result may be seen to be consistent with the streakline photograph of Figure 96b.

Thus the forced time dependent diffuser flows appear to have potential to improve the performance of the device. In the present case, the time dependency has been mechanically created. Of course, other possibilities exist which may have advantages in terms of construction, reliability or cost.

## SECTION X

### DETAILS OF THE FLOW PRODUCED BY THE ROTOR VORTEX GENERATOR

#### 1. Background

The existence of large scale, unsteady structures in flows which are nominally steady has been noted by Roshko and others.<sup>11</sup> These structures are currently under intense investigation due to their relationship to the turbulence structure and eventually to computational analysis, perhaps employing an eddy viscosity. The coherent structures seem to have a strong effect on the transport properties of flow systems. Their effect is yet amplified by the fact that they survive and remain coherent for very large characteristic flow times.<sup>51</sup>

Of course, large scale flow structures have often been employed to enhance the momentum transfer between various flow regions. The common vortex generators found on aircraft wings produced streamwise vorticity in order to energize the boundary layer and thereby avoid separation. Large scale streamwise vorticity

has also been employed to enhance the mixing of a jet with the surrounding fluid.<sup>52,53</sup> Perhaps more effective but certainly more difficult to produce is the generation of transverse vortices in the jet, lying parallel to the plane of the jet exit. Such structures have been produced by acoustical bombardment,<sup>1</sup> mechanical interference<sup>2</sup> and fluidic switching<sup>3,9</sup> and significantly improve the mixing rates.

The purpose of the present section is to examine the generation of transverse vortices near a wall and their effect on the overall flow. The mechanical vortex generator is shown in Figure 100 and consists of a simple cam shaped rotor. The flow is from left to right as shown and the rotor turns in the counter-clockwise sense. Each time the rotor surface discontinuity is exposed to the flow, a vortex is generated in a manner similar to the generation of a starting vortex by a rapidly accelerated airfoil section. The vortex then is swept downstream by the flow and causes the transfer of momentum in the vicinity of the wall.

## 2. Potential Applications

As discussed in the preceding sections, the vortex generator shown in Figure 100 has been tested in several flow geometries. Included are the case of a vortex generator on an airfoil to delay separation and stall (as shown schematically in Figure 50), vortex generation to allow the flow to turn a larger angle (as shown in Figure 59) and the use of vortex generation in a combustor to potentially improve the flowfield (as shown in Figure 73).

In both the airfoil and ramp applications, the advantage of the rotor technique is primarily the improvement of the time averaged flow, even though the flow must be unsteady to produce this benefit. In the case of the rearward facing step (Figure 73), the primary benefit is the actual time dependency produced by the rotor. The objective is to increase the interaction between the recirculation region behind the step and the remainder of the flowfield. The rotor causes the recirculation region length to pulsate and has potential application to the improvement of dump combustors.

## 3. Flow Visualization Results

The rotor shape shown in Figure 100 was originally a simple spiral in which the rotor surface gradually transitioned from a smaller radius to a larger one and then abruptly returned to the smaller radius. Then the step from the larger to smaller radius was undercut in order to produce a cusp at the rotor tip and thus improve the vortex generation process.

The flow structure produced by the spinning cam shaped rotor may be clearly seen by employing smoke flow visualization. The smoke is generated by dripping kerosine on an inclined resistance heater. The vaporized kerosine is released through tubes located at the tunnel inlet and entrained into the test section. The following photographs are obtained by the use of a strobe light so they indicate the instantaneous position of the smokelines. Since the flow is unsteady, these lines are not streamlines but rather streaklines. Their interpretation is less straightforward since their position represents the integrated effect of everything upstream. However, in this case the interpretation is considerably simplified by the fact that the flow can be observed dynamically. This is achieved by allowing a small frequency difference between the rotor and the strobe light, which effectively produces a slow motion version of the flowfield. The significance attributed to the following figures is guided by this dynamic view of the flow.

The tunnel itself is an open circuit low velocity, low turbulence tunnel with a dozen inlet screens to break up the large scale motions in the entrained air. The velocity in the test section is uniform within 4% without the rotor activated. The boundary layer thickness is less than .64 cm. (.25 inch). The velocity at the rotor position is 11.6 m/sec (38.1 ft/sec) and the rotor extends a distance of 2.54 cm (1 inch) into the flow in its fully extended position as shown in Figure 100. The resulting Reynolds Number is  $1.98 \times 10^4$ , based on the rotor size and freestream velocity. Of course, the Reynolds Number will change with relative velocity between the rotor tip and the freestream.

Six rotor speeds were examined by the flow visualization technique in order to examine the effect of generation frequency and vortex strength. The significant parameters are listed in Table 2.

Typical of the desired vortex generation is the result shown in Figure 101 for a rotor speed of 3000 rpm. The strobe lighted photographs have been arranged in the order of their occurrence, from top to bottom. As the rotor tip sweeps from right to left, the first hint of the vortex produced is seen in the lowest smokeline which begins to curl up in Figure 101a. By Figure 101b the rotor tip has disappeared and the vortex is evident, slightly farther downstream. The streaklines still appear to be relatively laminar but in Figure 101c the vortex flow appears to be turbulent with a smaller scale structure visibly. By Figure 101d the size of the vortex structure has grown considerably and it has translated

downstream as well as rising, higher above the surface of the plate. Its position yet farther downstream is shown in Figures 101a, b and c where its continued growth and interaction with the outer streaklines is evident. In summary, the vortex is produced by the rotor shape, grows and transitions to a turbulent state and is convected downstream. Its energization of the boundary layer flow can be inferred from the results cited in the preceding sections.

The tip of the rotor is moving in the upstream direction in the previous case and a strong vortex is apparent. Turning the rotor in the opposite direction at the same speed (i.e. - 3000 rpm) generates vortices at the same frequency and rotating in the same sense. This indicates that the relative velocity between the rotor and freestream is still in the same sense. For this case the relative velocity in Table 2 is in the opposite sense, indicating that the local streamwise velocity is slightly increased by the presence of the rotor. In general, for rotation in the clockwise direction the strength of the vortex is greatly reduced by the lowered relative velocity. Such a case is shown in Figure 102 for various rotor positions. The vortex is clearly formed, stays near the wall and eventually bursts into turbulence. The interaction with the stream is minor due to the weakness of the vortex.

Decreasing the rotor speed to +2000 rpm in Figure 103, produces a somewhat weaker vortex than the +3000 rpm case of Figure 101. The rolling up of the flow is very pronounced but the disturbance is not as strong. Turning the rotor in the clockwise sense so that the tip moves in the same direction as the free-stream velocity, results in a stronger vortex in this case (Figure 104,  $\omega = -2000$  rpm) than that produced in Figure 102 ( $\omega = -3000$  rpm). This is simply due to the fact that the relative velocity is increased between the rotor and the freestream.

Further results, Figures 105 and 106, compare the case of rotation at  $\pm 1000$  rpm. Again, the frequency of vortex generation is the same with rotation in either sense, but for this speed the vortices are rather weak in either case. Neither disturbance is very large and the curling up of the streakline is not very evident. The magnitude of the disturbance appears to be roughly the same in either case.

Thus the flow visualization results clearly show the existence of a vortex structure downstream of the spinning rotor. The frequency of generation depends upon the rotational frequency since each rotation produces one vortex. The strength of the vortex depends upon the relative velocity between the motion of the cusp tip and the freestream velocity.

#### 4. Quantitative Results

The flow geometry described above is examined quantitatively by employing a hot wire anemometer. A Flow Corporation (Now Datametrics) Model 900 constant temperature anemometer is employed in conjunction with a pair of Thermo Systems Inc. linearizers. Since the instantaneous velocity field is required to study the vortices and their effect, the hot wire signal must be conditioned so that the only velocity recorded is at a predetermined phase angle of the rotor's motion. The technique is to mount a magnetic pickup on the shaft of the rotor, so that the position of the rotor is known. As shown schematically in Figure 107, the triggering signal from the magnetic pickup is electronically manipulated and used to arm a Schmitt trigger which in turn controls a sample and hold circuit. The hot wire continuously samples the flow velocity, but the signals are only recorded when the rotor is in a particular orientation. Thus, all data recorded with the sampling electronics at a given setting apply to the same position of the rotor and the data is instantaneous (as long as the cycles are sufficiently repeatable).

Combining the streamwise,  $u$ , and transverse,  $v$ , velocities, the entire flow-field can be depicted by plotting the magnitude of the total velocity and its orientation as the length and angle of vector arrows in a field. Such a field is shown in Figure 108, where the rotor is in the  $\theta = 0^\circ$  (i.e. the maximum extension) position. The velocity vectors shown are the instantaneous values at that particular phase position of the rotor.

Examining Figure 108, there is no evidence of the existence of a vortex in the flowfield. However, in order to see the coherent motion of a portion of matter, the observer should be in a frame of reference moving with its center of mass (as discussed in Section III). In the field of Figure 108, this can be accomplished by simply subtracting the velocity of the center of the particular vortex. Of course, the location of the vortex center is unknown, so the process involves some trial and error. However, the flow structure which leads to a vortex can be isolated. It consists of a curved instantaneous streamline in the vicinity of which the magnitudes of the velocity vectors simultaneously increase with distance from the center of curvature of the streamline.

By the above method the approximate location of the vortex center may be located. In Figure 108a, for example, the instantaneous streamlines are highly curved and appear to satisfy the necessary form at a streamwise location  $\bar{X} = 7.5$ .

Choosing an intermediate streamwise velocity from this profile and subtracting it from all the velocities in the field reveals the structure of the vortex, Figure 108b. Its center is located at approximately  $\bar{X} = 7.5$ ,  $\bar{Y} = 3.5$ . No other vortex is apparent.

One third of a cycle later, the rotor is instantaneously positioned at an angle  $\theta = 120^\circ$  as shown in Figure 109a. At this time, the vortex located at  $\bar{X} = 7.5$  for  $\theta = 0^\circ$  must be located farther downstream. The anticipated structure is found and the transformed structure (obtained by subtracting a velocity 11.8 m/sec) is shown in Figure 109b, clearly illustrating a vortex centered at  $\bar{X} \approx 10.5$ ,  $\bar{Y} = 4.75$ .

Searching the field of Figure 109a, it appears that another vortex may be present very close to the rotor position itself. The velocity profiles are taken as continuous profiles, so additional detail is shown in Figure 109c. Identifying the typical structure and subtracting a velocity of 130.0 m/sec results in Figure 109d where the vortex is evident at a location  $\bar{X} \approx 1.5$ ,  $\bar{Y} = 1.25$ . That this vortex was not observed in the  $\theta = 0^\circ$  case indicates that it was not yet large enough to be identified.

One third of a cycle later, the rotor is in the  $\theta = 240^\circ$  position. The flowfield corresponding to this time is shown in Figure 110a. Searching for the typical structure described above, it is apparent that two vortex structures are present. Subtracting streamline velocities of 13.0 m/sec and 11.0 m/sec reveals vortices at locations  $\bar{X} = 4.5$ ,  $\bar{Y} = 2.0$  and  $\bar{X} = 13$ ,  $\bar{Y} = 5.75$  as shown in Figures 110b and c respectively.

Of course, the various vortex structures illustrated above are really the same vortex observed at different times as it is swept downstream. The various positions and phase angles are plotted in Figure 13 and show the trajectory of the vortex to be an almost linear rise after its structure is established. Based on the trajectory, the translational velocity of the vortex is approximately constant and equal to the undisturbed freestream velocity, 11.6 m/sec (38.1 ft/sec). The average translational velocity, based on the positions and phase angle shown, is 10.7 m/sec.

The trajectory of the vortex, as shown in Figure 111, also explains why the vortex generator is so effective even if it is submerged within a boundary layer as in Section VII. The vortex is created with a very small core which grows rapidly and it rises out of the boundary layer. Thus the scale of its influence becomes larger as it moves downstream and it moves into a better position from

which to energize the boundary layer.

The influence of the vortex on the streamwise velocity is shown in Figure 112. The streamwise velocity profiles are plotted along with the position of the instantaneous vortex. The vortex clearly produces an overshoot in the velocity profile; that is, a velocity higher than anywhere else in the field. This overshoot must be the result of the vortex since the rotor is turning in the wrong direction to generate such a streamwise increase. In addition, the vortex flow produces a flow to the wall which energizes the boundary layer.

Analytically, Theisen<sup>54</sup> has examined the character of boundary layers and wakes with discrete vortex structures. In agreement with experimental observations, he derived a separation criterion which is related to the flow intermittency and burst frequencies. Such a method could be especially useful in the optimization of a vortex generator from the point of view of frequency, once the optimum shape has been found. Walker and Abbott<sup>55</sup> have analyzed the case of a vortex moving near a wall. Unfortunately, their vortex rotates in the opposite sense. Nevertheless, the implications of some of their results parallel those above.

The identification of the vortex structures in the present case is rather straight-forward since the forced time dependent flow is so strong. If the unsteadiness is weaker compared to the mean flow, the structure may be more difficult to distinguish. A method to handle this situation has been developed employing a discrete Fourier Transform and will be discussed in the next section. The locations of the individual vortices may then be deduced from the angles produced in the transformed plane.

Another interesting aspect of the velocity profiles of Figure 112 is the apparent potential for viscous drag reduction. The existence of the vortex in the field lowers the velocity near the wall below that which would normally exist. In this way the velocity gradient at the wall is reduced, as is the instantaneous viscous drag. The effect of this reduction on the mean viscous drag is currently being investigated. The entire situation is reminiscent of the use of a vortex sheet to produce the required boundary condition in potential flow.

## 5. Discussion

The results presented above show the generation and subsequent dynamics of the unsteady vortices produced by a mechanical rotor operating near a wall.

The very large scale vorticity and structure shown here has two main applications. One is to explain the success achieved with vortex generators in various applications. The second is to use these readily identifiable structures in order to test methods of determining large scale vortex structures in nominally "steady" boundary layers. Success in identifying the large scale steady structures would then allow the modeling of a real steady turbulent boundary layer with both its large scale structure and small scale viscous structure.

## SECTION XI

### DATA ANALYSIS TO IDENTIFY LARGE SCALE VORTEX STRUCTURES

#### 1. Background

The recent interest<sup>11</sup> in large scale coherent flow structure is due, to a large extent, to the inadequacy of present analytical and empirical methods of treating turbulent flow. The large scale structure leads to an increased mixing rate and is thus of great importance in systems which are mixing limited. However, the presence of the structure is difficult to determine in a quantitative fashion. Qualitative results in nominally steady flow have been presented by Brown and Roshko<sup>14</sup> among others. An example of a large scale structure in an unsteady jet is shown in Figure 3, employing smoke flow. The quantitative difficulties are, to a large extent, due to the fact that the large scale structures are convected with the local fluid velocity. Therefore, in order to correctly identify the structure, one needs to know the approximate convection velocity. Of course errors in the assumed convection velocity would also change the appearance of the large scale structure. Therefore, it is desirable to develop a method of identification of the large scale motions and thus determine their convection velocities.

The present method applies a discrete Fourier transformation to a general velocity field on a point by point basis. The resulting transformed field yields a distinctive signature of the passing large scale structure. Then knowing the locations of the large scale structure, the convection of these points can be determined.

The eventual aim of this approach is to identify the existence of large scale structures in places where one might not easily find them, such as in transition from laminar to turbulent boundary layer flow. Their existence in such places would yield valuable information on the transition process itself.

Coherent structure is also expected in fully turbulent jets and boundary layers.

The question of how to define a vortex in more complicated flowfields has been treated by Lugt,<sup>56</sup> who points out that there exist situations in which a flow may have instantaneous streamlines which form a closed loop and yet the actual flow does not swirl (i.e. the path lines are not closed). The question may be especially difficult in the case of time dependent flows. In the unsteady situation, Lugt's definition of a vortex requires that it be possible to find an inertial frame in which the streamlines are closed and the centers of the closed regions do not move. This is a much stronger definition than simply closed streamlines. It implies that the vortex pattern must be convected at a constant velocity. Perhaps the definition should be extended slightly to simply state that, in order to ensure that a vortex exists, one needs to find instantaneous closed streamlines and to show that this pattern is convected with the mass of which it is composed, regardless of how the translational velocity changes with time.

## 2. The Transformation Technique

The discrete Fourier transformation maps a complex matrix of size  $N_1$  by  $N_2$  into another complex matrix of the same size by the equation:

$$F(m,n) = \sum_{k=0}^{N_1-1} \sum_{\ell=0}^{N_2-1} f(k,\ell) e^{-j \left( \frac{2\pi}{N_1} km + \frac{2\pi}{N_2} \ell n \right)} \quad (1)$$

where  $f(k,\ell)$  is the discrete function in the original plane at points  $k,\ell$  and  $F(m,n)$  is the corresponding spectrum.

### 2a. A Single Vortex on Axis

The original two dimensional spatial plane, which contains complex velocity components as a function of position, is mapped into a two dimensional frequency domain as shown in Figure 113. The velocity distribution in the physical plane is shown in Figure 113a. By the transformation Equation (1), the resulting transformed plane is shown schematically in Figure 113b. At each matrix location, the transformed plane is complex, the horizontal direction being real while the vertical direction is imaginary. Thus each entry in the matrix consists of the magnitude and phase angle of the spectral components.

For this particular case of the vortex existing on the axis of the physical plane, the complex entries in the first matrix row are all real and have phase angles  $\phi = 0$ . The entries in the first matrix column are all purely imaginary and have phase angles  $\phi = -\pi/2$ . In the present case the vortex is rotating in the counter-clockwise direction. If the vortex rotation is reversed to the clockwise direction, the directions of the entries in the first row and first column are also reversed, resulting in phase angles of  $\phi = \pi$  in the first row and  $\phi = \pi/2$  in the first column. The actual phase angles are shown in Table 3.

#### 2b. A Single Shifted Vortex

Now consider the case where the vortex is not located at the axis of the real plane but rather at some arbitrary location shown in Figure 114a. The vortex is shifted by Q units out of a total of  $N_2$  matrix points in the horizontal direction and by P units out of a total of  $N_1$  matrix points on the vertical axis. The effect of this shift of the vortex center upon the transformed matrix is shown in the schematic of Figure 114b. The phase angle of any point in the matrix is shifted from its original value (for the vortex at the axes) to a new value which is proportional to the product of the vortex shift distance and the particular matrix location.

So for any point in the first row of the matrix

$$\phi(0,n) = \phi_0(0,n) - \frac{2\pi}{N_2} n Q \quad (2)$$

where  $n$  is the matrix column number,  $Q$  is the shift distance from Figure 114a and  $\phi_0$  is the phase angle in the unshifted case. Thus, by examining the difference between the phase angles of the shifted and unshifted vortices, the shift distance  $Q$  may be identified. Likewise, the phase angle change for the matrix points in the first column is

$$\phi(m,0) = \phi_0(m,0) - \frac{2\pi}{N_1} m P \quad (3)$$

where  $m$  is the matrix row number,  $P$  is the shift distance from Figure 114a and  $\phi_0$  is the phase angle in the unshifted case. At a general transformed point

$$\phi(m,n) = \phi_0(m,n) - \frac{2\pi}{N_1} m P - \frac{2\pi}{N_2} n Q \quad (4)$$

However, for the purpose of identifying the vortex location, the axis values are the simplest to handle.

The actual spectrum phase angles for the shifted vortex case are shown in Table 4. The shift of the vortex may be computed from Equations (3) & (4) to be  $P = 50$  and  $Q = 64$  (out of an  $89 \times 89$  matrix) and may be verified by the shift shown in Figure 114a.

#### 2c. A Constant Magnitude Rotation

The two previous examples have dealt with a classical vortex velocity distribution with a solid body rotation near the center (i.e. velocity proportional to radius) and velocity inversely proportional to radius farther out from the center. In order to ensure that the particular velocity distribution in the rotational flow does not affect the technique proposed to locate the center of the motion, consider the case shown in Figure 115. The magnitude of the velocity is constant throughout the plane and the center of the motion is on axes. The phase angles in the most important portion of the frequency plane are shown in Table 5 and confirm the result that the spectrum is real in the first row and imaginary in the first column.

#### 2d. A Convected Vortex

Consider now the case of a vortex which is not at rest relative to the coordinate system but rather is convected with the flow at some translational velocity. The velocity, as shown in Figure 116a, is then more complicated at least in the sense that the vortex center may not be clearly seen. As discussed earlier, the vortex may be seen in a coordinate frame moving with the velocity of the vortex center itself. Of course, in order to find that frame, the vortex center must be found. Since the present field is a generated example, the translational velocity field is known and its transformed matrix may be examined separately. The variation of translational velocity is shown in Figure 116b while the superimposed vortex is that in Figure 114a.

The transformed matrix of the entire flowfield of Figure 116a is shown in Table 6, while the transformed matrix of only the translational component, Figure 116b, is shown in Table 7. The translational component only produces a change in the first column of the matrix while the rest is zero. Thus the inclusion of the translational flow variation only contaminates the first column of the entire transformed flow as shown in Table 6. This may also be seen by

comparing Table 6 with Table 4, the transformed vortex alone.

Thus the location of the vortex being convected in this parabolic translational flow can be found by applying Equation (4) to any other matrix points except those in the first column. In general, the original angle in the unshifted case  $\phi_0$  would not be known since it would depend to some extent on the velocity distribution in the vortex. The Q shift could be found by applying Equation (4) to the first row where  $\phi_0$  is known to be zero. Then knowing Q, the P shift may be found by applying Equation (4) to the diagonal elements of the matrix where it is known that the  $\phi_0$  values are all equal.

The vortex location is identified by the above method and the translational velocity at that point determined. Subtracting the local velocity at the center of the vortex from every point in the velocity field transforms the observer into a coordinate frame moving with the vortex. The result of this computation is shown in Figure 116c.

If the velocity in the  $N_1$  direction varies only with the  $N_2$  direction and simultaneously the velocity in the  $N_2$  direction varies only with the  $N_1$  direction, then the effect on the transformed frequency plane is only to contaminate the data in the first row in addition to the contamination of the first column. In this case it will be necessary to again make use of the fact that the diagonal of the transformed unshifted vortex has equal elements in the angle matrix. Since the phase shift is linear, Equation (4) can be applied to two sets of points on the diagonal to generate two equations for the two unknowns, P and Q.

### 3a. Identifying A Single Vortex In A Real Flow

The instantaneous flowfield structure of an oscillating jet has been determined in Sections II & III and found to contain large scale unsteady vortices which are convected downstream. A time slice of this flowfield is shown in Figure 117 and corresponds to the instant that the jet is in the horizontal position and sweeping from top to bottom. No vortex is apparent in Figure 117 for the same reason none could be seen in Figure 116a. Transforming the velocities of Figure 117 by Equation (1) results in the partial matrix shown in Table 117. Applying Equation (4) and the techniques of the preceeding section results in identifying the vortex center shifted  $P = 8.34$ ,  $Q = 2.15$  from the upper left corner point. The total velocity at that point is found and subtracted from every point in the physical plane, Figure 117, and results in the structure shown in Figure 118. Here

the coordinate frame is moving with the velocity of the point identified as the vortex center and indeed a vortex is apparent, centered at the identified point.

### 3b. Identification Of Multiple Vortices

In general, there is no reason to limit the search for vortices in a flowfield to a single vortex. Depending upon the size of the region and the type of fluid flow problem, there may be a number of vortices present. The technique shown below to determine the location of two vortex centers in the field may be extrapolated to as many more as necessary.

The two-vortex velocity field is shown in Figure 119. Not only are there two vortices in the field but the fields of the individual vortices strongly overlap one another. The transformation of this velocity field by the discrete Fourier Transformation, Equation (1), results in the partial matrix of phase angles and magnitudes shown in Table 9.

The flowfield containing two vortex centers, as shown schematically in Figure 120a, can be transformed into a single matrix. This one matrix can in turn be degenerated into two component matrices, each of which represents one of the component vortices as shown in the schematic Figures 120b and 120c. Choosing four matrix points in each of the transformed planes, an equation of the form of Equation (1) can be written for each of the points. Then the eight points in Figures 120b and 120c result in eight equations and 12 unknowns  $Q_1$ ,  $Q_2$ ,  $P_1$ ,  $P_2$ ,  $a_{nm}$ ,  $a_{mn}$ ,  $a_{n'n'}$ ,  $a_{n'm'}$ ,  $b_{mn}$ ,  $b_{nm}$ ,  $b_{n'm'}$ ,  $b_{m'n'}$ . However the magnitudes of the spectrum are symmetric about the diagonal so  $a_{mn} = a_{nm}$ ,  $b_{nm} = b_{mn}$  etc. Then the system is reduced to eight equations with eight unknowns and solved to yield the vortex locations  $P_1$ ,  $Q_1$  and  $P_2$ ,  $Q_2$ .

Numerically, the solution is accomplished in the following manner. A guess is made for the vortex locations,  $P_1$ ,  $Q_1$  and  $P_2$ ,  $Q_2$ . With these four variables defined the system is reduced to eight equations and four unknowns. This will then yield two solutions for each of the four unknowns. The guess of the vortex locations resulting in the smallest difference between these two solutions is the correct location of the vortices.

Such a search has been accomplished for the double vortex generated velocity field shown in Figure 119 and resulted in vortex locations of 64,50 and 60,39 in the 89 by 89 matrix which are the exact positions of the computer generated vortices. Thus the technique works well for a set of well defined vortices.

#### 4. Multiple Vortices In Real Flows

The same technique is applied to a real flow containing multiple vortices by examining the flow shown schematically in Figure 100. A cam shaped rotor is turned in the counter-clockwise direction in a freestream flow from left to right. Each time the surface discontinuity is exposed, a clockwise vortex is generated and is convected downstream as shown in the smoke photograph of Figure 101. This flowfield has been discussed in Section X. An example of the instantaneous velocity field is shown in Figure 121, based on conditionally sampled hot wire anemometry data. In Section X, this data was shown to contain two convected vortices as may be seen in Figure 109 at a different instant of time.

Analyzing the velocity field of Figure 121 by the multiple vortex technique described in part 2f results in the identification of two vortex centers located at positions 13,4 and 7,22. By a visual technique of examining the wave pattern produced by the convected vortices in the velocity field, the location of the vortex centers have been estimated at 10,3 and 3,19. Thus the multiple vortex transformation analysis produces reasonable accuracy in spite of the fact that it only employs four data points in the vortex field. This is even more remarkable when one considers that the real vortices are imperfect due to the accuracy limitations of the measurements and the existence of other constituents in the field.

The accuracy of the technique could be improved by employing more data points or perhaps a regression analysis. However, one objective of the present effort is to develop a technique which can be applied to fields where the data is sparse. In addition, the numerics are purposely held to a minimum in order to allow the examination of large flow areas.

Having determined estimates of the vortex locations as described above, the velocity fields in the coordinate frames moving with those vortices are found by subtracting the translational velocities at the centers from each velocity vector in the field. The results are shown in Figure 122a for the upstream vortex and in Figure 122b for for the downstream vortex. The presence of the vortex structure is clear in each case and having thus been found, their effect on the overall flowfield can be examined.

Thus the discrete Fourier transformation technique discussed above appears to merit further examination as a tool to identify coherent large scale structure in real flow systems. In the generated test cases the transformation method identifies the center very well. In the real flow cases, the success is not as dramatic but still quite good.

## REFERENCES

1. Crow, S.C. and Champagne, F.H.: Orderly Structure in Jet Turbulence, J. Fluid Mech., Vol. 48, Part 3, 1971, pp. 547-591.
2. Binder, G. and Favre - Marinet, M.: Mixing Improvement in Pulsating Turbulent Jets, ASME Symposium on Fluid Mechanics of Mixing, June 1973.
3. Viets, H.: Flip-Flop Jet Nozzle, AIAA Journal, Vol. 13, No. 10, October 1975, pp. 1375-1379. (See also U.S. Patent No. 3,926,373.
4. Williams, J.R., Ambrosiani, J.P. and Palmer, W.E.: Analysis of a Pulsating Wall Jet, Columbus Aircraft Division/North American Rockwell Report NR 72H-325, October 1972.
5. Anon.: The Pulse-Combustion Furnace, GRI Digest, Vol. 1, No. 2, June 1978. (Published by the Gas Research Institute, Chicago, Illinois).
6. Lighthill, Sir J.: Mathematical Biofluidynamics, published by the Society for Industrial & Applied Mathematics (SIAM), Philadelphia, Pa., 1975.
7. DeLaurier, J.D. and Harris, J.: Aerodynamics of Flapping Wing Flight, Seminar, Wright State University, Dayton, Ohio, May 1978.
8. Bushnell, D.M., Hefner, J.N. and Ash, R.L.: Compliant Wall Drag Reduction for Turbulent Boundary Layers, Physics of Fluids, Vol. 20, S31, 1977.
9. Viets, H., Balster, D. and Toms, H.L.: Time Dependent Fuel Injectors, AIAA Paper No. 75-1305, AIAA/SAE 11th Propulsion Conference, Anaheim, California, 1975 (See also U.S. Patent No. 3,998,386).
10. Simmons, J.M., Platzer, M.F. and Smith, T.C.: Velocity Measurements in an Oscillating Plane Jet Issuing Into a Moving Air Stream, J.F.M., Vol. 84, Part 1, 1978, pp. 33-53.
11. Roshko, A.: Structure of Turbulent Shear Flows: A New Look, AIAA Journal, Vol. 14, No. 10, 1976, pp. 1349-1357.
12. Michalke, A.: On Spatially Growing Disturbances in an Inviscid Shear Layer, J. Fluid Mech., Vol. 23, Part 3, 1965, pp 521-544.
13. Moore, D.W. and Saffman, P.G.: The Density of Organized Vortices In A Turbulent Mixing Layer, J. Fluid Mech., Vol. 69, 1975, pp. 465-473.
14. Brown, G.L. and Roshko, A.: The Effect of Density Difference on the Turbulent Mixing Layer, Turbulent Shear Flows, AGARD-CP-93, 1971, pp. 23 (1-12)

15. Bevilaqua, P.M. and Lykoudis, P.S.: Mechanism of Entrainment in Turbulent Wakes, AIAA Journal, Vol. 9, No. 8, Aug. 1971, pp. 1657-59.
16. Stoker, J.J.: Water Waves, Interscience Publishers, New York, 1957.
17. Piatt, M. and Viets, H.: Conditioned Sampling in an Unsteady Jet, AIAA Paper No. 79-1857, AIAA Aircraft Systems and Technology Meeting, New York City, August 1979.
18. Schlichting, H.: Boundary Layer Theory, McGraw-Hill Book Co. Inc., New York, 1960, pg. 400.
19. Mitchell, C.G.B.: Assessment of the Accuracy of Gust Response Calculations by Comparison with Experiments, J. Aircraft, Vol. 7, No. 2, March-April 1970, p. 117-125.
20. Gilman, Jean Jr. and Bennett, Robert M.: A Wind Tunnel Technique for Measuring Frequency Response Functions for Gust Load Analyses, J. Aircraft, Vol. 3, No. 6, 1966, pp 535-540.
21. Horlock, J.H.: An Unsteady Flow Wind Tunnel, Aero Quart., Vol. 25, Part 2, May 1974.
22. Ostdiek, F.R.: A Cascade in Unsteady Flow - A Progress Report, Unsteady Flows in Jet Engines, SQUID Workshop, July 1974, F.O. Carta, Ed., p. 347-376.
23. Sawyer, R.A.: Design and Operation of a Low Speed Gust Tunnel, AGARD CP - 174, Wind Tunnel Design and Testing Techniques, London, UK, Oct. 1975.
24. Ham, N.D., Bauer, P.H. and Lawrence, T.L.: Wind Tunnel Generation of Sinusoidal Lateral and Longitudinal Gusts by Circulation Control of Twin Parallel Airfoils, Report ASRL TR 174-3, Mass. Inst. of Tech., Aug. 1974.
25. Simmons, J.M. and Platzer, M.F.: Experimental Investigation of Incompressible Flow Past Airfoils with Oscillating Jet Flaps, J. Aircraft, Vol. 8, No. 8, Aug. 1971, p. 587-592.
26. Viets, H.: High Frequency Gust Tunnel, AGARD Conference Proceedings No. 174 on Windtunnel Design and Testing Techniques, London, England Oct. 1975.
27. Simmons, J.M., Platzer, M.F. and Smith, T.C.: Velocity Measurements in an Oscillating Plane Jet Issuing into a Moving Air Stream, J. Fluid Mechanics, Vol. 84, part 1, 1978, pp. 33-53.

28. Lin, C.C.: Motion in the Boundary Layer with a Rapidly Oscillating External Flow, in the Proceedings of the Ninth International Congress on Applied Mechanics, Vol. 4, p. 155, Elsevier, Inc., Amsterdam, 1957.
29. McCormack, P.D., Cochran, D. and Crane, L.: Periodic Vorticity and Its Effect on Jet Mixing, Physics of Fluids, Vol. 9, No. 8, August 1966, p. 1555.
30. Pai, S.I. and Hsieh, T.Y.: Linearized Theory of Three Dimensional Jet Mixing With and Without Walls, J. Basic Engineering, Vol. 92, March 1970, pp. 93-100.
31. Schlichting, H.: Boundary Layer Theory, McGraw-Hill Inc., New York, 1968, Chapter XV, p. 391.
32. McCormick, W.S.: Personal Communication, Wright State University, 1978.
33. Liepmann, H.W. and Roshko, A.: Elements of Gas Dynamics, Wiley, 1957.
34. Kendall, J.M.: The Turbulent Boundary Layer Over A Wall With Progressive Surface Waves, J. Fluid Mechanics, Vol. 41, Part 2, 1970, pp. 259-281.
35. McCroskey, W.J.: Recent Developments in Dynamic Stall, Unsteady Aerodynamics, R.B. Kinney, Ed., University of Arizona, 1975.
36. Kramer, M.: Die Zunahme des Maximalauftriebes von Tragflugeln bei plotzlicher Anstellwinkervergrosserung (Böeneffekt), Z. Flugtech. u. Motorluftshif, Vol. 23, 1932, pp. 185-189, (also NACA T.M. 678, 1932.)
- 37a. McAllister, K.W. and Carr, L.W.: Water Tunnel Experiments on an Oscillating Airfoil at  $Re = 21,000$ , NASA TM78446, March 1978.
- 37b. McCroskey, W.J.: Personal Communication, October, 1978.
- 38a. Keesee, J.E., Francis, M.S. and Lang, J.D.: Technique for Vorticity Measurement in Unsteady Flow, AIAA Journal, Vol. 17, No. 4, April 1979.
- 38b. Keesee, J.E., Francis, M.S. Sparks, G.W., Jr. and Sisson, G.E.: Aerodynamic Characteristics of an Unsteady Separated Flow, AIAA Journal, Vol. 17, No. 12, Dec. 1979, pp. 1332-1339.
39. Quinn, B.P.: Acoustic Wing Stall Delaying Device, United States Patent No. 3,774,867; November 1973.

40. Drewry, J.E.: Fluid Dynamic Characterization of Sudden-Expansion Ramjet Combustor Flowfields, AIAA Journal, Vol. 16, April 1978, pp. 313-319.
41. Craig, R.R., Drewry, J.E. and Stull, F.D.: Coaxial Dump Combustor Investigations, AIAA Paper No. 78-1107, 1978.
42. Edelman, R.B. and Harsha, P.T.: Application of Modular Modeling to Ramjet Performance Predictions, AIAA Paper 78-944, AIAA/SAE 14th Joint Propulsion Conference, July 1978.
43. Viets, H. and Drewry, J.E.: Quantitative Prediction of Dump Combustor Flowfields, AIAA Paper 79-1481, AIAA Fluid and Plasma Dynamics Meeting, Williamsburg, Va., July 1979.
44. Choudhury, P.R. and Gerstein, M.: Turbulent Vortex Flame Stability and Spreading with Gas Jet Impriming, AFOSR Contractors Meeting on Air-Breathing Combustion Dynamics, Dayton, Ohio, October 1978.
45. Anon: The Pulse-Combustion Furnace, GRI Digest, Vol. 1, No. 2, June 1978 (Published by the Gas Research Institute, Chicago, Illinois).
46. Rose, W.G.: A Swirling Round Turbulent Jet. 1 - Mean Flow Measurements, Journal of Applied Mechanics, December 1962, pp. 615-625.
47. Stull, F.D., and Velkoff, H.R.: Effects of Transverse Ribs on Pressure Recovery in Two Dimensional Subsonic Diffusers, AIAA Paper No. 72 - 1141, Nov. 1972.
48. Haight, C.H. and O'Donnell, R.M.: Experimental Mating of Trapped Vortex Diffusers with Large Area Ratio Thrust Augmentors, U.S. Air Force Aerospace Research Laboratories Report TR 74-0115, Sept. 1974.
49. Stenning, A.H. and Schachenmann, A.A.: Oscillatory Flow Phenomena in Diffusers at Low Reynolds Numbers, ASME Paper No. 73-FE-14, 1973.
50. Schachenmann, A. and Rockwell, D.O.: Prediction of Diffuser Core Flow Fluctuations Caused by Oscillating Turbulent Flow, J. Aircraft, Vol. 15, No. 6, June 1975.
51. Papailiou, D.D. and Lykondis, P.S.: Turbulent Vortex Streets and the Mechanism of Entrainment, J.F.M., Vol. 62, 1974, pp. 11-31.
52. Quinn, B.: Compact Ejector Thrust Augmentation, J. Aircraft, Vol. 10, No. 8, August 1973, pp. 481-486.

53. Bevilaqua, P.M. and Toms, H.L., Jr.: A Comparison Test of the Hypermixing Nozzle, U.S.A.F. Aerospace Research Laboratories Report TR-74-0006, January 1974.
54. Theisen, J.G.: A New Turbulent Boundary Layer Separation Criterion Based on Flow Dynamics, Lockheed Georgia Company, Report LG78ER0007, March 1978.
55. Walker, J.D.A. and Abbott, D.E.: Implications of the Structure of the Viscous Wall Layer, Turbulence in Internal Flows, (Murthy, Ed.), Hemisphere, 1977.
56. Lugt, H.: The Dilemma of Defining a Vortex, in Recent Developments in Theoretical and Experimental Fluid Mechanics, Muller, Roesner and Schmidt (eds.), Springer-Verlag, Berlin-Heidelberg, 1979.

Portions of the present paper have been published in the following papers:

1. Viets, H. and Piatt, M.: Linearized Unsteady Jet Analysis, Proceedings of the NASA-Air Force-Navy Workshop on Thrust Augmenting Ejectors, Moffett Field, California, NASA CP-2093, June 1978.
2. Viets, H., Piatt, M., and Ball, M.: Unsteady Wing Boundary Layer Energization, Proceedings of the U.S.A.-Germany Data Exchange Meeting, Meersburg, West Germany, April 1979 (also AIAA Atmospheric Flight Mechanics Meeting, Paper No. 79-1631, Boulder, Colo., August 1979).
3. Viets, H., Piatt, M. and Ball, M.: Boundary Layer Control by Unsteady Vortex Generation, Proceedings of the Symposium on the Aerodynamics of Transportation, June 1979, Published by the ASME. Also Journal of Industrial Aerodynamics, Spring 1981, In Press.
4. Viets, H. and Piatt, M.: Induced Unsteady Flow in A Dump Combustor, (with M. Piatt), Proceedings of the 7th International Colloquium on Gasdynamics of Explosions and Reactive Systems, Gottingen, Germany August 1979. Also AIAA Progress in Aeronautics and Astronautics Series. In Press.
5. Piatt, M. and Viets, H.: Conditioned Sampling in an Unsteady Jet, AIAA Paper No. 79-1857, AIAA Aircraft Systems and Technology Meeting, New York, August 1979.
6. Viets, H.: Coherent Structures in Time Dependent Flow, - Proceedings of the NATO/AGARD Specialists Meeting on Turbulent Boundary Layers, The Hague, Netherlands, September 1979.
7. Viets, H., Ball, M. and Piatt, M.: Experiments in a Subscale Pilot Gust Tunnel, AIAA Paper No. 80-0453, Aerodynamic Testing Conference, Colorado Springs, Colo., March 1980. Also AIAA Journal, Spring 1981, In Press.
8. Viets, H., Piatt, M. and Ball, M.: Forced Vortices Near a Wall, - Proceedings of the U.S.-Germany Data Exchange Meeting, U.S. Naval Academy, Annapolis, Md., April 1980. Also AIAA Paper No. 81-0256, Aerospace Sciences Meeting, St. Louis, Mo., Jan. 1981.

9. Bethke, R.J. and Viets, H.: Data Analysis to Identify Coherent Flow Structures, AIAA Paper No. 80-1561, AIAA Atmospheric Flight Mechanics Conference, Danvers, Mass., Aug. 1980.
10. Viets, H., Ball, M. and Bouginé, D.: Large Scale Structures in Driven Unsteady Diffuser Flows: Proceedings of the International Flow Visualization Symposium, Ruhr University, Bochum, Germany, Sept. 1980.
11. Viets, H., Ball, M., and Bouginé, D.: Performance of Forced Unsteady Diffusers, AIAA Paper No. 0154, Aerospace Sciences Meeting, St. Louis, Mo., Jan. 1981.

Table 1. Maximum and Average Streamwise Tip  
Speeds Relative to Freestream for  
the Present Geometry and a Nominal  
Velocity of 123.5 ft/sec.

$\omega$	$\frac{V_{rel}}{V_{fs}}$ max	$\frac{V_{rel}}{V_{fs}}$ av.
1000	1.026	1.017
-1000	.974	.983
2500	1.066	1.042
-2500	.934	.958
4000	1.106	1.067
-4000	.894	.933
5000	1.132	1.084
-5000	.868	.916

Table 2

Figure No.	RPM	$V_{rel} (m/sec)$	$V_{rel}/V_{\infty}$	$Re(x10^4)$
				$Re = \rho \frac{V_{rel} H}{\mu}$
4	3000	23.60	2.03	4.02
5	-3000	-.42	-.03	.015
6	2000	19.61	1.69	3.35
7	-2000	3.64	.31	.61
8	1000	15.61	1.34	2.65
9	-1000	7.63	.66	1.31

TABLE 3.

		n						
		0	1	2	3	4	5	6
m	0	--	0	0	0	0	0	0
	1	-1.571	-.786	-.374	-.133	-.064	-.765	-.413
	2	-1.571	-1.197	-.786	-.375	-.244	-.667	-.672
	3	-1.571	-1.438	-1.196	-.786	-.505	-.549	-.709
	4	-1.571	-1.507	-1.327	-1.066	-.785	-.536	-.450
	5	-1.571	-.806	-.904	-1.022	-1.035	-.785	-.317
	6	-1.571	-1.158	-.899	-.862	-1.121	-1.254	-.785

Table 3. Spectrum angles for the case of a single vortex at the axis of the physical plane and turning in the counter-clockwise direction as shown in Figure 113a.

TABLE 4.

m	n						
	0	1	2	3	4	5	6
0	--	1.765	-2.753	-.989	.777	2.541	-1.977
1	1.182	-2.551	.374	1.632	-2.817	-1.753	.363
2	-2.348	-.209	1.968	-2.140	-.244	1.098	2.857
3	.406	2.304	-1.973	.203	2.248	-2.314	-.709
4	-3.124	-1.295	.650	2.675	-1.562	.452	2.303
5	-.371	2.159	-2.457	-.810	.942	2.956	-1.094
6	2.383	-1.723	.302	2.103	-2.674	-1.042	1.191

Table 4. Spectrum angles for the case of a single vortex shifted from the axis of the physical plane to a position of  $P = 50$ ,  $Q = 64$  and turning in the counter-clockwise direction as shown in Figure 114a.

TABLE 5.

	n						
	0	1	2	3	4	5	6
0	--	0.0	0.0	0.0	0.0	0.0	0.0
1	-1.571	-.786	-.299	.179	2.480	-2.609	-.614
2	-1.571	-1.272	-.786	.240	1.047	-1.439	-1.006
m 3	-1.571	1.749	-1.811	-.786	-.151	-.492	-1.125
4	1.571	2.232	-2.619	-1.420	-.785	-.183	.314
5	1.571	1.039	-.132	-1.079	-1.388	-.785	.056
6	-1.571	-.958	-.565	-.446	-1.885	-1.627	-.785

Table 5. Spectrum angles for the case of a constant magnitude velocity rotational flow.

UNCLASSIFIED

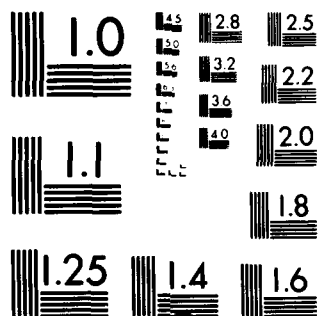
AFWAL-TM-81-148-FIMM

**F/6 20/4**

NL

2.3

100



MICROCOPY RESOLUTION TEST CHART

NATIONAL BUREAU OF STANDARDS-1963-A

TABLE 6.

m	n						
	0	1	2	3	4	5	6
0	--	1.765	-2.753	-.989	.777	2.541	-1.977
1	1.285	-2.551	-.374	1.632	-2.817	-1.753	.363
2	1.825	-.209	1.968	-2.140	-.244	1.098	2.857
3	1.294	2.304	-1.973	.203	2.248	-2.314	-.709
4	1.748	-1.295	.650	2.675	-1.562	.452	2.303
5	1.657	2.159	-2.457	-.810	.942	2.956	-1.094
6	1.822	-1.723	.302	2.103	-2.674	-1.042	1.191

Table 6. Spectrum angles for the case of a vortex convected in a parabolic flow varying in the  $N_1$  direction as shown in Figure 116a.

TABLE 7.

m	n						
	0	1	2	3	4	5	6
0	0	0	0	0	0	0	0
1	1.301	0	0	0	0	0	0
2	1.485	0	0	0	0	0	0
3	1.572	0	0	0	0	0	0
4	1.634	0	0	0	0	0	0
5	1.685	0	0	0	0	0	0
6	1.731	0	0	0	0	0	0

Table 7. Spectrum angles for a parabolic flow varying in the  $N_1$  direction as shown in Figure 116b.

TABLE 8.

m	n					
	0	1	2	3	4	
0	.081	-2.955	-2.230	-1.544	-.919	
1	2.691	.049	1.234	1.463	2.260	
2	-2.294	3.119	2.802	2.615	-2.993	
3	-1.483	-2.380	-1.843	-2.464	-.415	
4	1.798	-.675	-1.406	-.985	.761	
5	-3.012	.227	.471	-1.193	-1.437	
6	-1.545	-2.994	2.157	.683	.848	

Table 8. Spectrum angles for the case of the instantaneous structure of an oscillating jet, transformed from Figure 117.

TABLE 9.

	<i>n</i>			
	0	1	2	3
0	0.0/--	3172.0/-1.236	3820.1/.671	2183.6/2.577
1	2965.5/-1.571	3163.1/1.120	2748.9/-2.845	1432.1/-.698
2	2837.3/1.571	2131.9/-2.433	1199.6/-.115	512.4/2.201
3	945.8/-1.571	544.4/.468	174.3/2.616	16.3/1.791

Magnitude/Angle

Table 9. Partial magnitude/phase angle matrix produced by the transformation of the two-vortex velocity field of Figure 118.

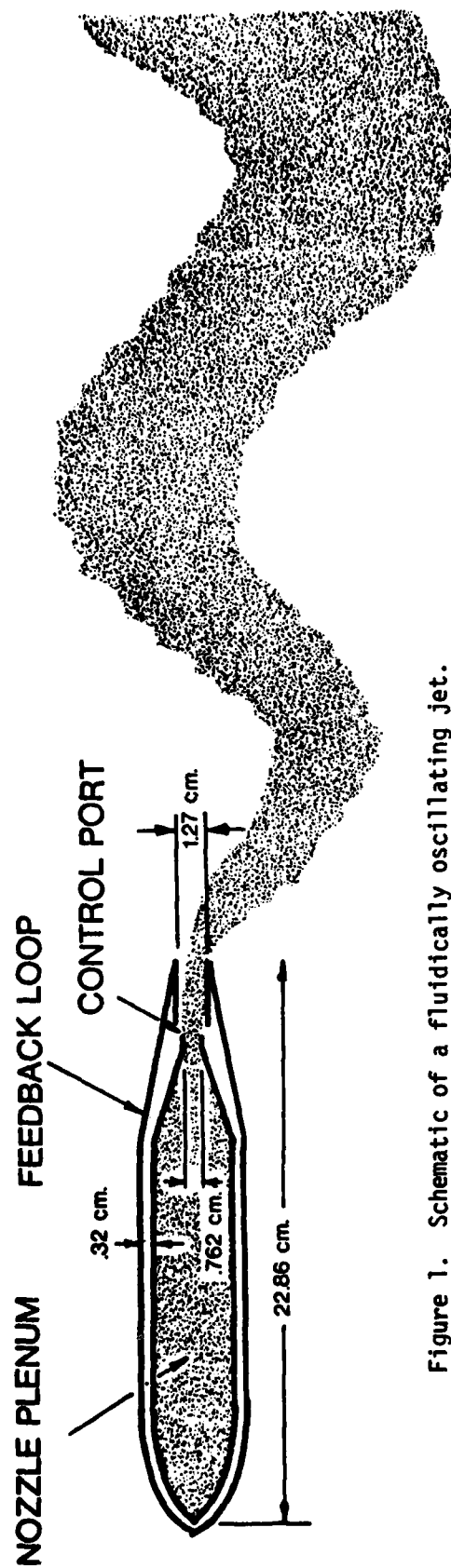


Figure 1. Schematic of a fluidically oscillating jet.

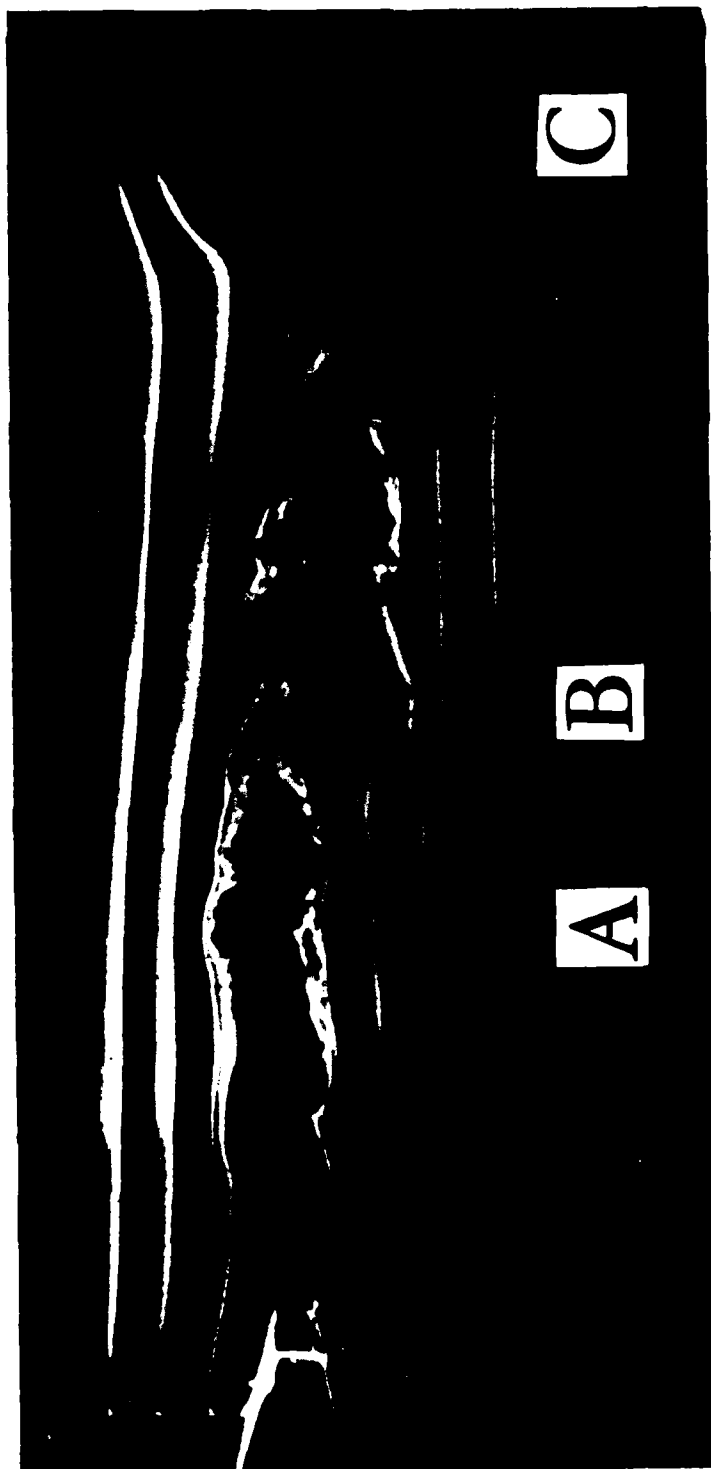


Figure 2. Smoke flow visualization of the oscillating jet in a coflowing stream of 45.8% of the jet velocity.

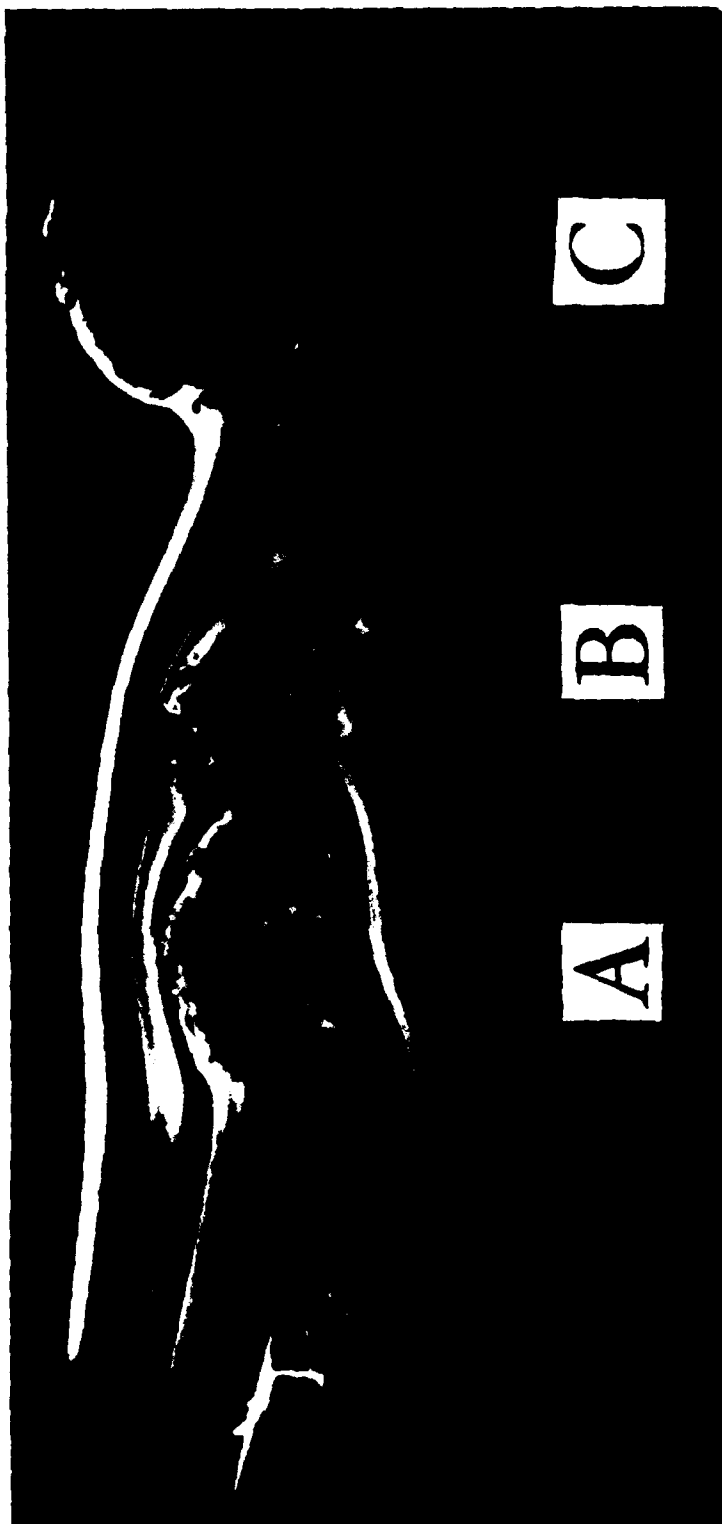


Figure 3. Smoke flow visualization of the oscillating jet in a coflowing stream of 28% of the jet velocity.

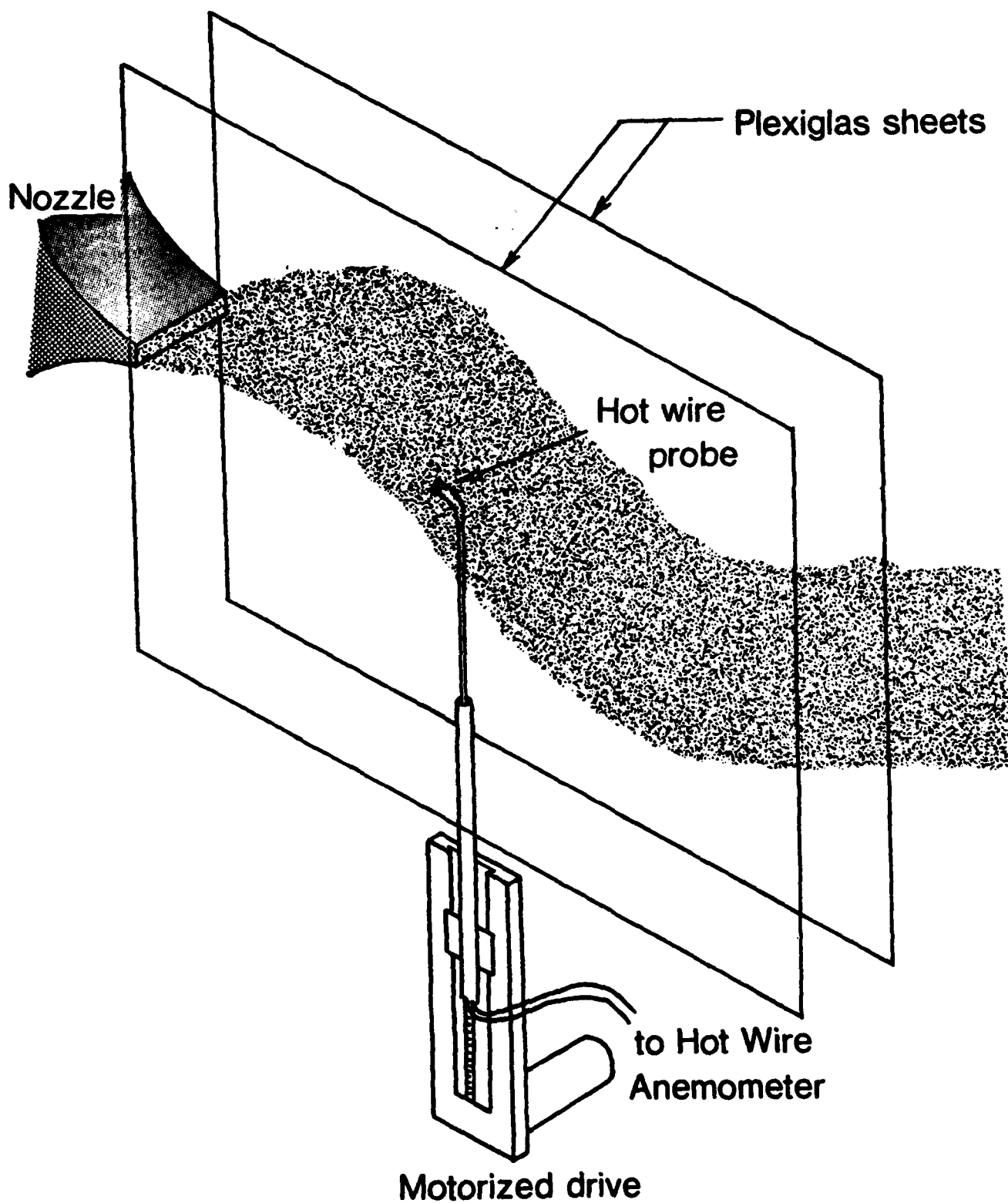


Figure 4. Experimental Setup

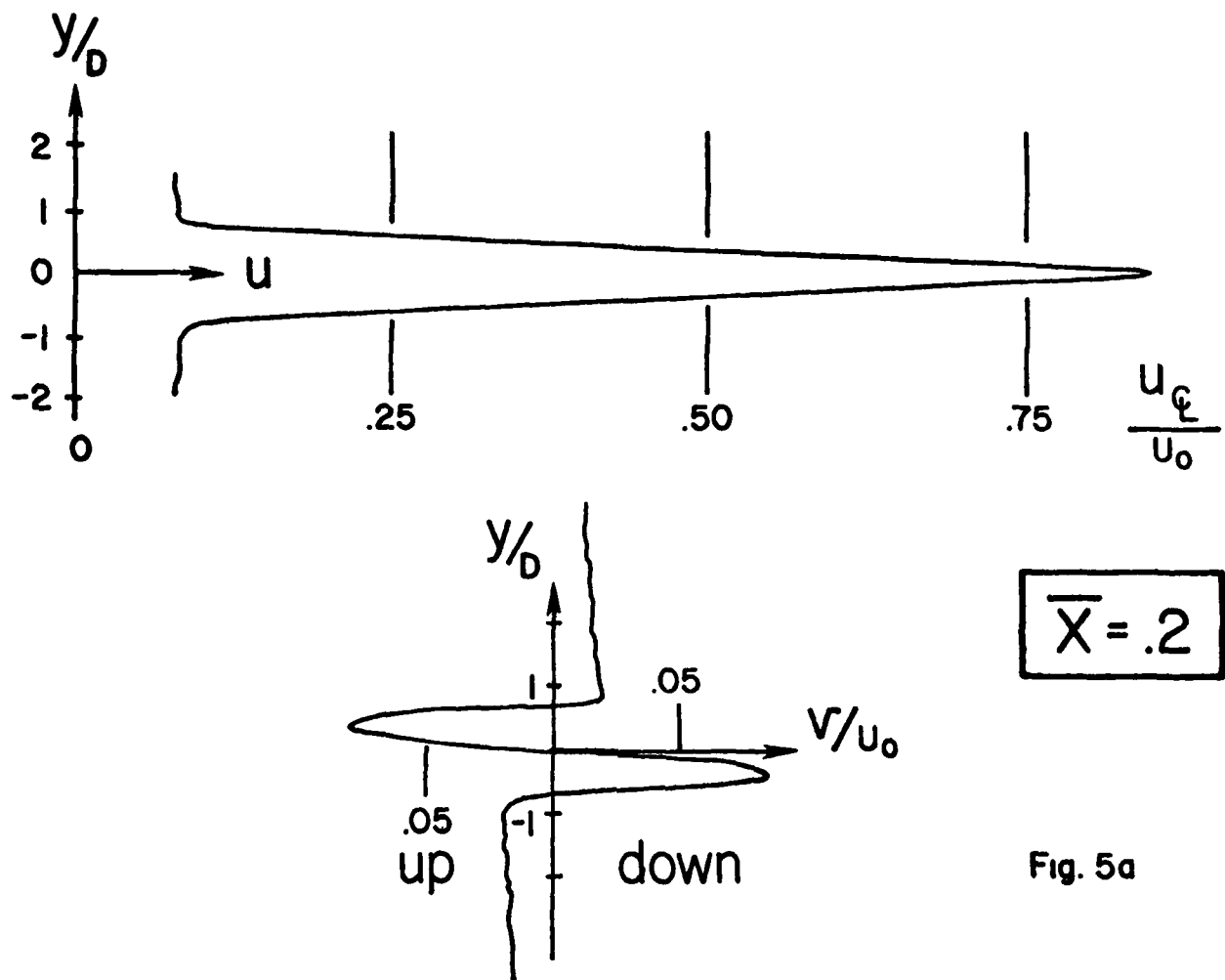


Figure 5a. Time averaged velocity measurements in the oscillating jet,  $U_0=43$  m/sec,  $\omega=12$  Hz.

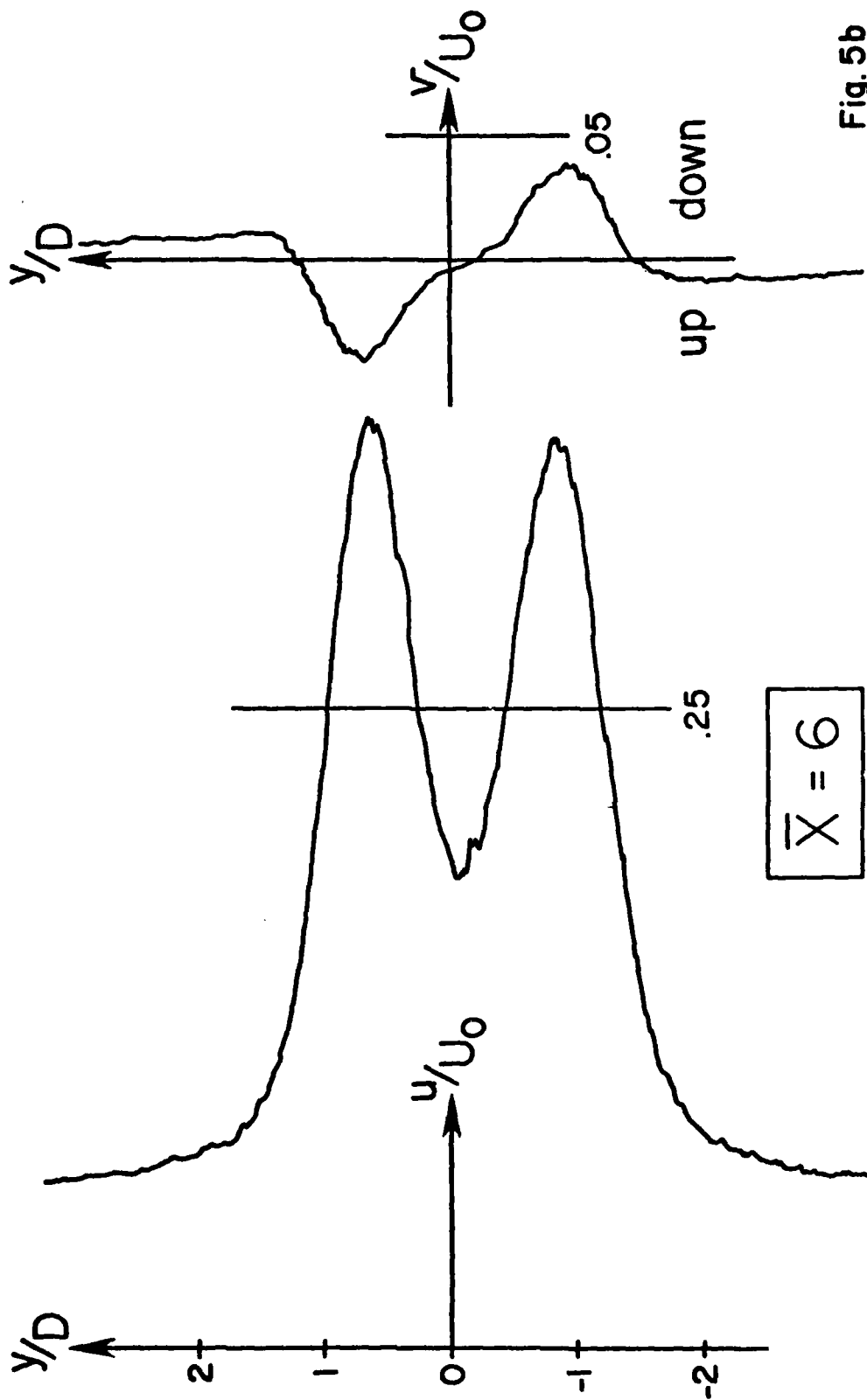


Fig. 5b

Figure 5b. Continued

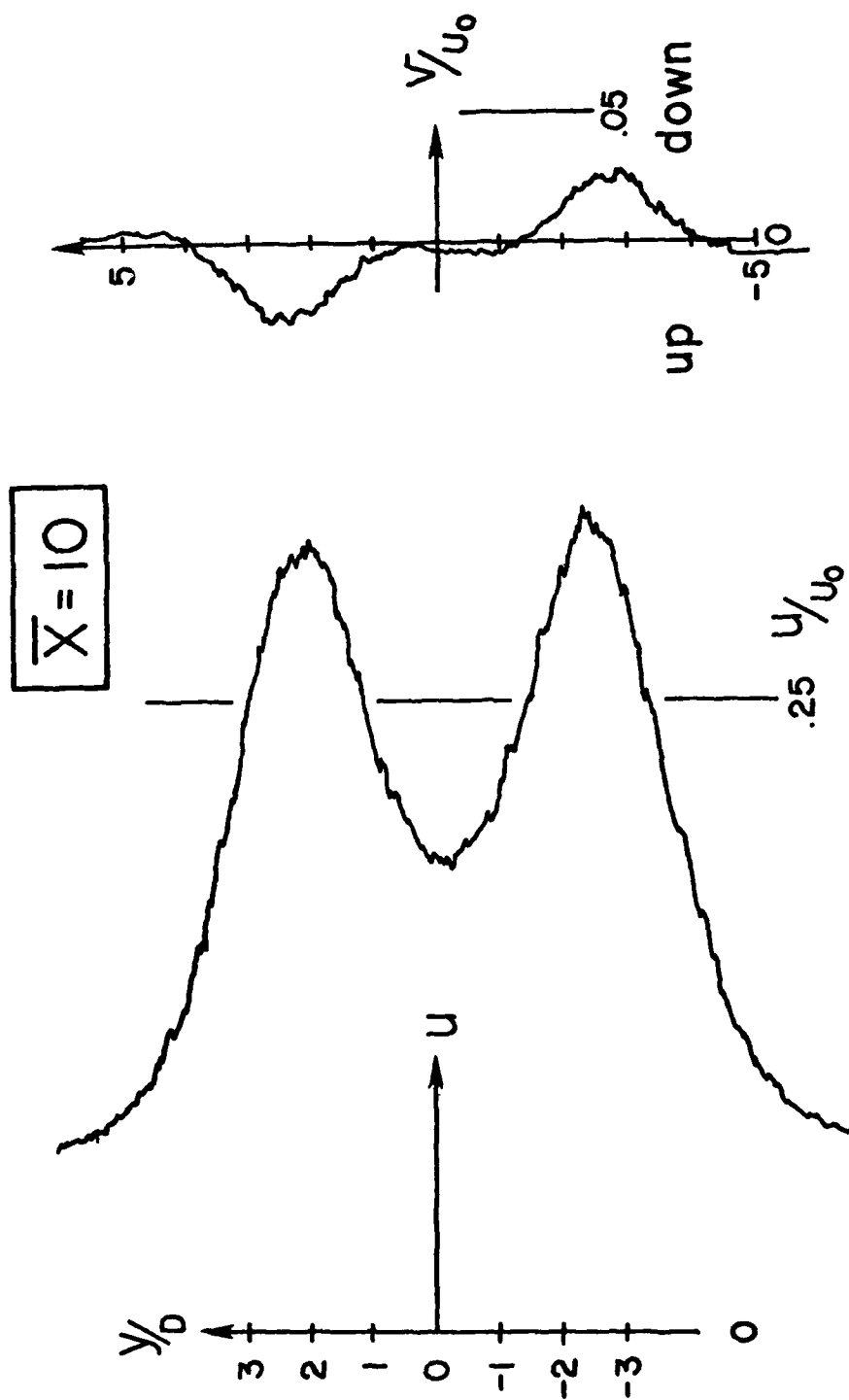


Figure 5c. Continued

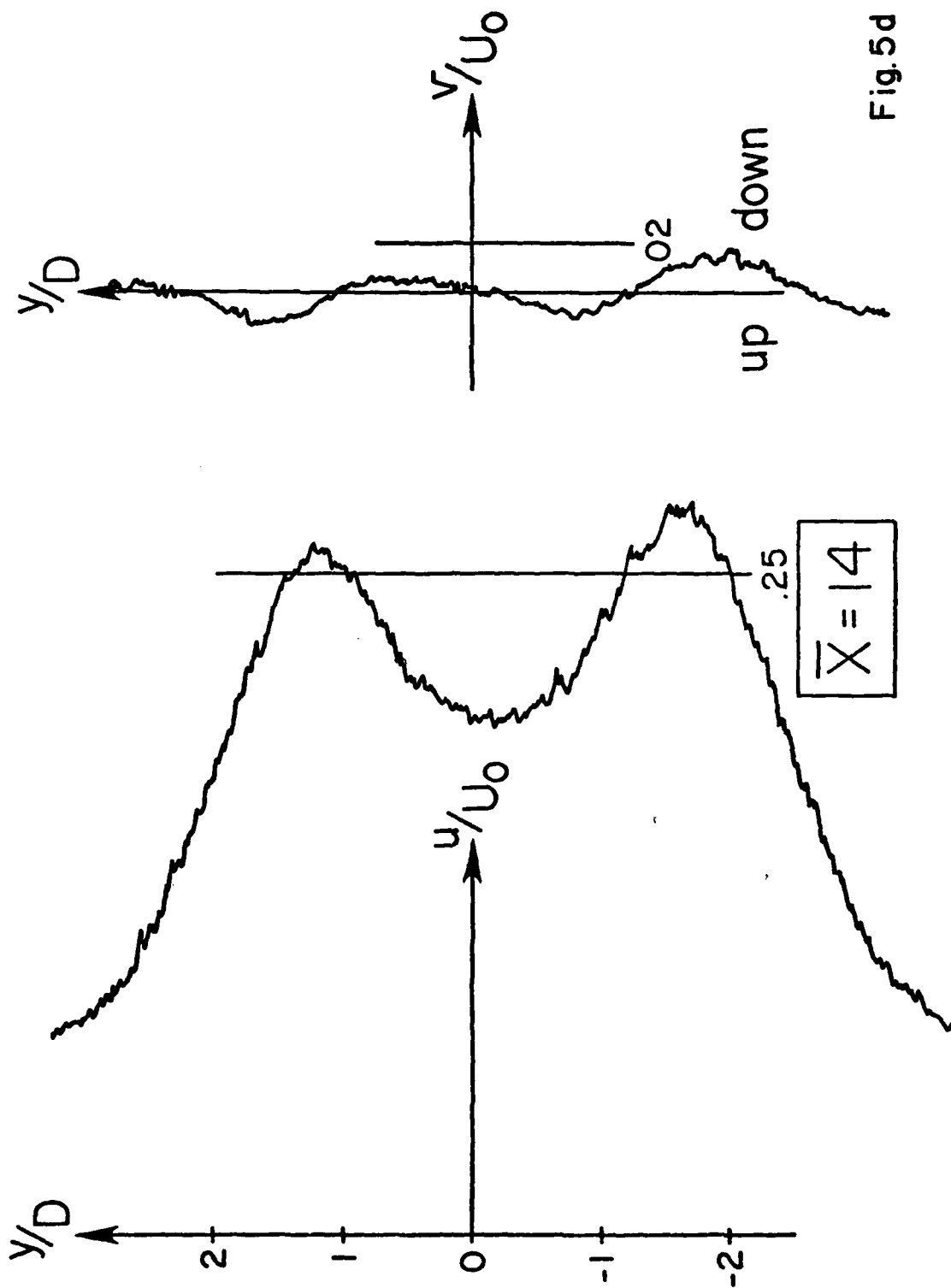


Fig. 5d

Figure 5d. Continued

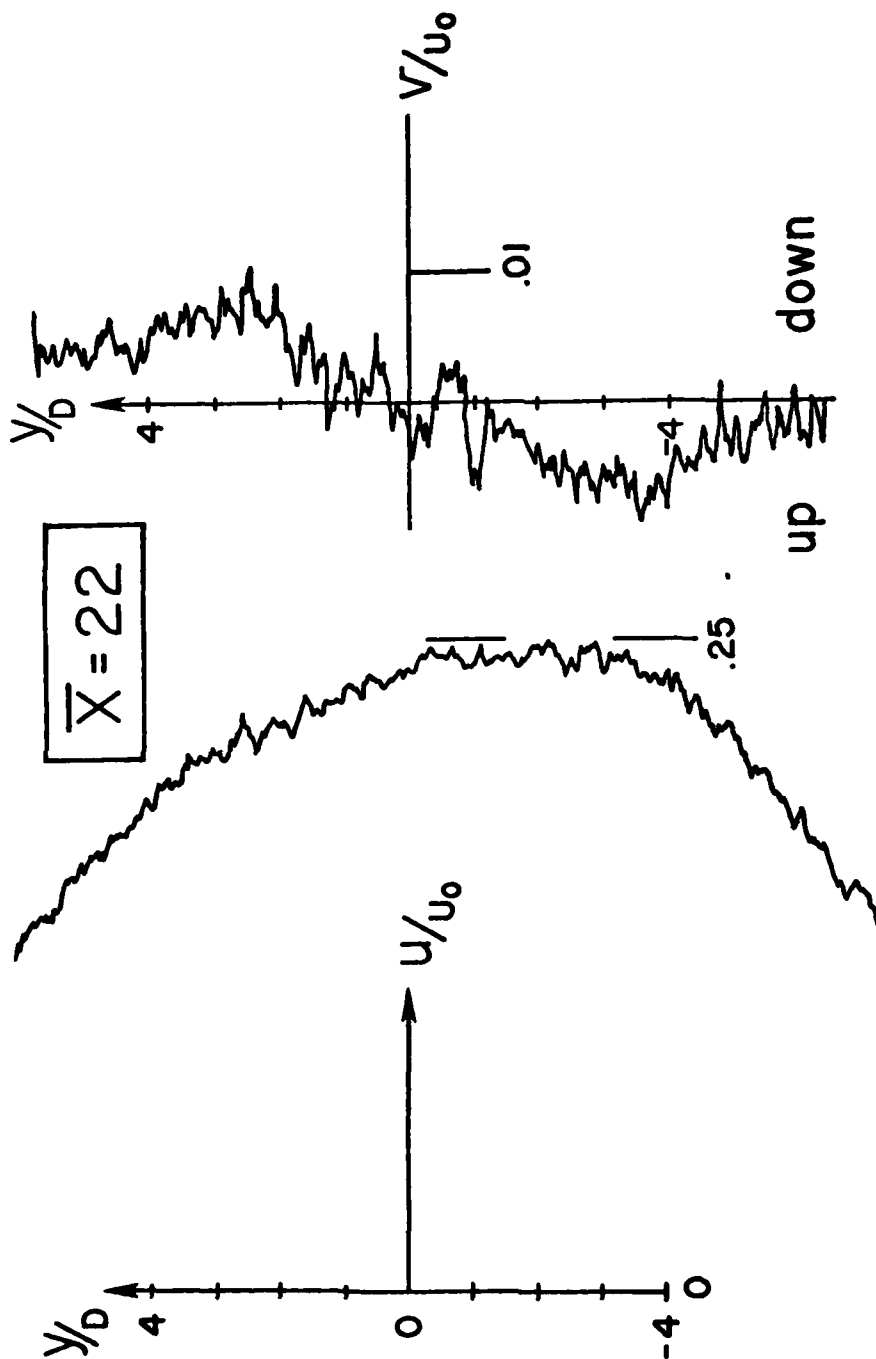


Figure 5e. Continued

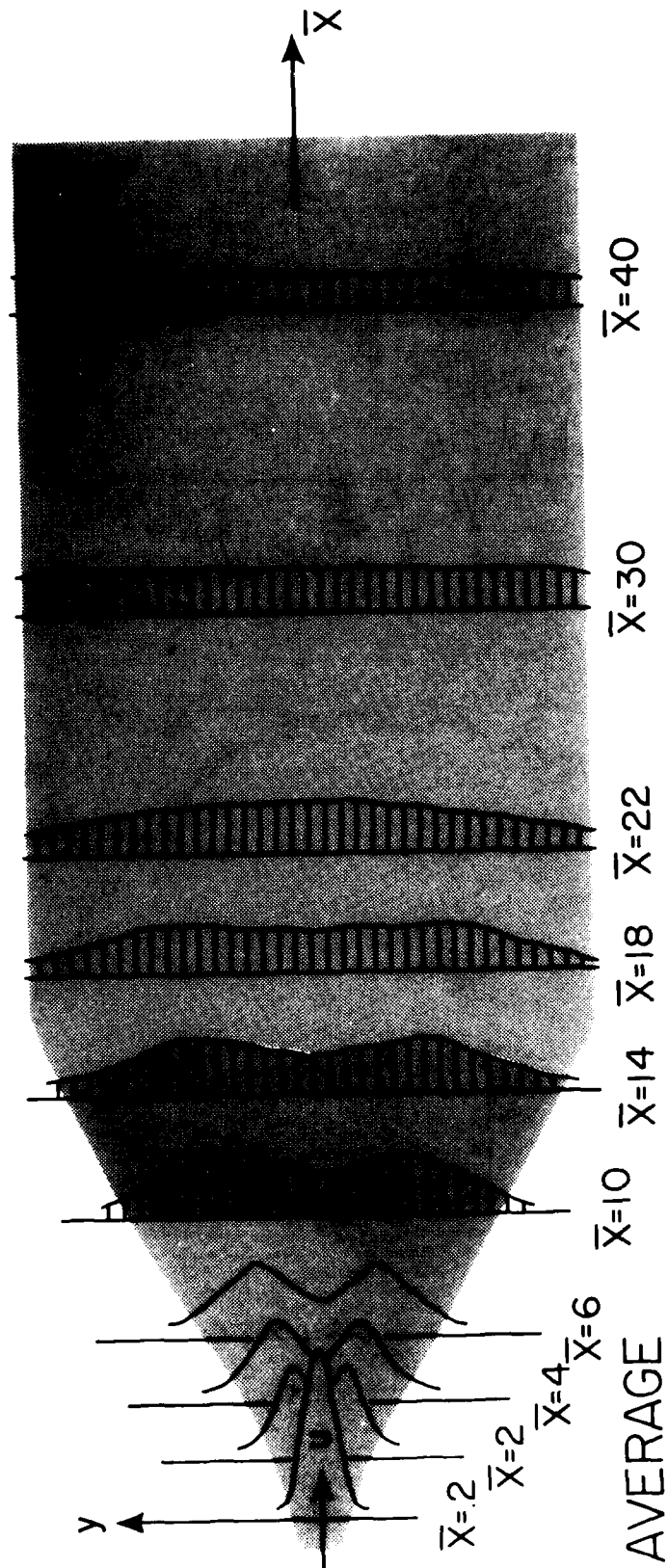


Figure 6. Composite view of the time average oscillating jet.

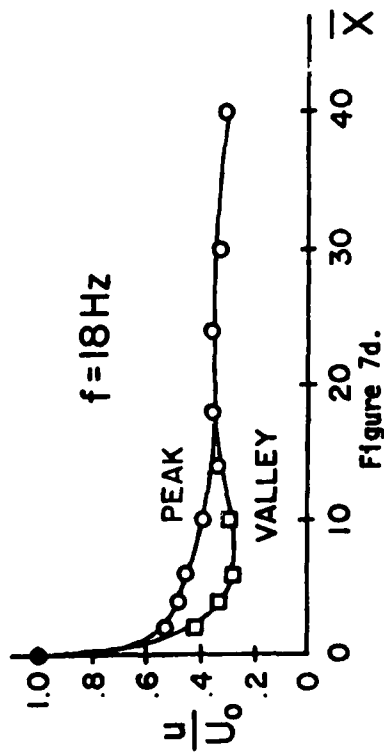
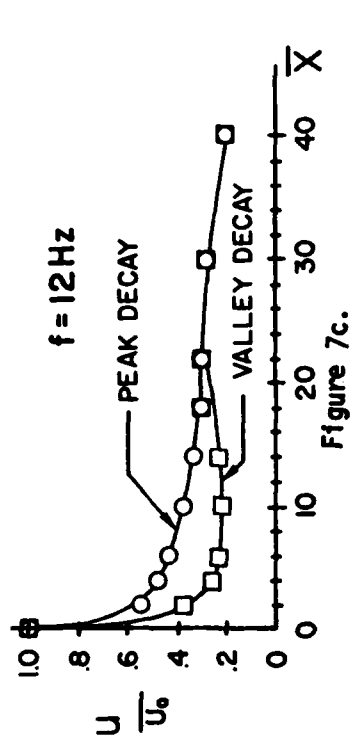
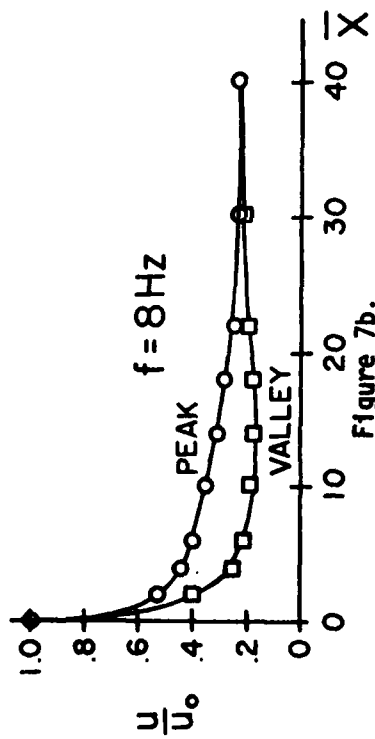
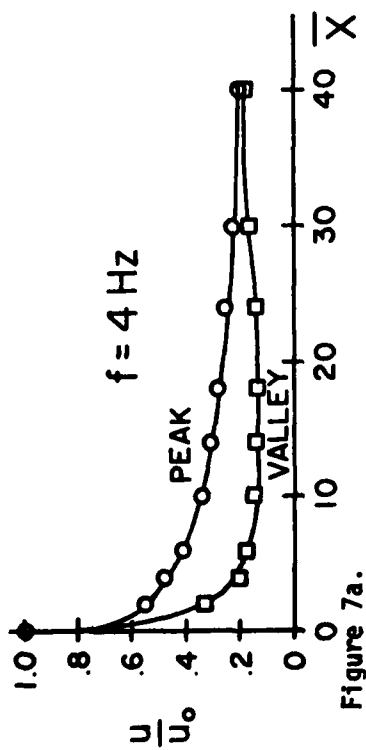


Figure 7. Centerline and peak velocity decay for various frequencies in the time averaged oscillating jet.

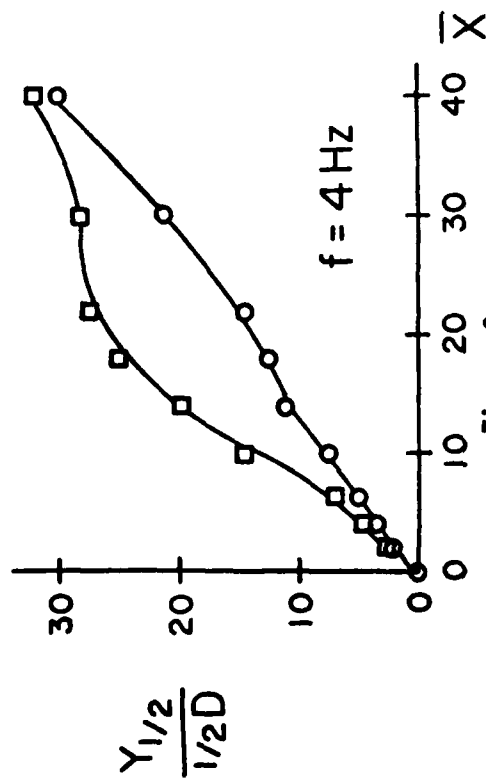


Figure 8a.

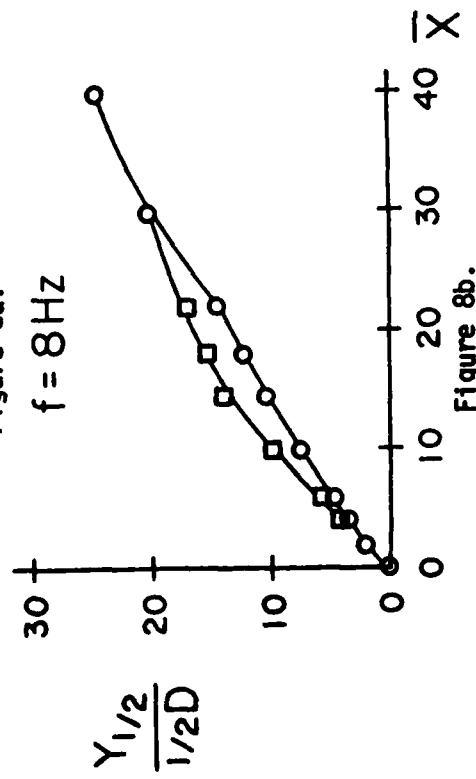


Figure 8b.

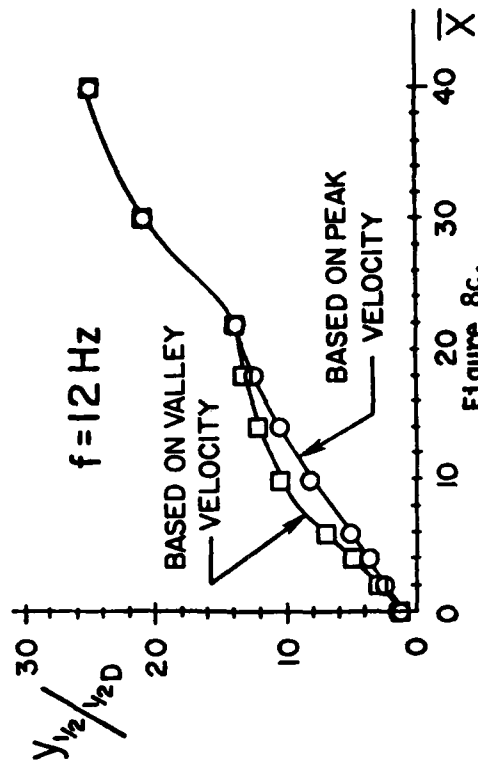


Figure 8c.

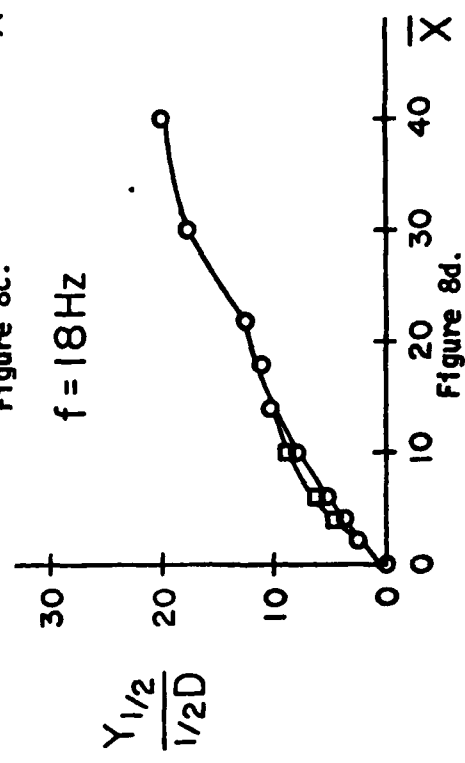


Figure 8d.

Figure 8. Half width growth in the time averaged oscillating jet for various frequencies.

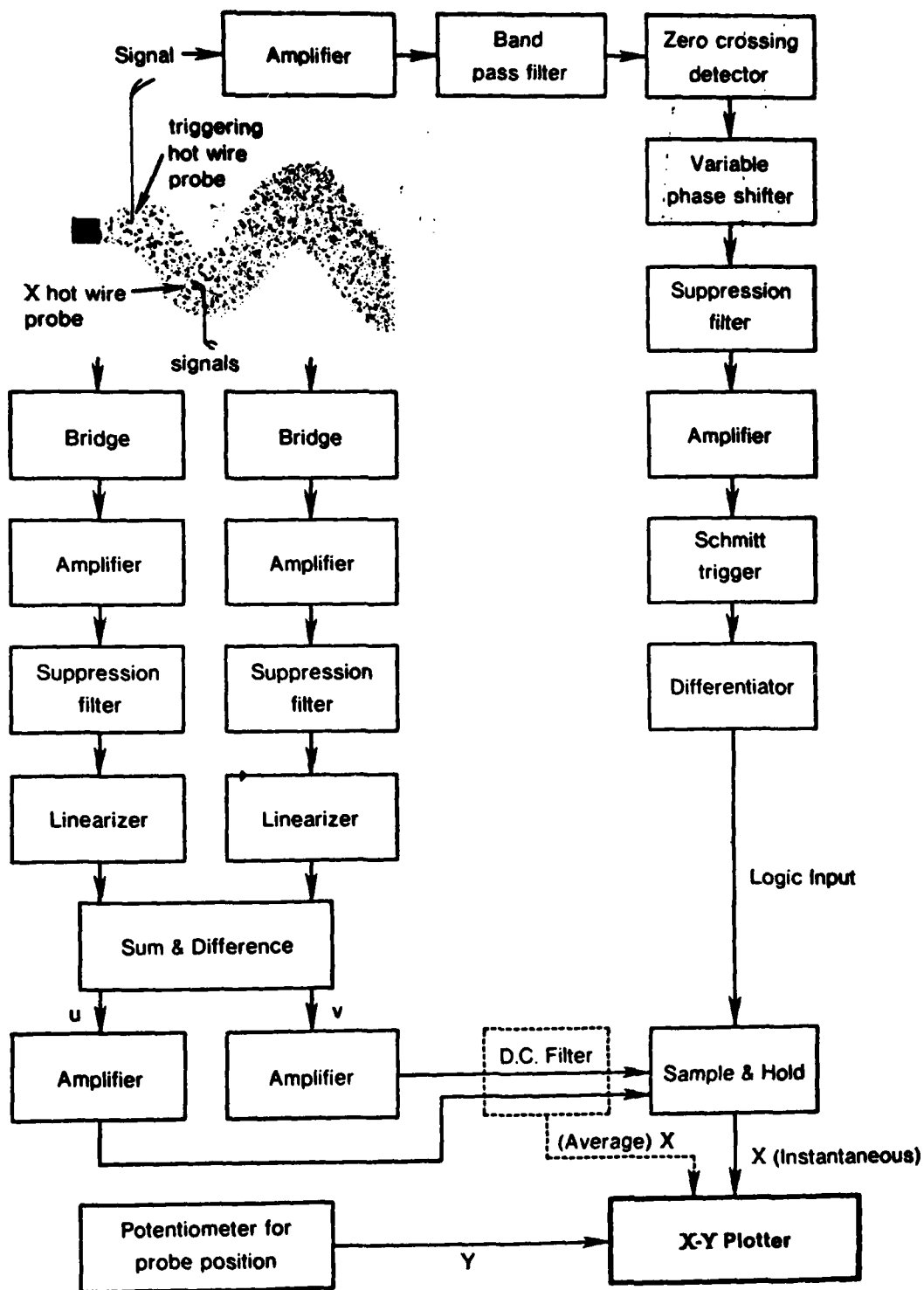


Figure 9. Schematic of the electronic circuitry employed to conditionally sample the unsteady jet flowfield.

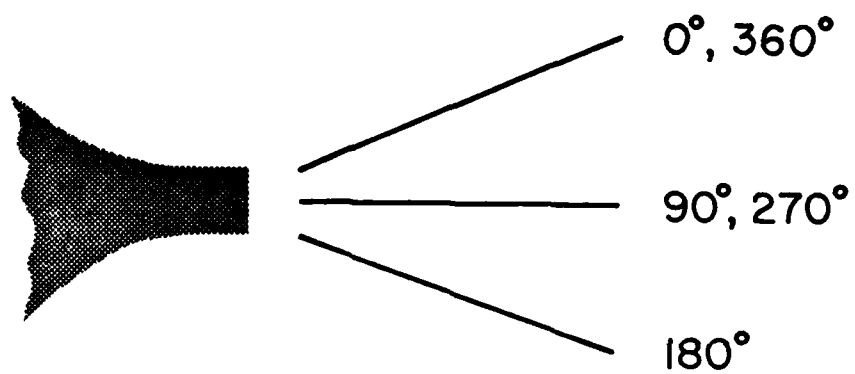


Fig. 10

Figure 10. Definition of the jet phase angle in terms of jet orientation.

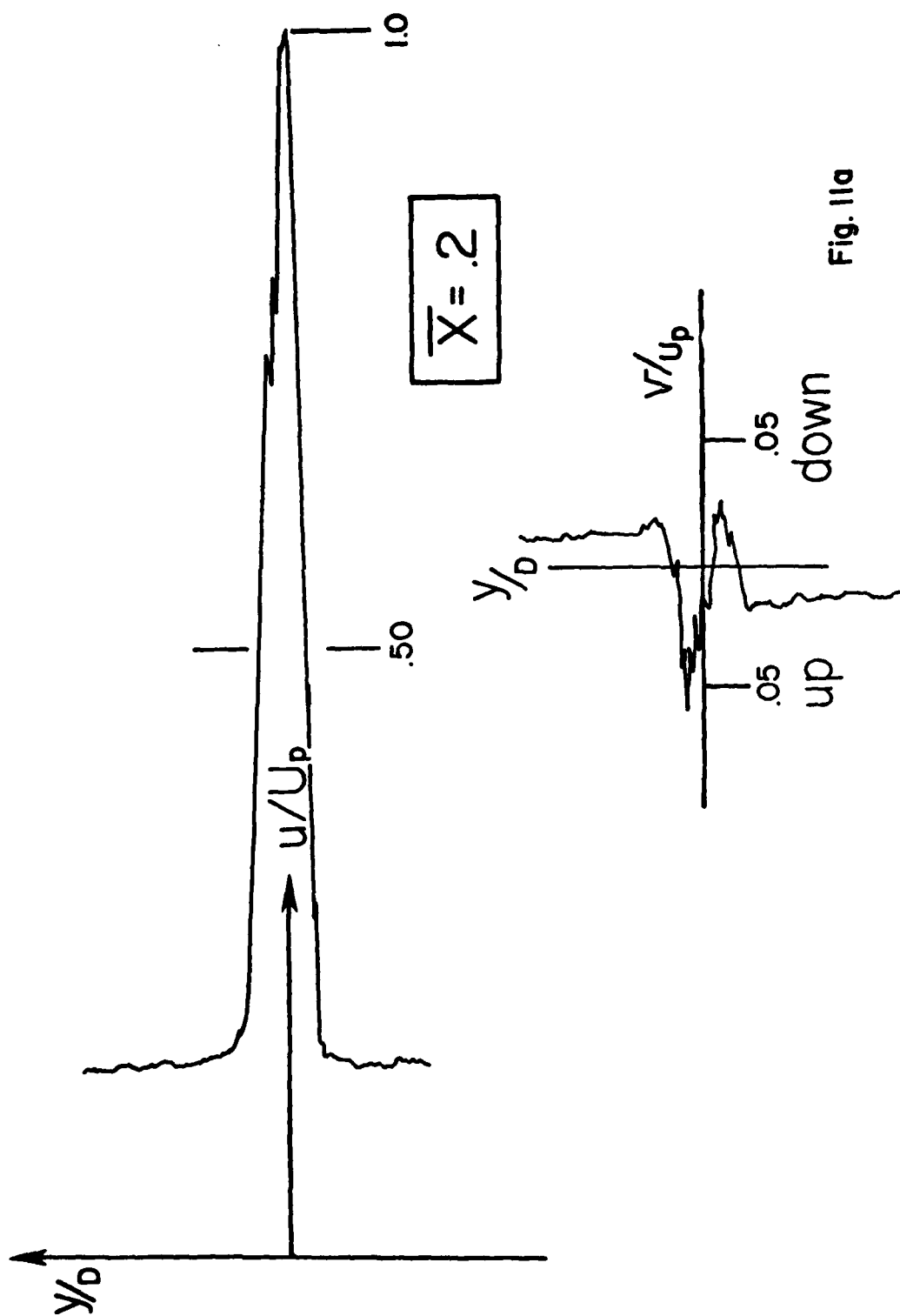


Fig. 11a

Figure 11a. Instantaneous velocity profiles in the oscillating jet at a frequency  $f=12$  Hz and a phase angle  $\theta=90^\circ$ .

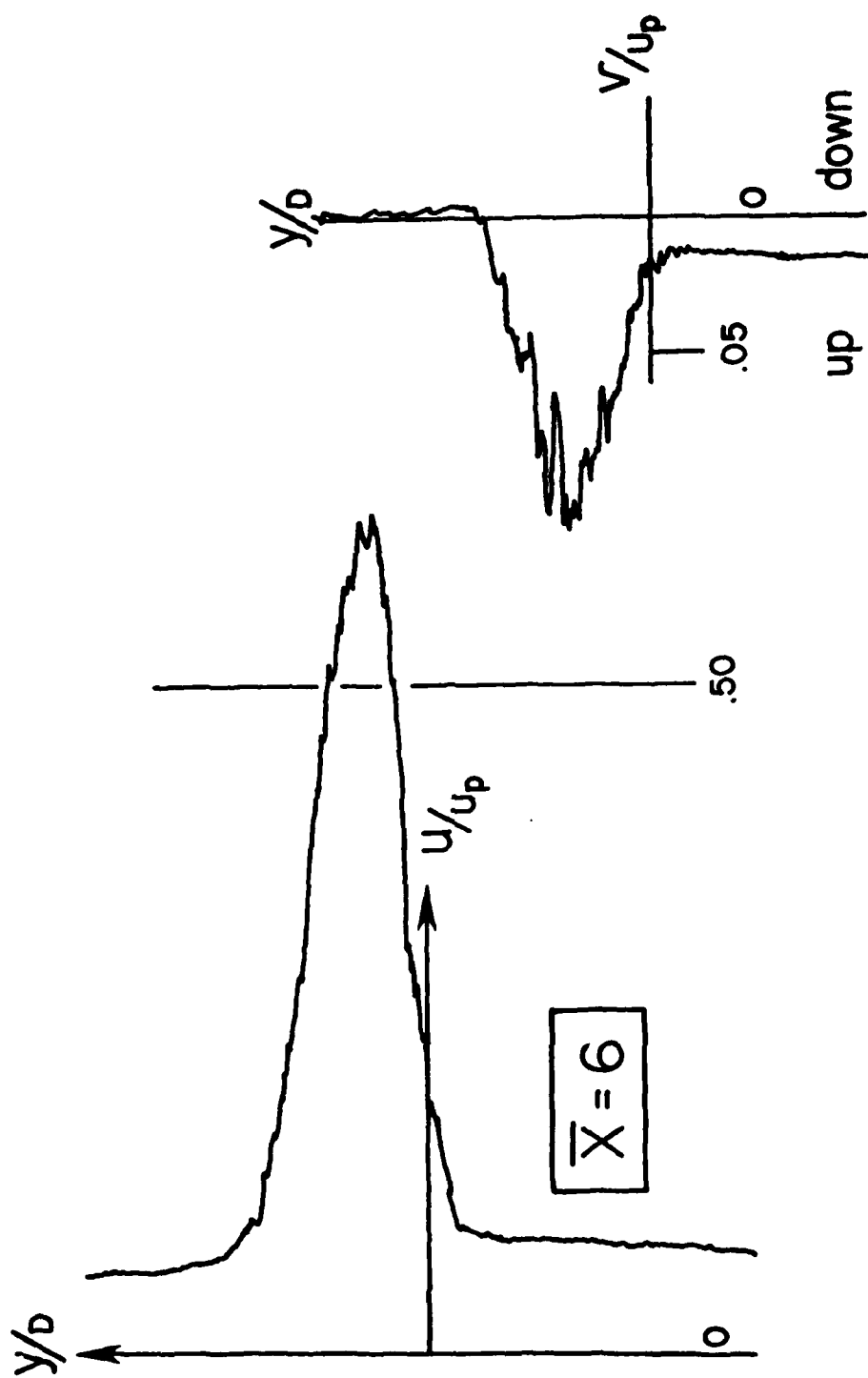


Fig. 11b

Figure 11b. Continued

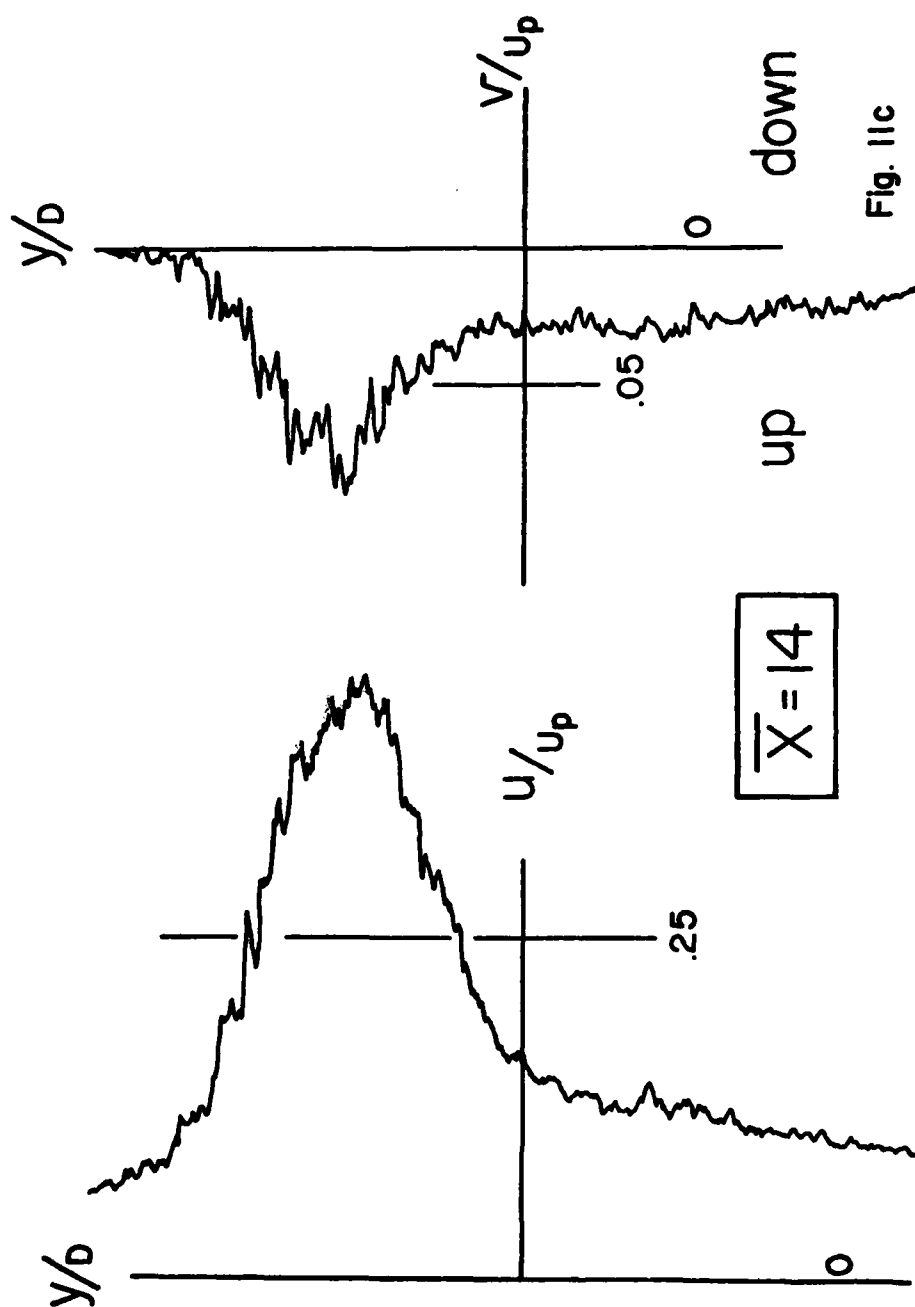


Fig. 11c

Figure 11c. Continued

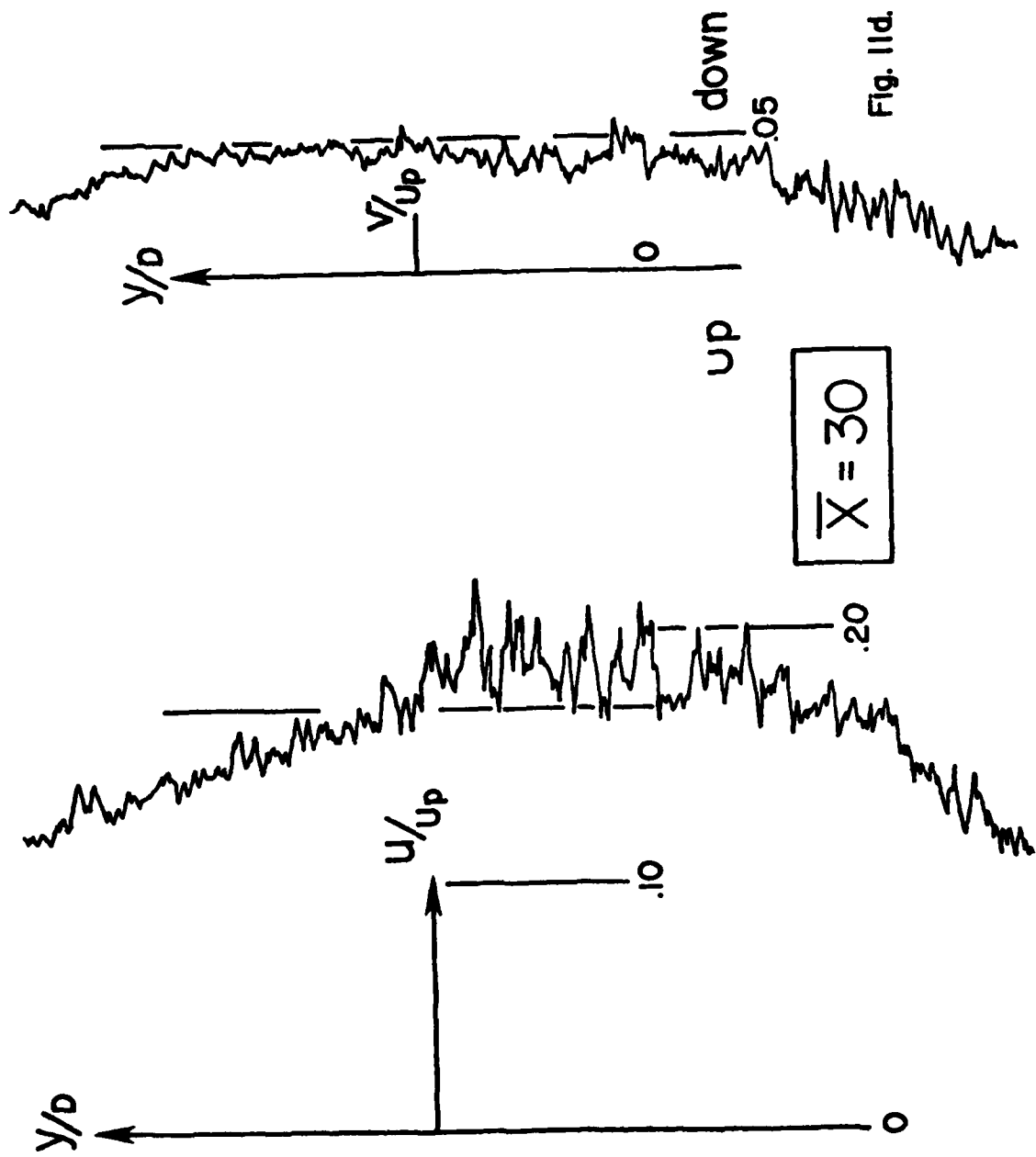


Figure 11d. Continued

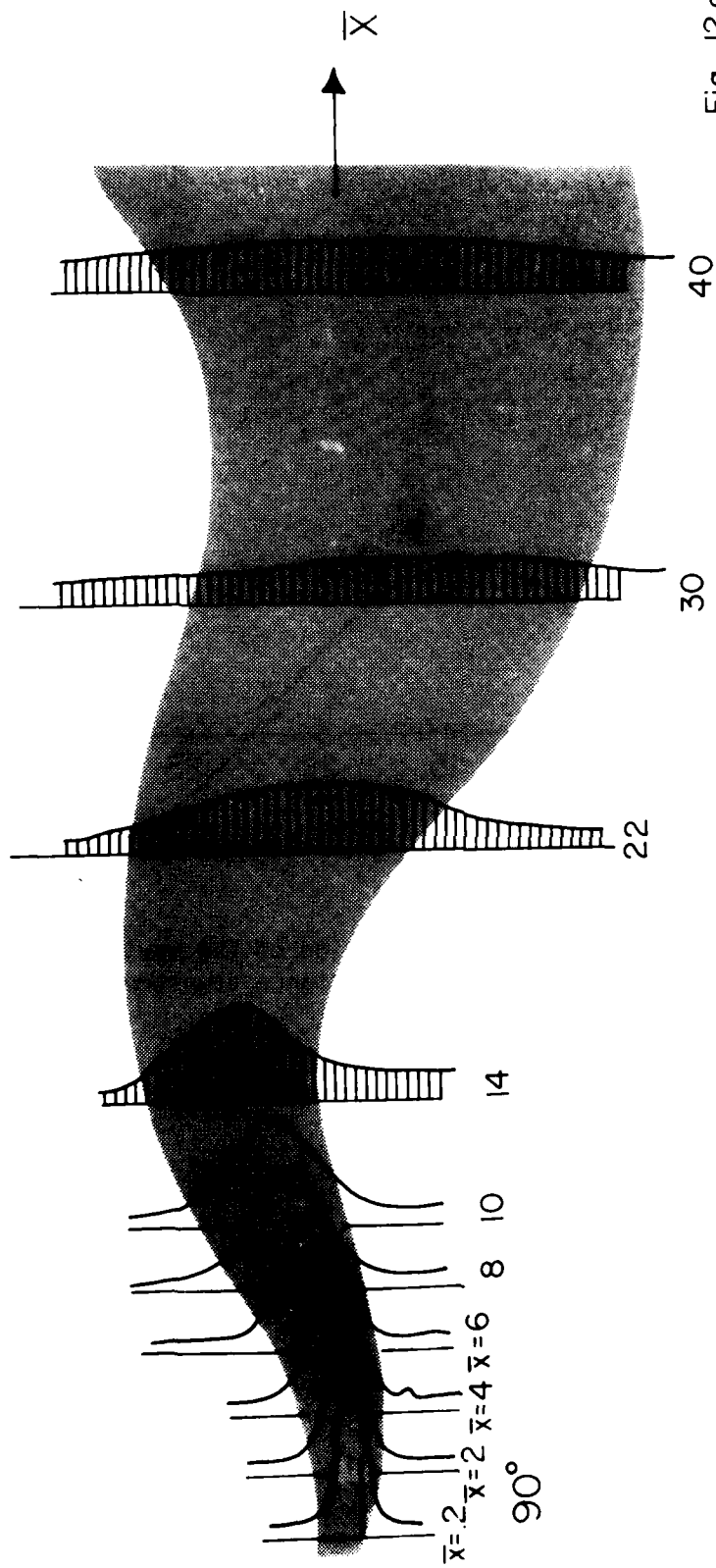


Fig. 12a

Figure 12a. Composite of the instantaneous streamwise velocity profiles for  $f=12$  Hz,  $\theta=90^\circ$ .

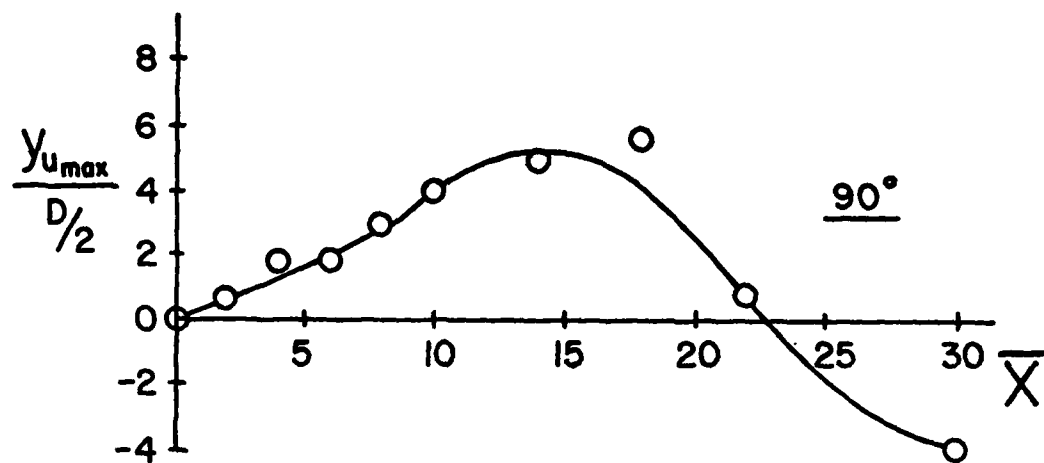


Fig. 12 b

Figure 12b. Transverse location of the maximum streamwise velocity with distance downstream,  $\theta=90^\circ$ .

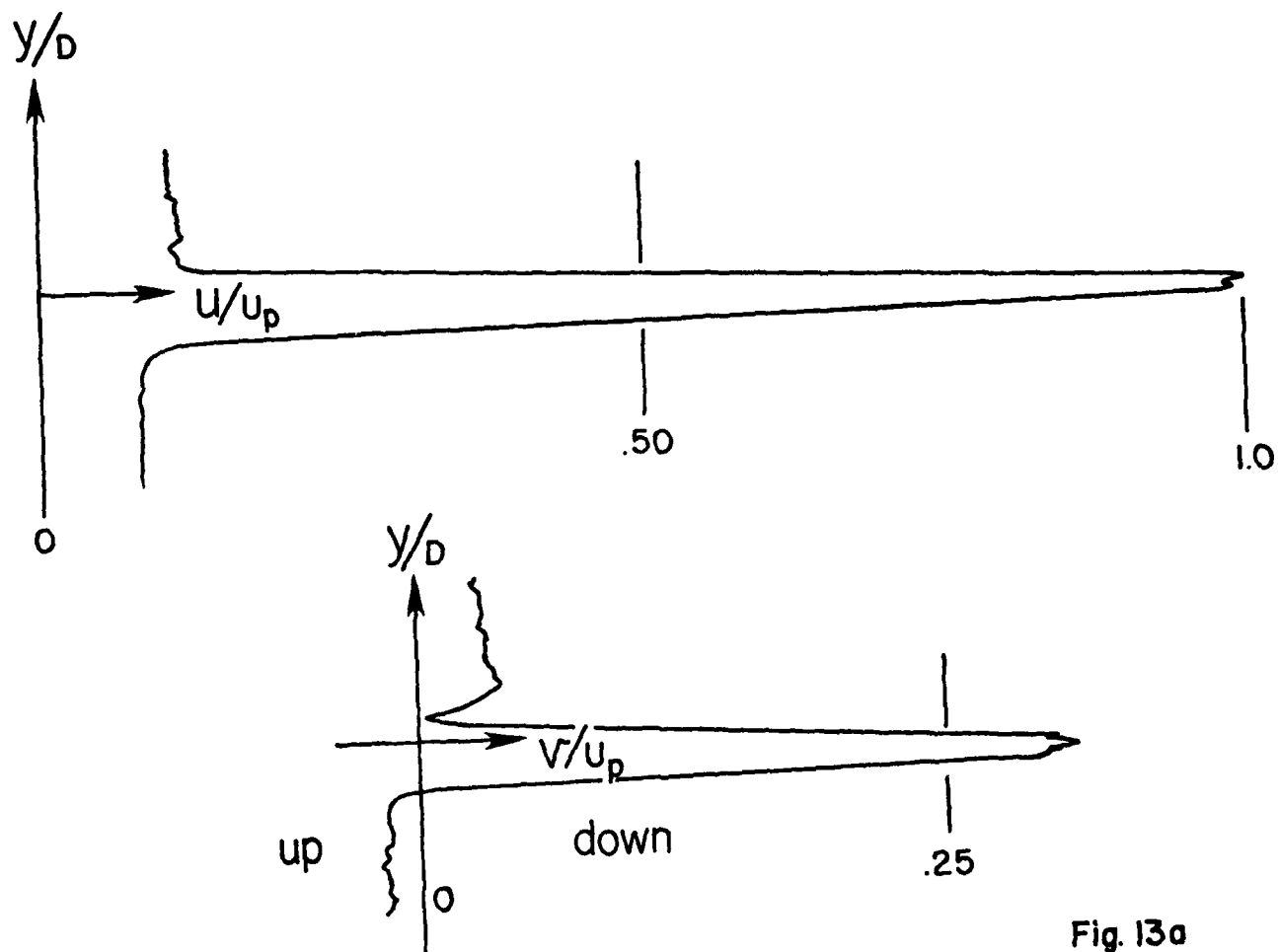


Fig. 13a

Figure 13a. Instantaneous velocity profiles in the oscillating jet at a frequency  $f=12$  Hz and a phase angle  $\theta=180^\circ$ .

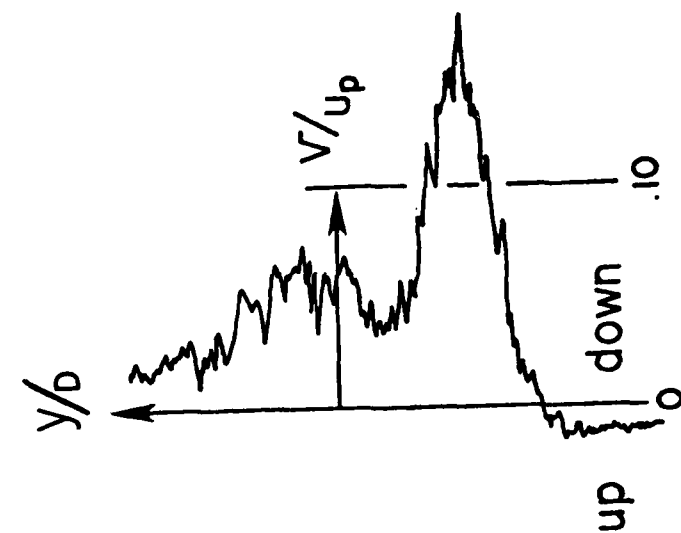


Fig. 13b

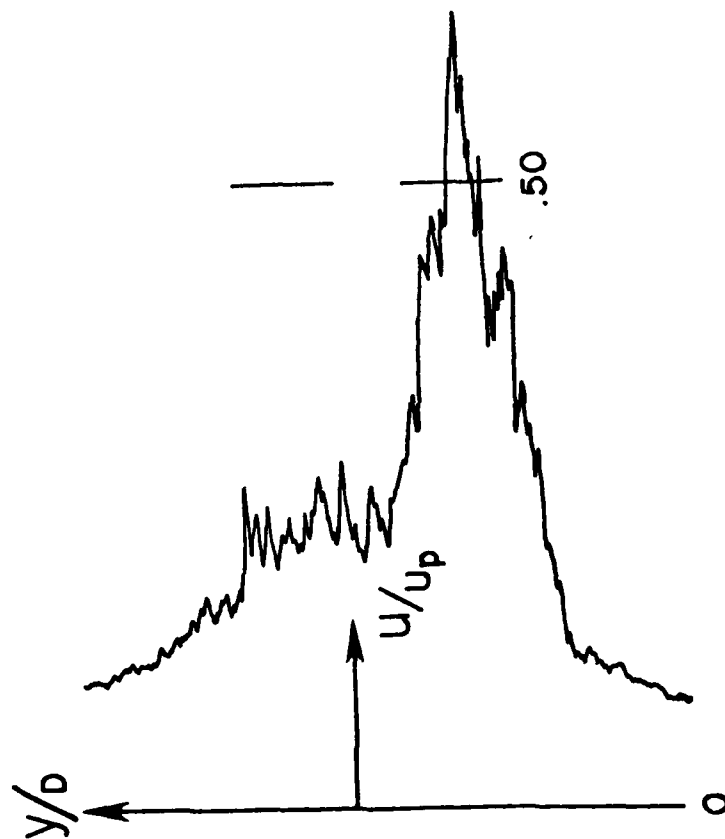


Figure 13b. Continued

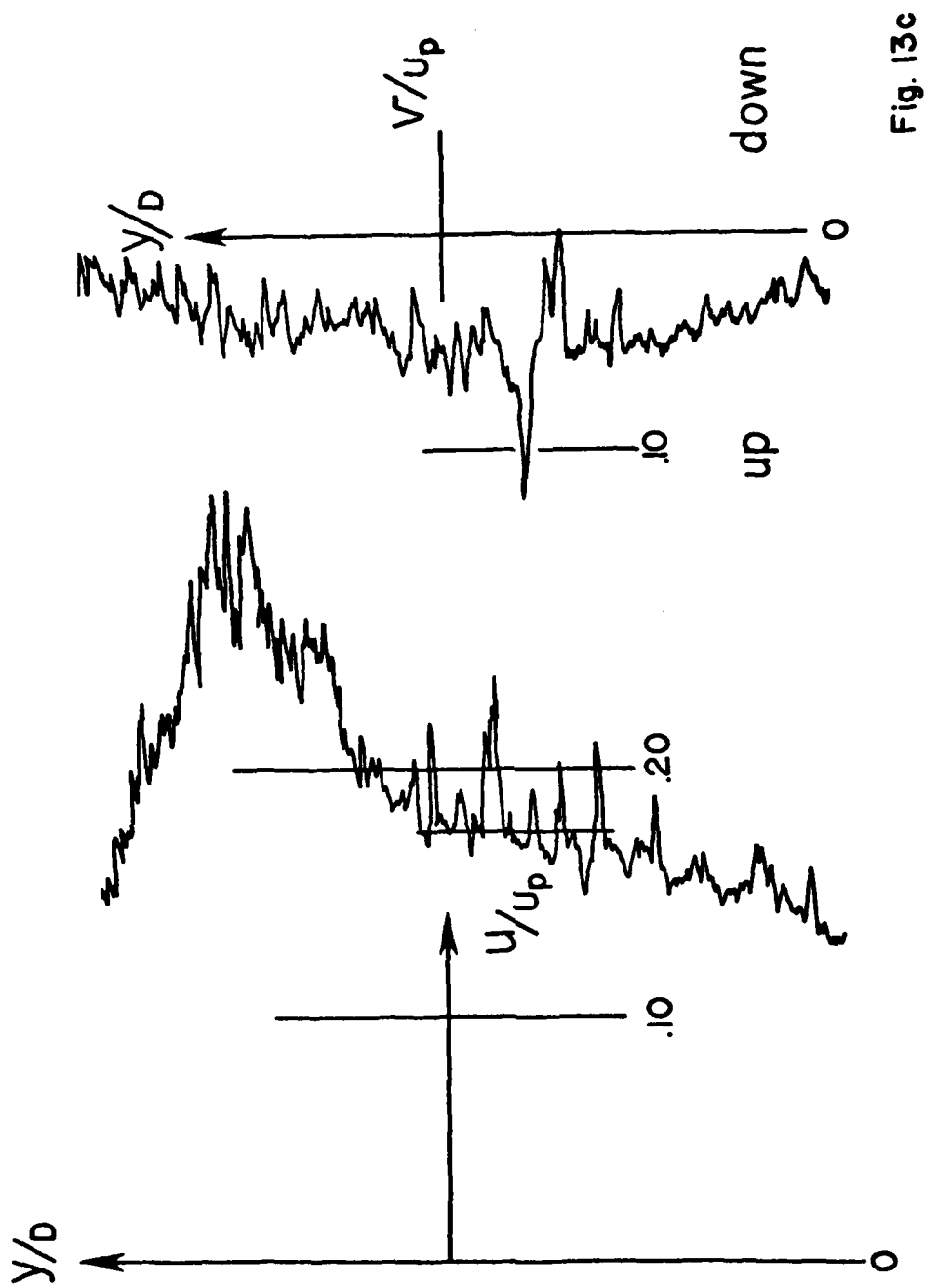


Fig. 13c

Figure 13c. Continued

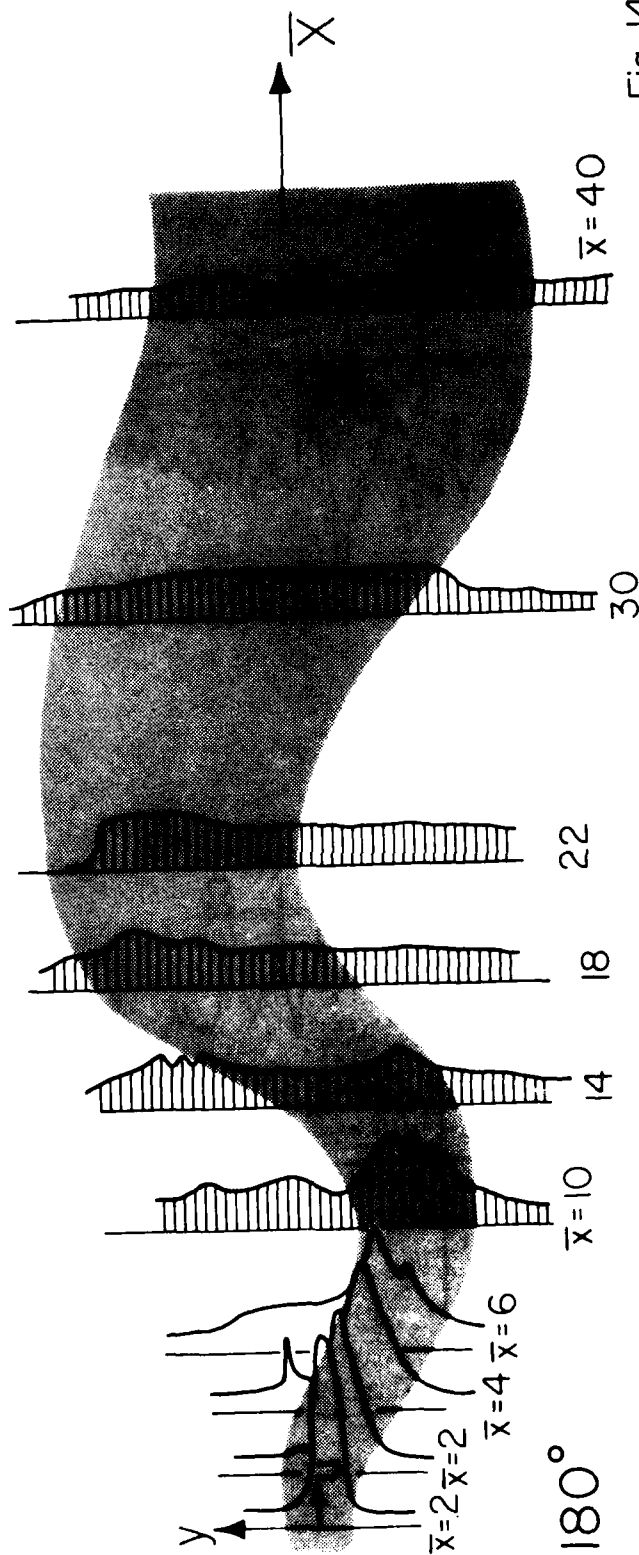


Fig. 14a

Figure 14a. Composite of the instantaneous velocity profiles for  $f=12$  Hz,  $\theta=180^\circ$ .

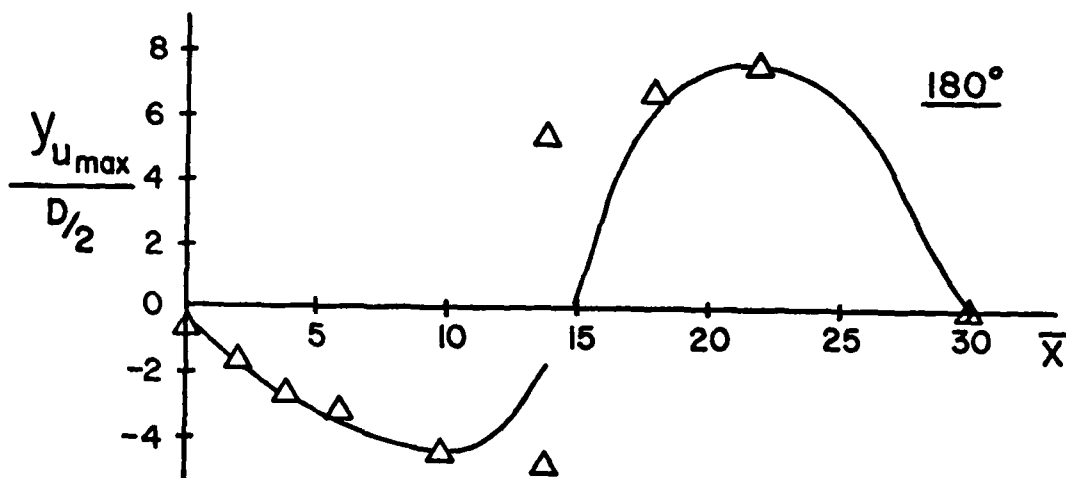


Fig. 14b.

Figure 14b. Transverse location of the maximum streamwise velocity with distance downstream,  $\theta=180^\circ$ .

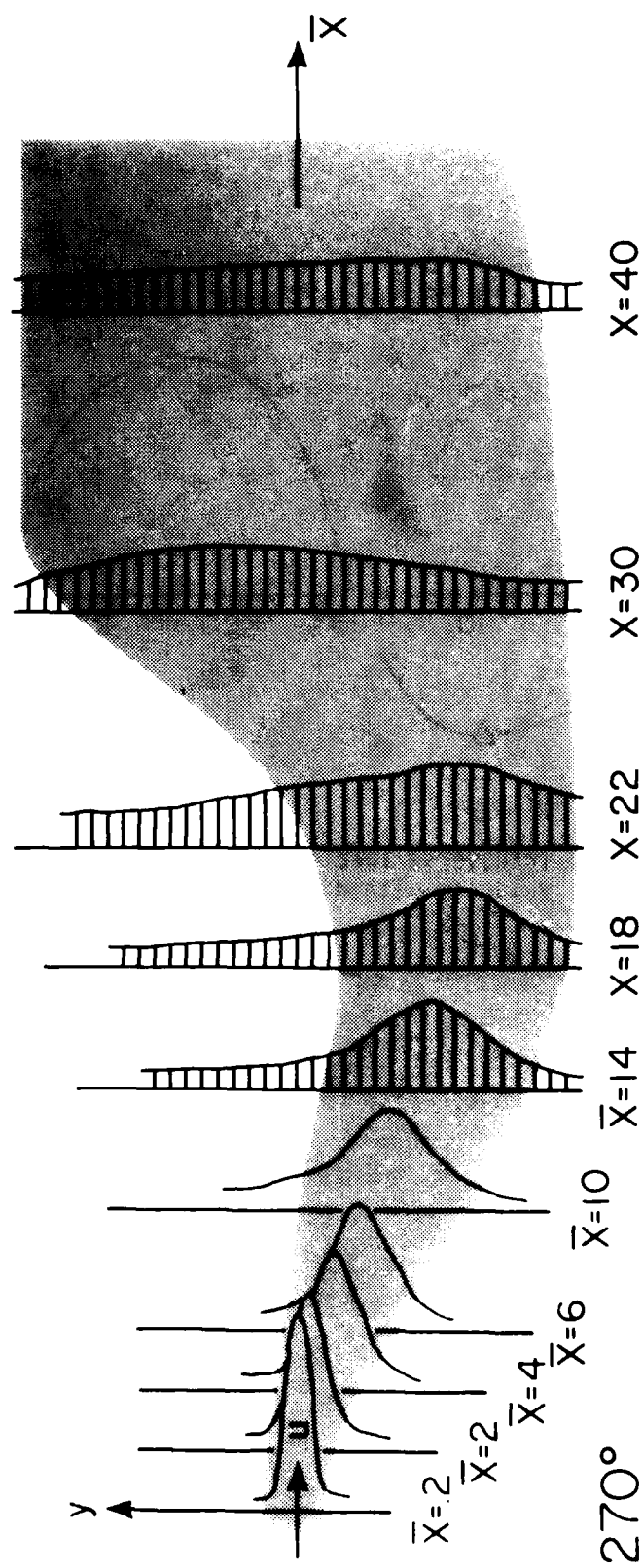


Figure 15a. Composite of the instantaneous velocity profiles for  $f=12$  Hz,  $\theta=270^\circ$ .

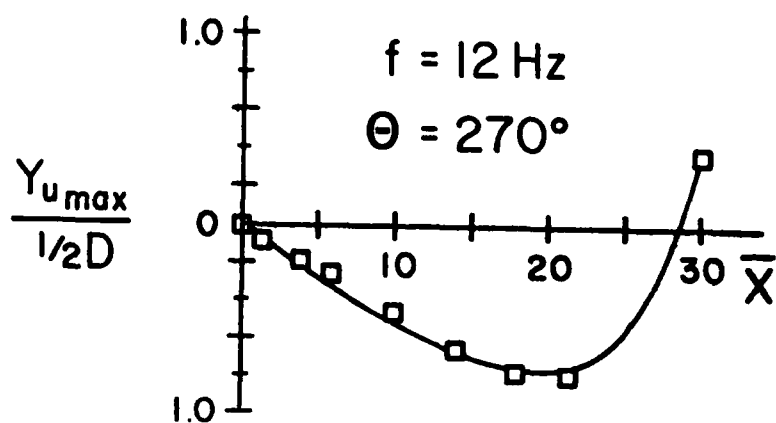


Figure 15b. Transverse location of the maximum streamwise velocity with distance downstream,  $\theta=270^\circ$ .

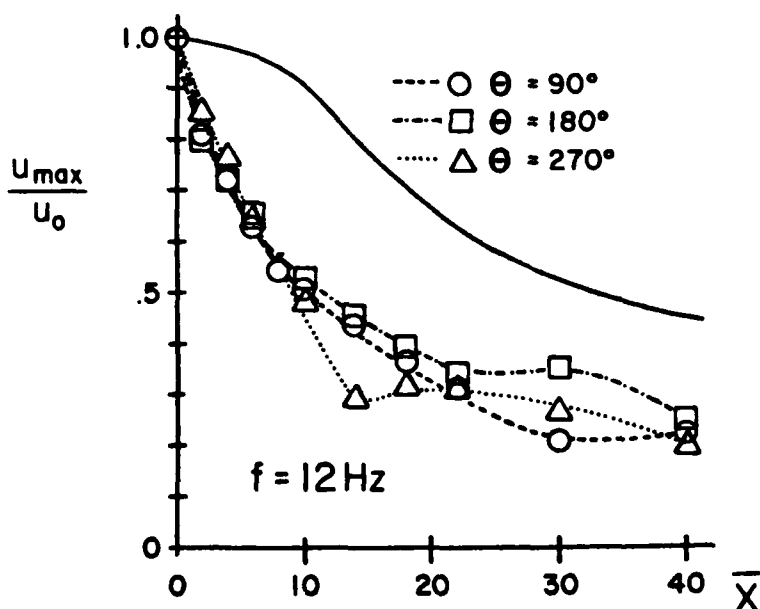


Figure 16a. Instantaneous velocity decay for various phase angles and a frequency  $f=12 \text{ Hz}$ .

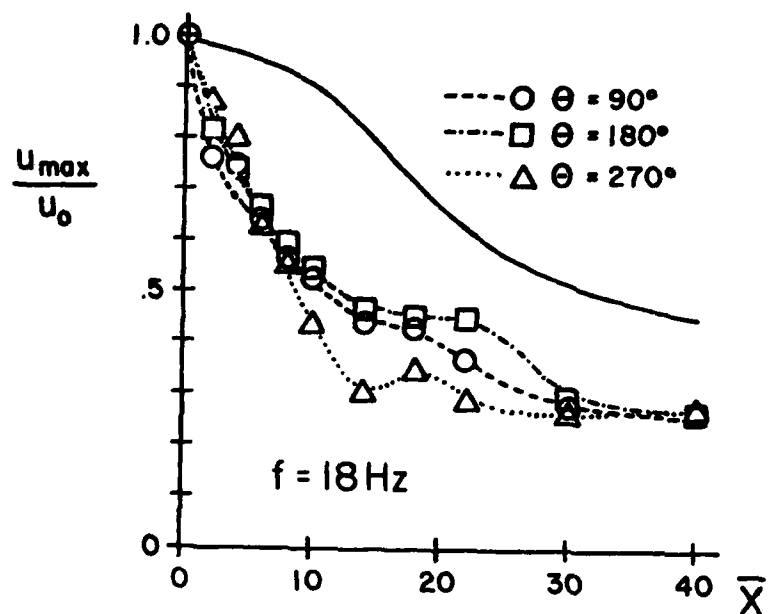


Figure 16b. Instantaneous velocity decay for various phase angles and a frequency  $f=18 \text{ Hz}$ .

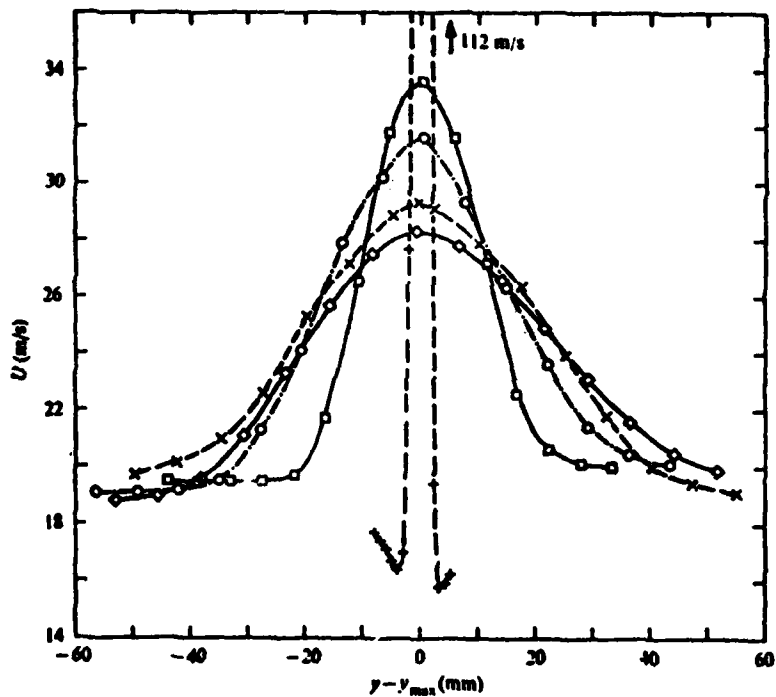


Figure 17. Typical velocity profiles from Simmons, Platzer and Smith, Reference 5.



Figure 18. Smoke flow visualization of the oscillating jet in a coflowing stream of 28% of the jet velocity.

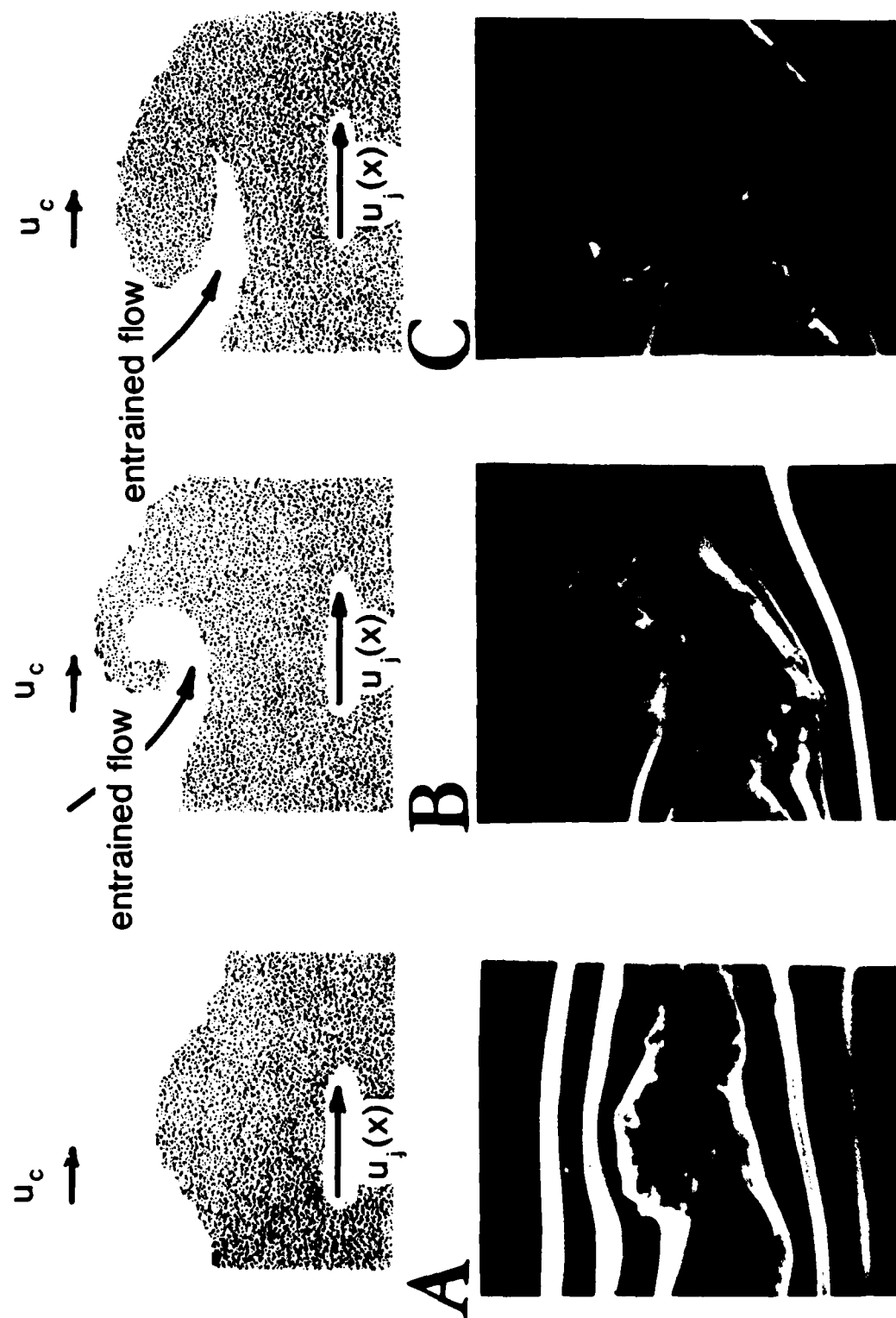


Figure 19. Evolution of the jet surface waves.

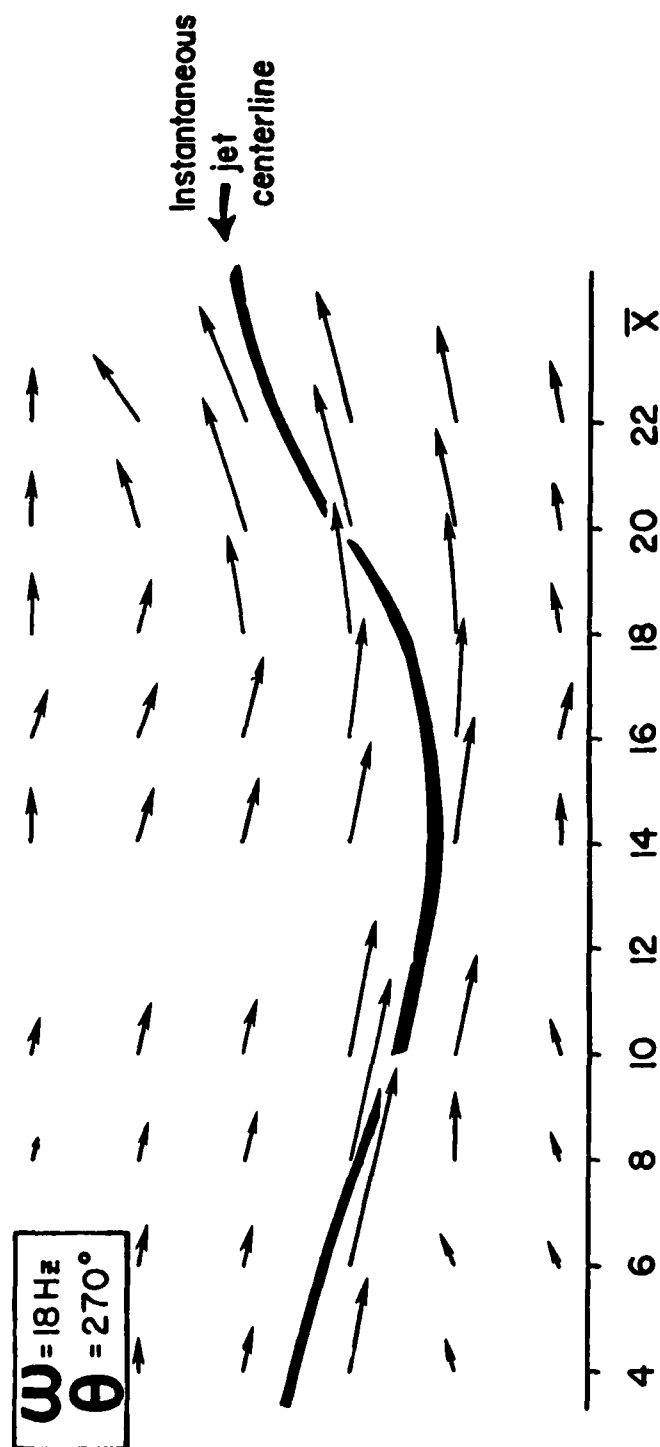


Figure 20a. Jet velocity field at a frequency  $\omega = 18 \text{ Hz}$  and phase angle  $\theta = 270^\circ$ .

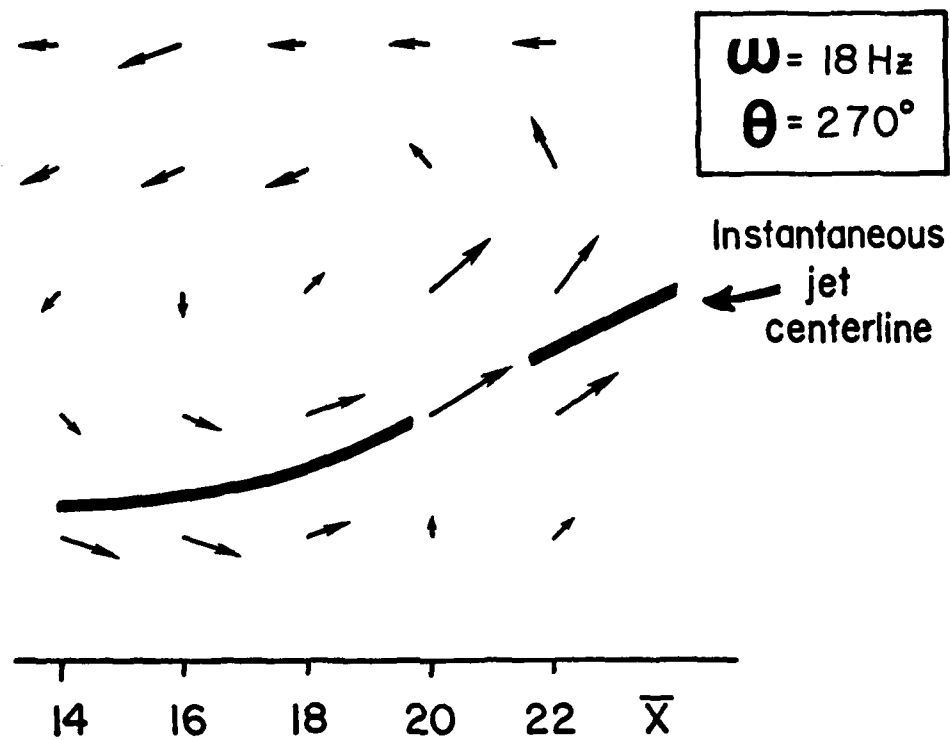


Figure 20b. Coherent structure of the jet seen in a moving coordinate system.

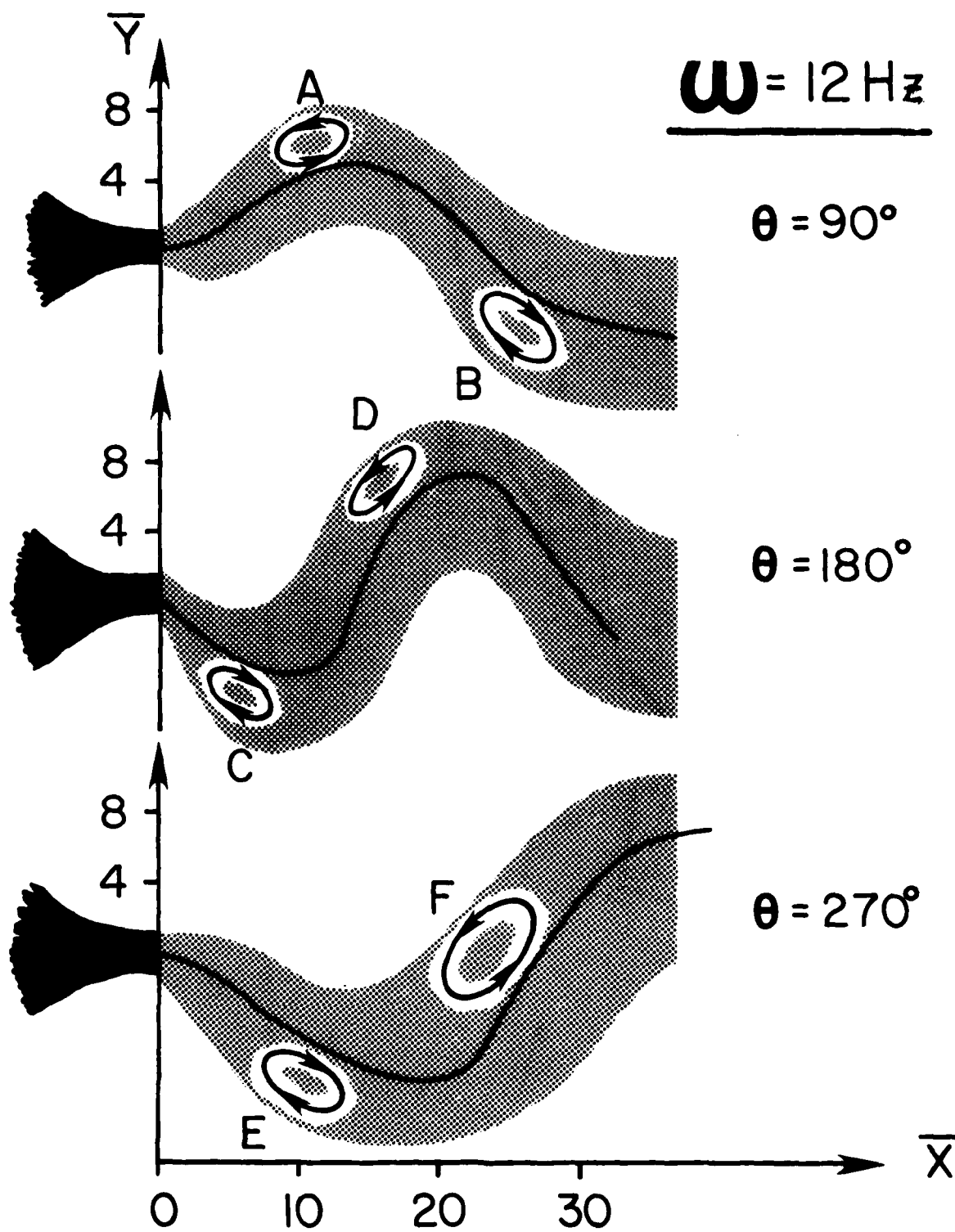


Figure 21. Anticipated vortex locations based on flow visualization results.

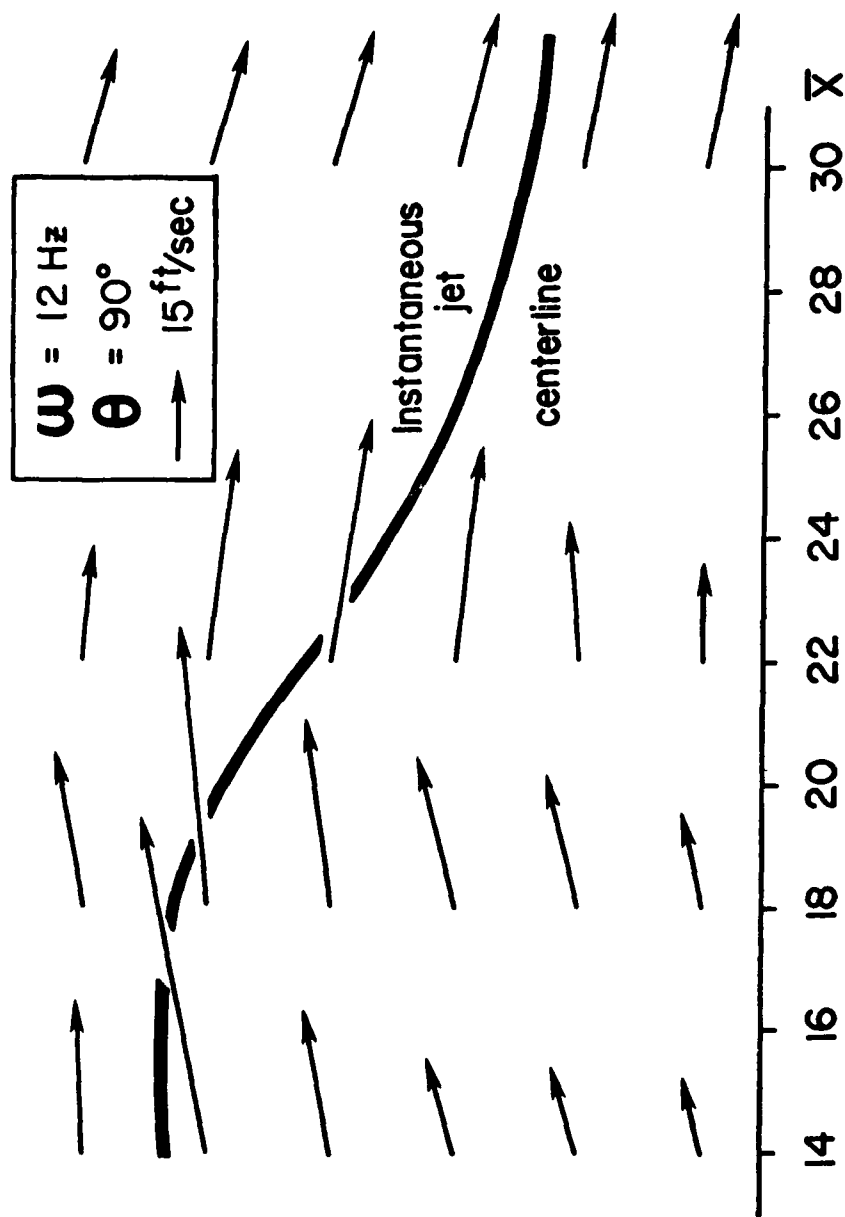


Figure 22a. Jet velocity field at a frequency of  $\omega=12 \text{ Hz}$  and phase angle  $\theta=90^\circ$ .

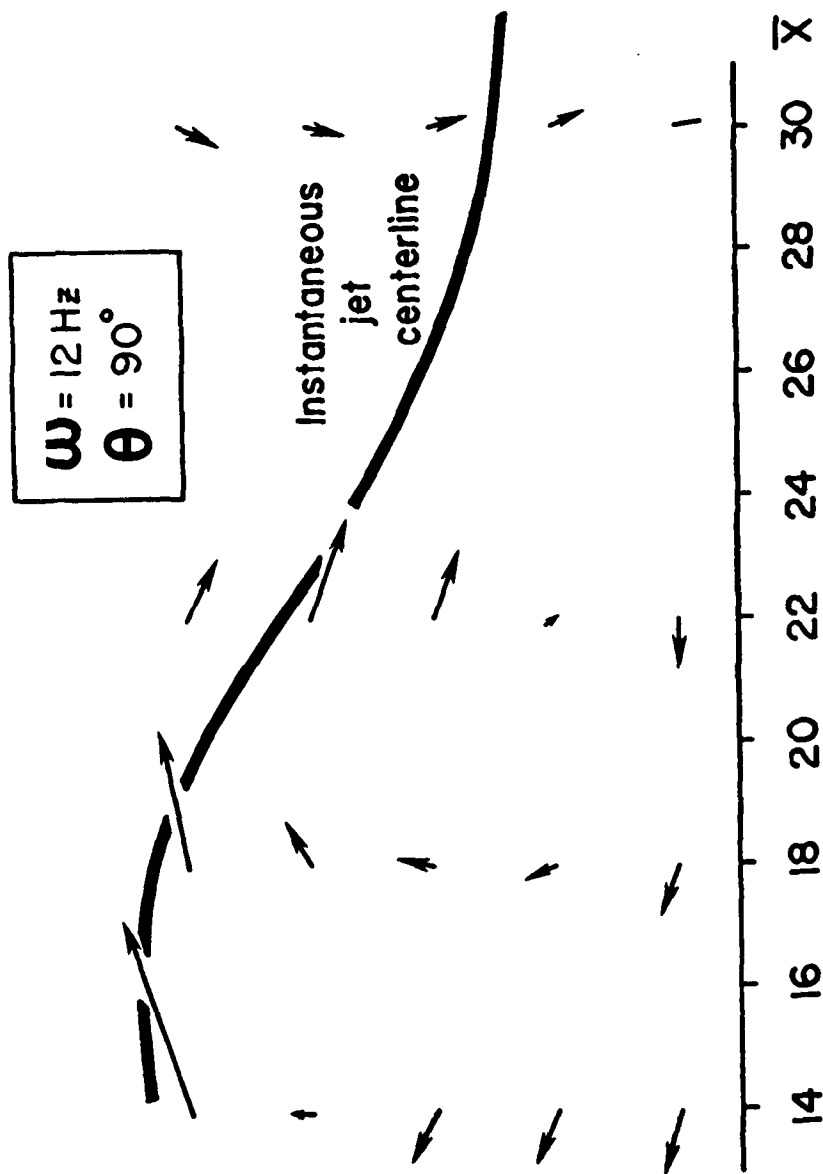


Figure 22b. Coherent structure of Vortex B in a moving coordinate system.

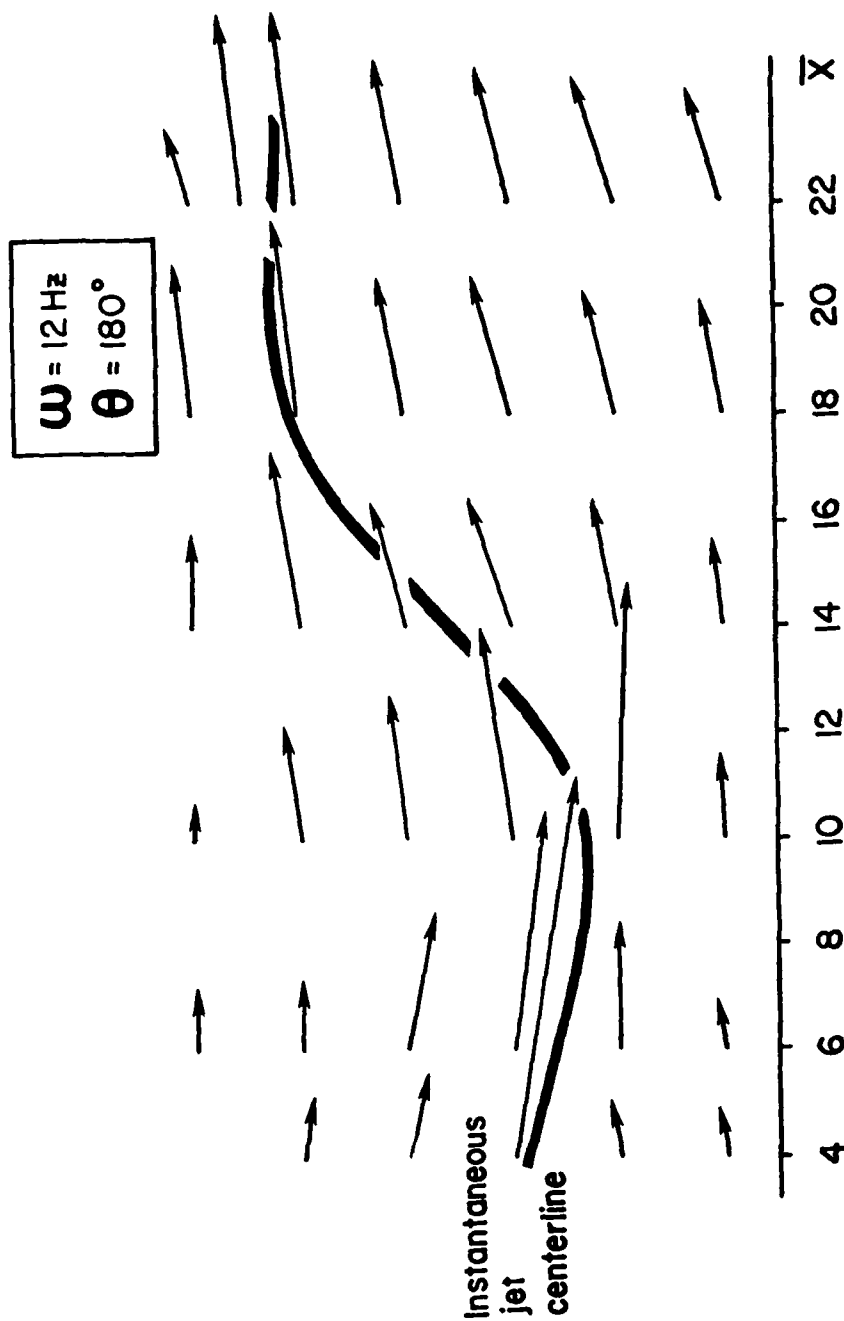


Figure 23a. Jet velocity field at a frequency of  $\omega=12 \text{ Hz}$  and a phase angle  $\theta=180^\circ$ .

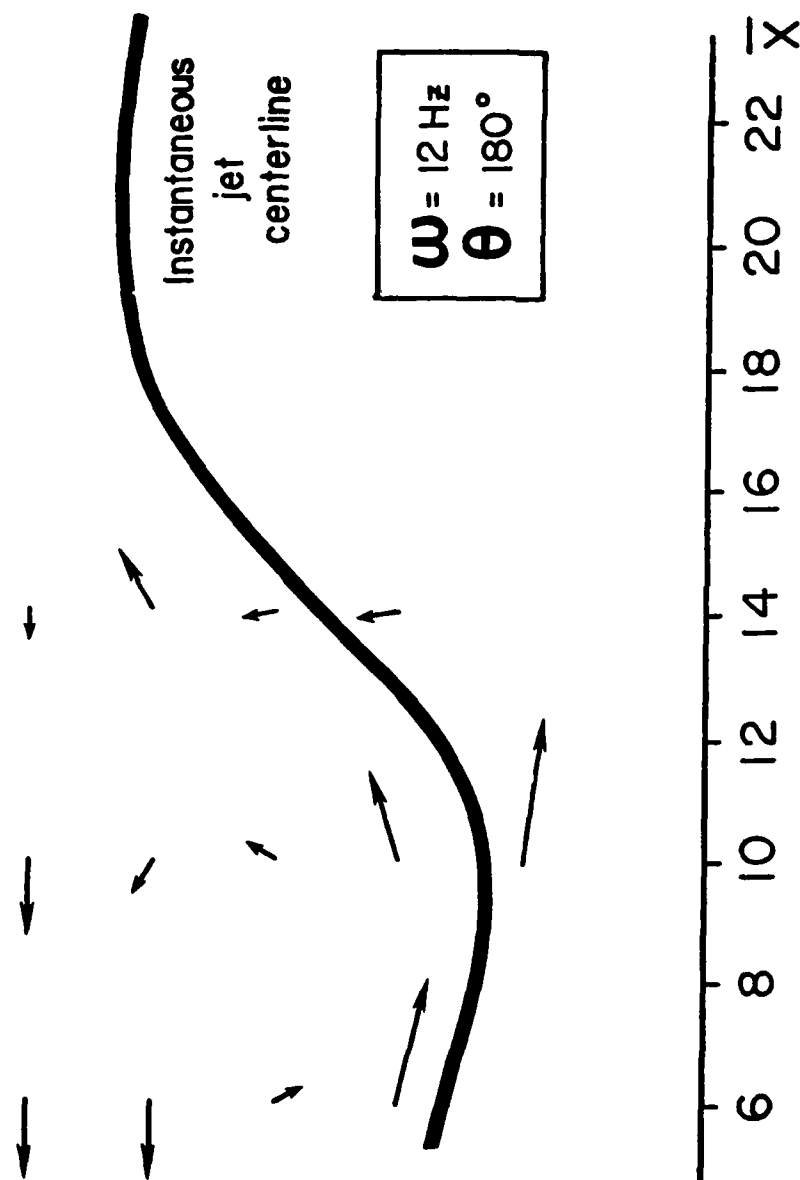


Figure 23b. Coherent structure of Vortex D in a moving coordinate system.

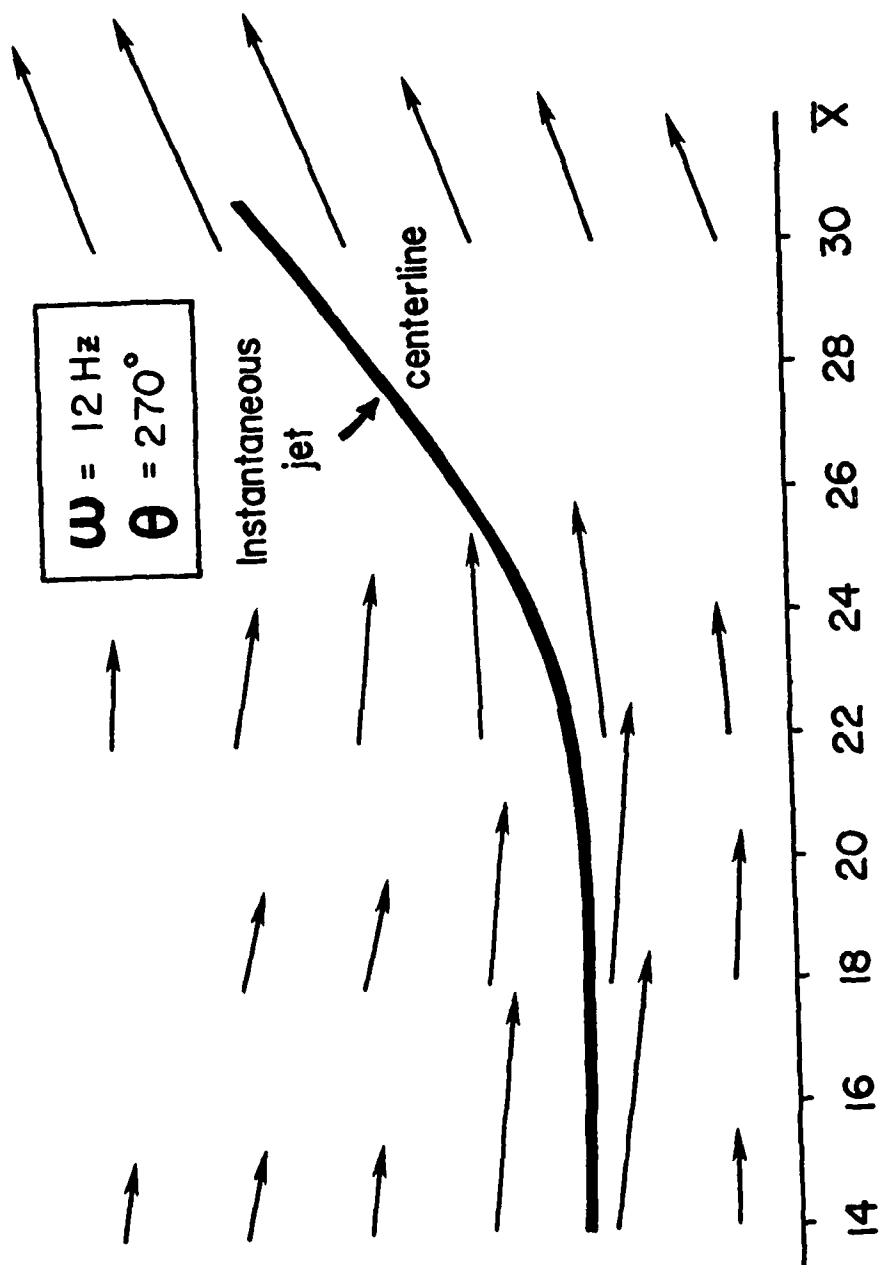


Figure 24a. Jet velocity field at a frequency of  $\omega=12 \text{ Hz}$  and a phase angle of  $\theta=270^\circ$ .

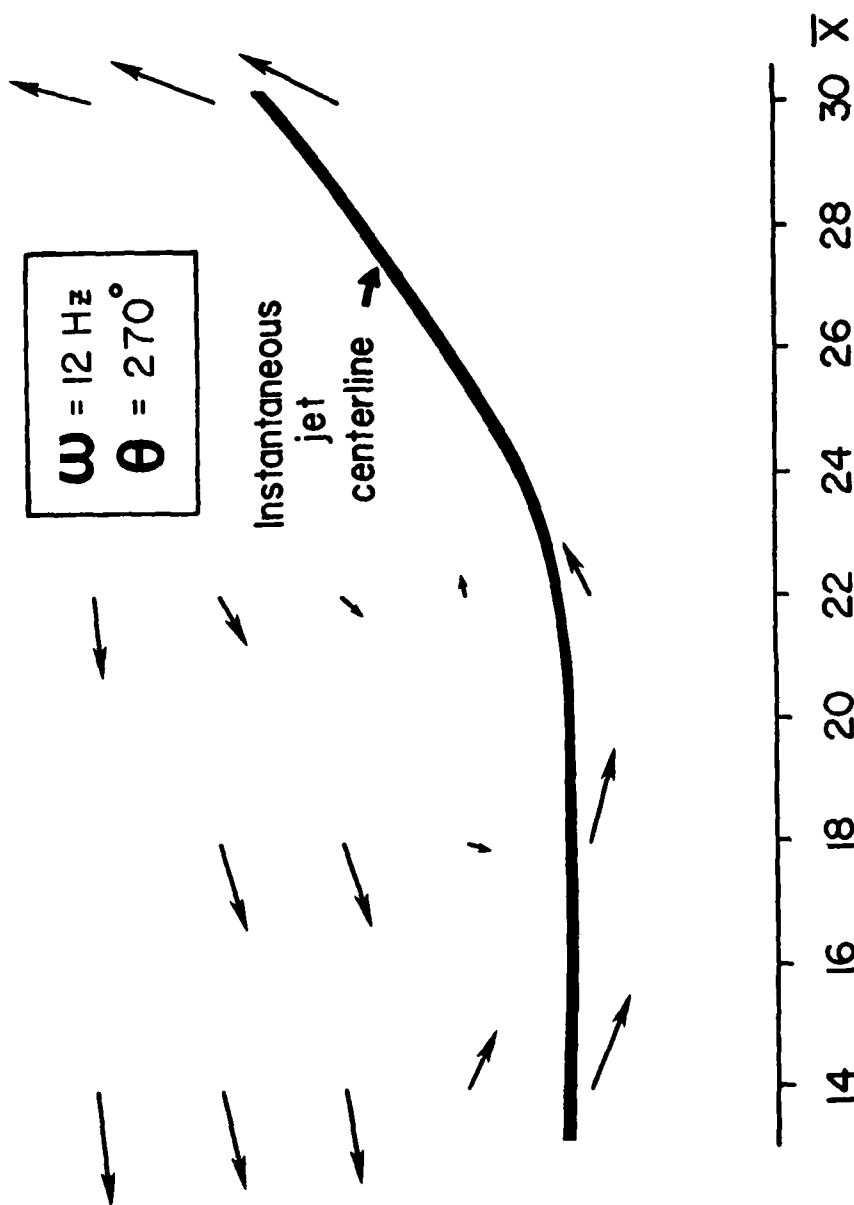


Figure 24b. Coherent structure of Vortex F in a moving coordinate system.

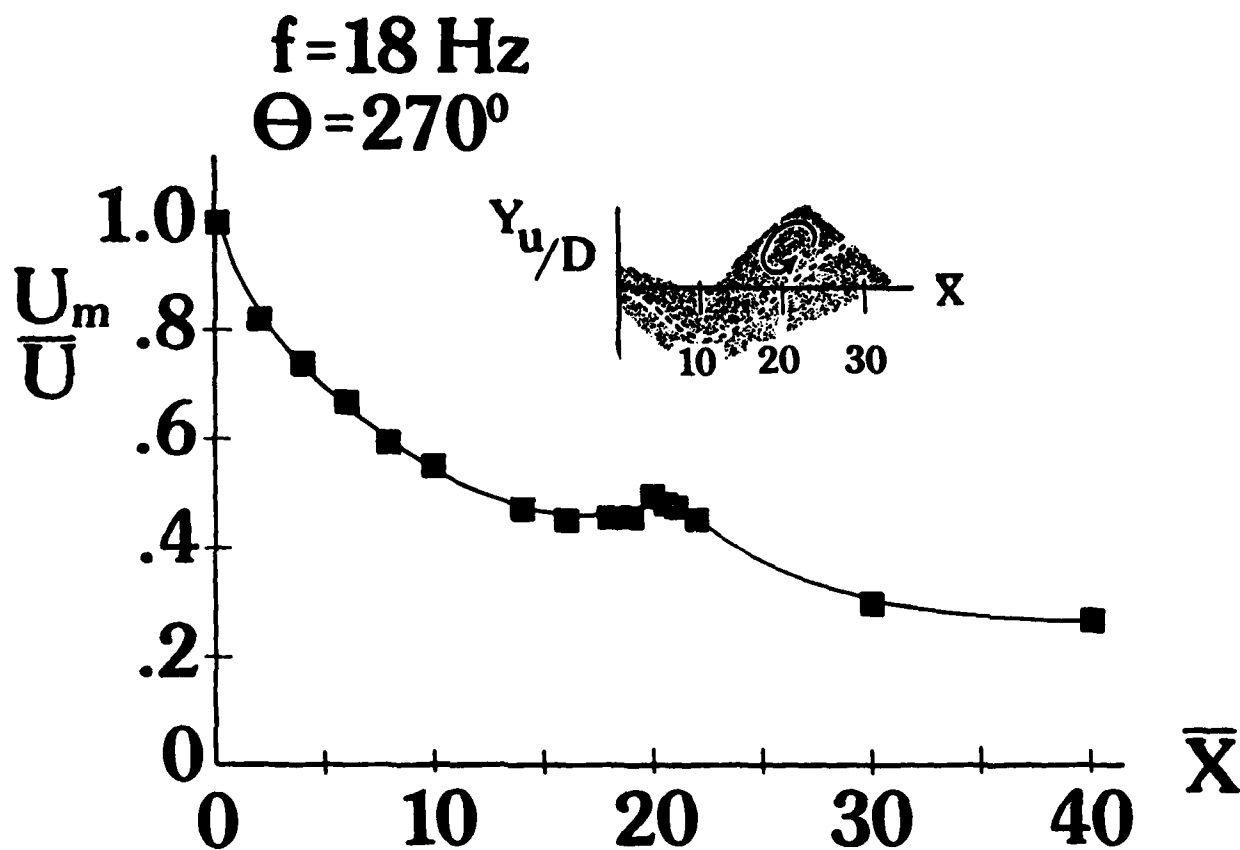


Figure 25. Effect of the vortex structure on the instantaneous jet velocity decay.

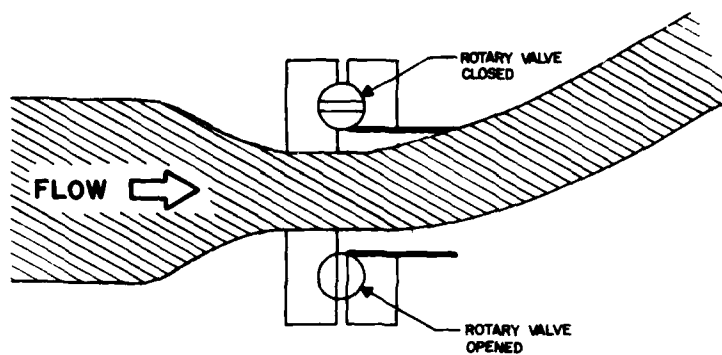


Figure 26. Schematic of mechanically controlled, fluidically activated nozzle.

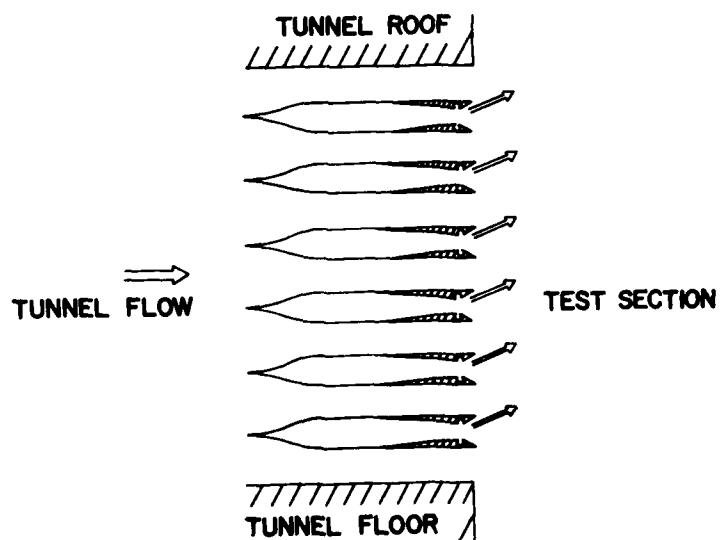


Figure 27. Schematic of jet controlled gust tunnel.

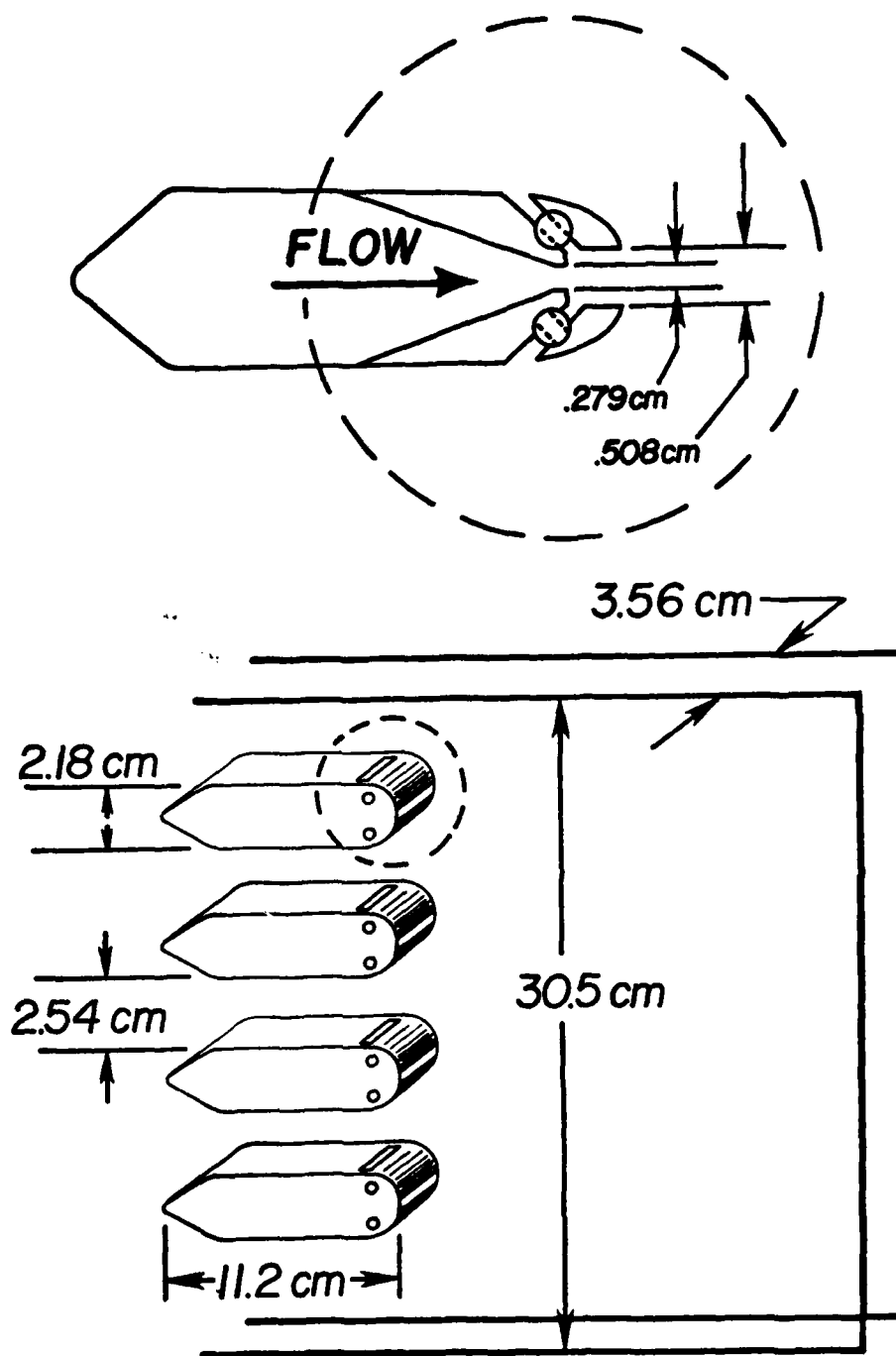
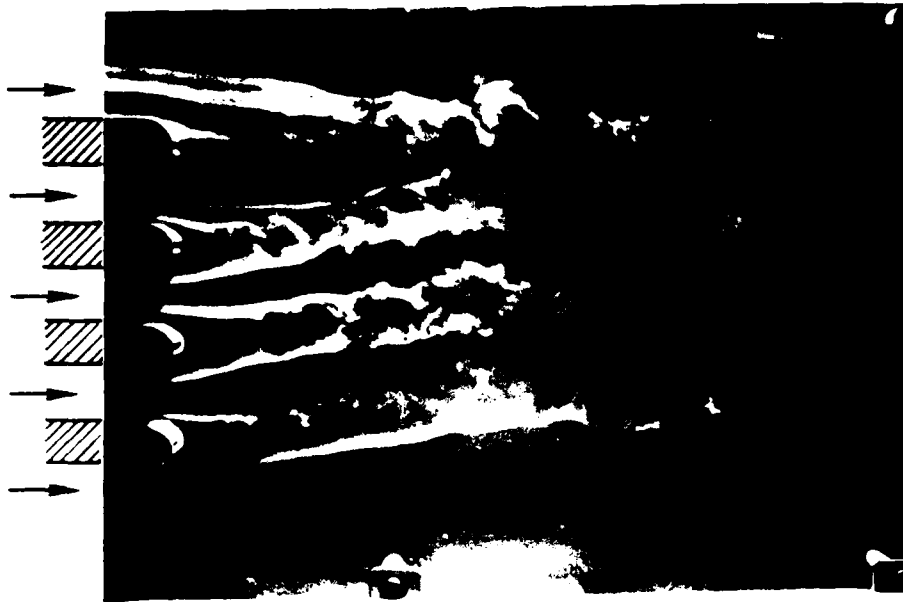


Figure 28. Geometry of the experimental subscale pilot gust tunnel.



*60 Hz, 0° Phase*



*60° Hz, 180° Phase*

Figure 29. Flow visualization of the in-phase configuration in the up and down orientations.

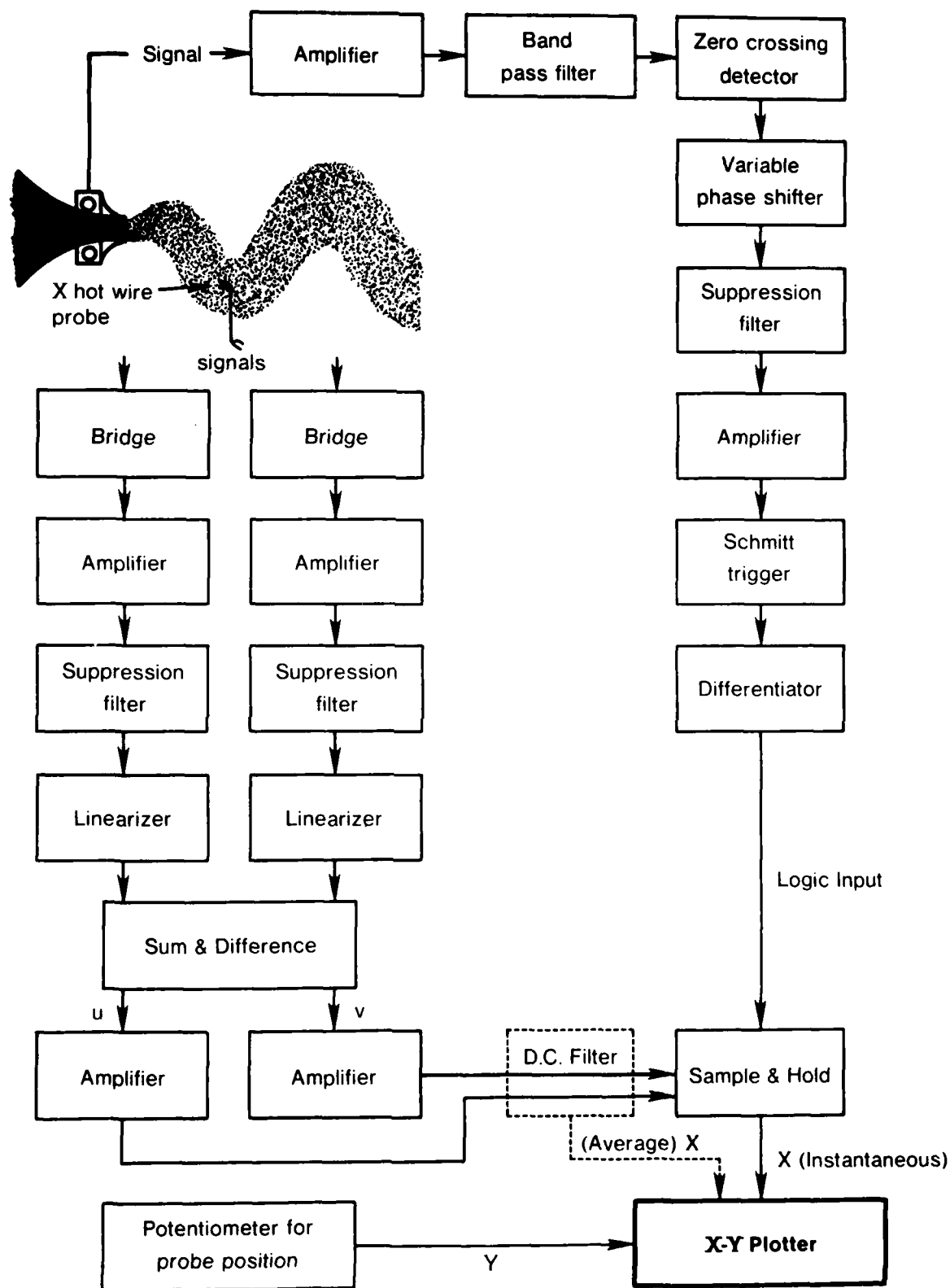


Figure 30. Schematic of conditional sampling electronics.

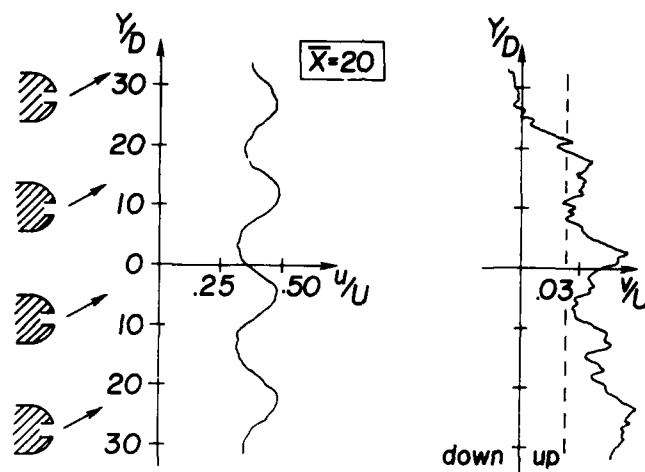


Figure 31. Flowfield at  $\bar{X} = 20$  for the in-phase configuration in the upward orientation.

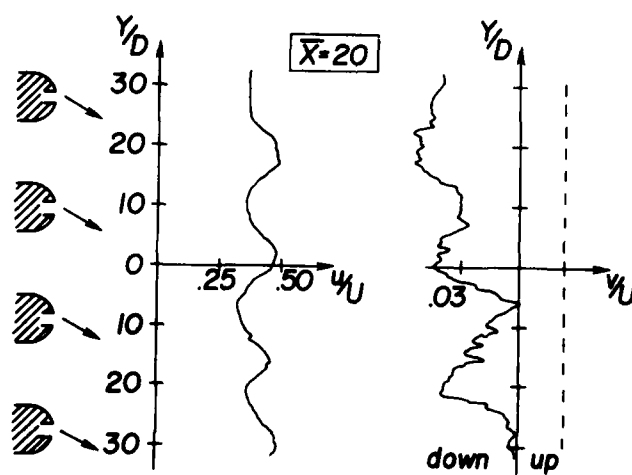


Figure 32. Flowfield at  $\bar{X} = 20$  for the in phase configuration in the downward orientation.

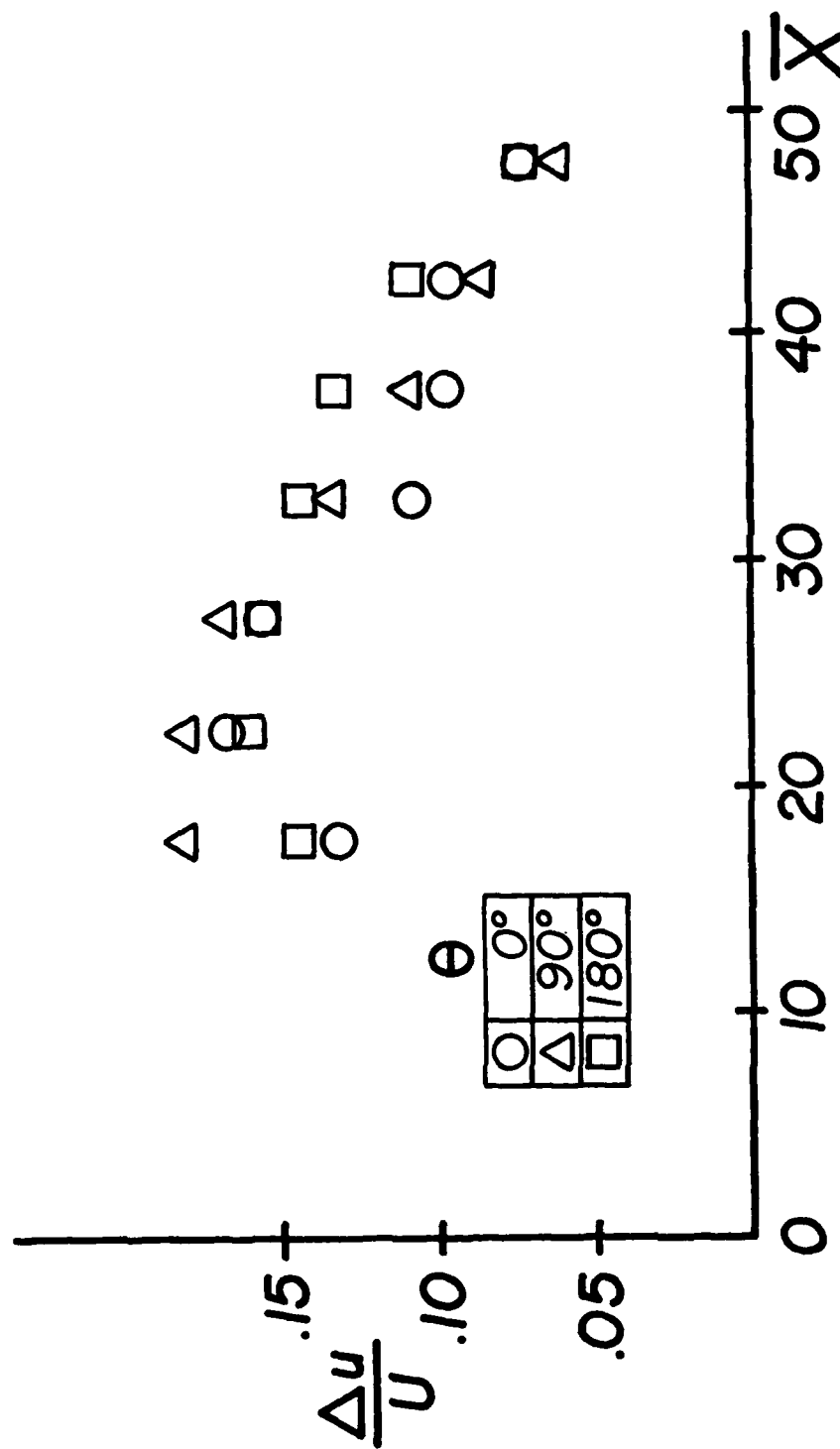


Figure 33. Decay of the velocity non-uniformity in the flowfield.

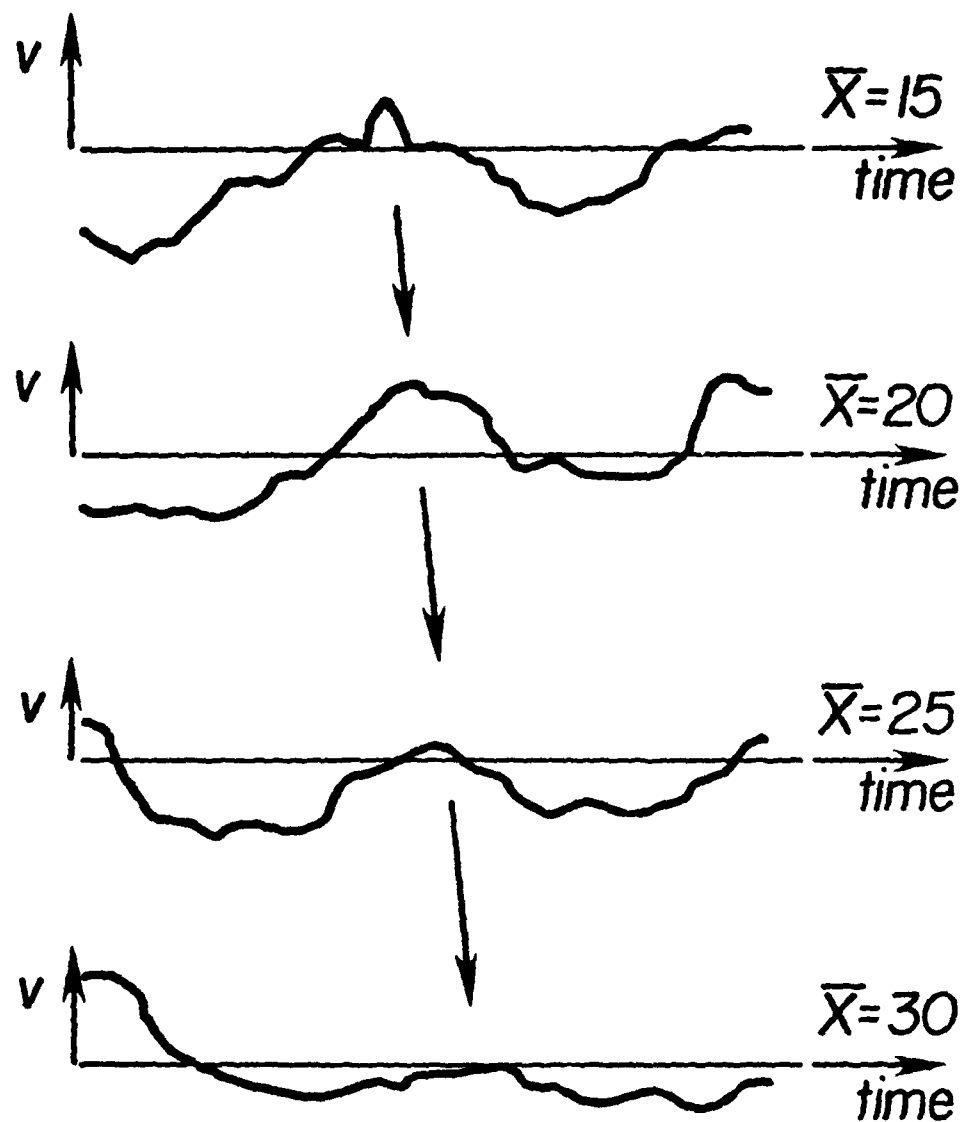


Figure 34. Variation of the centerline transverse velocities with time at several stream-wise positions.

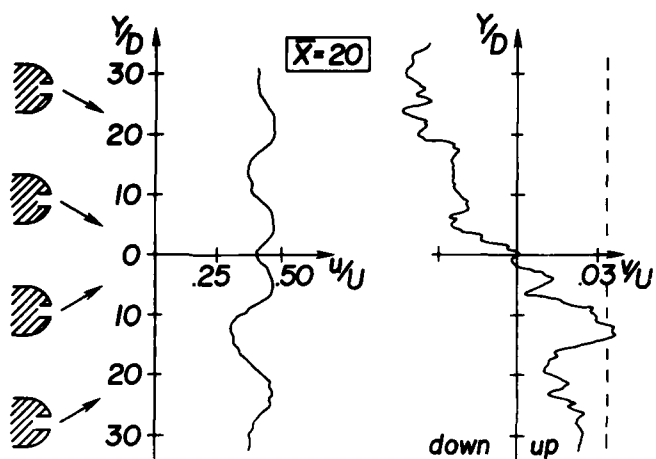


Figure 35. Flowfield at  $\bar{X} = 20$  for the out of phase configuration and an inward orientation.

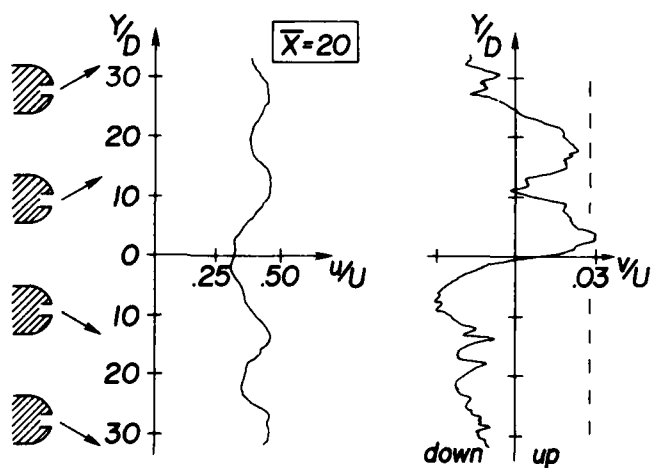


Figure 36. Flowfield at  $\bar{X} = 20$  for the out of phase configuration and an outward orientation.

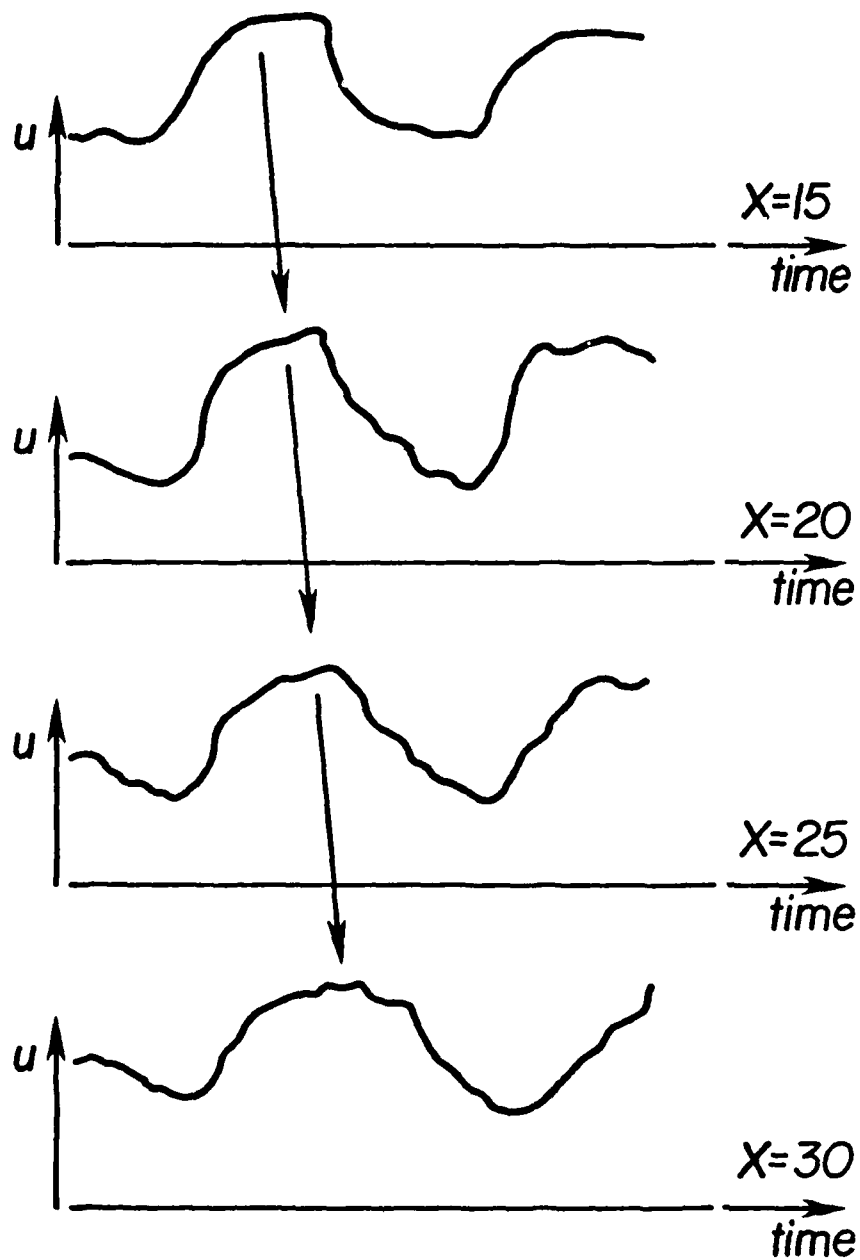


Figure 37. Variation of the centerline streamwise velocities with time at several streamwise positions.

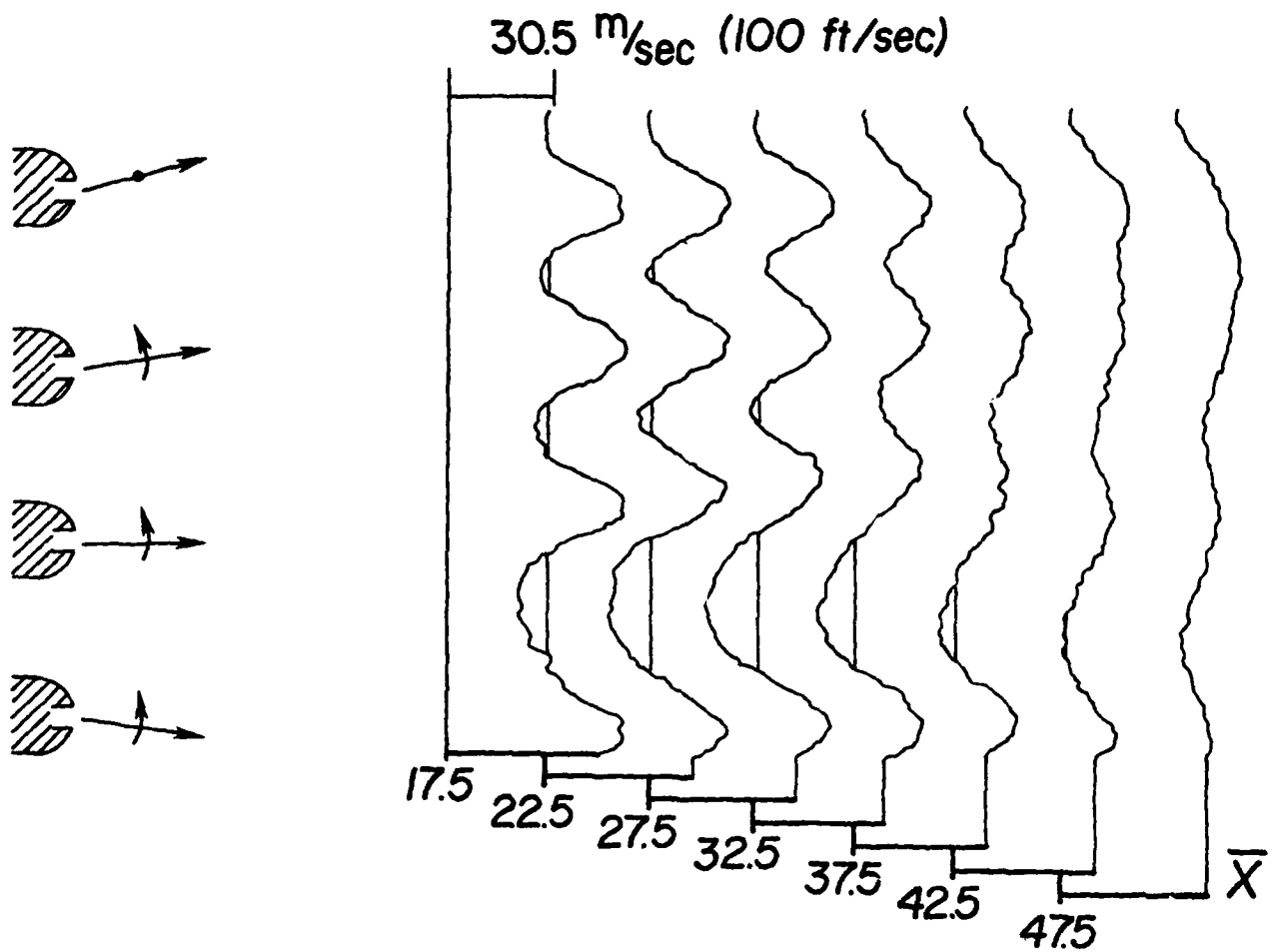


Figure 38. Streamwise velocities at various positions with a  $45^\circ$  phase lag between the nozzles and the upper nozzle in the upward orientation.

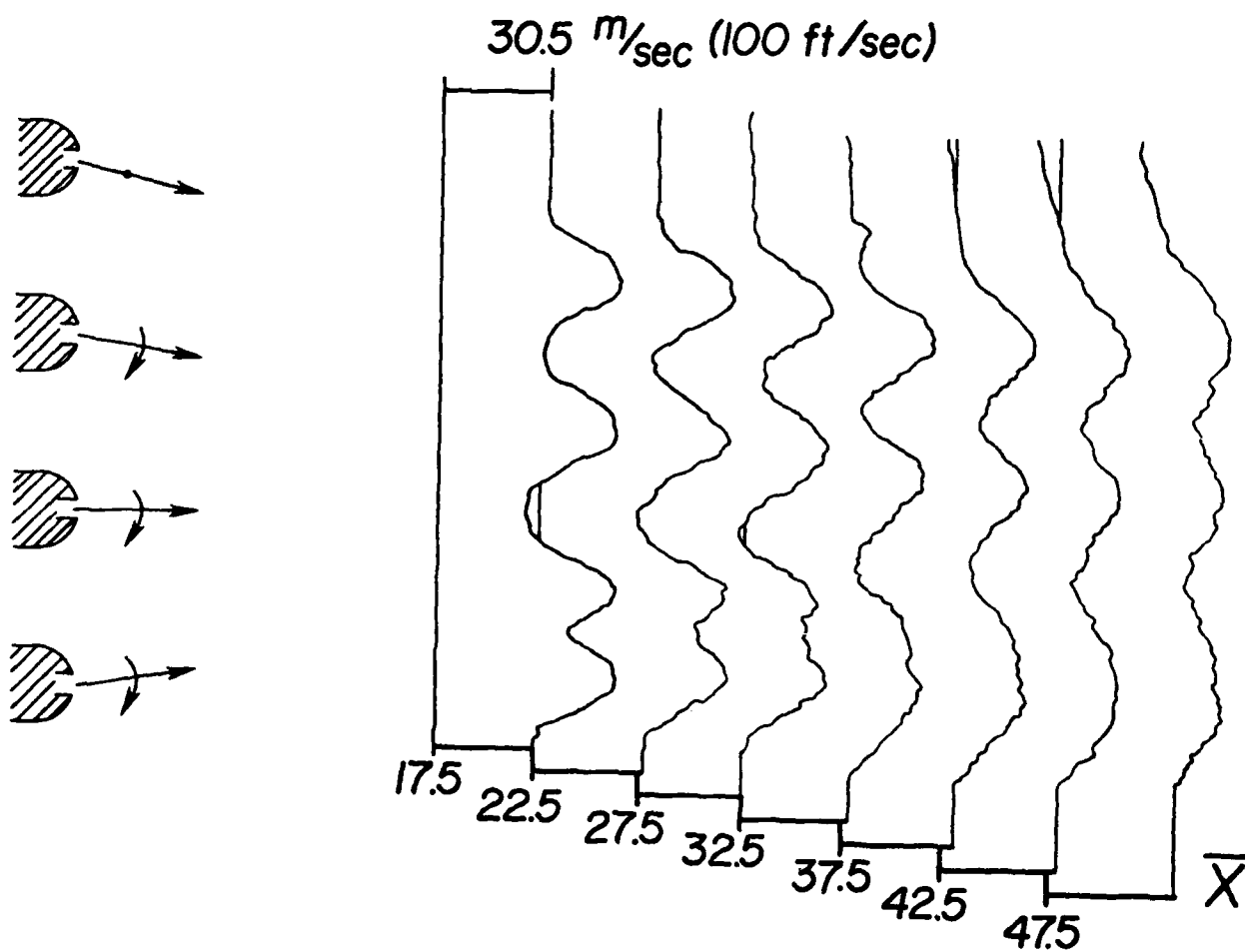


Figure 39. Same nozzle configuration as Figure 13 but with the upper nozzle in the downward orientation.

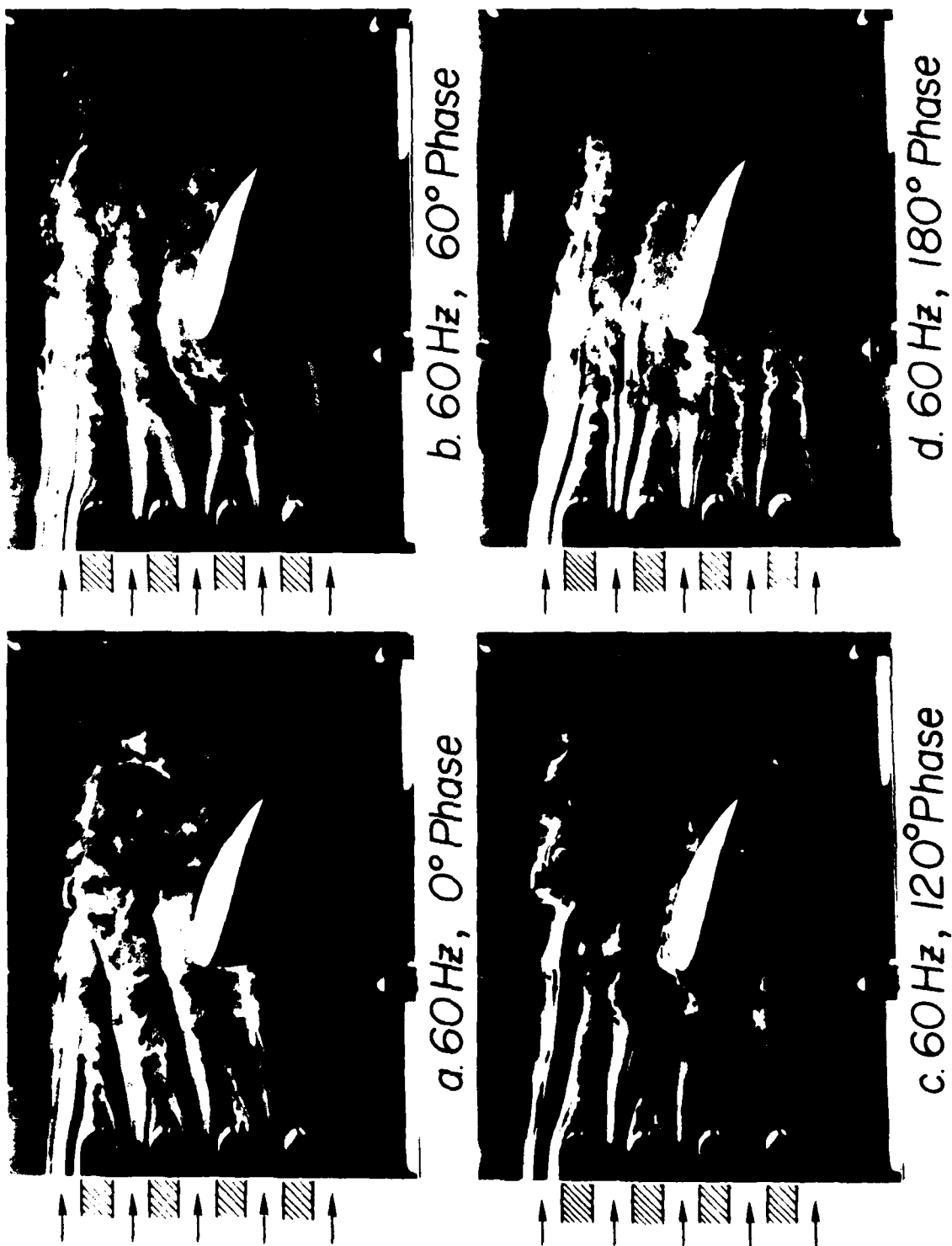


Figure 40. Flow visualization of the in-phase gust flow over an airfoil at various phase angles.



f. 60Hz, 300° Phase



e. 60Hz, 240° Phase



g. 60Hz, 360° Phase

Figure 40. Continued



Figure 41. Schematic of the vibrated jet studied by McCromack, Cochran and Crane.<sup>29</sup>

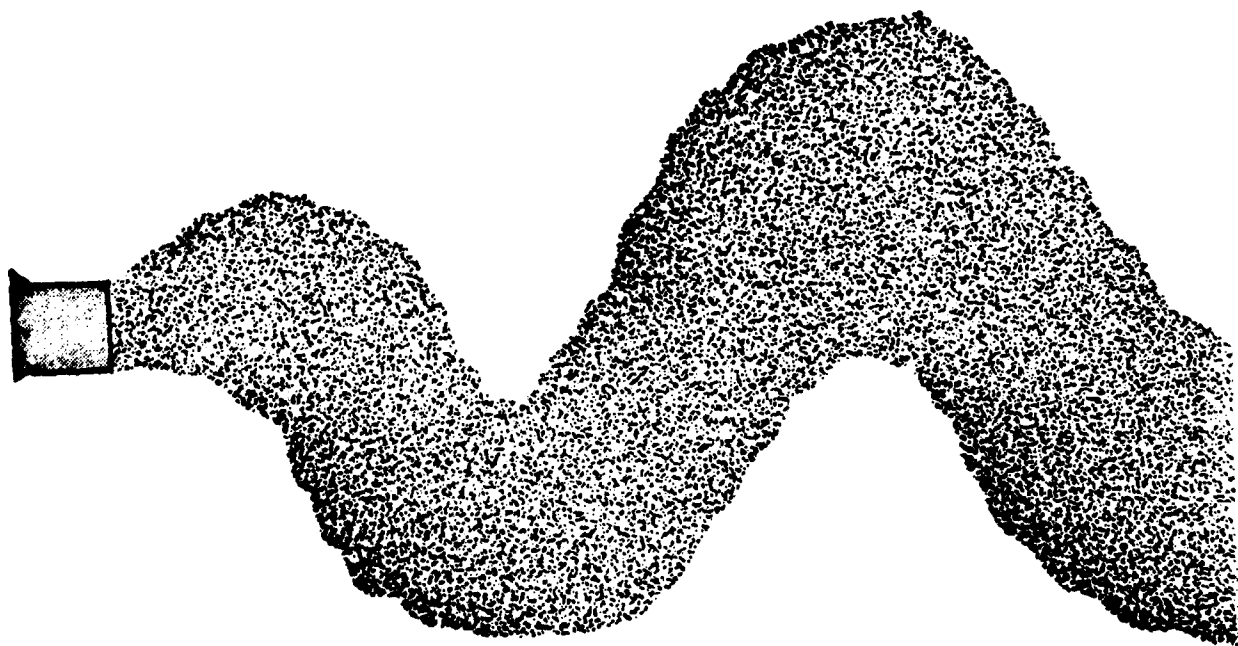


Figure 42. Flapping jet with angular time variation at the exit studied by Viets et al.<sup>3,45</sup> and Platzler et al.<sup>10</sup>

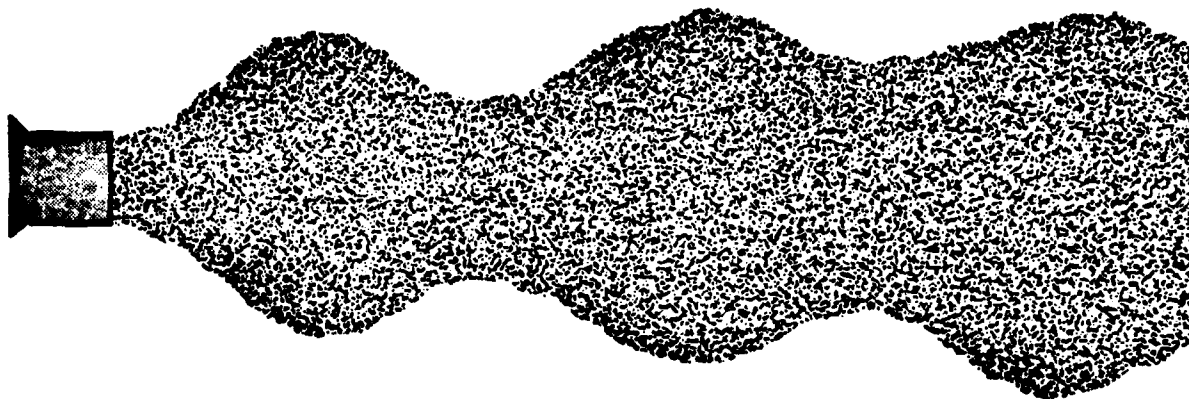


Figure 43. Jet with time dependent mass flow studied by Binder and Favre-marinet and Curtet and Girad.<sup>2</sup>

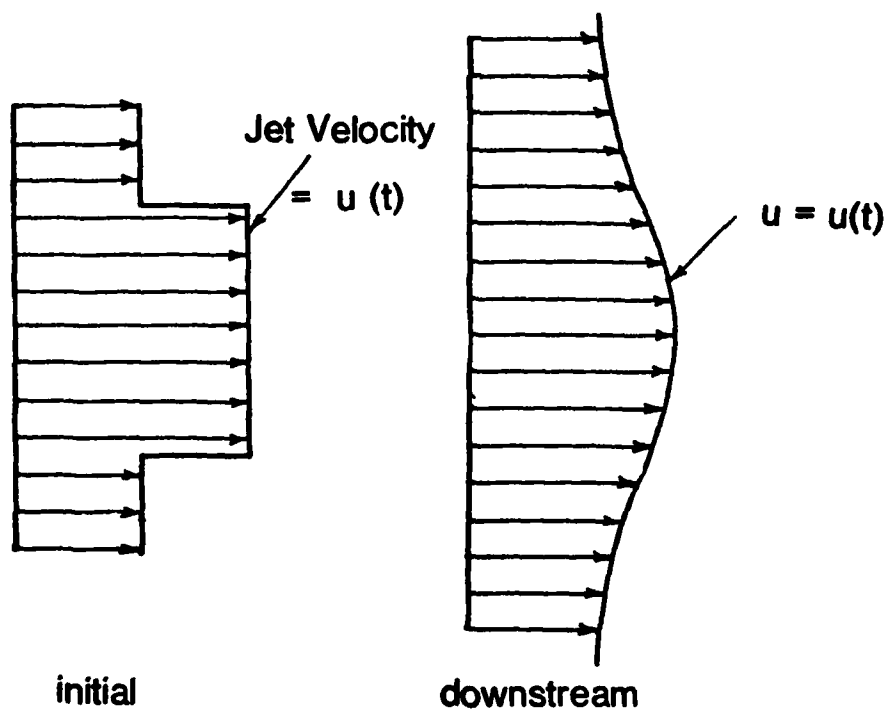


Figure 44. Initial and downstream velocity profiles.

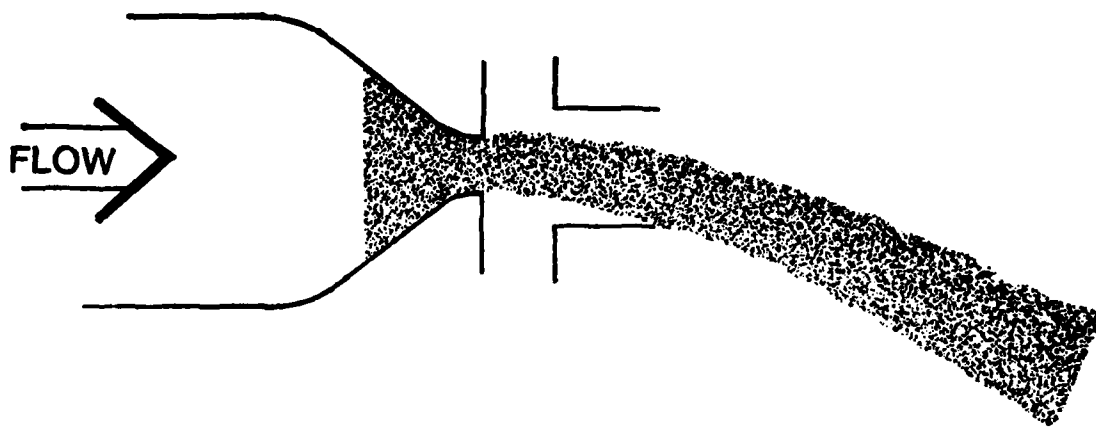
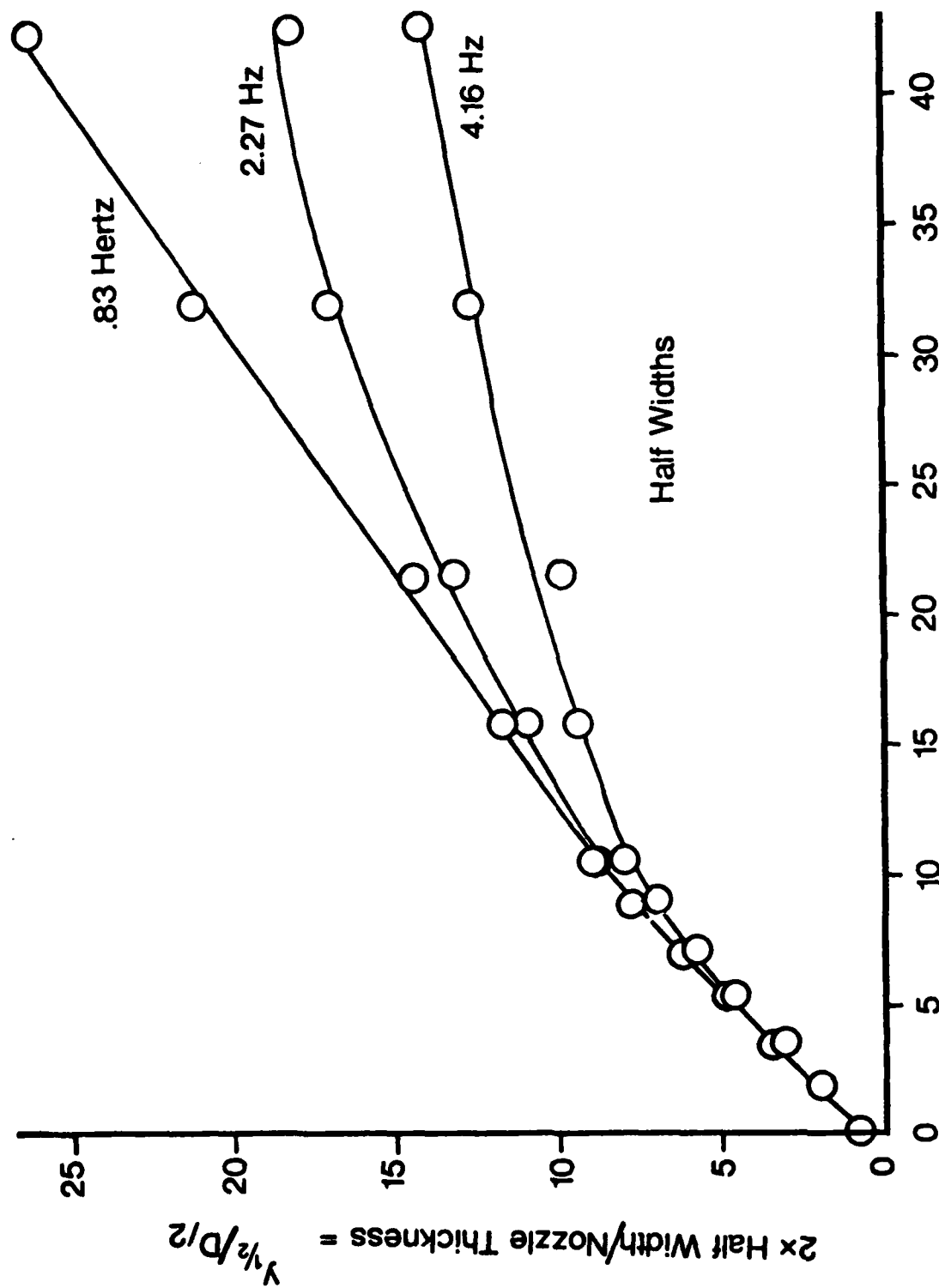


Figure 45. Fluidically Controlled Jet Nozzle Design.



Downstream Distance / Nozzle Thickness =  $x/D$

Figure 46. Half width growth dependent upon oscillation frequency.

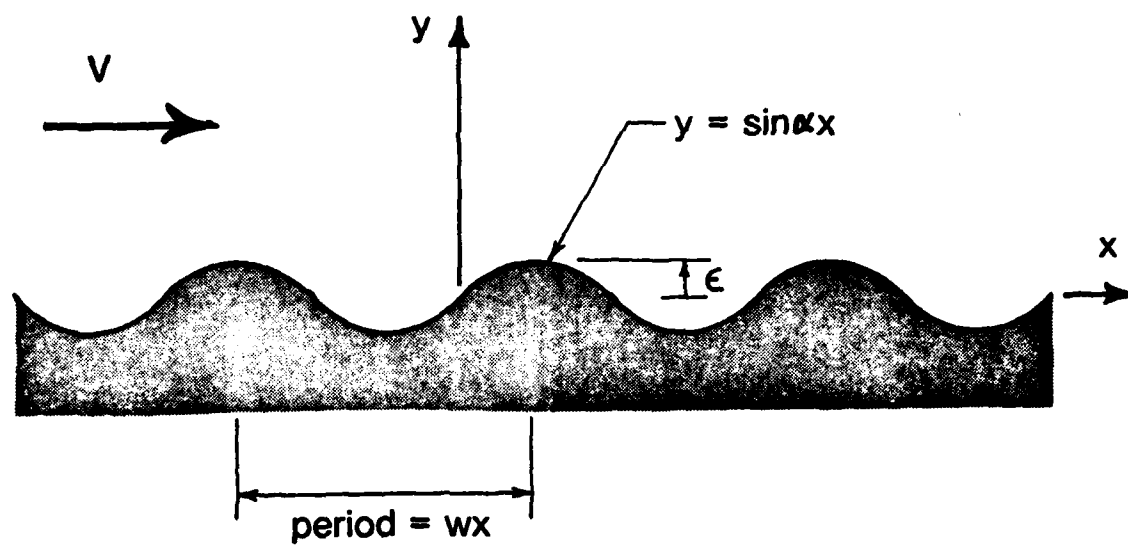
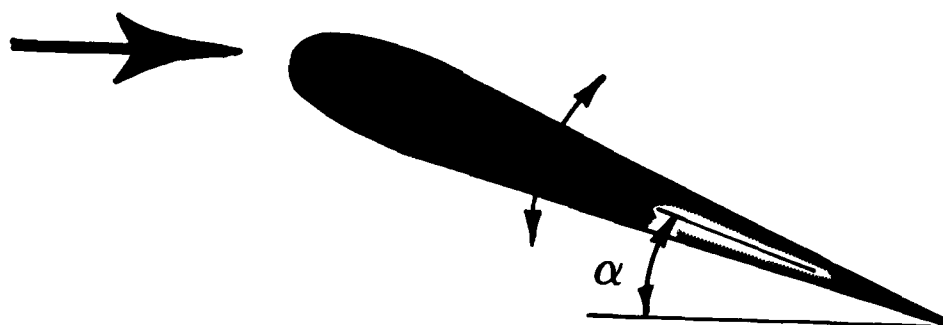
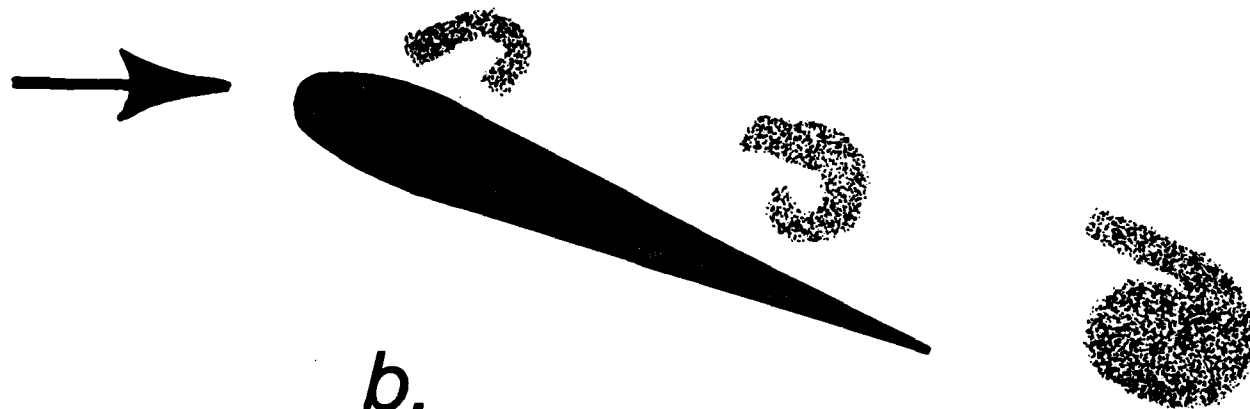


Figure 47. Flow over a wavy wall



$$\alpha = \alpha_0 + \alpha' \sin \omega t$$

*a.*



*b.*

Figure 48. Geometry and Flowfield of an Oscillating Airfoil.



Figure 49. Hydrogen Bubble Flow Visualization of the Field  
Around an Oscillating Airfoil (from McAllister  
and Carr, Ref. 37A)

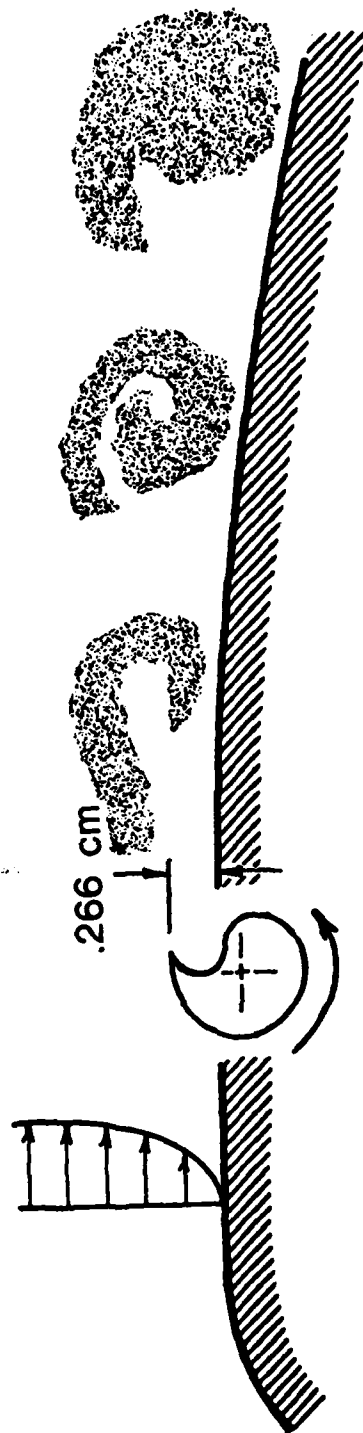


Figure 50. Vortex Generation by an Embedded Rotor.

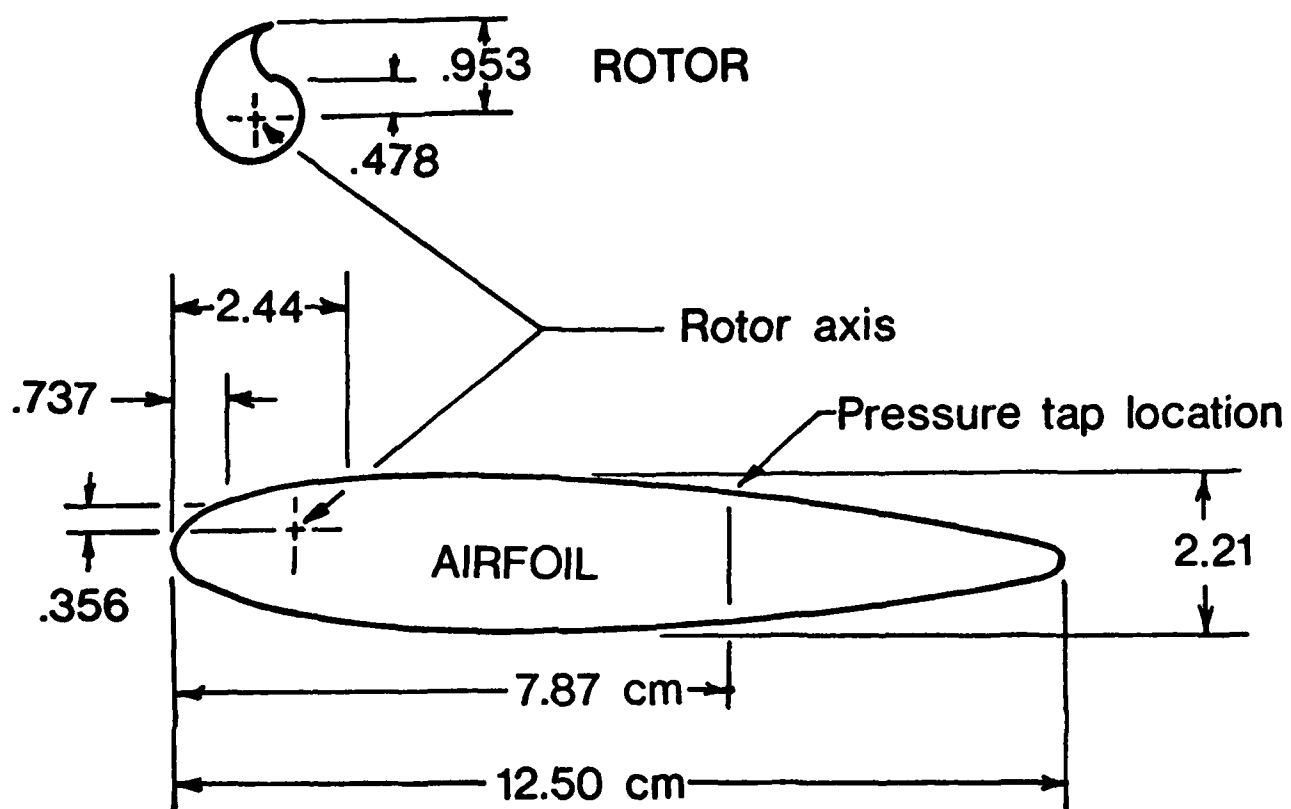


Figure 51. Airfoil and Rotor Geometry.

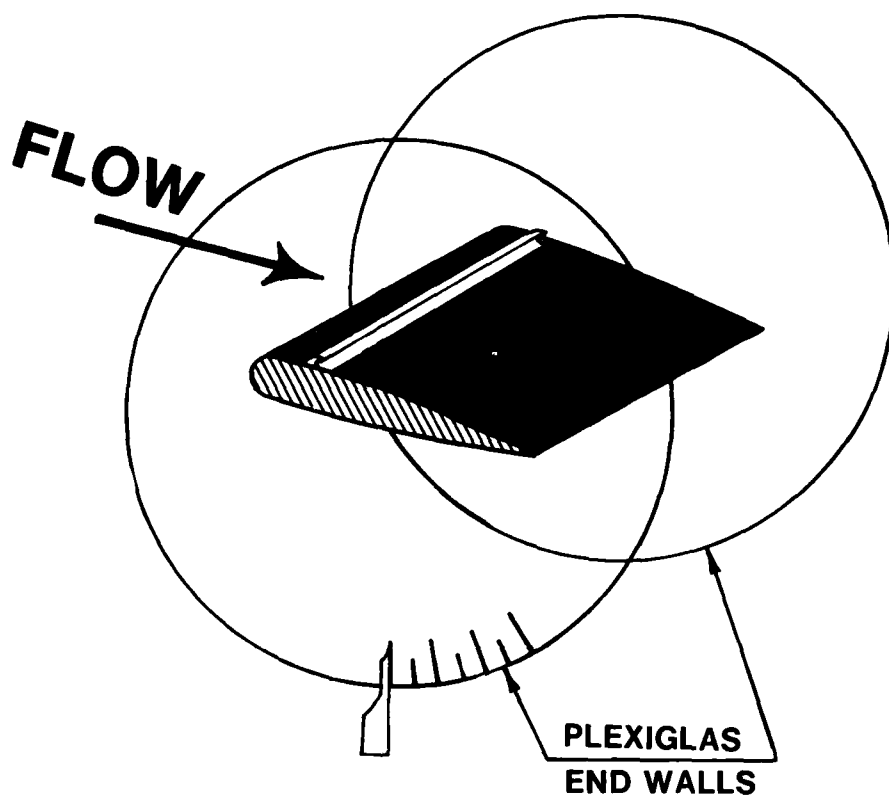
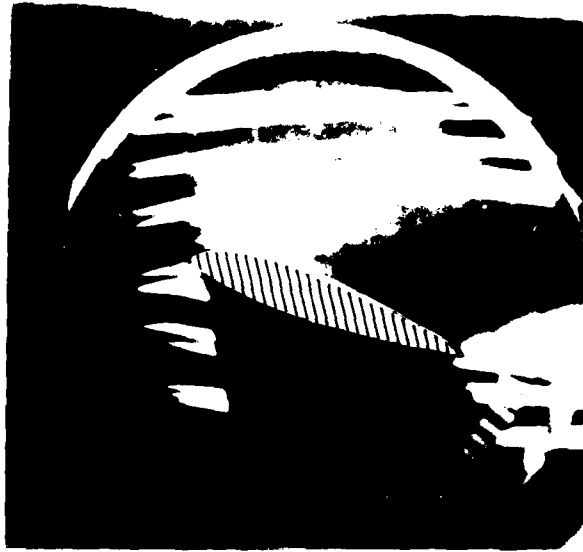


Figure 52. Airfoil Mounted for Low Speed Wind Tunnel.



↑  
Rotor location

Figure 53. Vortex Structure Behind the Rotor on a Flat Plate.



a.  $\omega = 0$



b.  $\omega = 2400$

Figure 54. Flow Visualization of the Flow Structure at  $\alpha = 20^\circ$ .

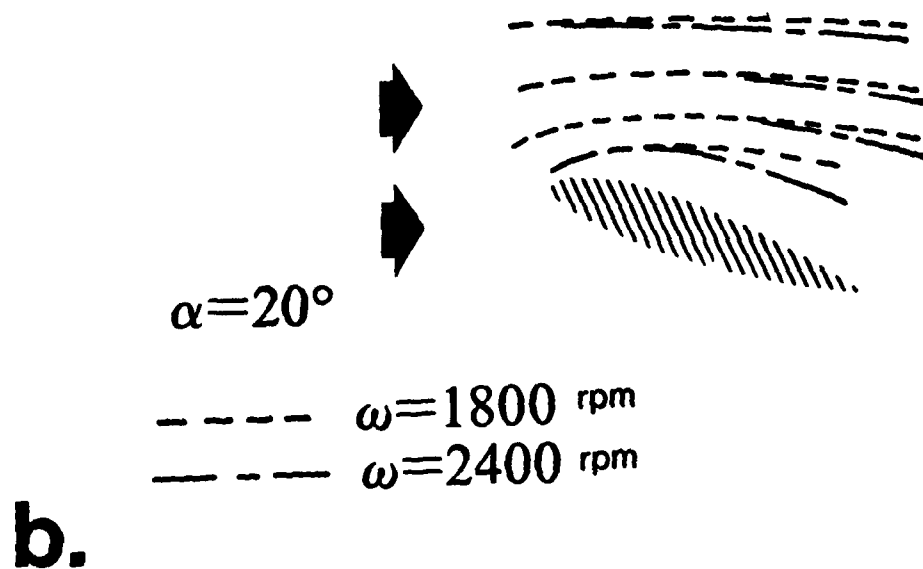
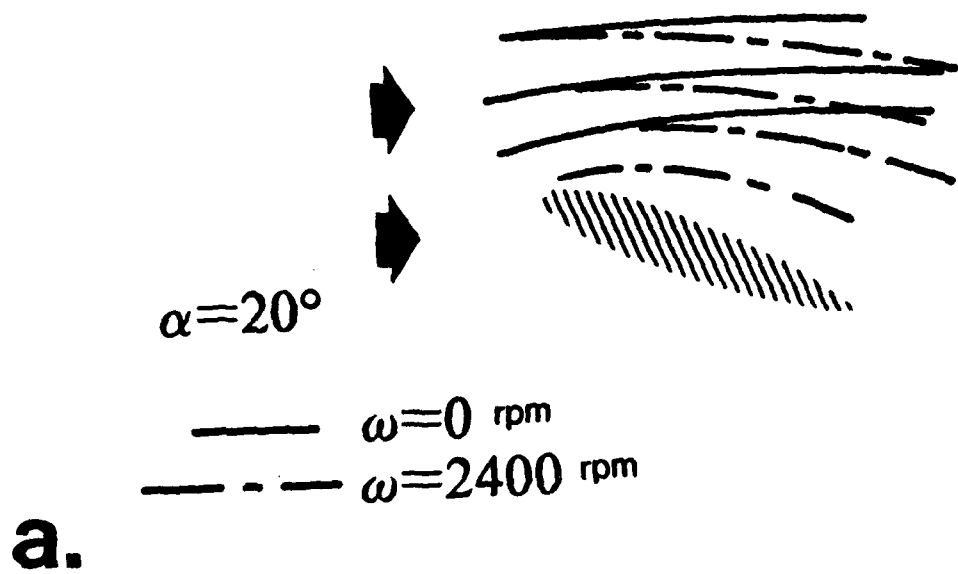


Figure 55. Effect of the Rotor Speed on the Streamline pattern over the Airfoil.

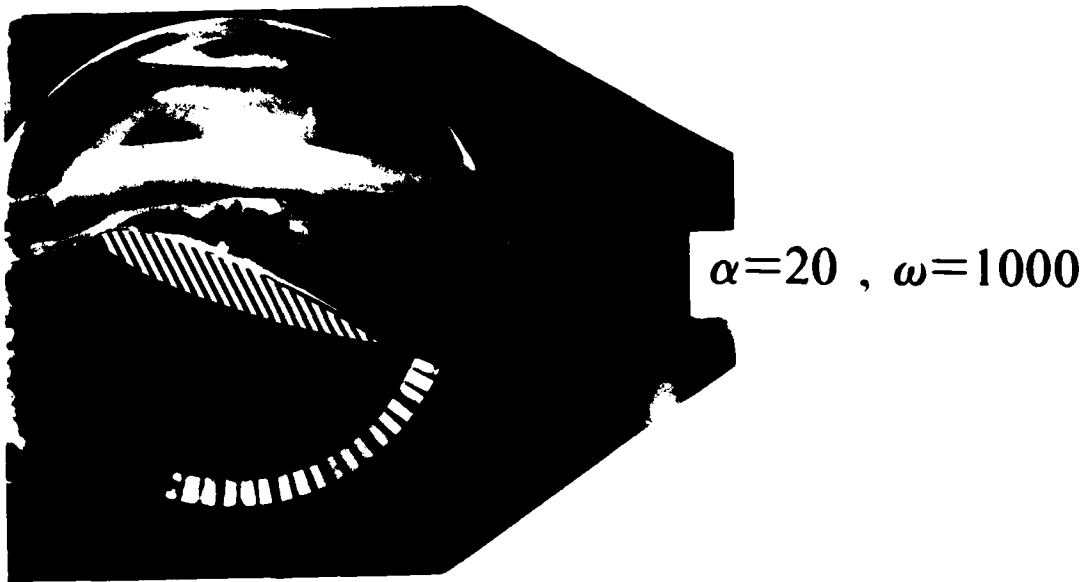


Figure 56. Instantaneous Vortex Structure on the Airfoil  
for  $\alpha = 20^\circ$ ,  $\omega = 1000$  rpm.

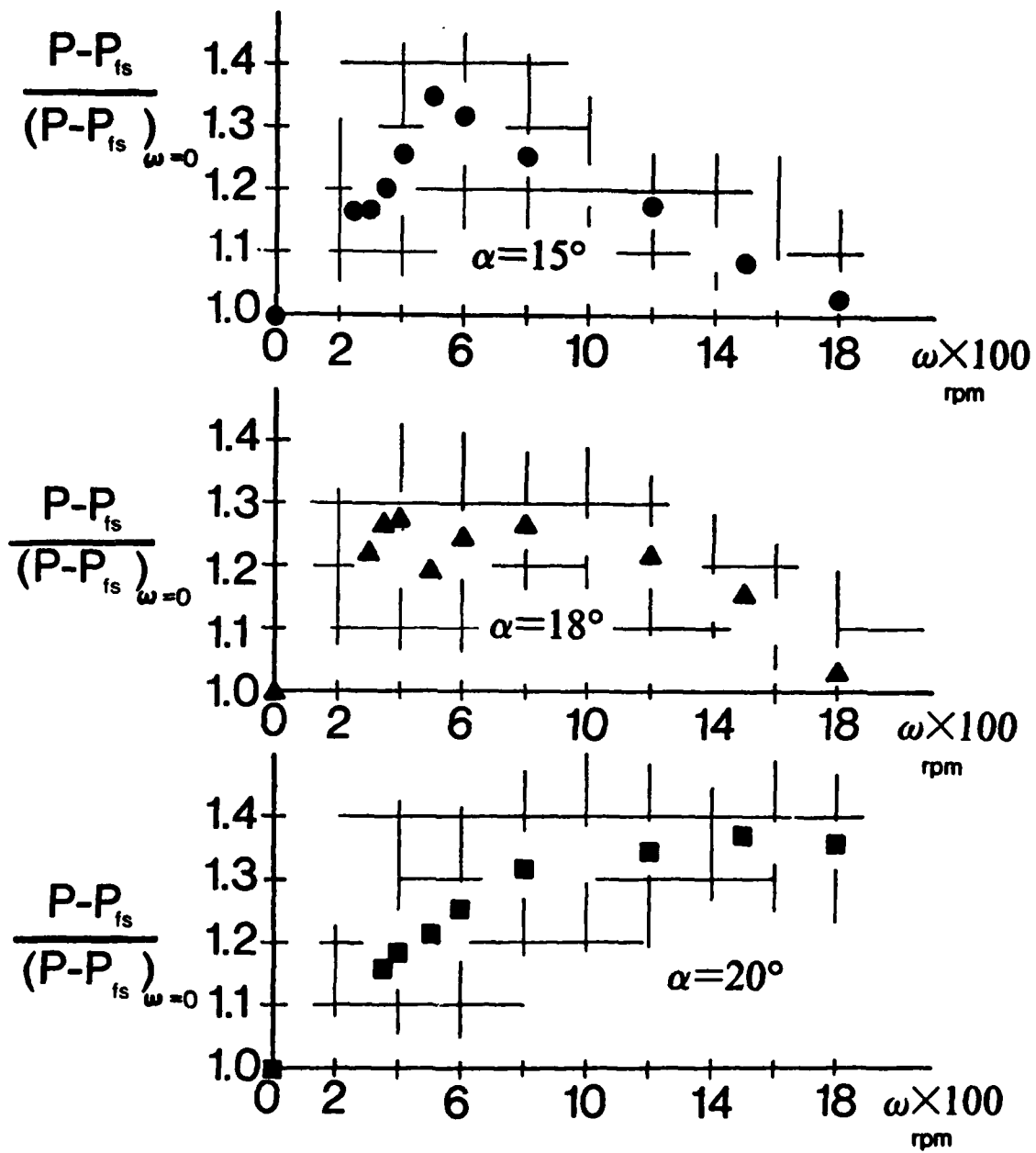


Figure 57. Pressure Variation with Rotor Speed for Three Angles of Attack.

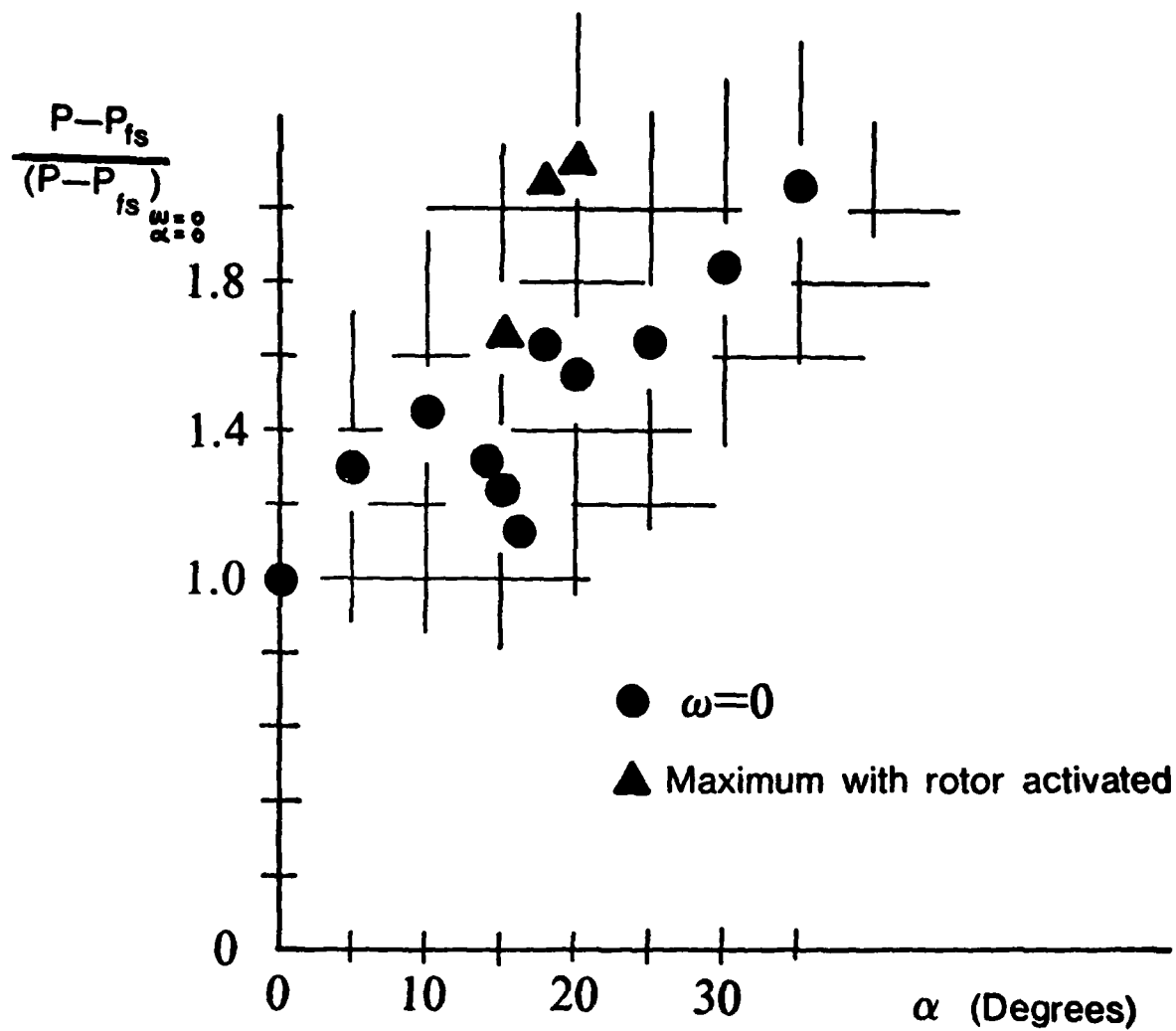


Figure 58. Pressure Variation with Angle of Attack with/without Activated Rotor.

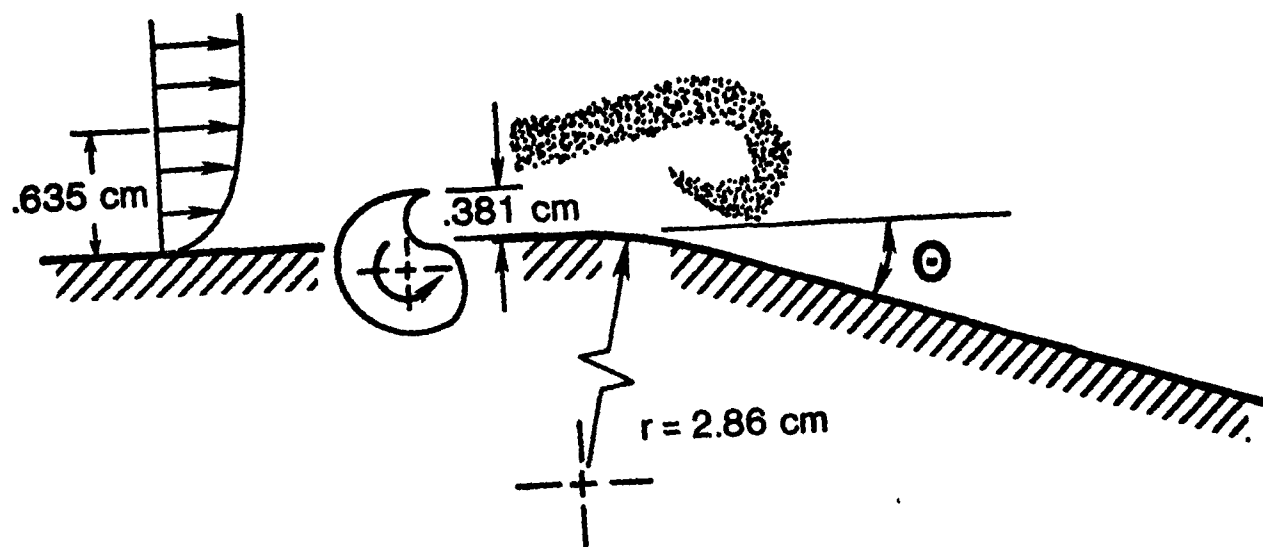


Figure 59a. Unsteady Ramp Flow Configuration

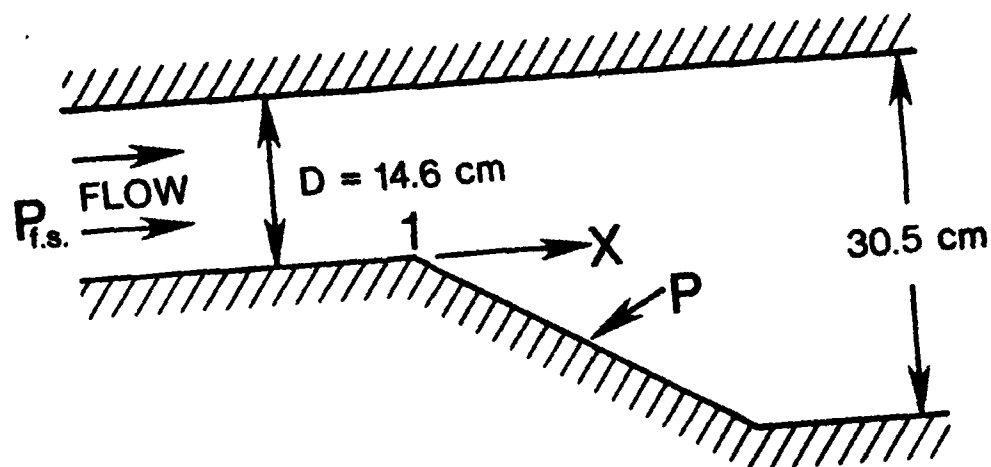


Figure 59b. Tunnel Geometry

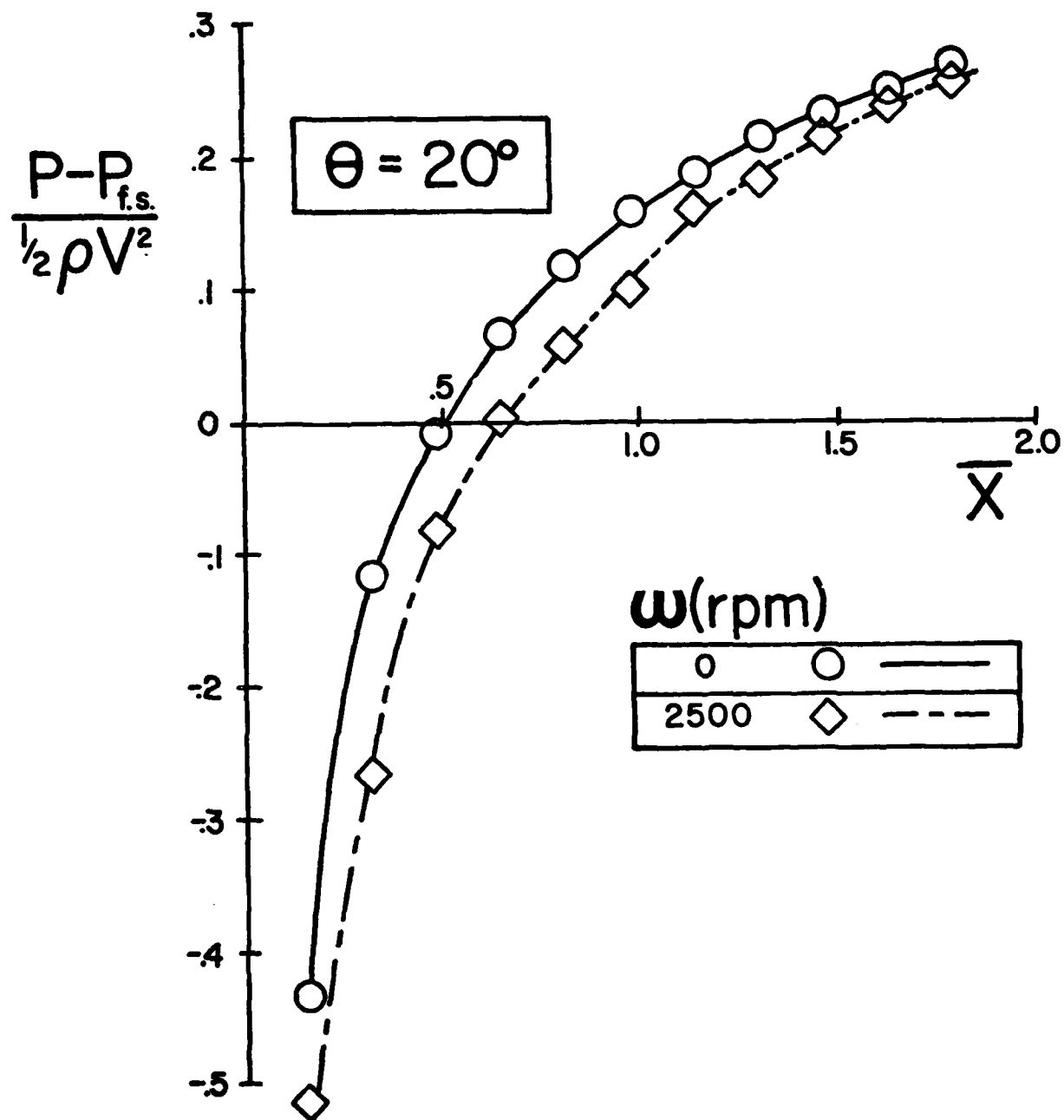


Figure 60. Pressure Distribution on the Ramp for  $\theta = 20^\circ$ .

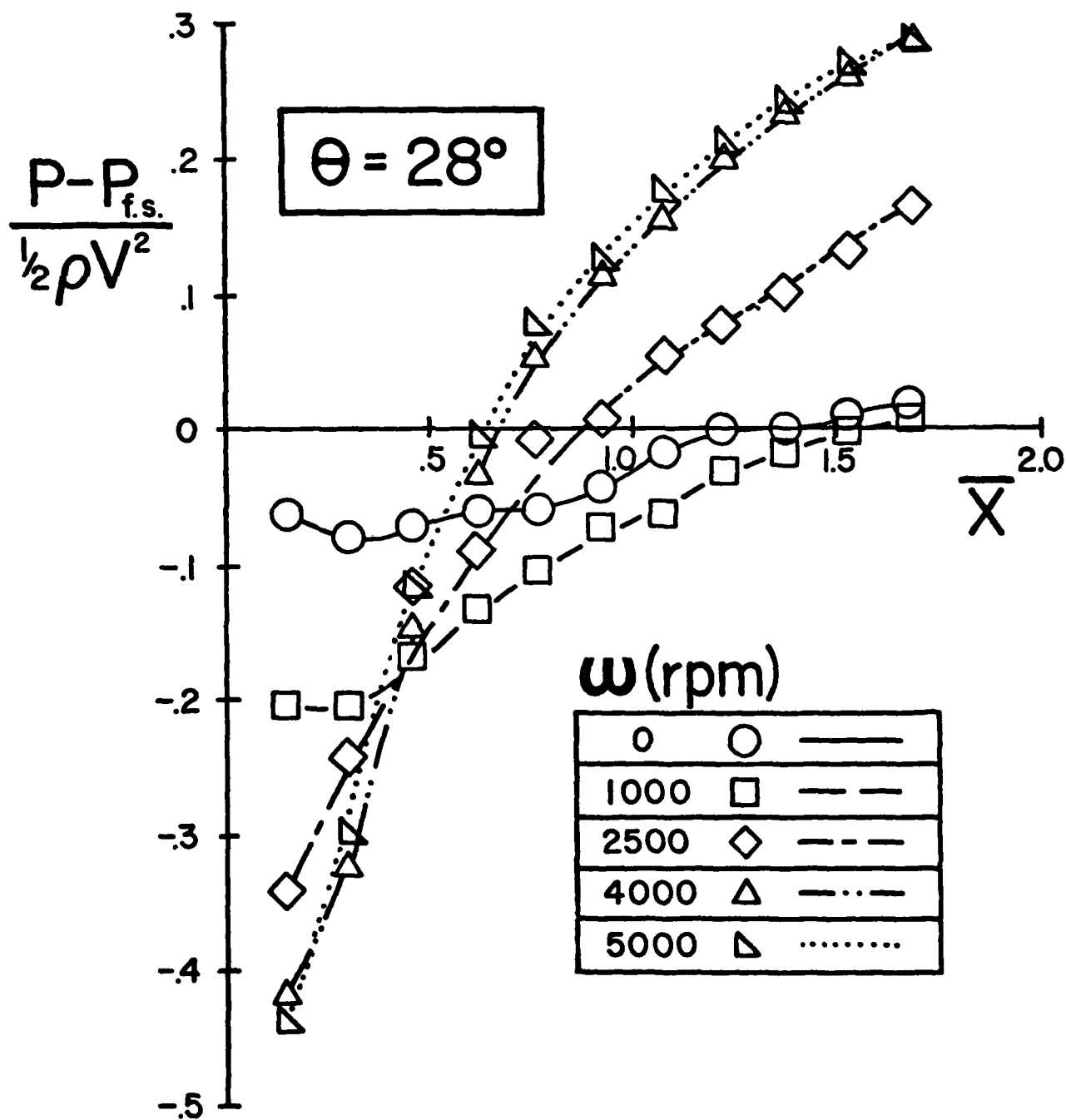


Figure 61. Pressure Distribution on the Ramp for  $\theta = 28^\circ$

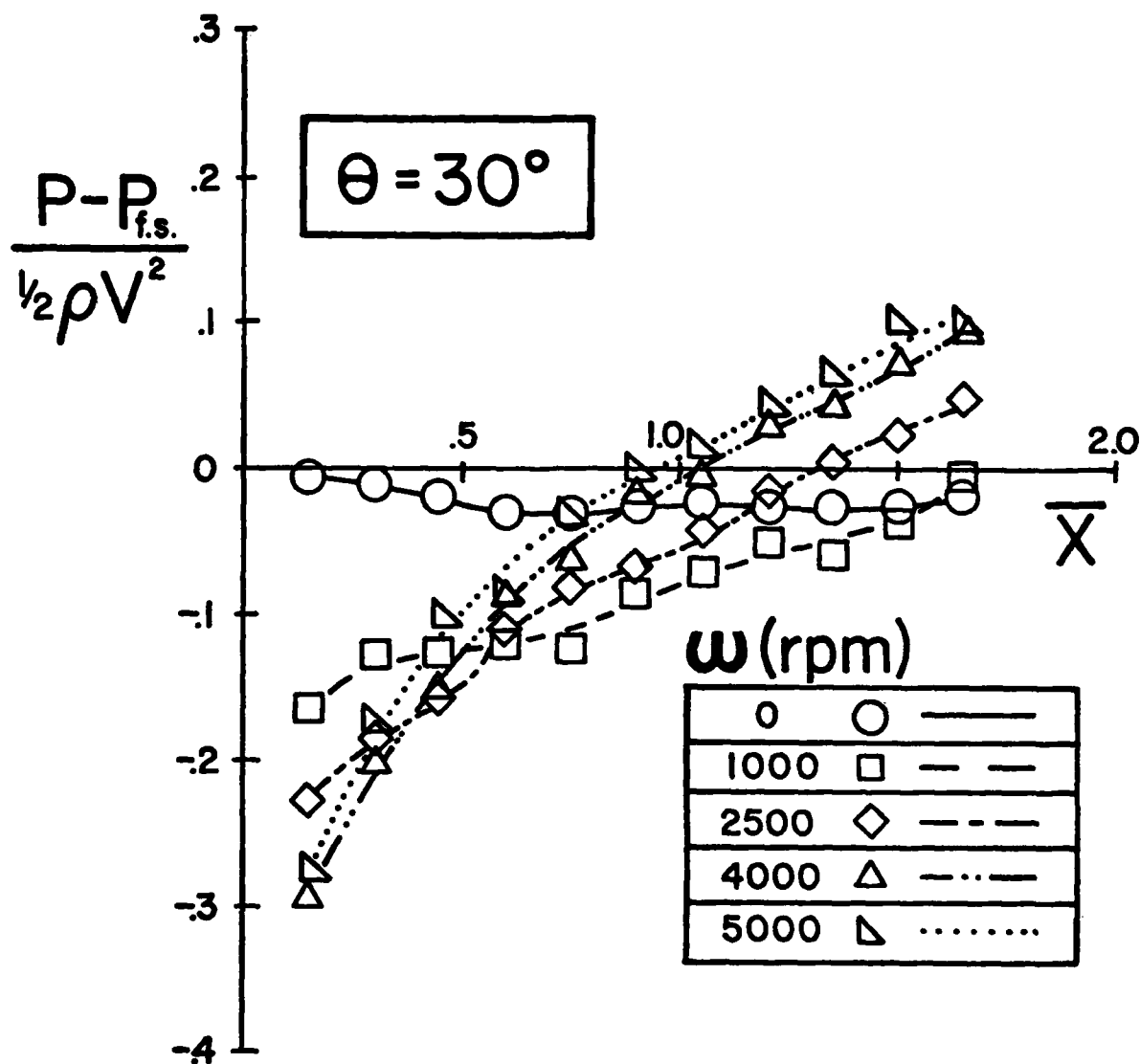


Figure 62. Pressure Distribution on the Ramp for  $\theta = 30^\circ$ .

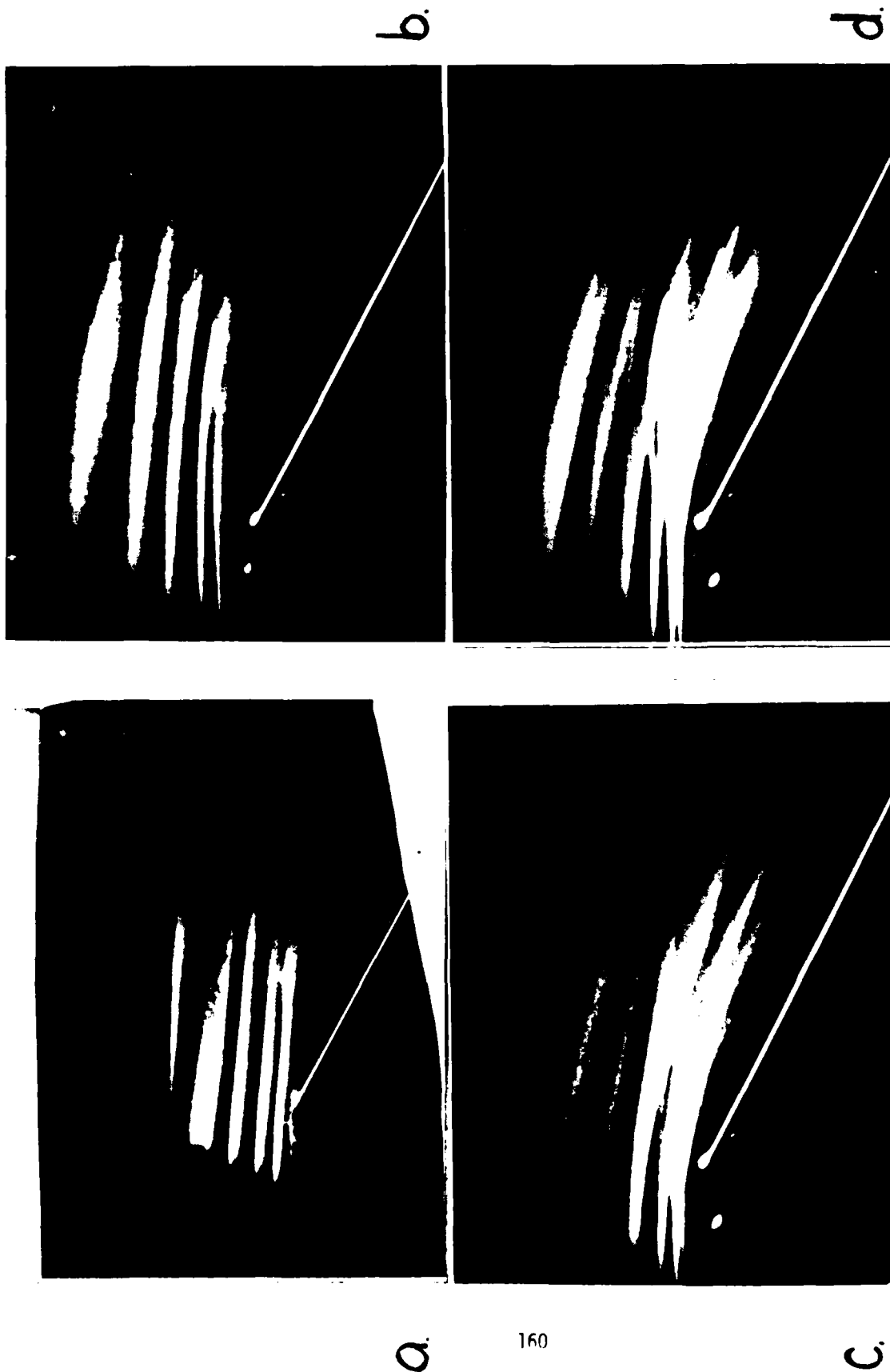
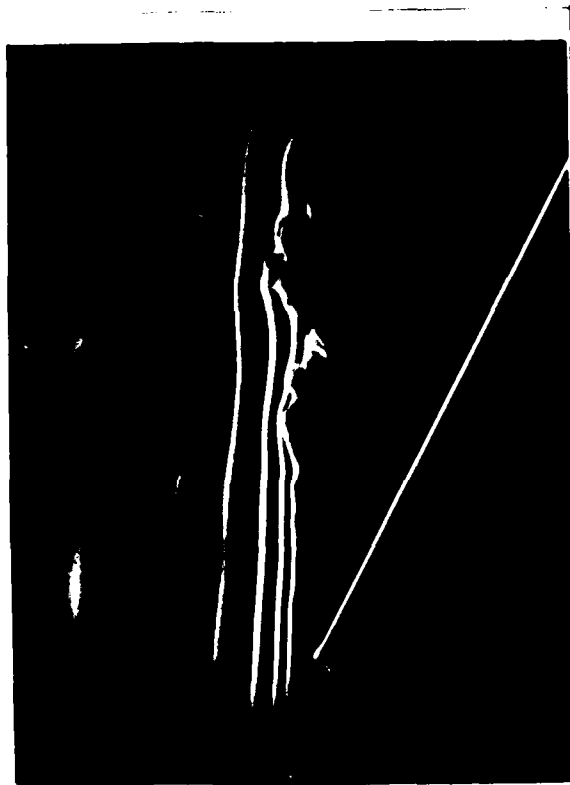


Figure 63. Time averaged Flow for  $\theta = 28^\circ$ .



a.



b.



c.

Figure 64. Instantaneous Streakline Photographs for Various Rotor Speeds at  $\theta = 28^\circ$ .



e.



d.

f.



Figure 64. Continued

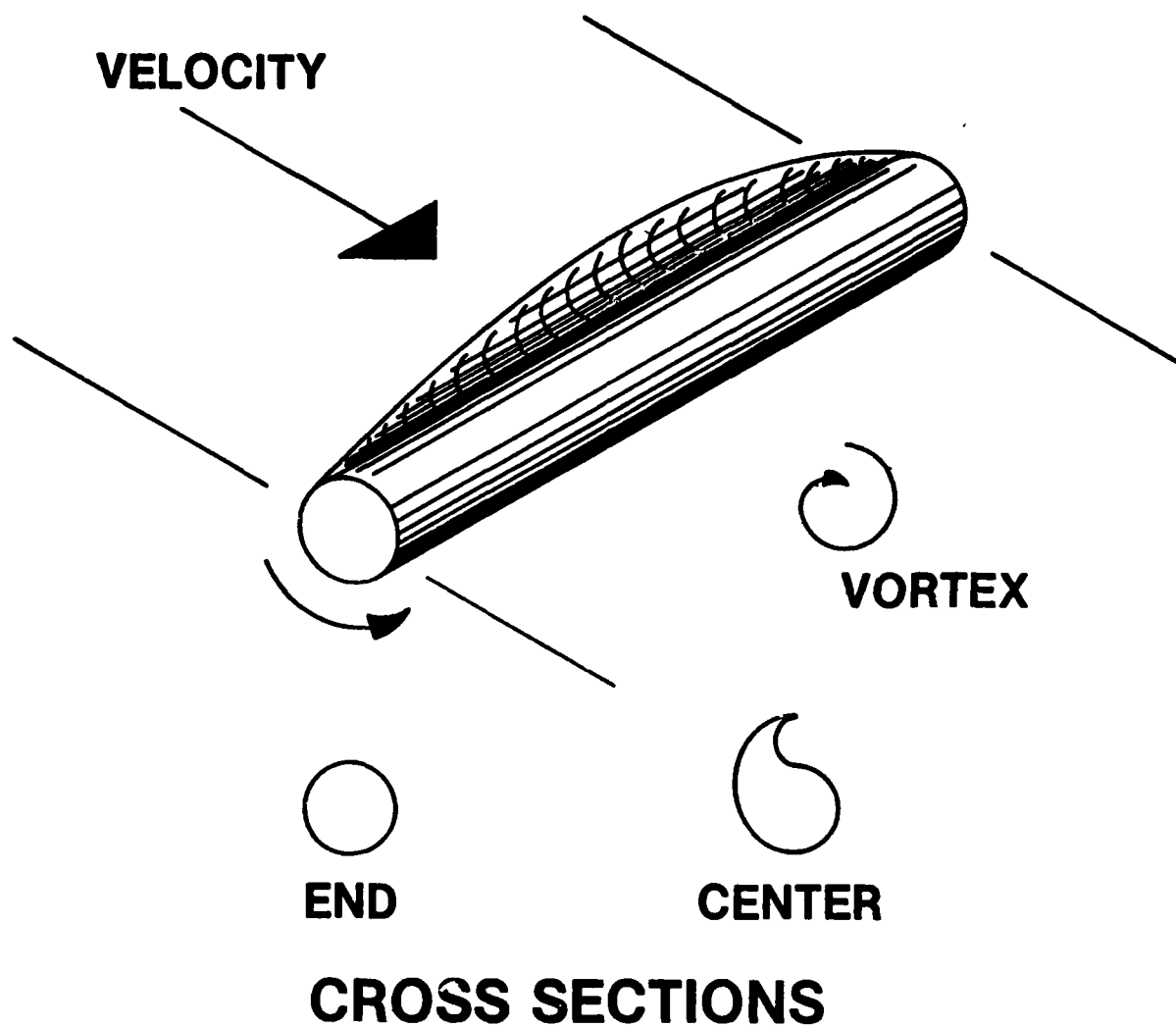


Figure 65. Schematic of a three dimensional rotor geometry (Tapered rotor).

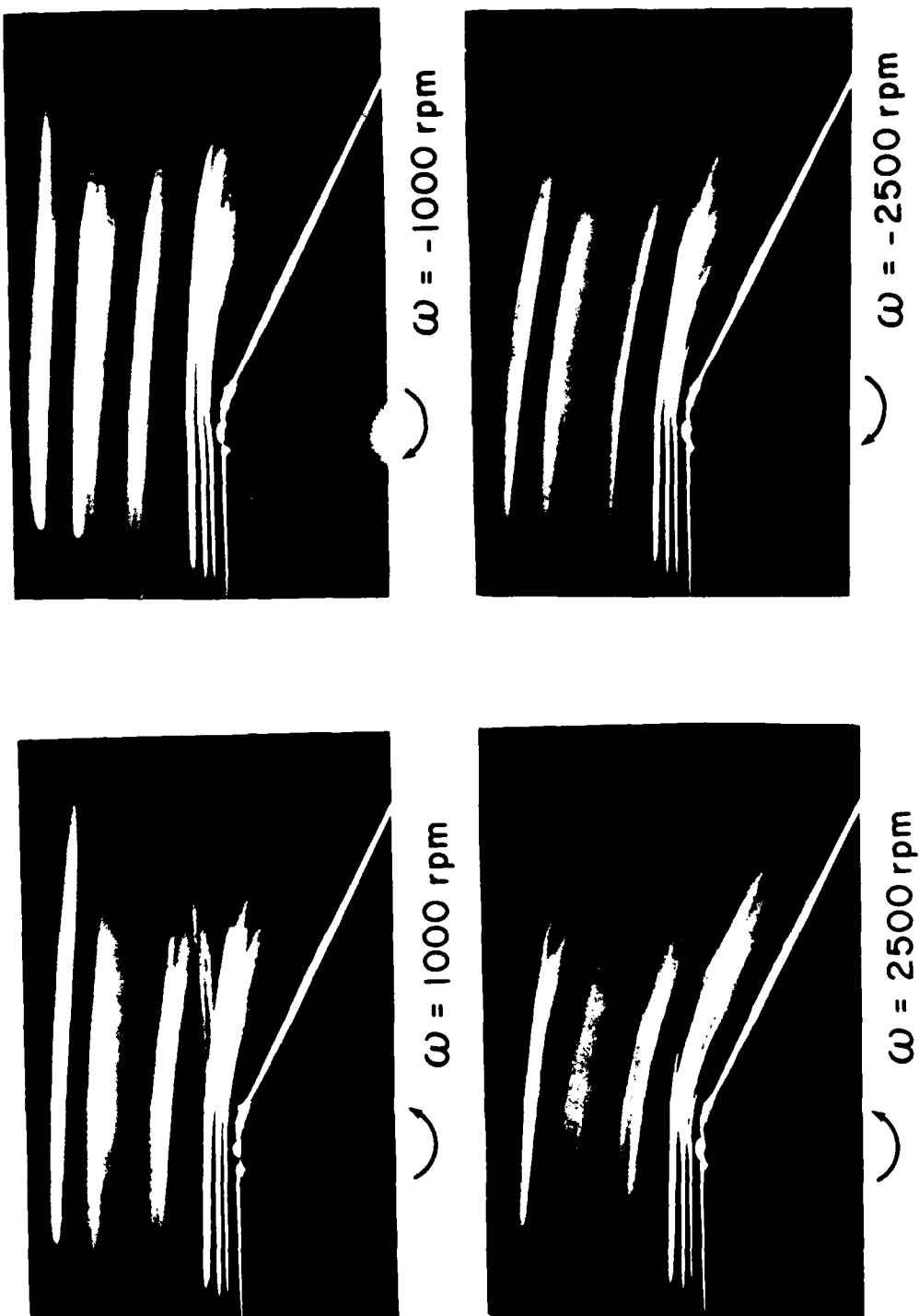
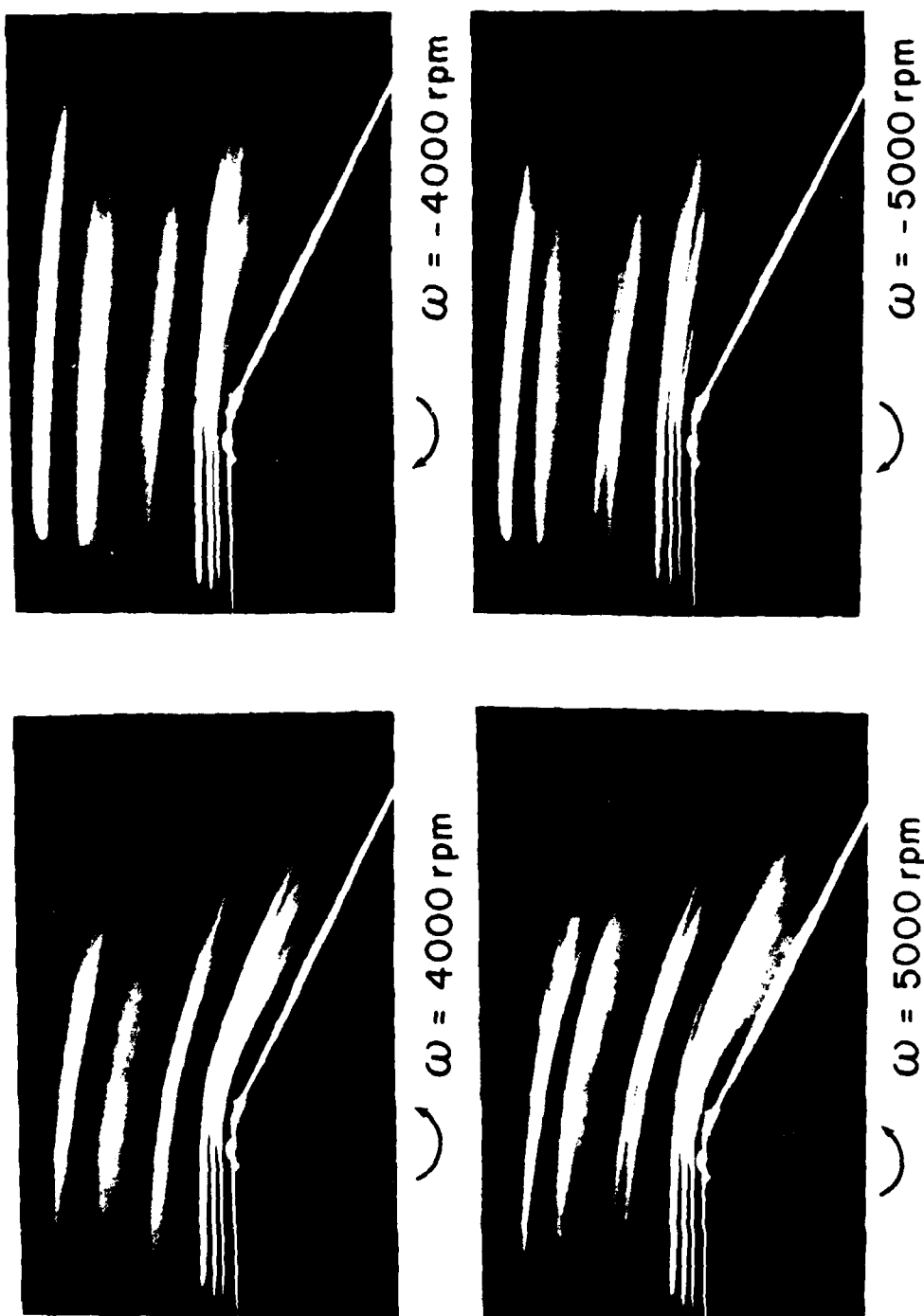


Figure 66. Comparison between rotor motion in the upstream (+) and downstream (-) directions for  $\omega = 1000$  and  $2500$  rpm, and a tapered rotor.



$\Theta = 28^\circ$   
TAPERED ROTOR

Figure 67. Same as Figure 66 for  $\omega = 4000$  and  $5000$  rpm.

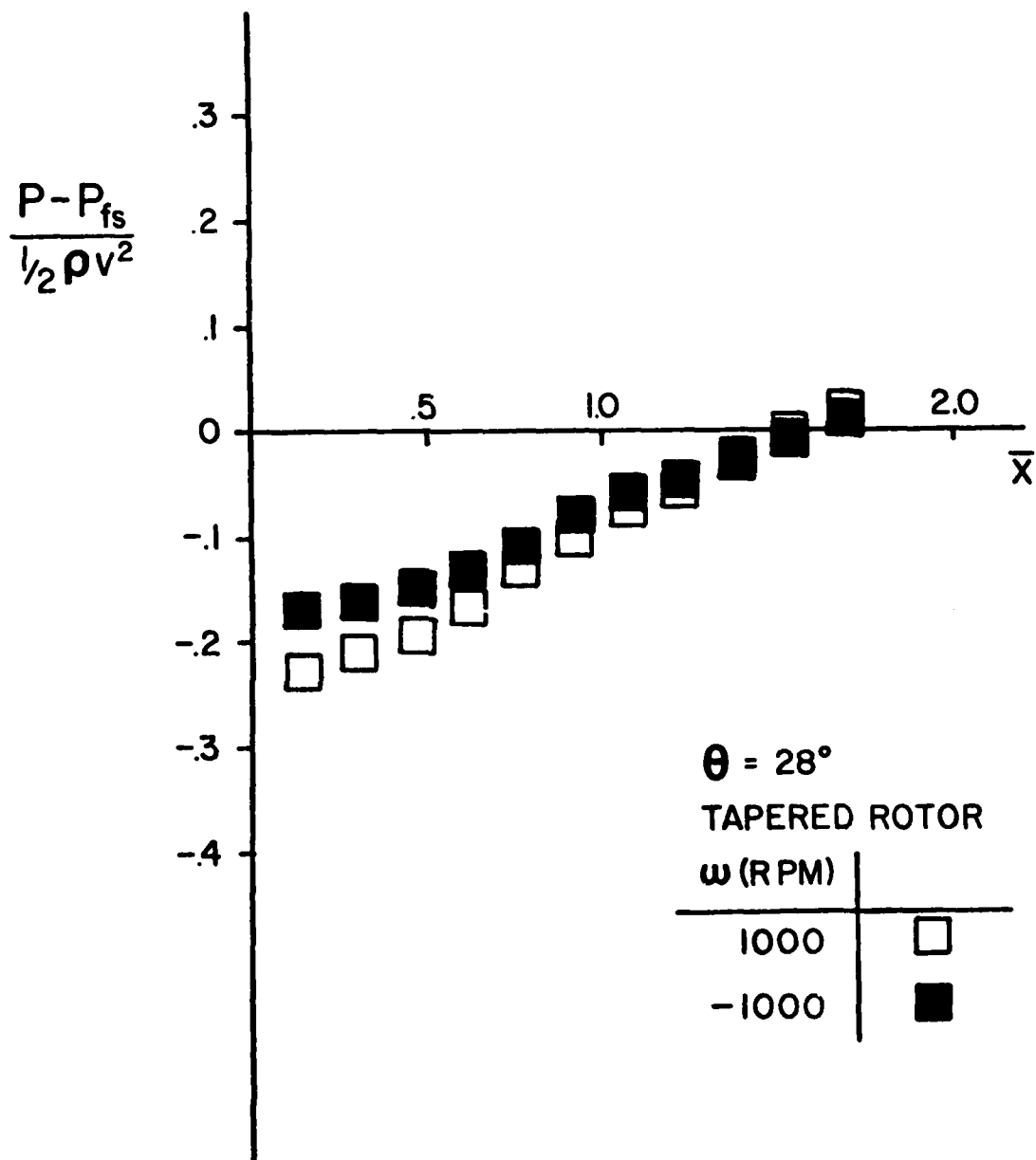


Figure 68. Pressure rise down the ramp for  $\pm$  1000 rpm and a tapered rotor.

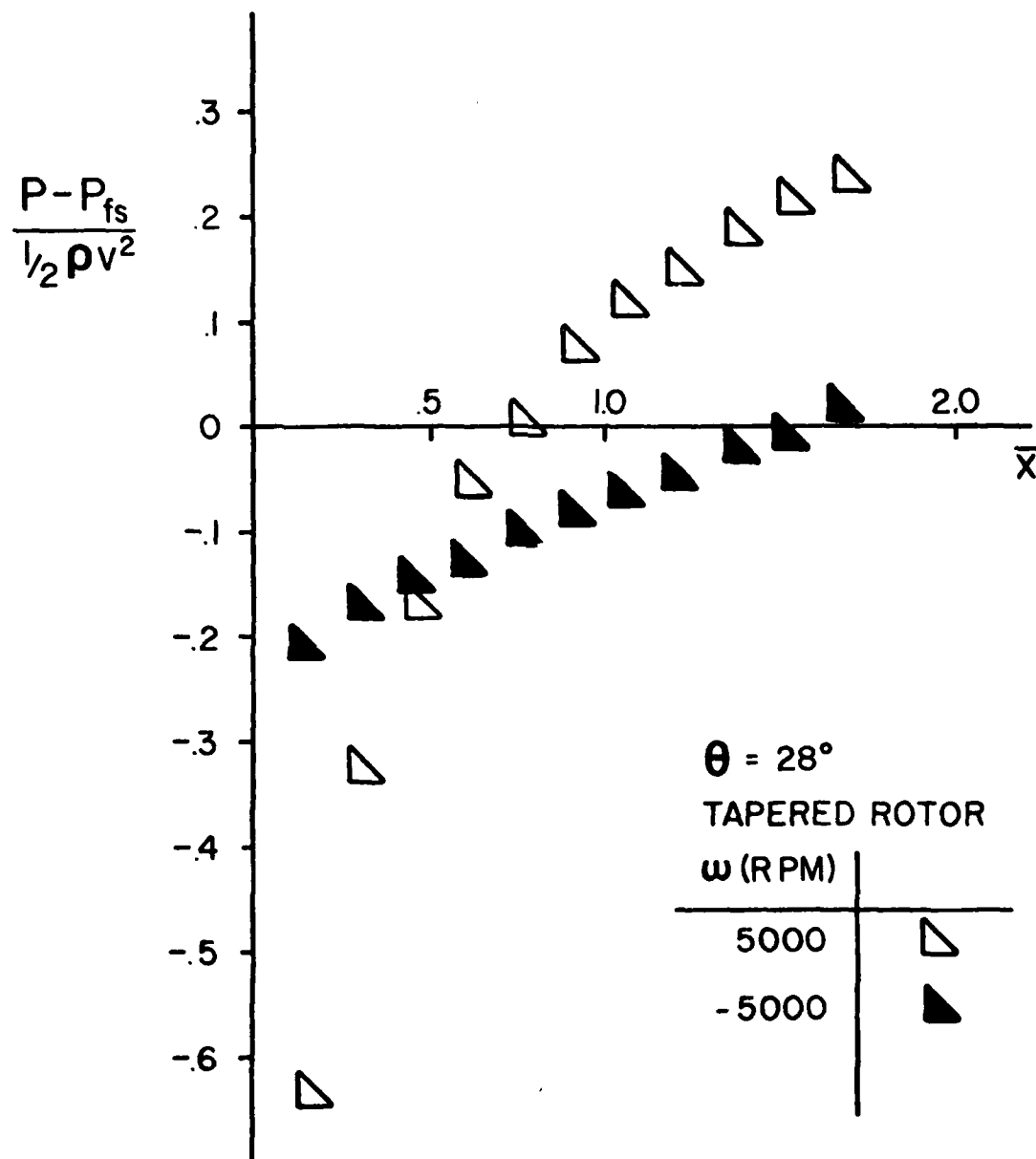


Figure 69. Pressure rise down the ramp for  $\pm 5000$  rpm and a tapered rotor.



$\omega = -1000 \text{ rpm}$



$\omega = -2500 \text{ rpm}$



$\omega = 1000 \text{ rpm}$



$\omega = 2500 \text{ rpm}$

# $\Theta = 28^\circ$ TAPERED ROTOR

Figure 70. Streaklines in the ramp flowfield for a tapered rotor moving in the counter-clockwise (+) and clockwise (-) directions.



$\omega = 4000 \text{ rpm}$



$\omega = 5000 \text{ rpm}$



$\omega = 4000 \text{ rpm}$



$\omega = 5000 \text{ rpm}$



# $\Theta = 28^\circ$ TAPERED ROTOR

Figure 71. Same as Figure 70 for higher rotor speeds.

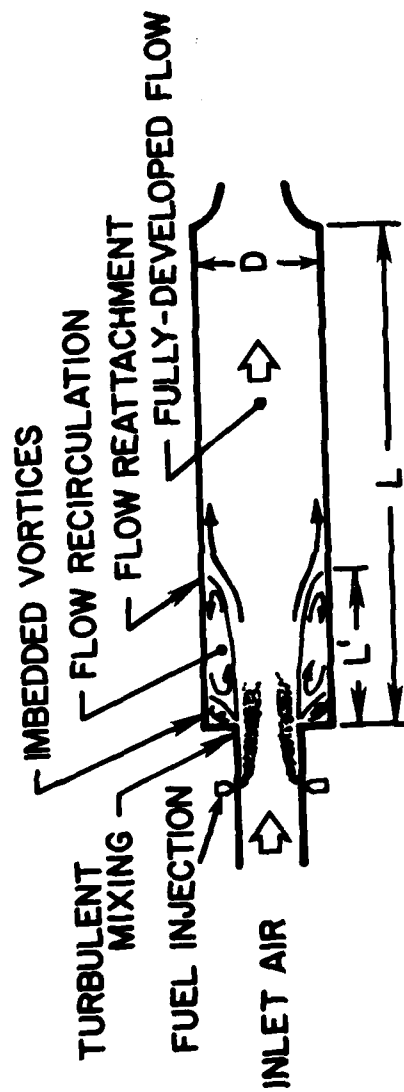


Figure 72. Ramjet Combustor Flowfield.

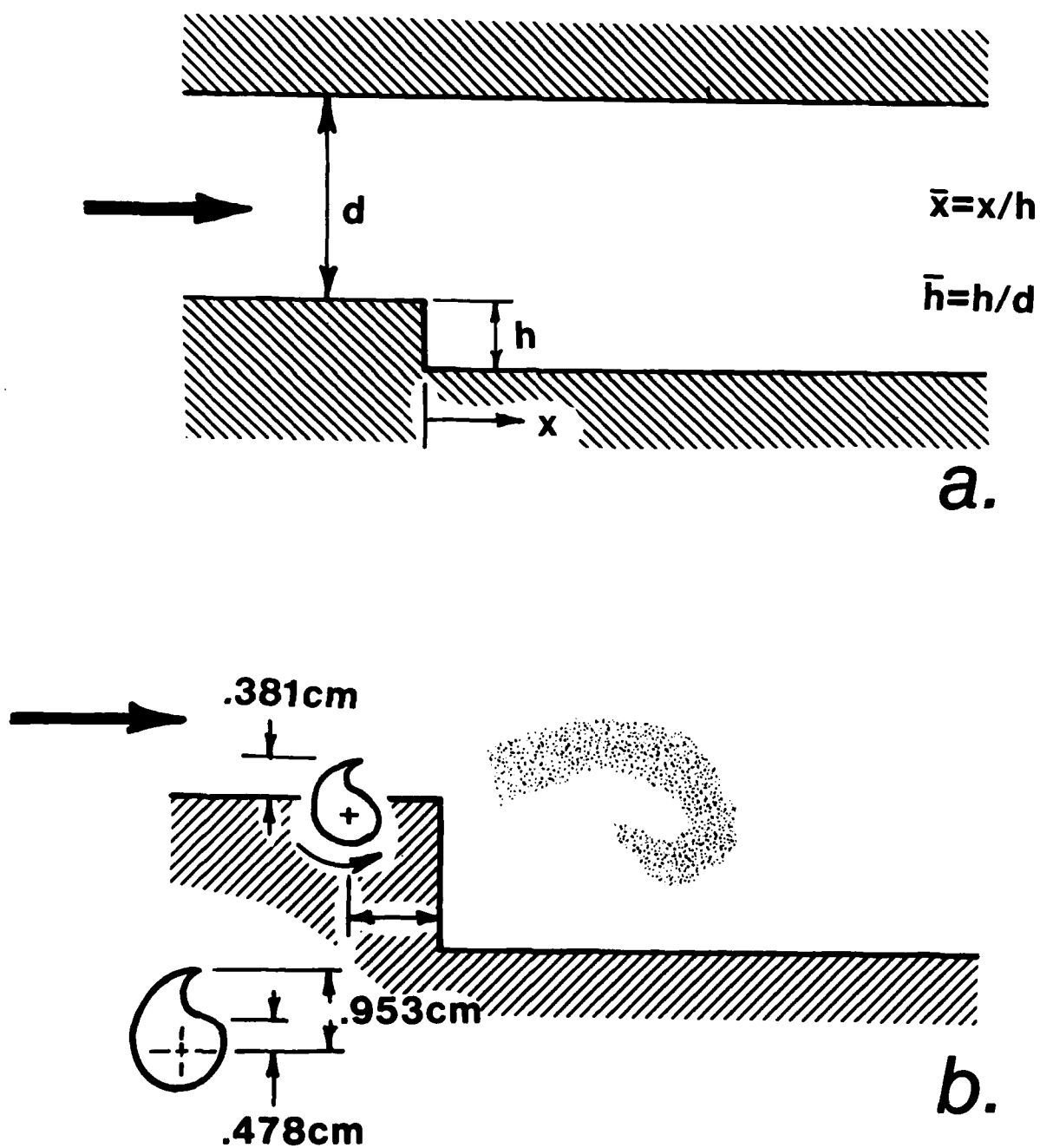


Figure 73. Experimental Geometry and Rotor Flowfield.

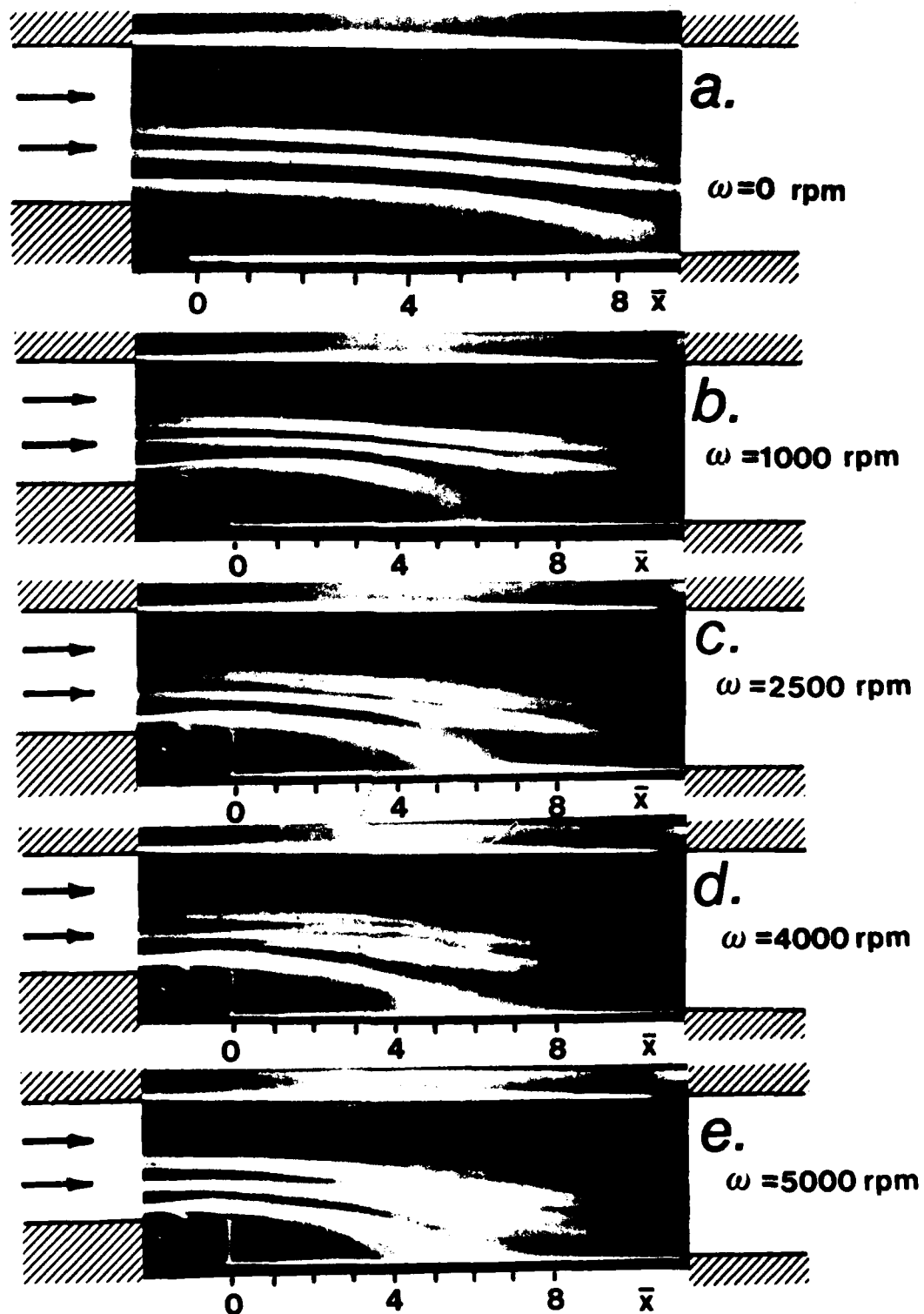


Figure 74. Streamline Shapes for Various Rotor Speeds,  
 $h = 1/3$ .

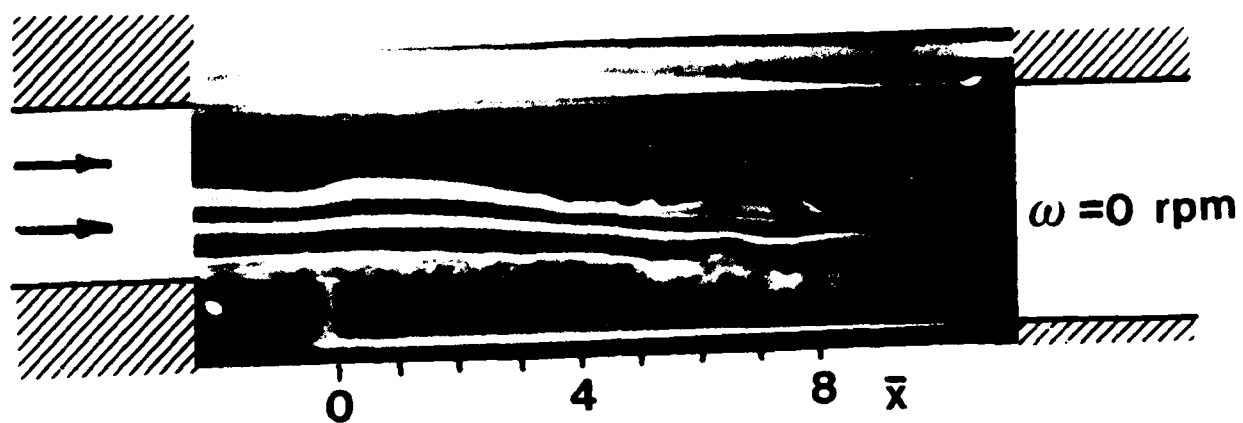
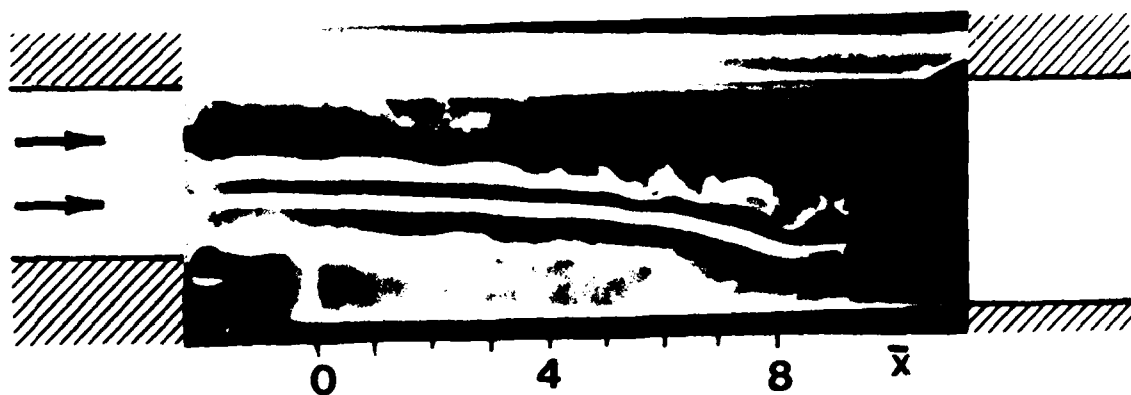
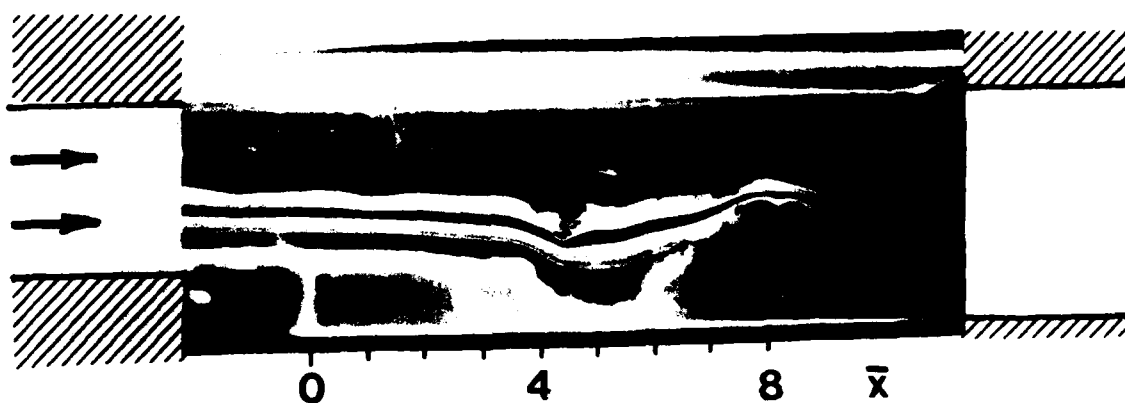


Figure 75. Instantaneous Streaklines for  $\omega = 0$ ,  $h = 1/3$ .



**a.**  $\omega = 2500\text{rpm}$



**b.**  $\omega = 2500\text{rpm}$



**c.**  $\omega = 2500\text{rpm}$

Figure 76. Streaklines at Three Different Instants,  
 $\omega = 2500\text{ rpm}$ ,  $\bar{h} = 1/3$ .

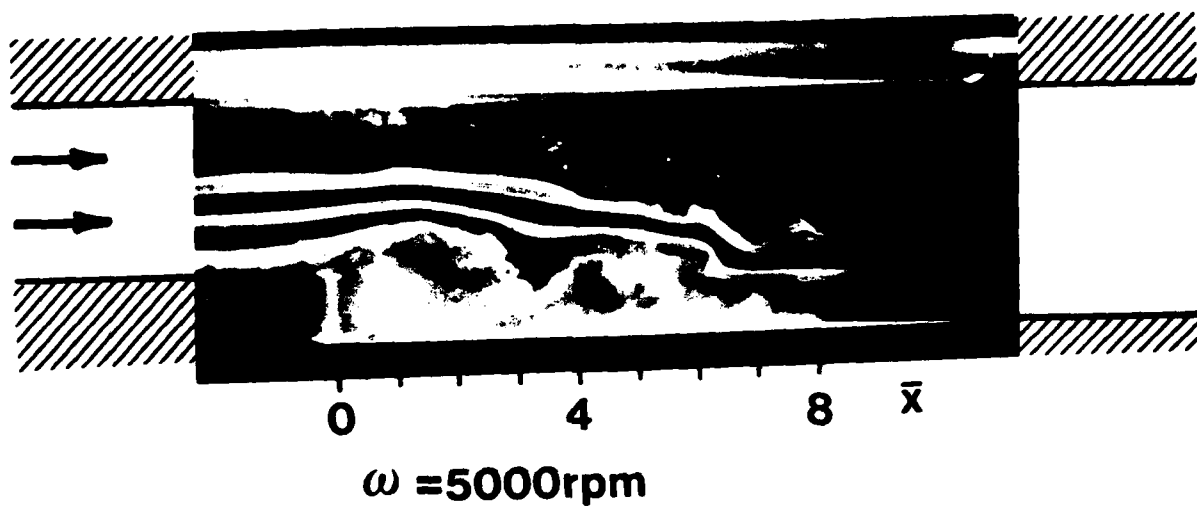


Figure 77. Streaklines for  $\omega = 5000 \text{ rpm}$ ,  $h = 1/3$ .

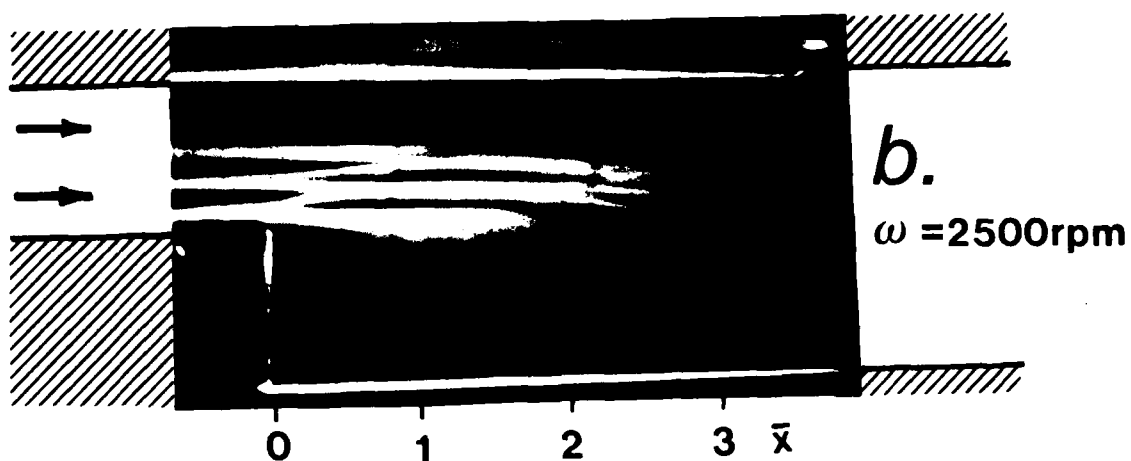
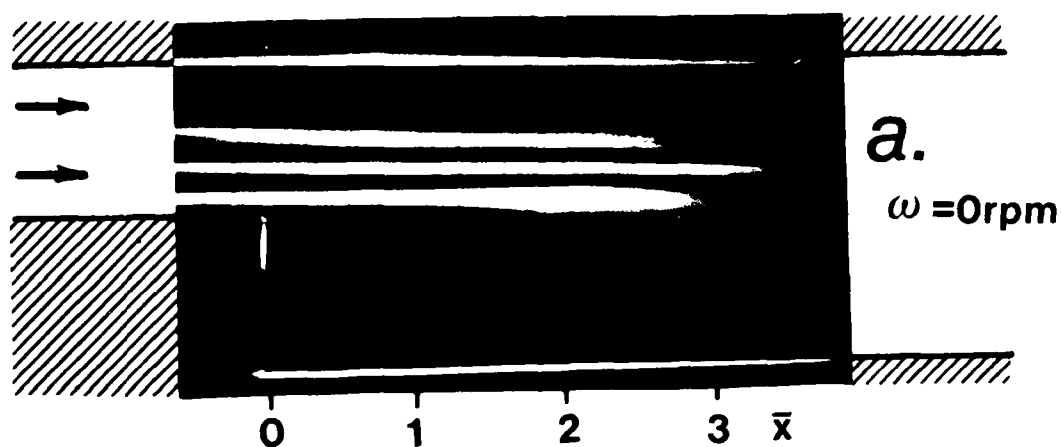


Figure 78. Streamline Shapes for Various Rotor Speeds,  
 $\bar{h} = 1.$

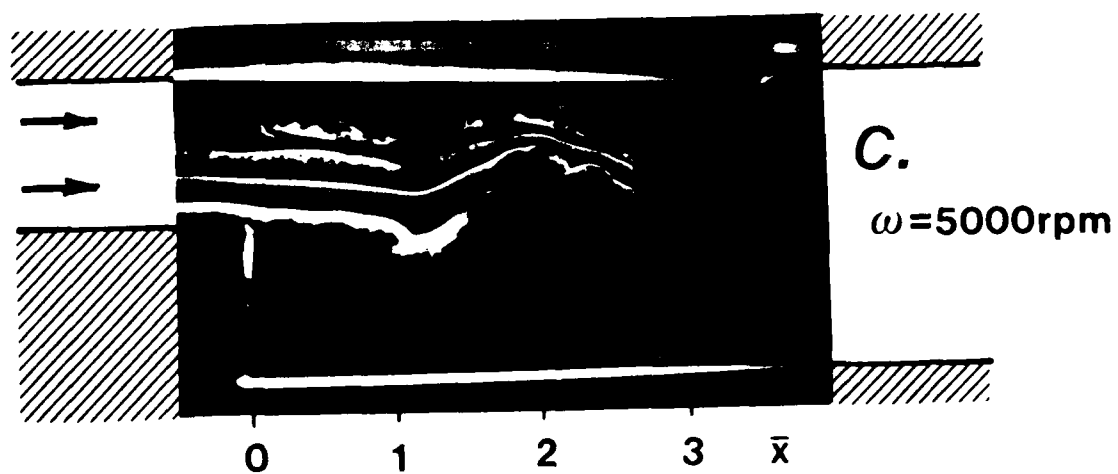
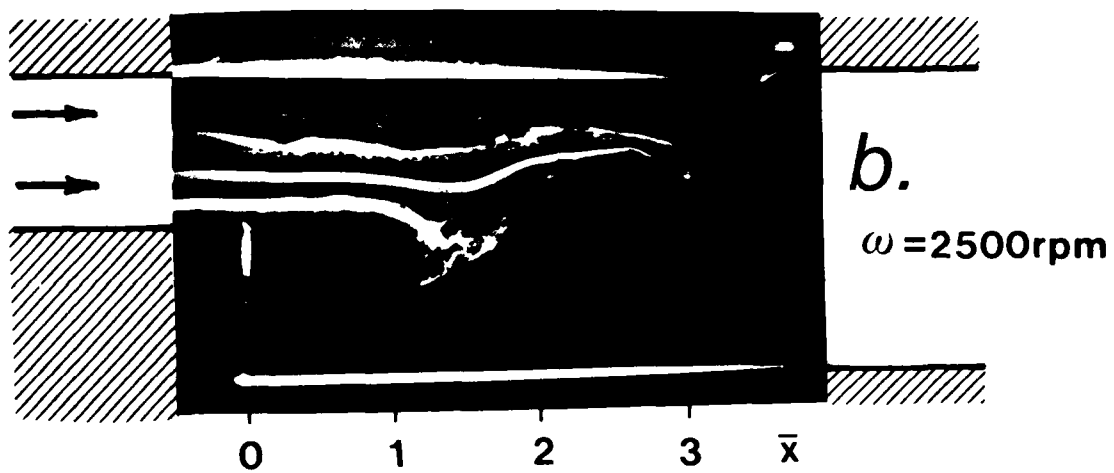
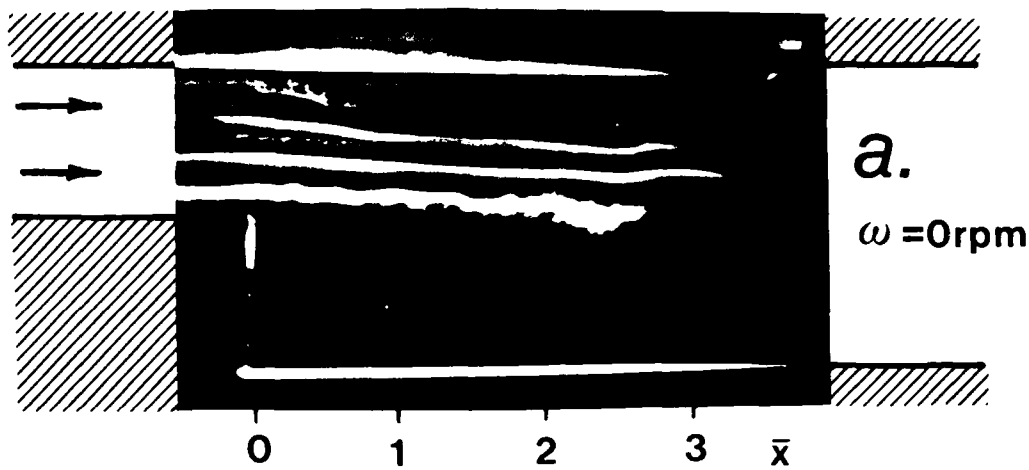


Figure 79. Streaklines for Various Rotor Speeds,  $\bar{h} = 1$ .

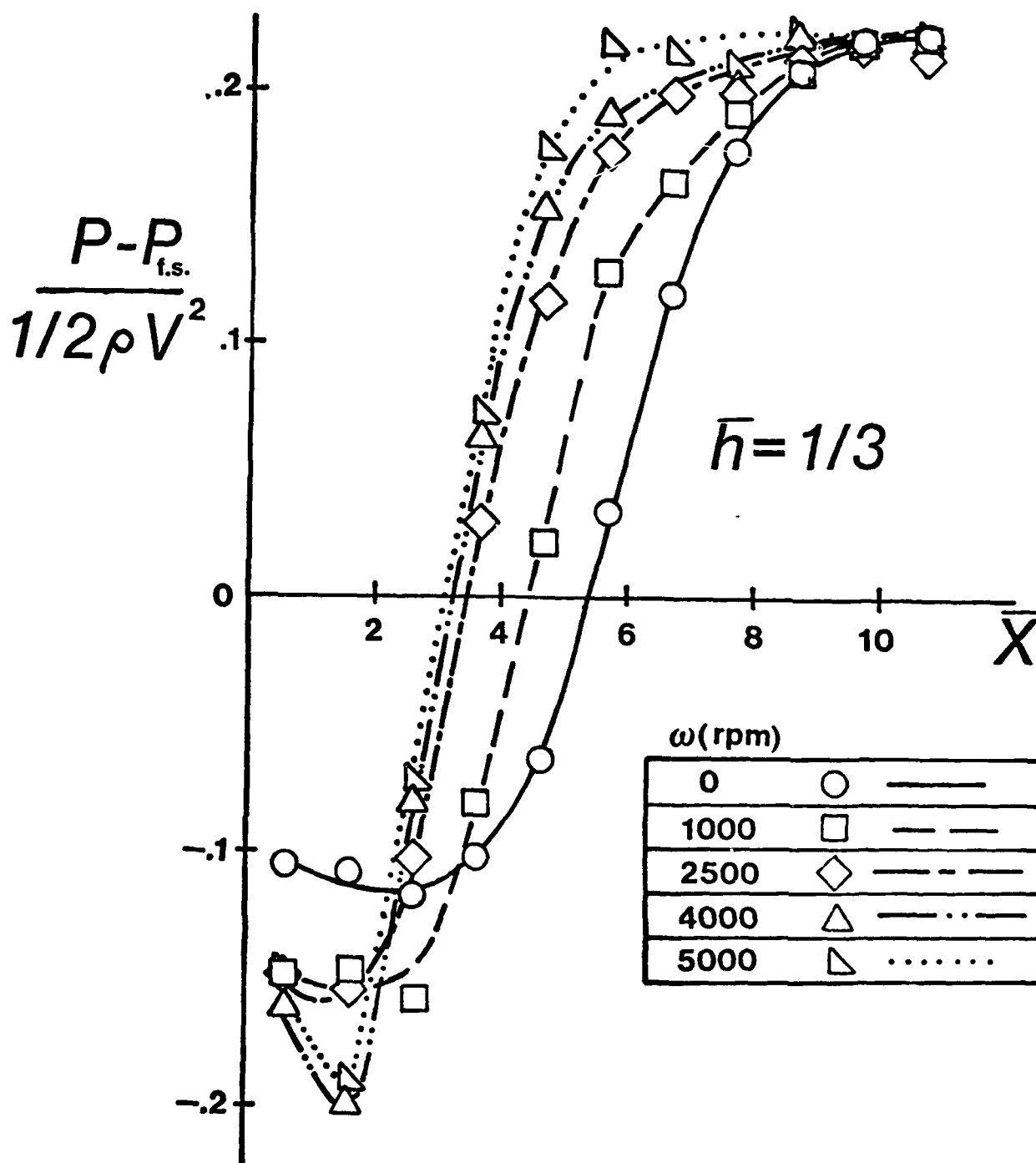


Figure 80. Pressure Distribution Downstream of the Dump Station;  $\bar{h} = 1/3$ , Various Rotor Speeds.

AD-A110 291

WRIGHT STATE UNIV DAYTON OHIO  
PROBLEMS IN FORCED UNSTEADY FLUID MECHANICS.(U)  
NOV 81 M VIETS, M PIATT, M BALL, R J BETHKE

F/G 20/4

AFOSR-78-3525

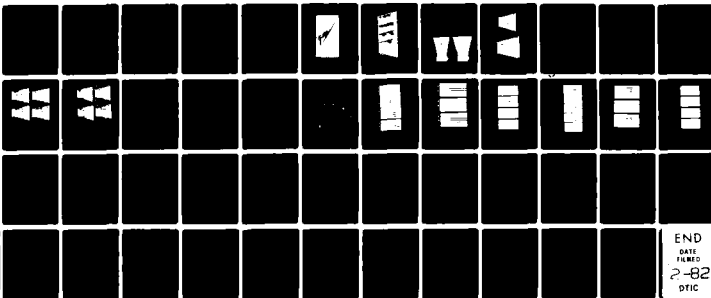
UNCLASSIFIED

AFWAL-TM-81-148-FIMM

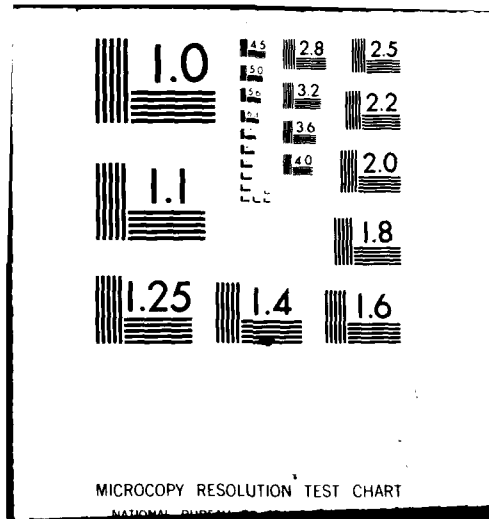
NL

3 x 3

10/2/81



END  
DATE  
FILMED  
2-82  
DTIC



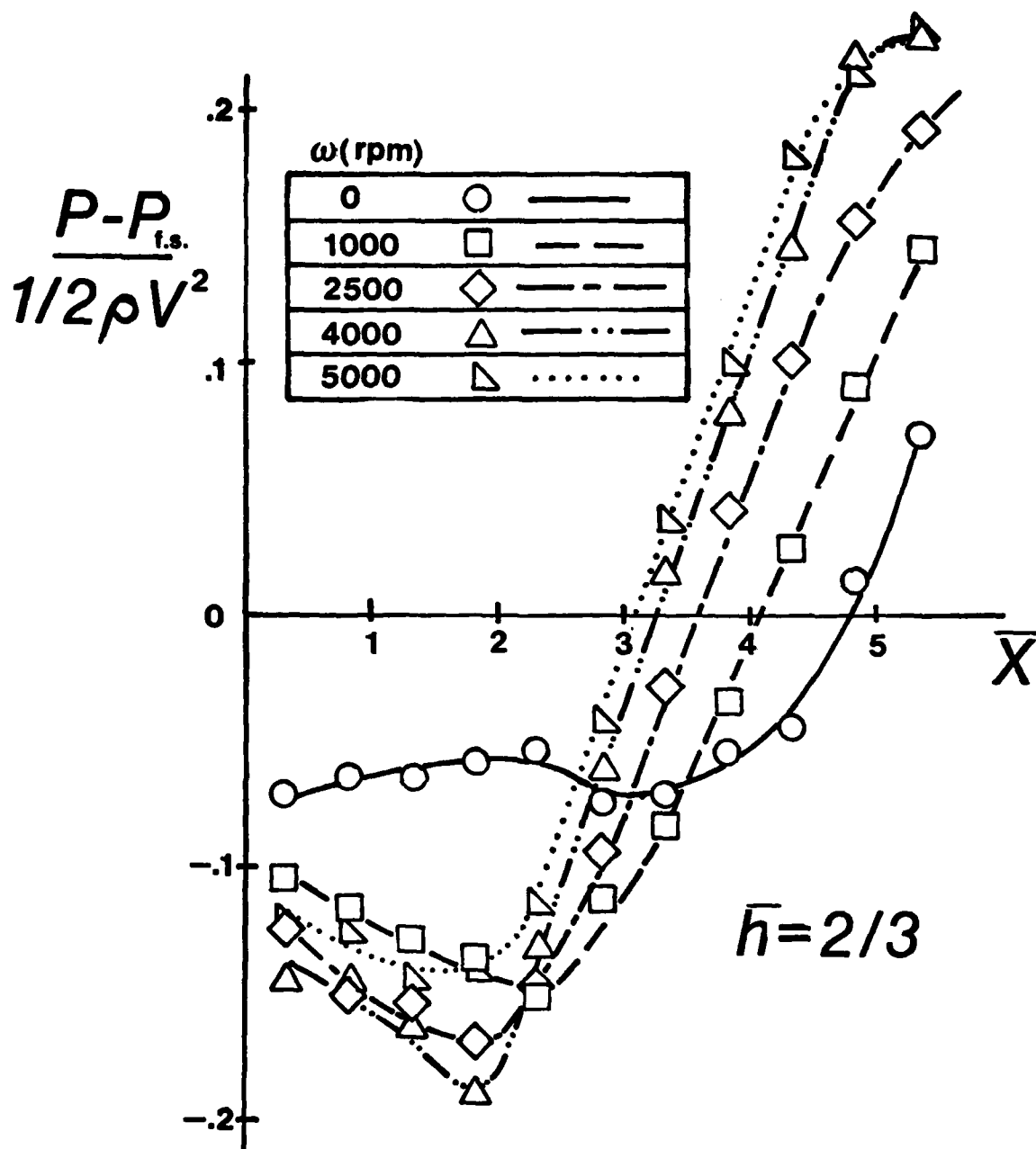


Figure 81. Pressure Distributions Downstream of the Dump Station;  $\bar{h} = 2/3$ , Various Rotor Speeds.

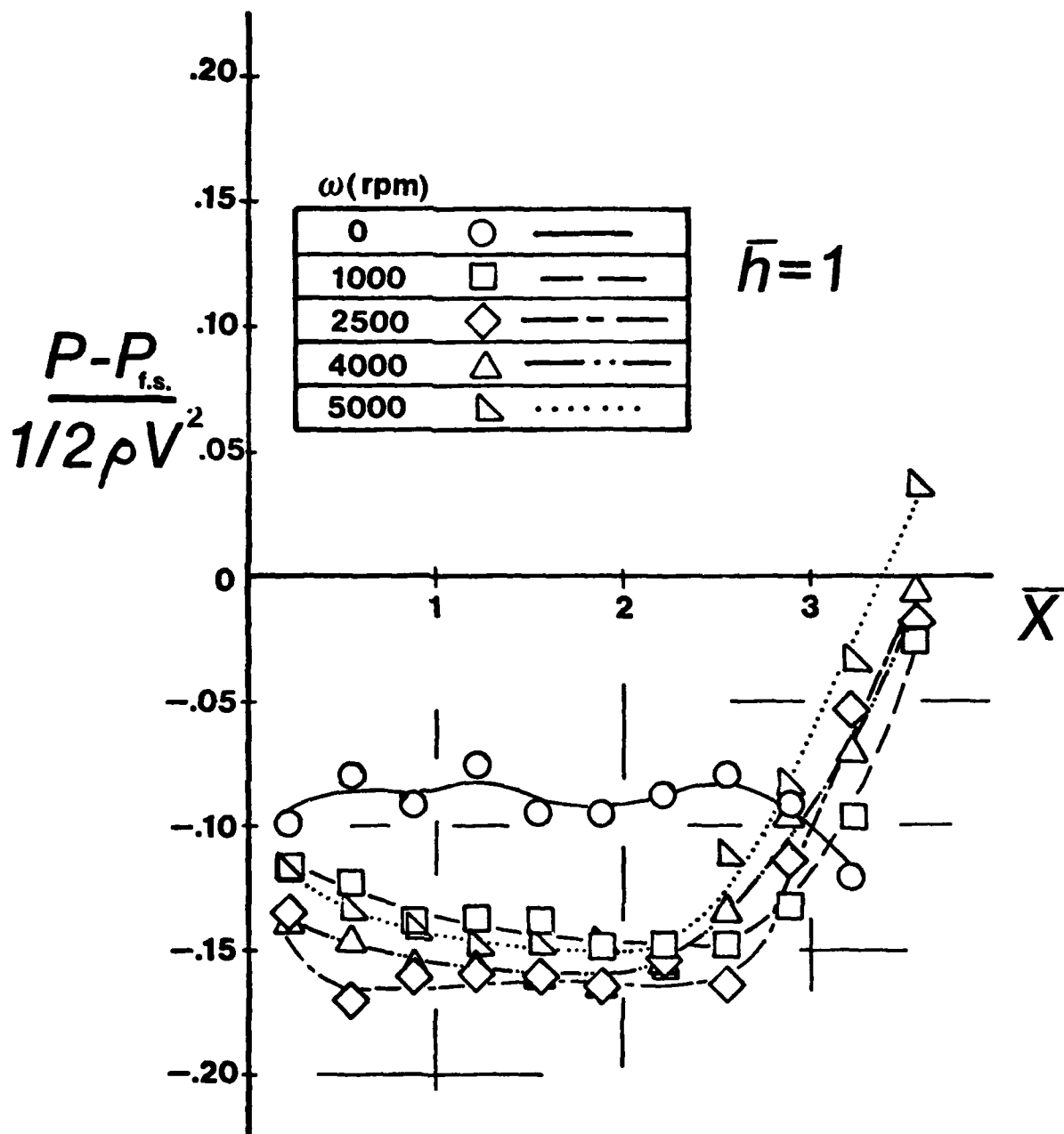


Figure 82. Pressure Distributions Downstream of the Dump Station;  $\bar{h} = 1$ , Various Rotor Speeds.

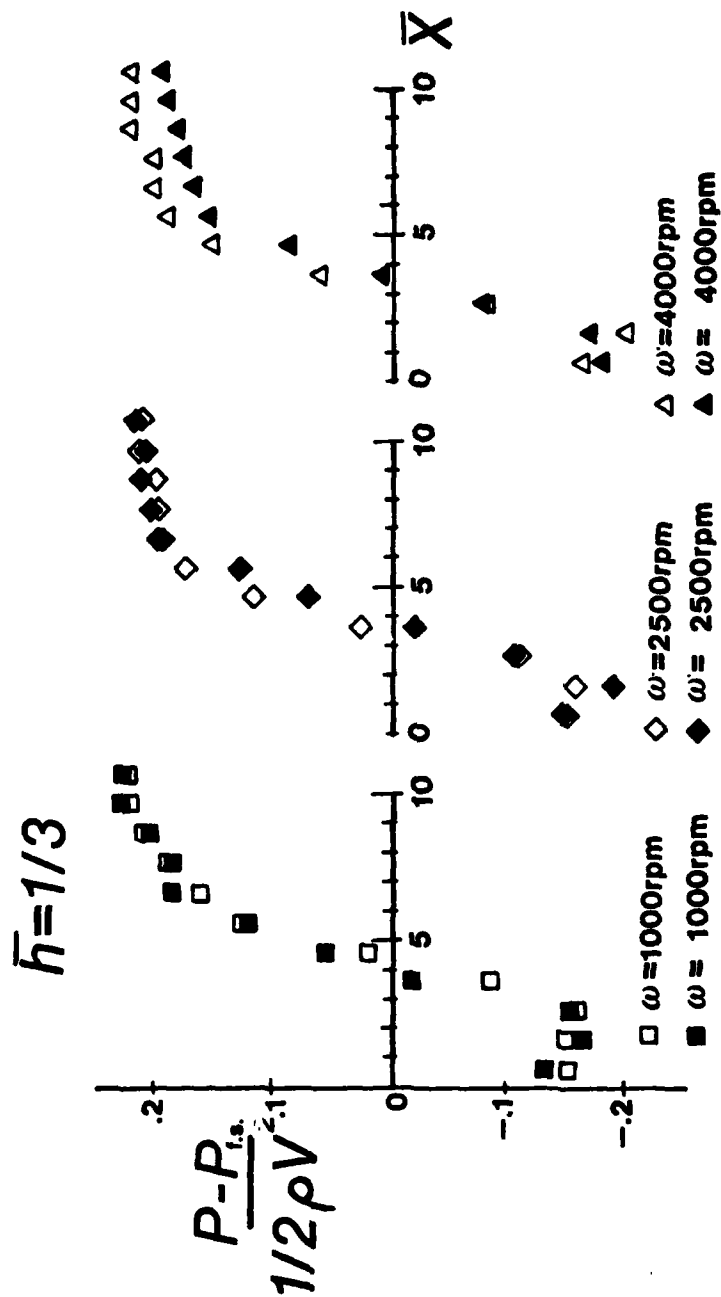


Figure 83. Effect of Rotation Direction on Pressure Distributions.

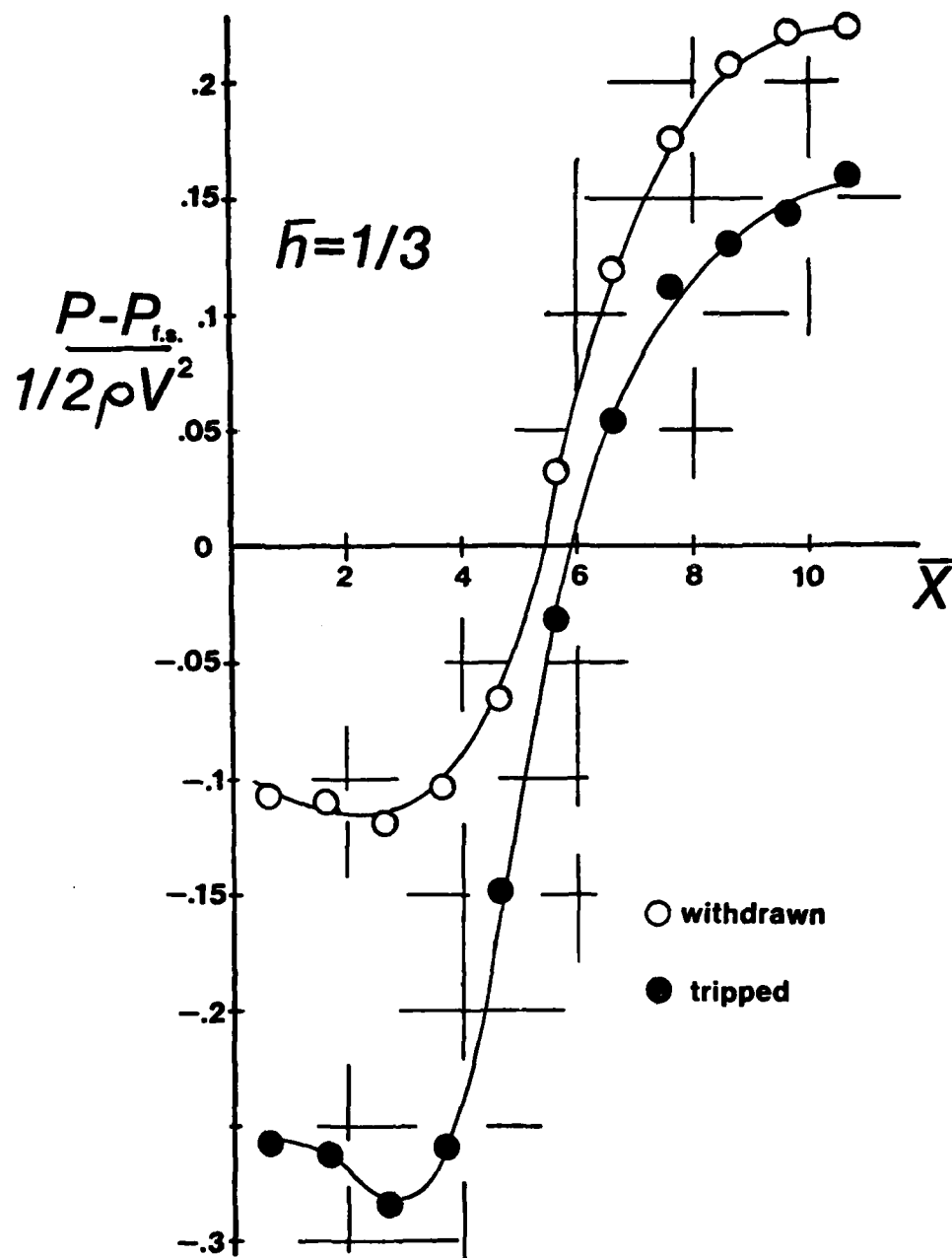
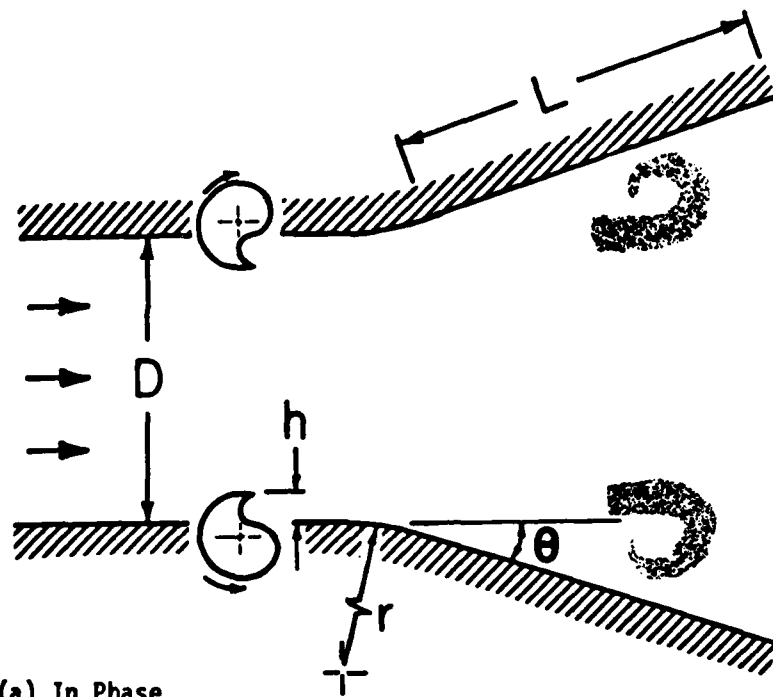
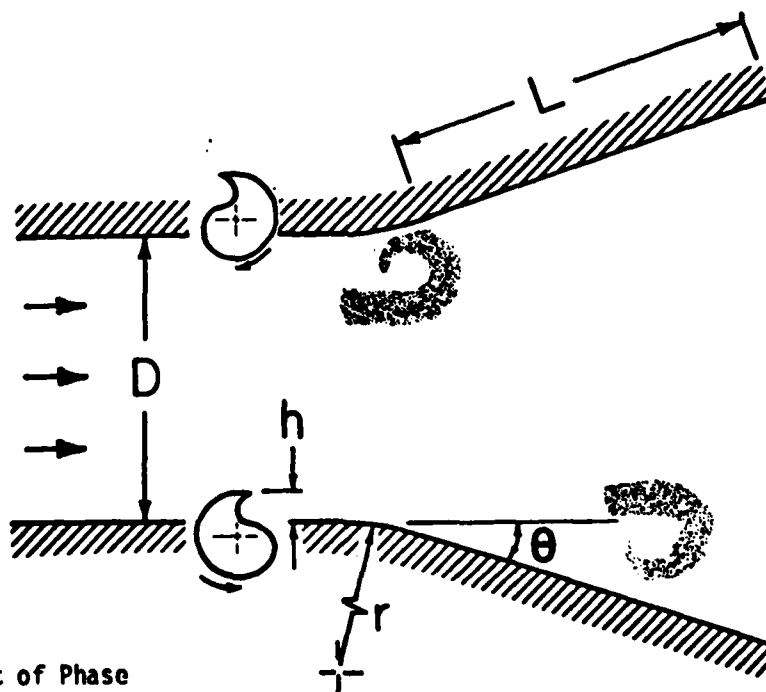


Figure 84. Effect of Rotor Geometry as a Passive Trip.



(a) In Phase



(b) Out of Phase

Figure 85. In phase and out of phase rotor orientations.



Figure 86. Vortex produced near the corner of the diffuser.

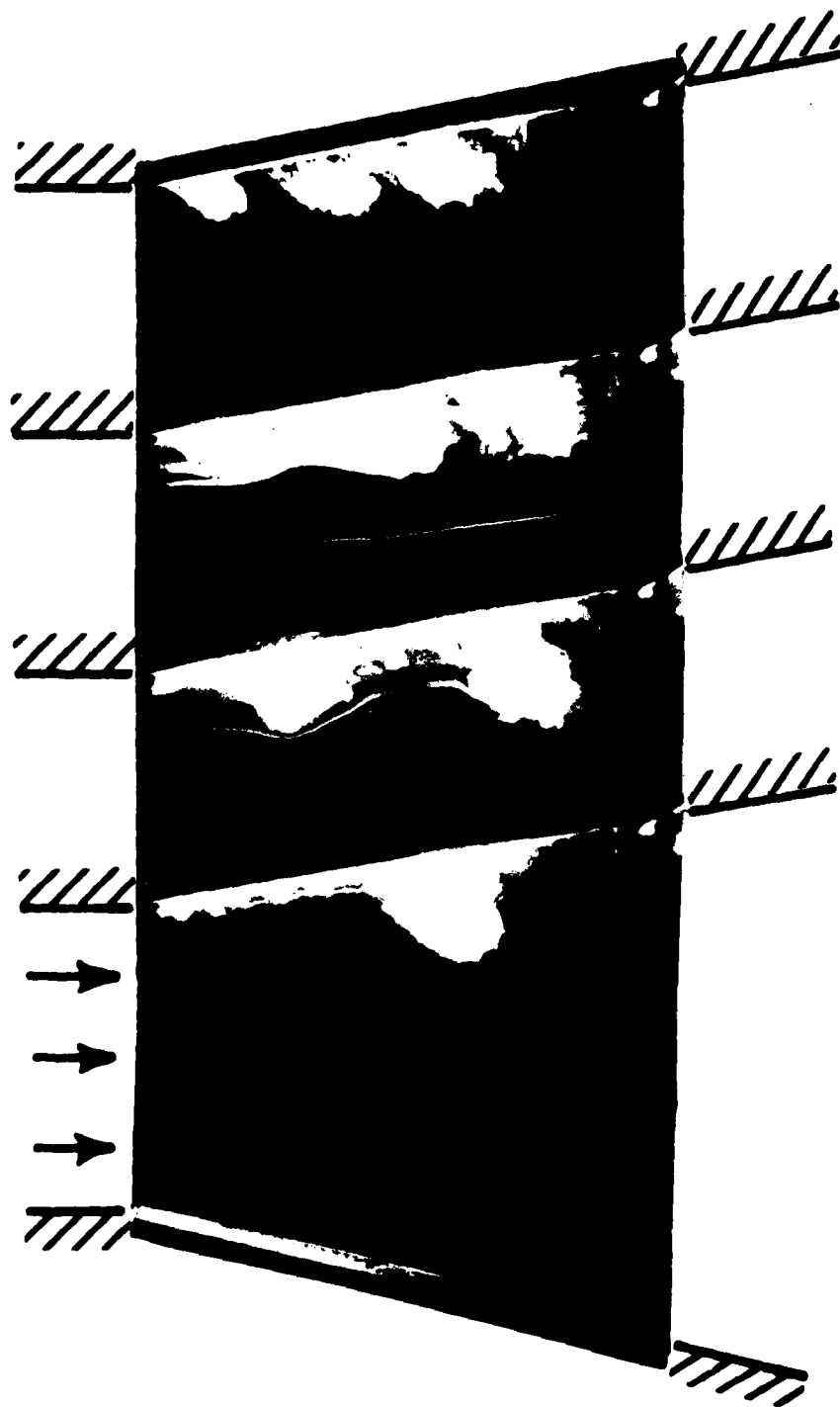


Figure 87. Multiple vortices produced in the diffuser by increasing the speed of the rotor.

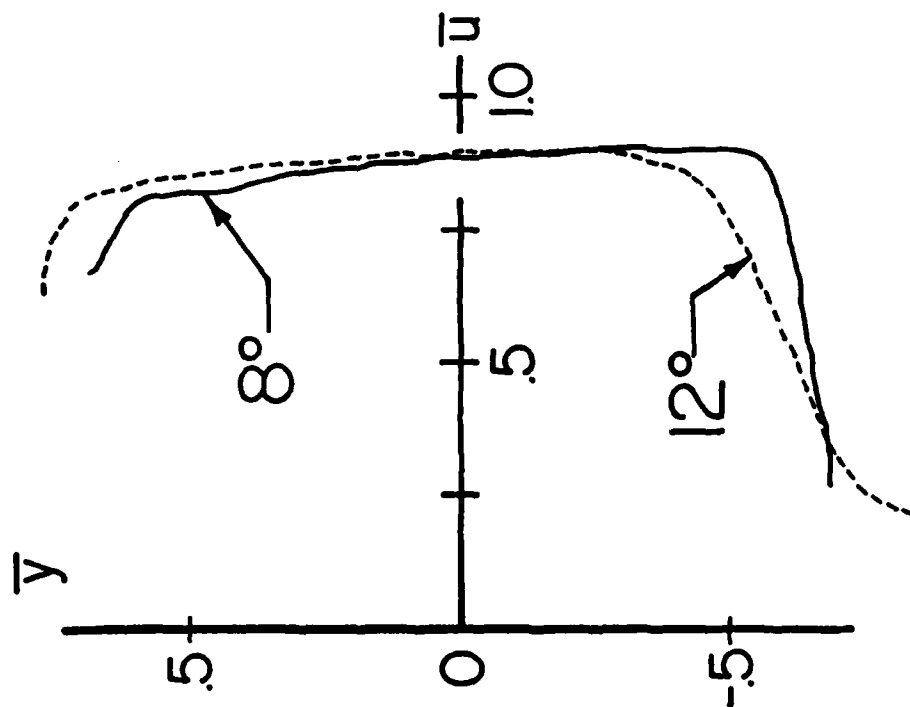
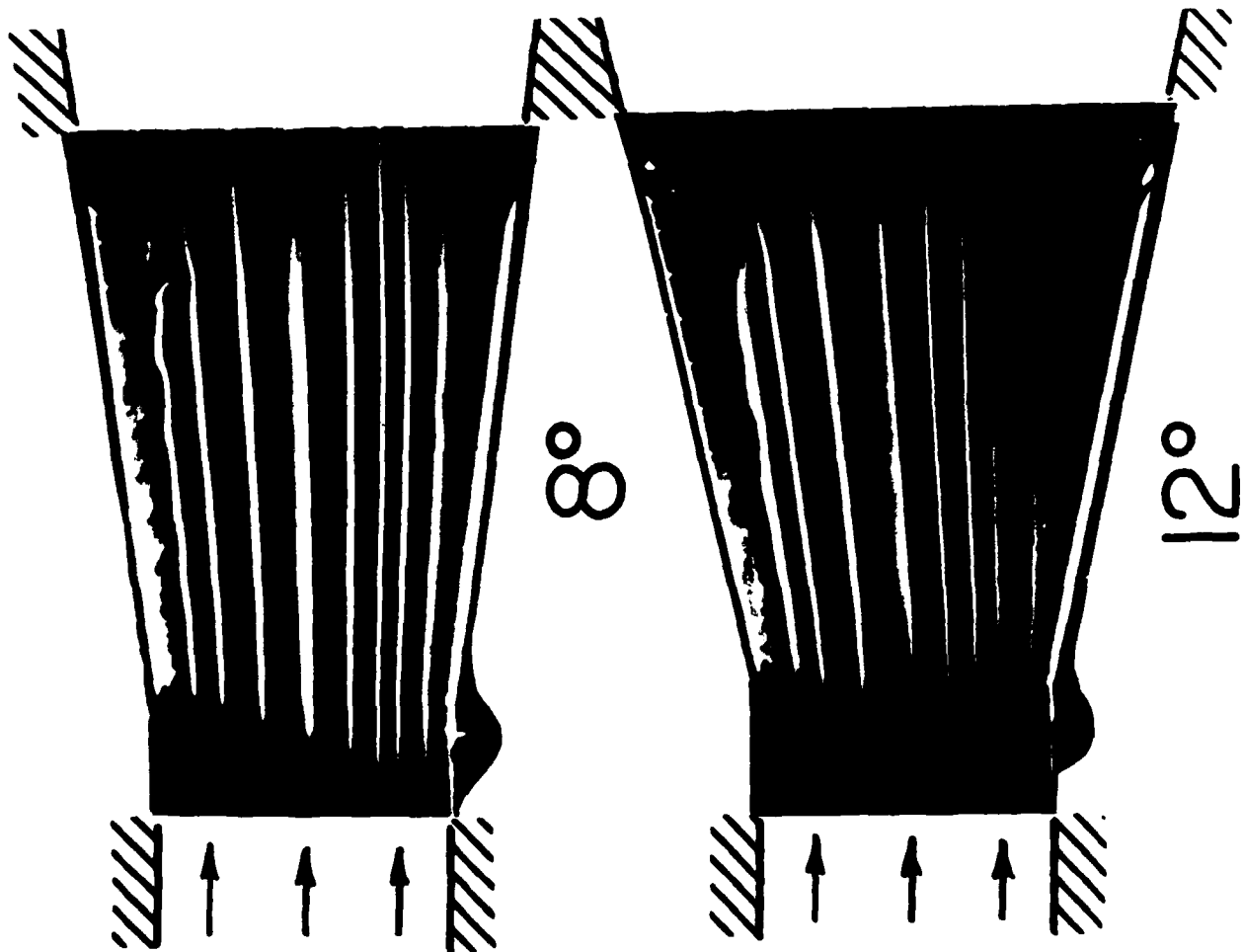


Figure 88.

Streaklines produced for  $\theta = 8^\circ$  and  $12^\circ$  showing separation at  $12^\circ$  and time averaged velocity profiles taken at the diffuser exit verify the separation.

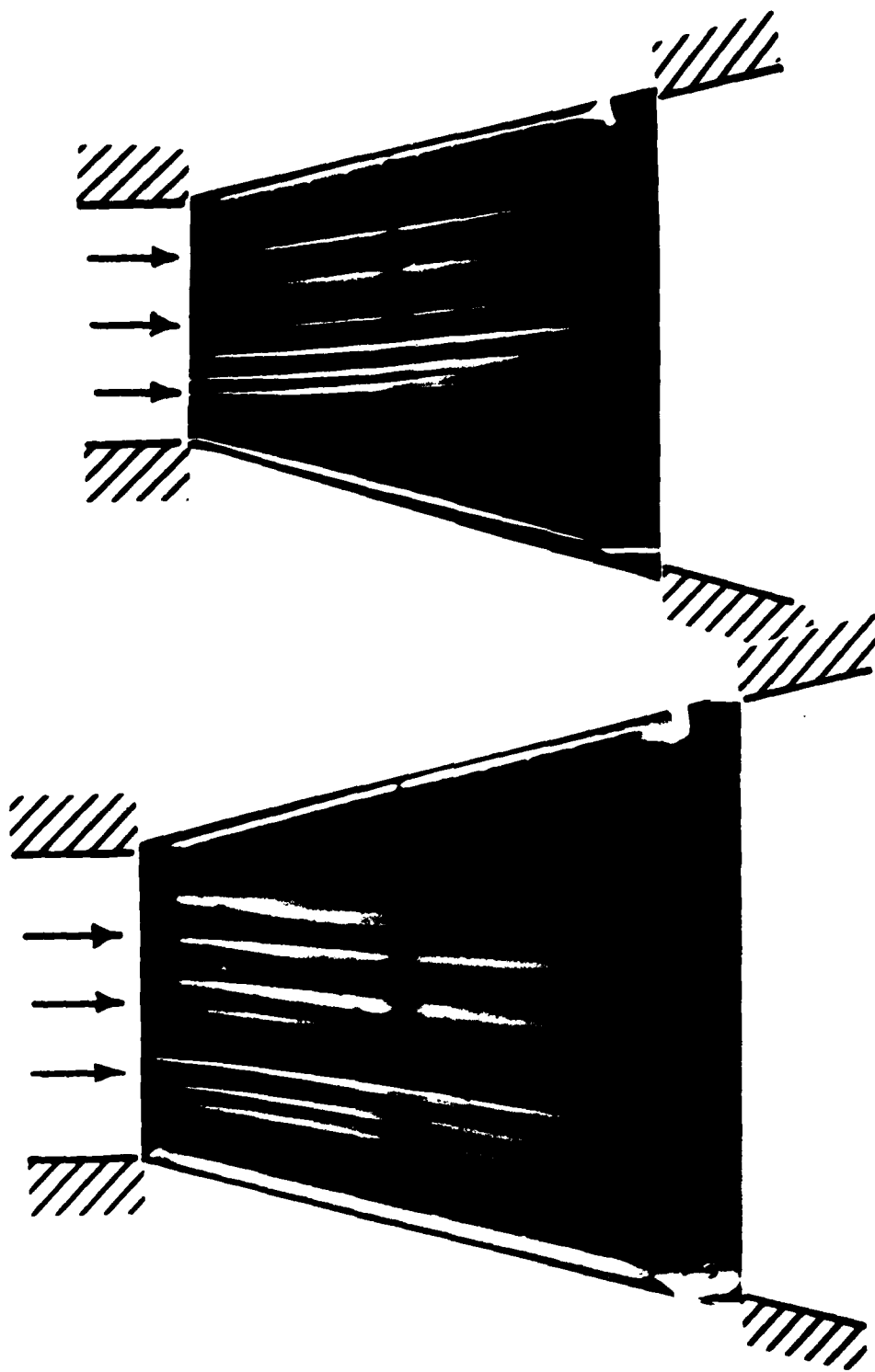


Figure 89. Longer exposure streamline photographs for  $2\theta = 30^\circ$ . (a). Separation at the bottom for  $\omega = 0$  (b). Weaker separation at the top for  $\omega = 11.84$  (both in phase)

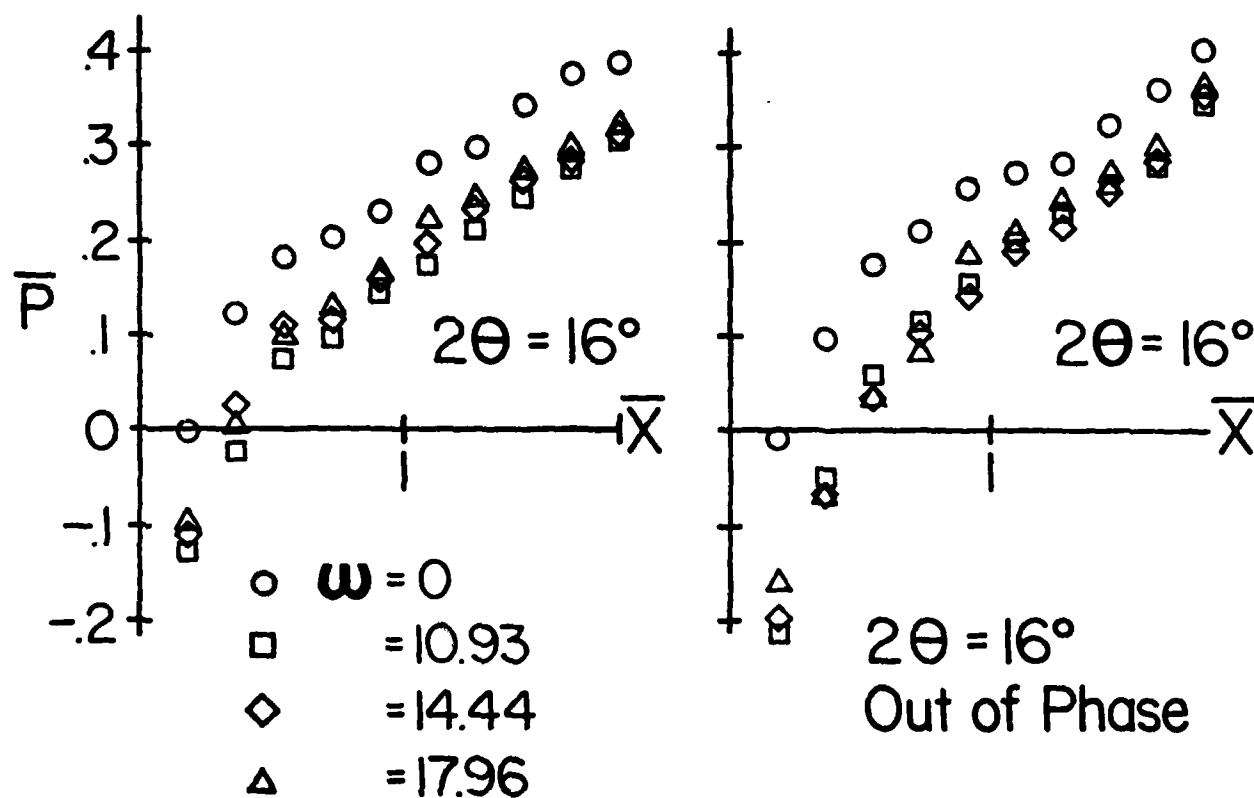


Figure 90. Pressure rise through the diffuser for  $2\theta=16$  and various rotor speeds, out of phase.

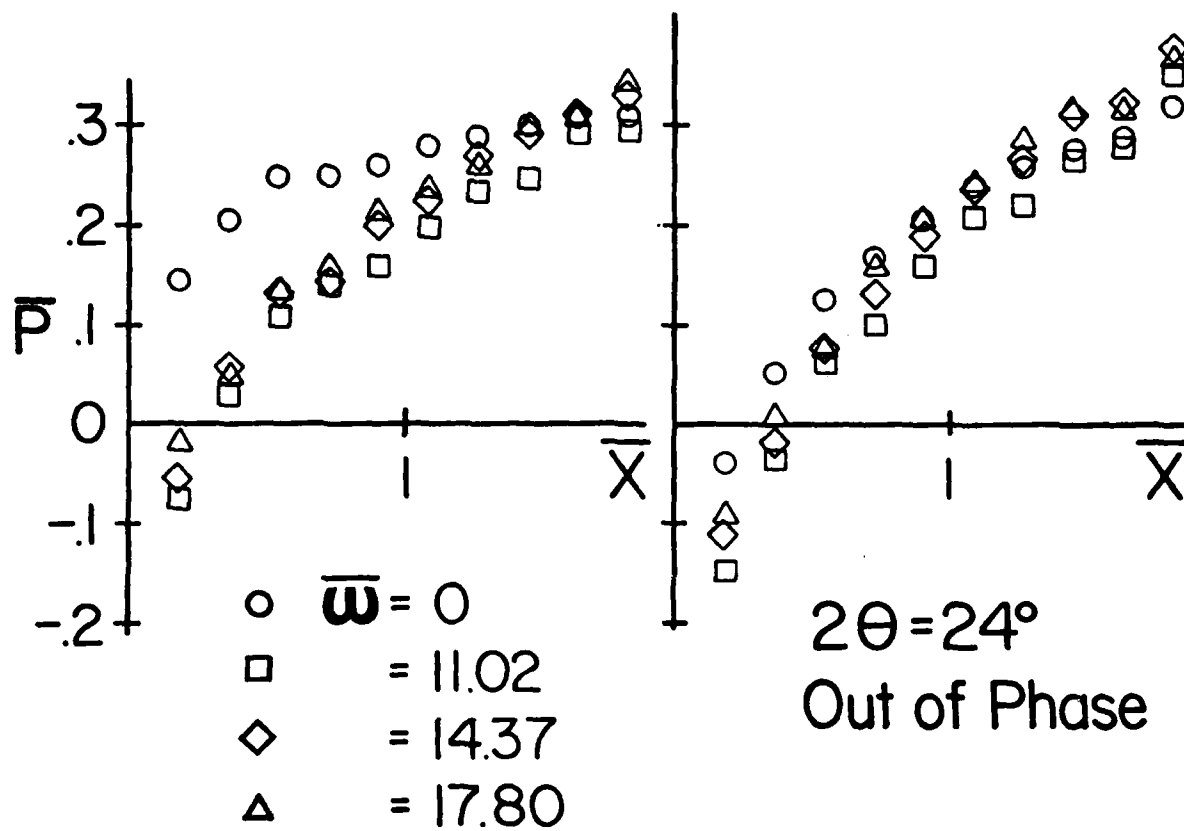


Figure 91. Pressure rise for larger angle diffuser,  $2\theta = 24^\circ$ , out of phase.

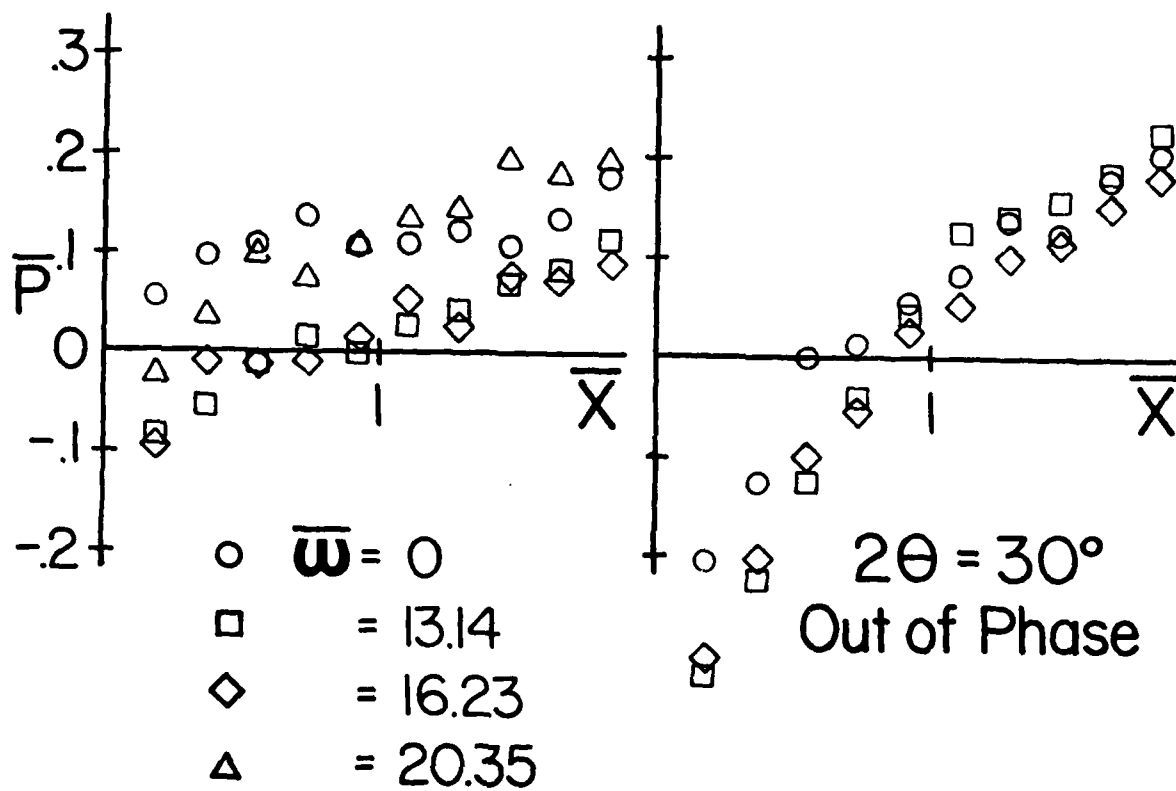


Figure 92. Pressure rise for  $2\theta = 30^\circ$ , out of phase.

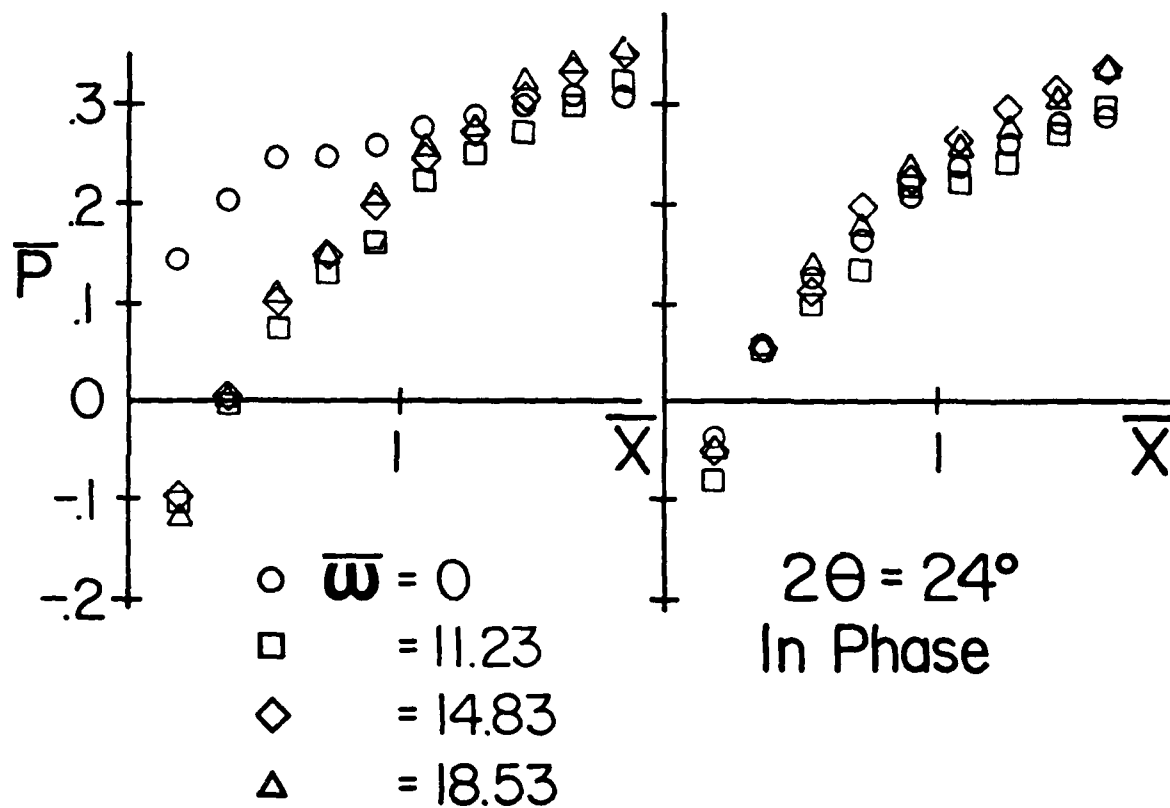


Figure 93. Diffuser performance for rotors set in phase and  $2\theta = 24^\circ$ , in phase rotors.

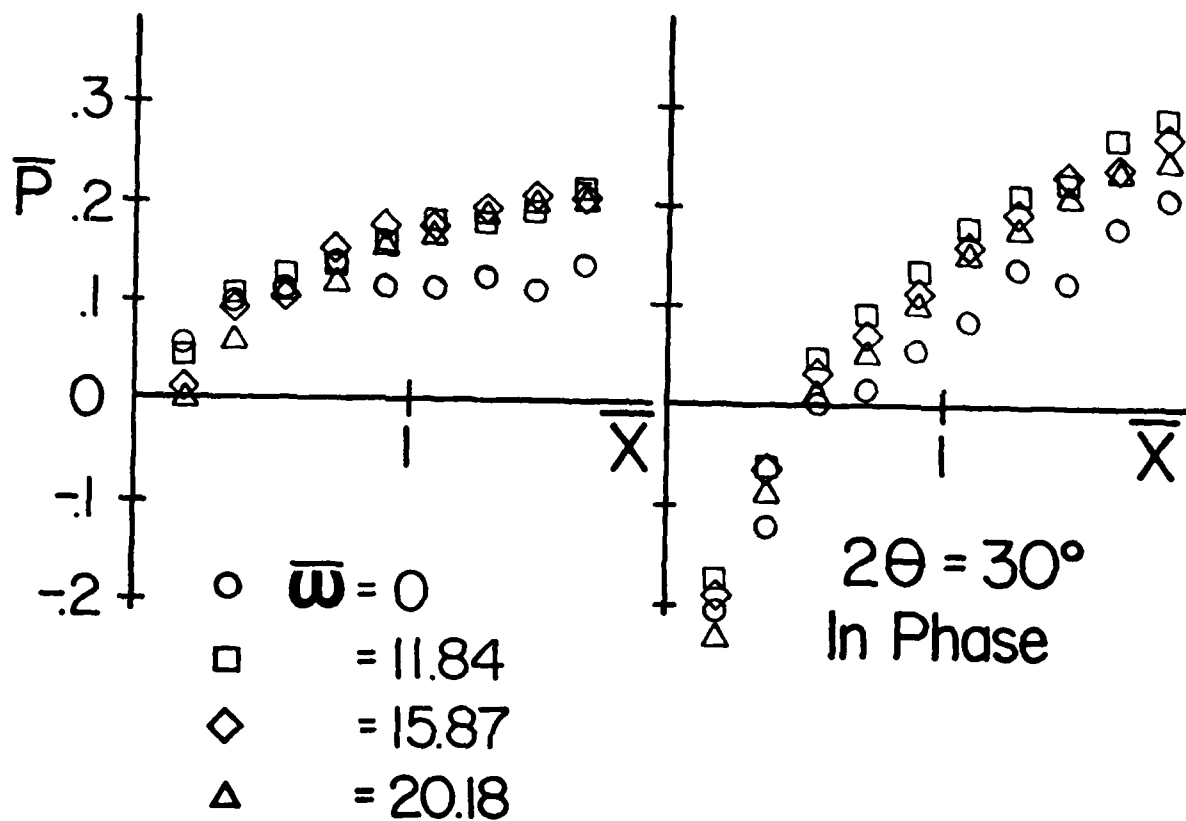
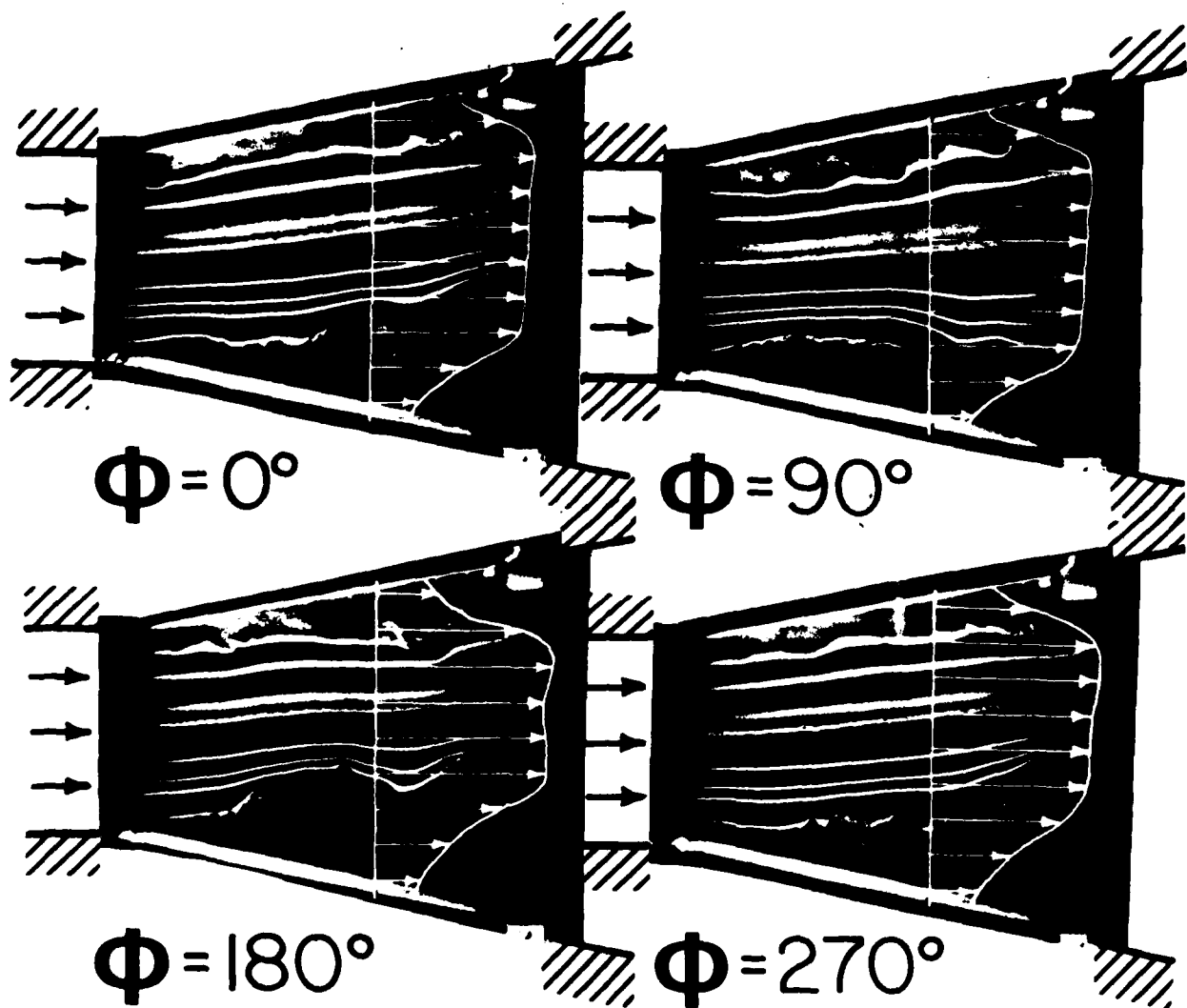


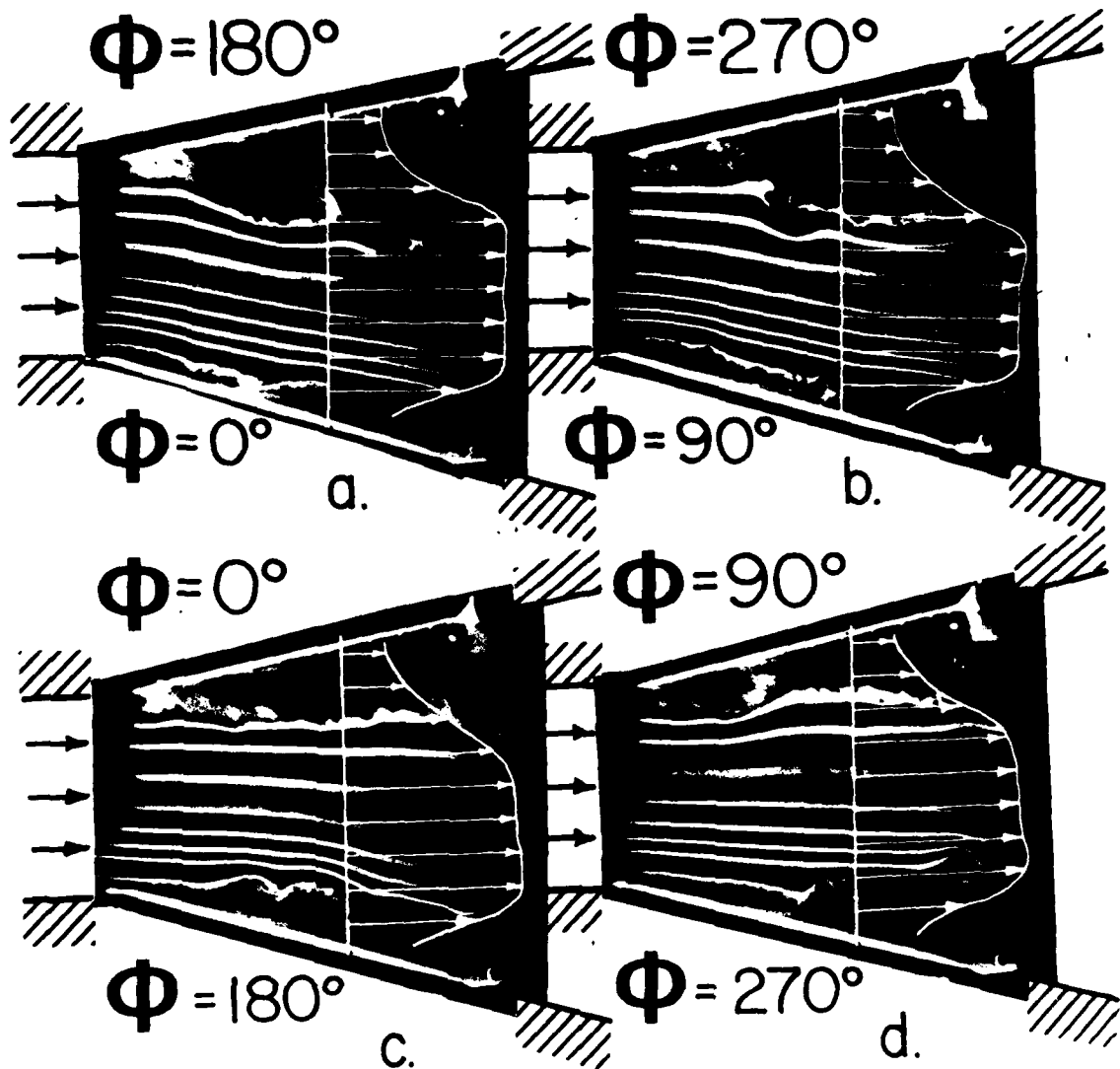
Figure 94. In phase pressure rise for  $2\theta = 30^\circ$ , and rotors in phase.



$$2\theta = 24^\circ ; \bar{\omega} = 11.23$$

In Phase

Figure 95. Streakline photographs of the diffuser flow at different phase positions with superimposed instantaneous velocity profiles.



$$2\theta = 30^\circ; \bar{\omega} = 13.14$$

Out of Phase

Figure 96. Streakline photographs for a larger diffuser angle and for the out of phase rotor orientation.

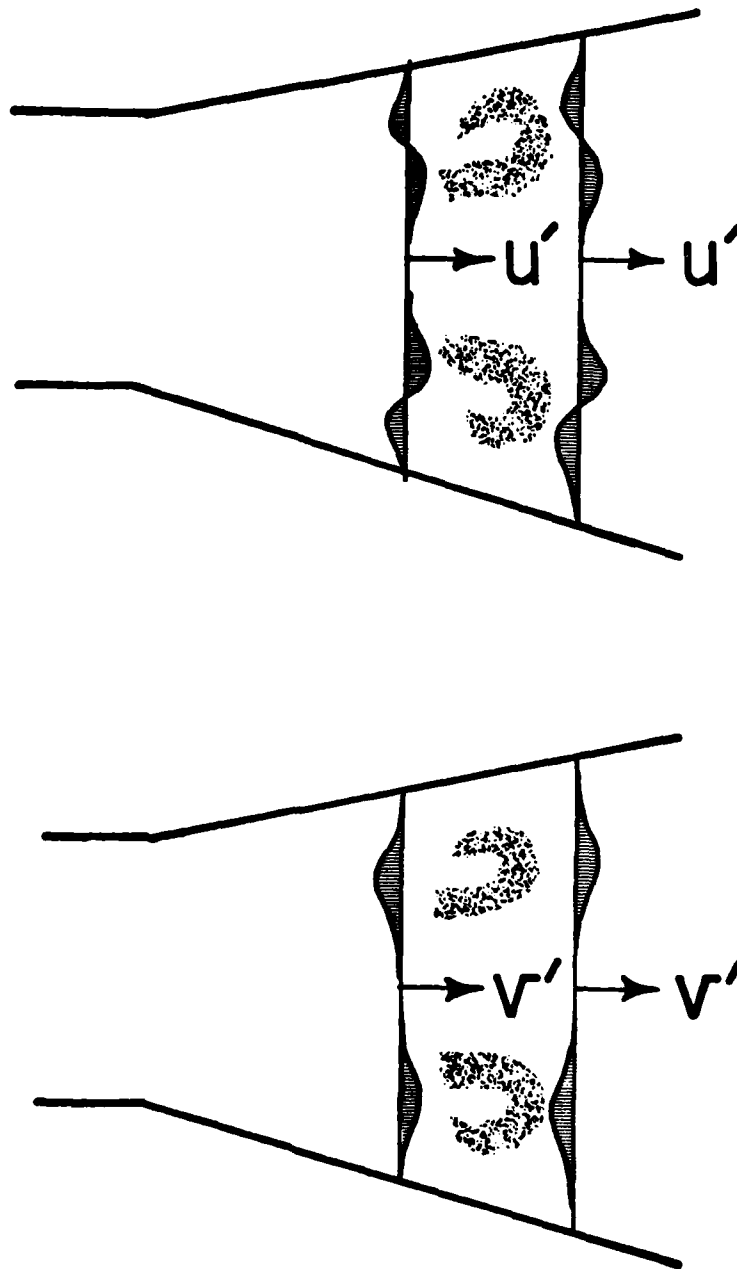


Figure 97. The presence of a counter-clockwise vortex near the upper wall or a clockwise vortex near the lower wall leads to instantaneous velocity changes in the streamwise ( $u'$ ) and transverse ( $v'$ ) directions.

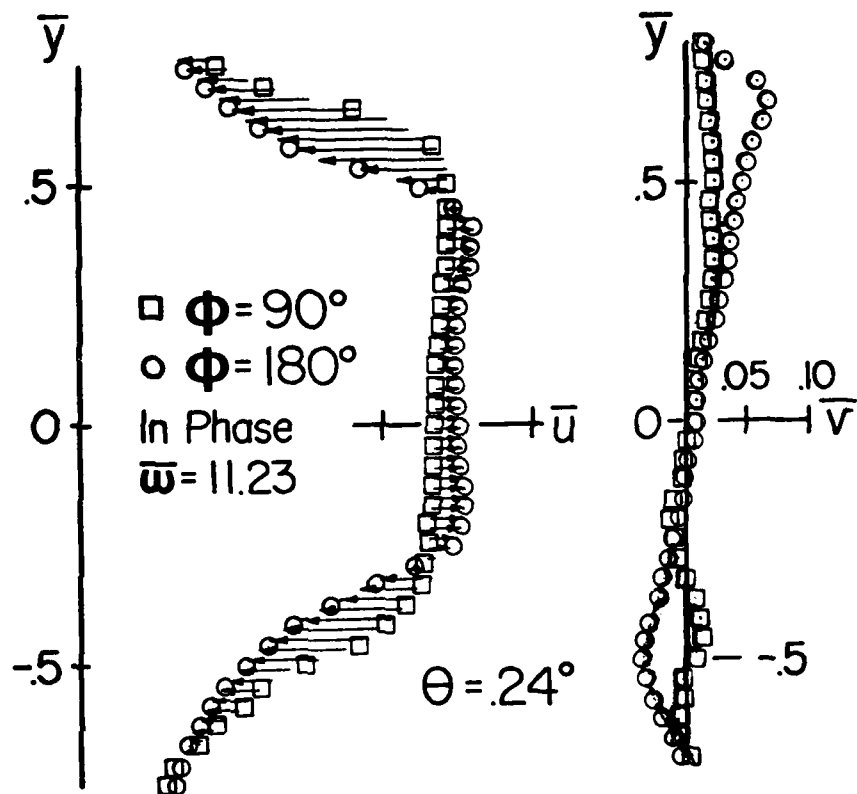


Figure 98. Velocity difference between the presence of a vortex pair ( $\phi = 180^\circ$ ) and no vortex ( $\phi = 90^\circ$ ).

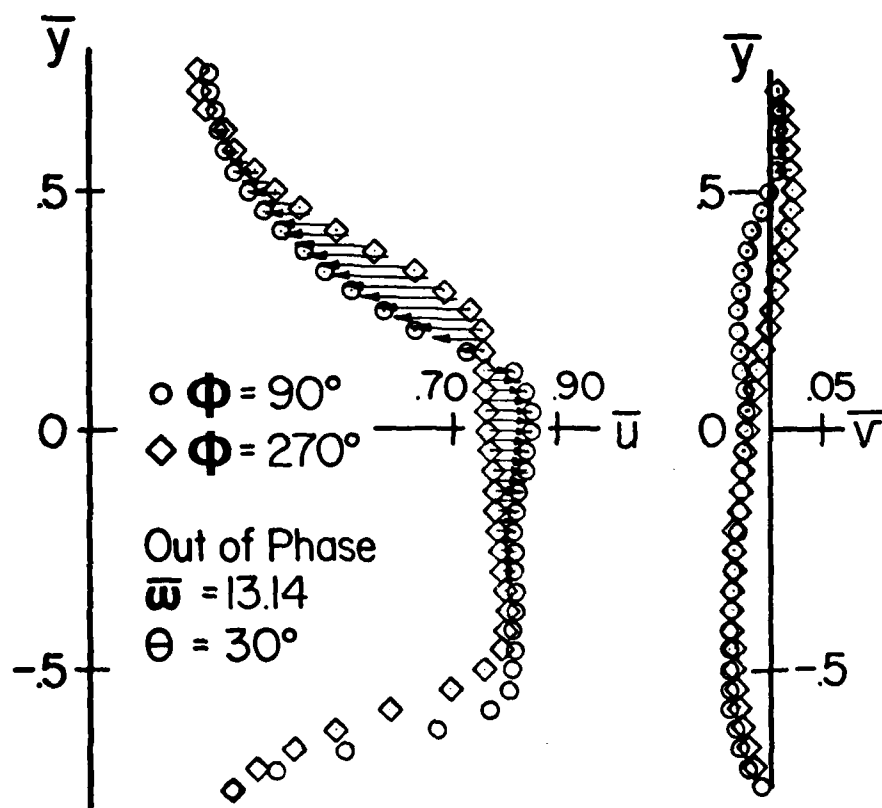


Figure 99. The velocity changes due to the presence of a single vortex in the out of phase condition. The profiles are those in Figure 96 (b) and (d).

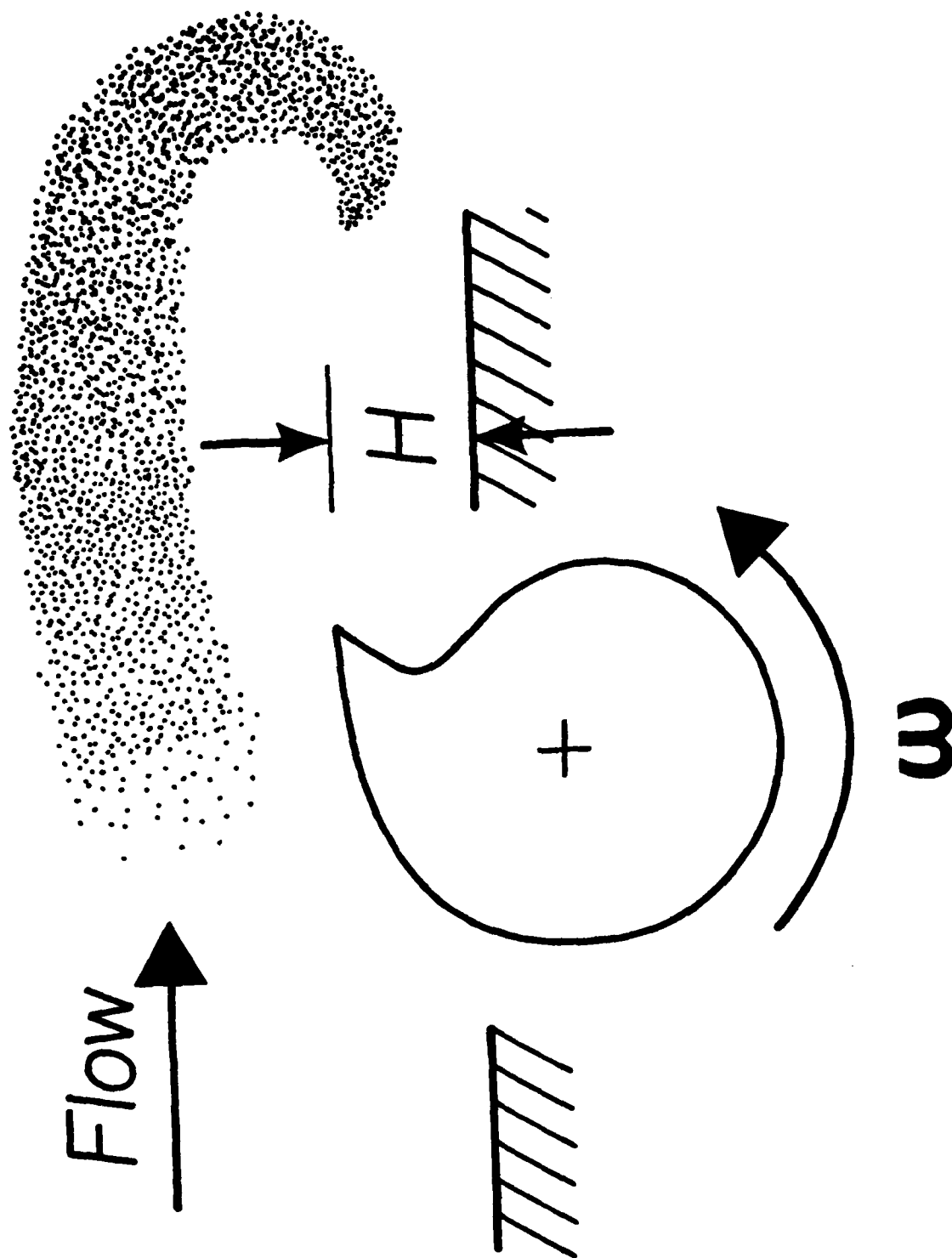
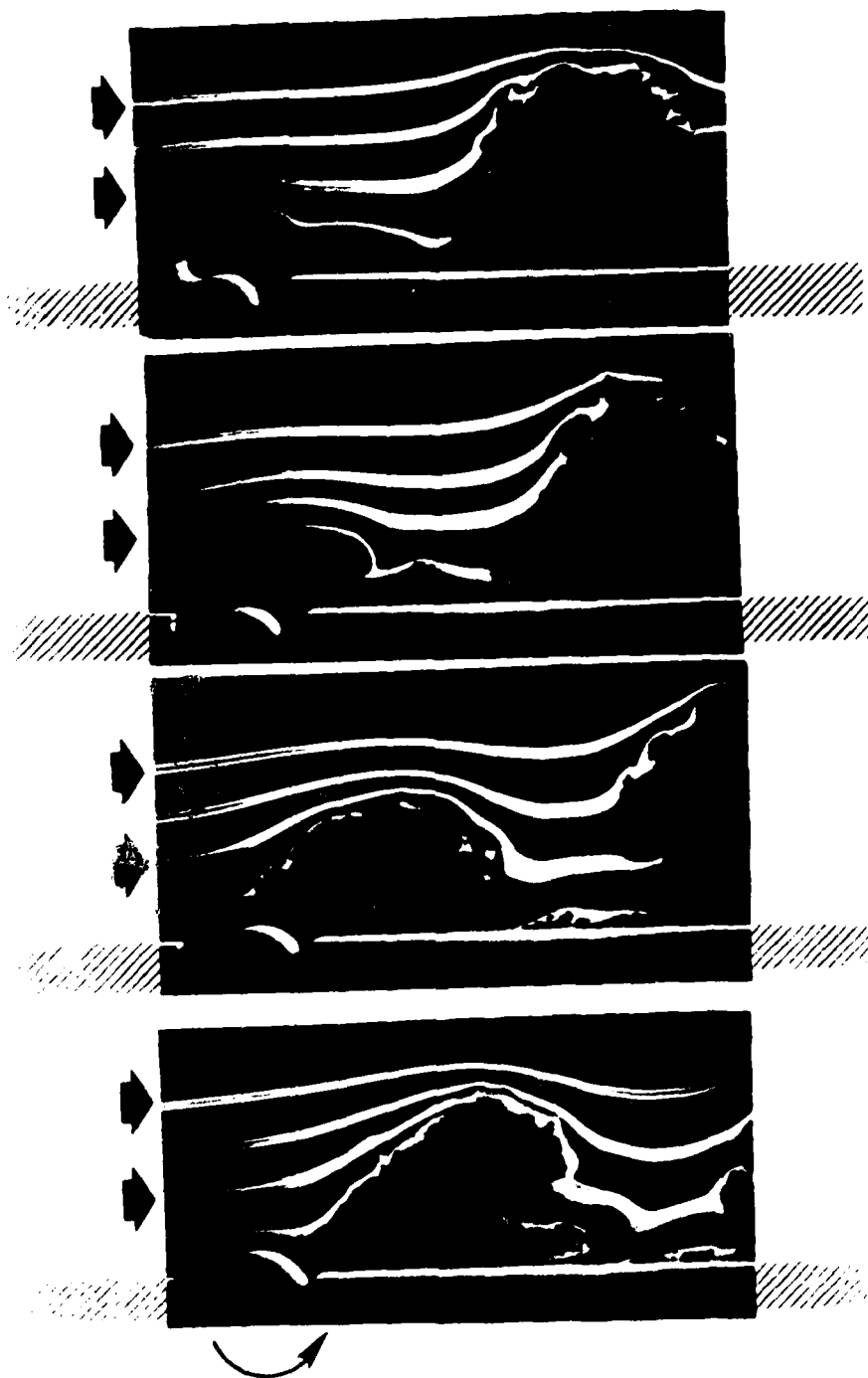
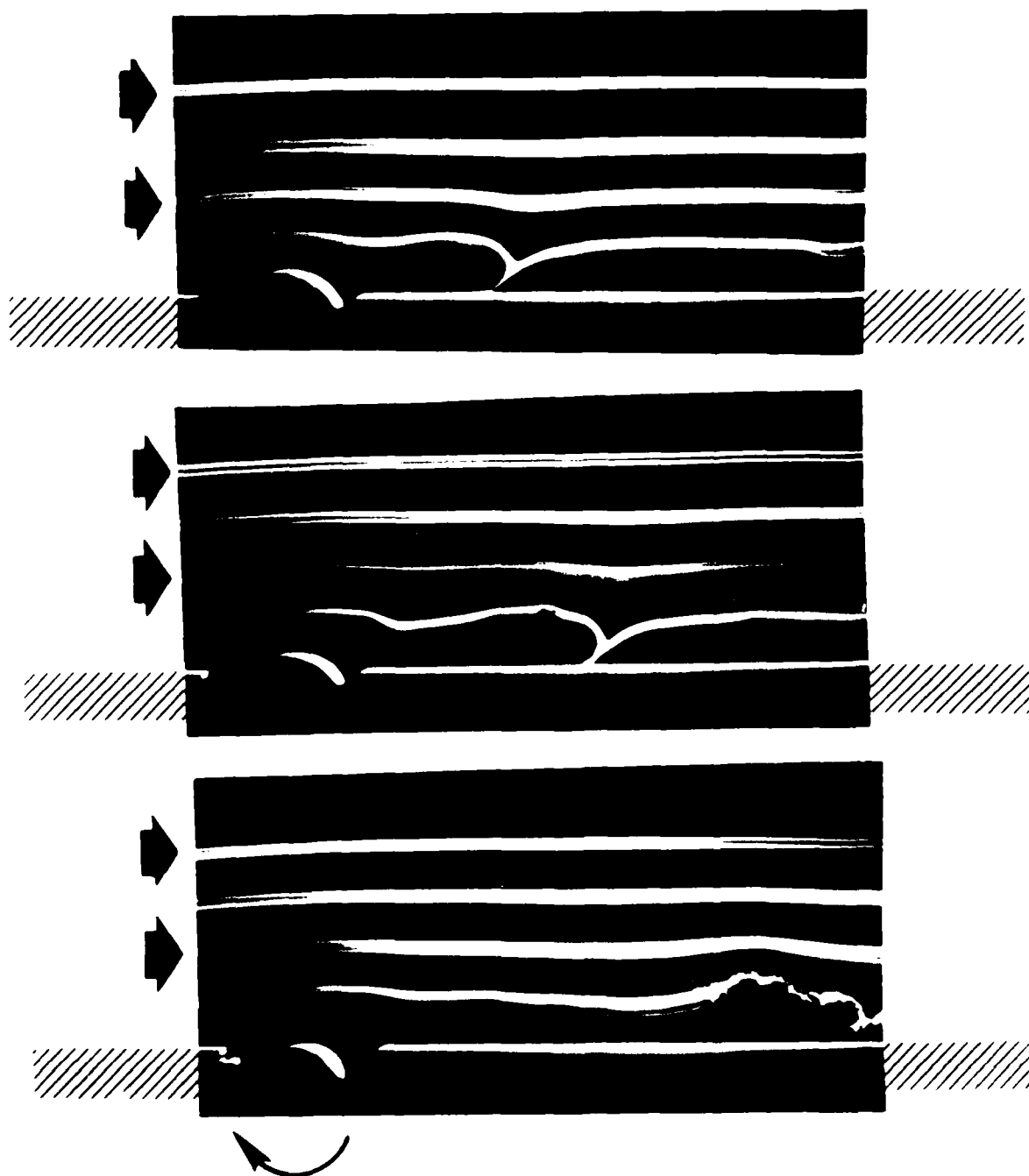


Figure 100. Schematic of the vortex flow generated by a cam shaped rotor.



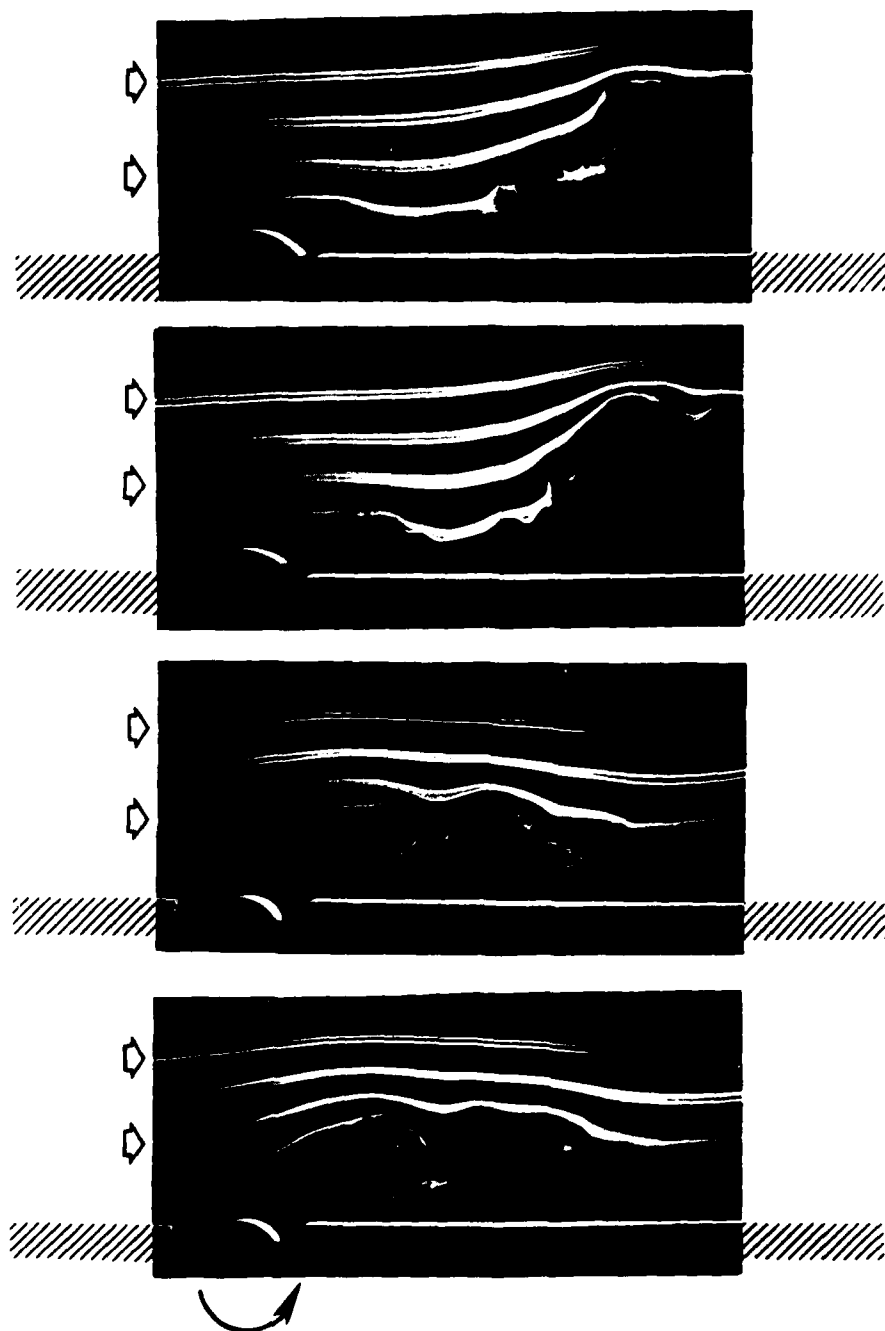
$\omega = + 3000 \text{ rpm}$

Figure 101. Flow visualization of vortex structure produced by the vortex generator with  $\omega = 3000 \text{ rpm}$ .



$$\omega = -3000 \text{ rpm}$$

Figure 102. Flow visualization of vortex structure produced by the vortex generator with  $\omega = -3000$  rpm.



$$\omega = + 2000 \text{ rpm}$$

Figure 103. Flow visualization of vortex structure produced by the vortex generator with  $\omega = 2000 \text{ rpm}$ .

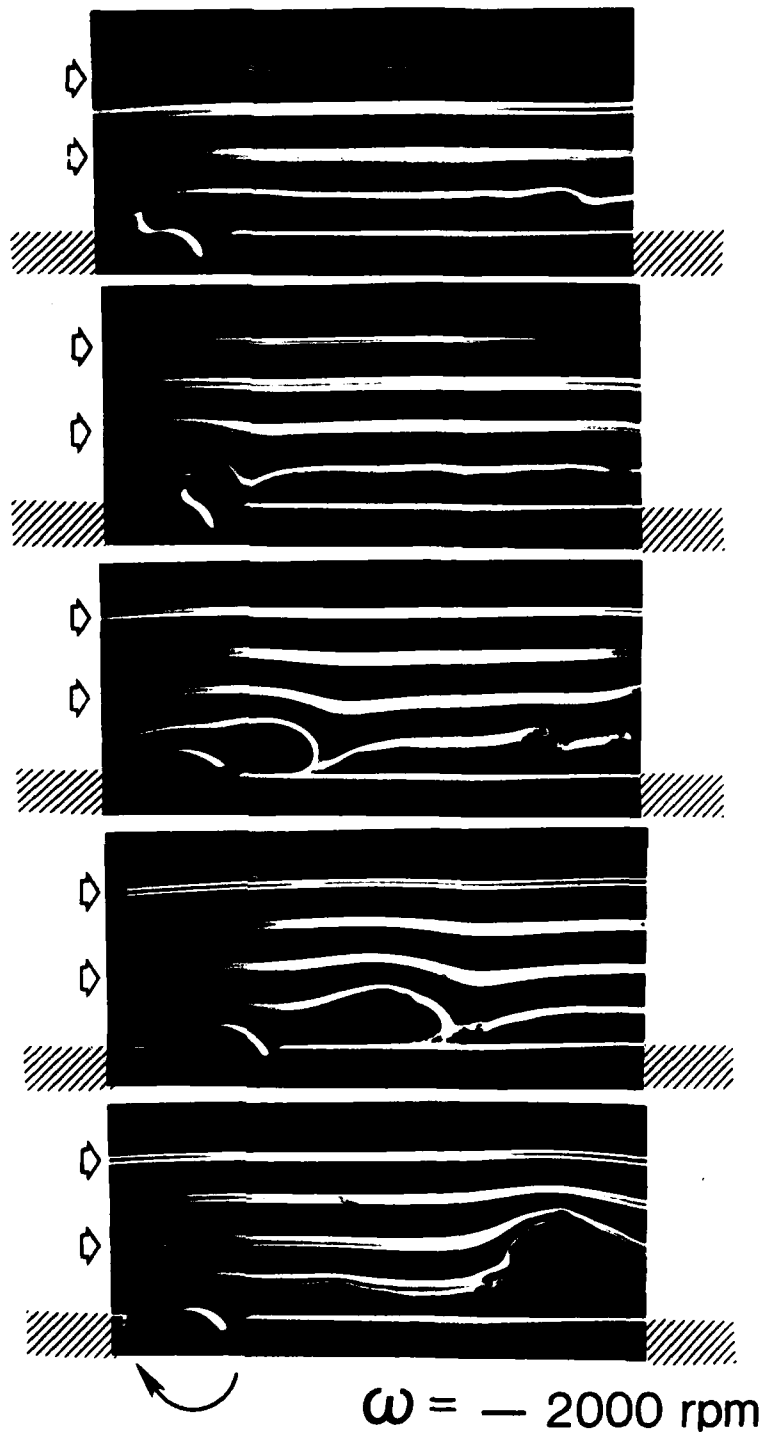


Figure 104. Flow visualization of vortex structure produced by the vortex generator with  $\omega = -2000 \text{ rpm}$ .

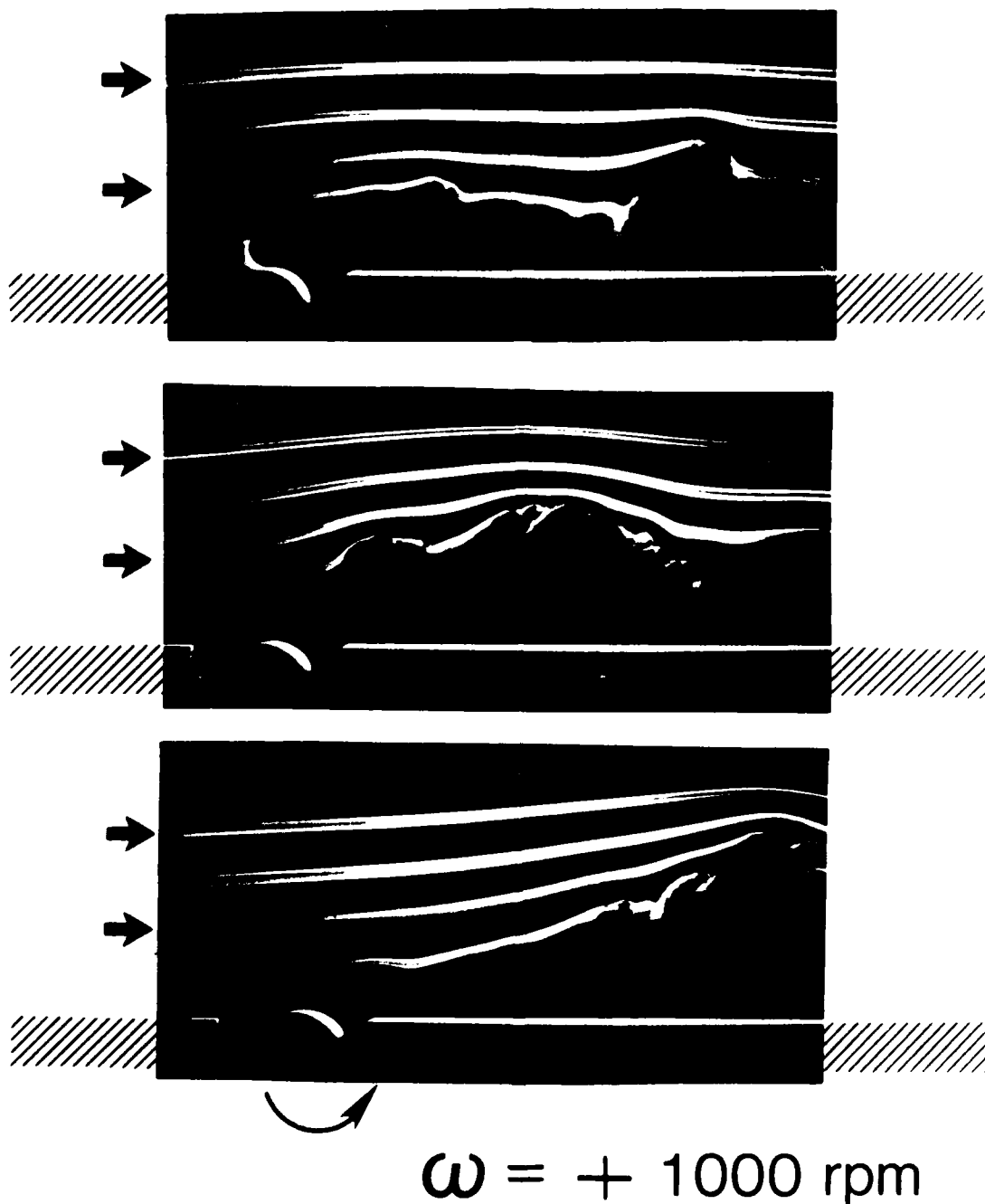


Figure 105. Flow visualization of vortex structure produced by the vortex generator with  $\omega = 1000 \text{ rpm}$ .

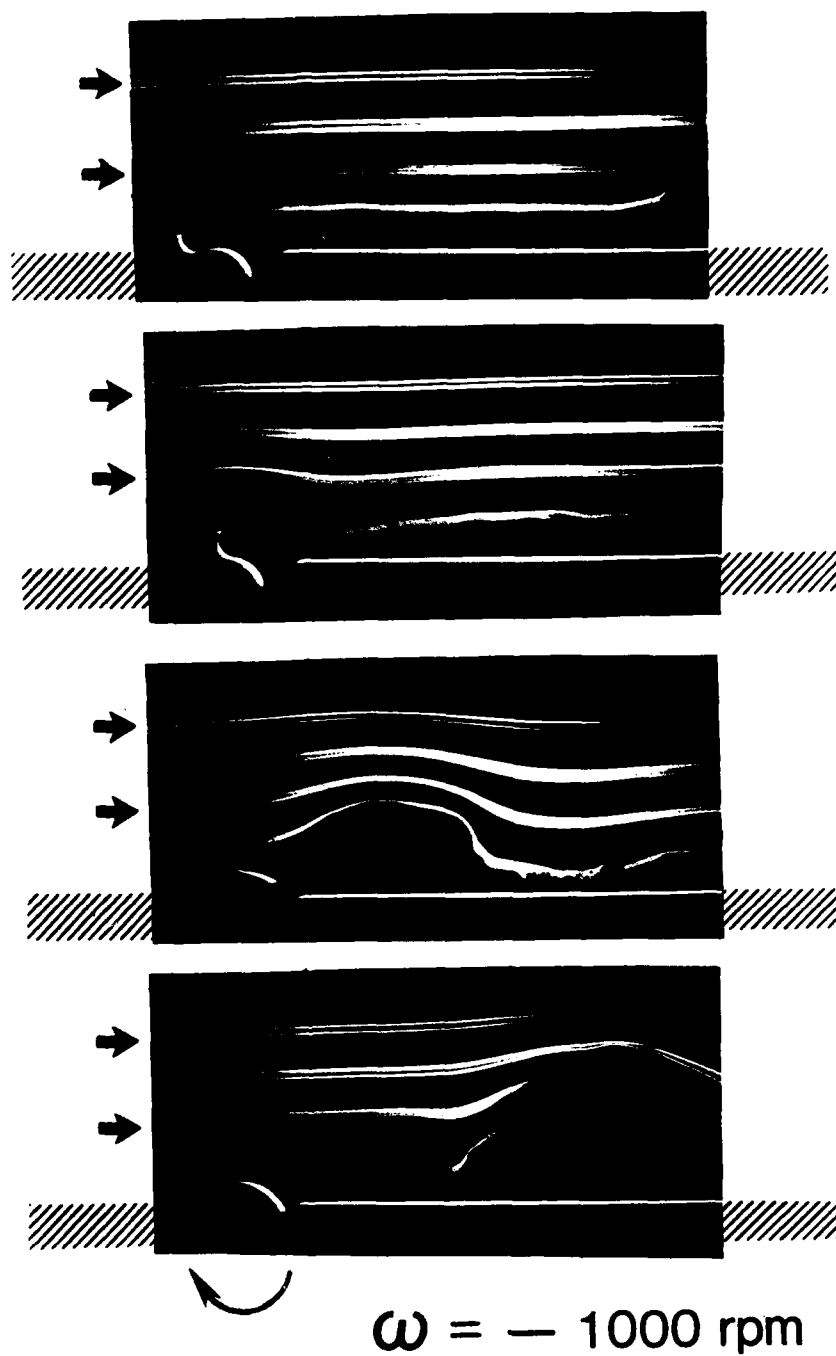


Figure 106. Flow visualization of vortex structure produced by the vortex generator with  $\omega = -1000 \text{ rpm}$ .

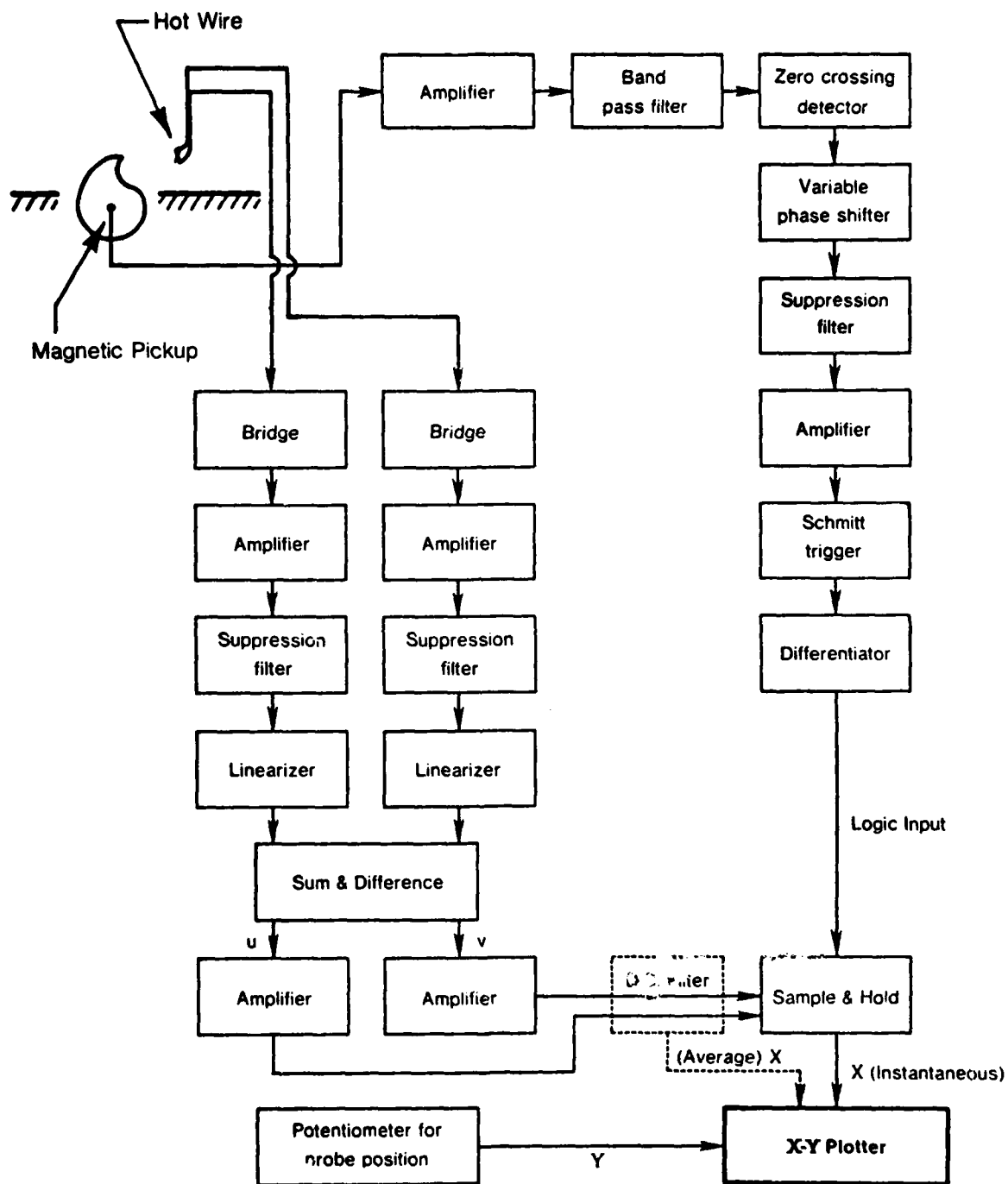


Figure 107. Schematic of conditioned sampling apparatus.

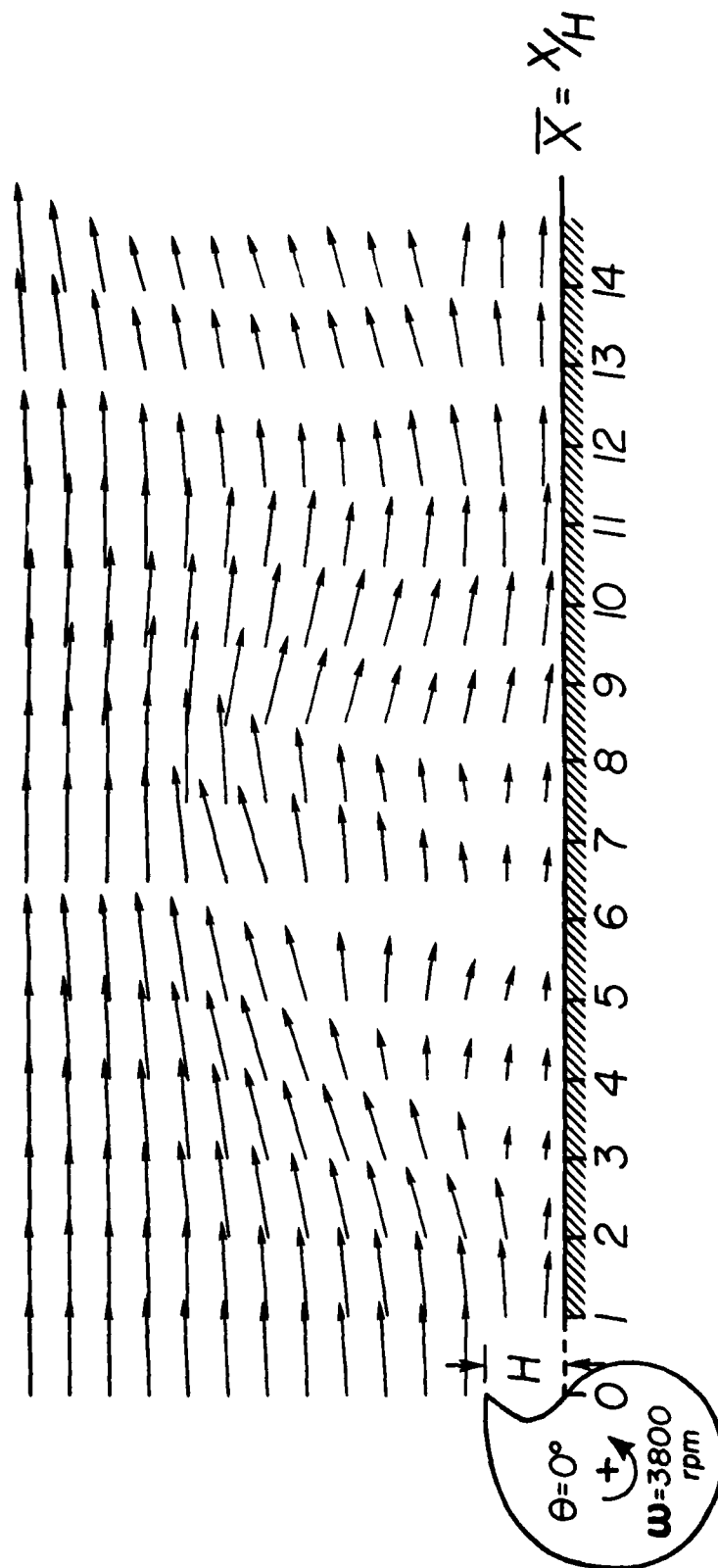


Figure 108. Instantaneous velocity field with the rotor fully extended in the  $\theta = 0^\circ$  position.

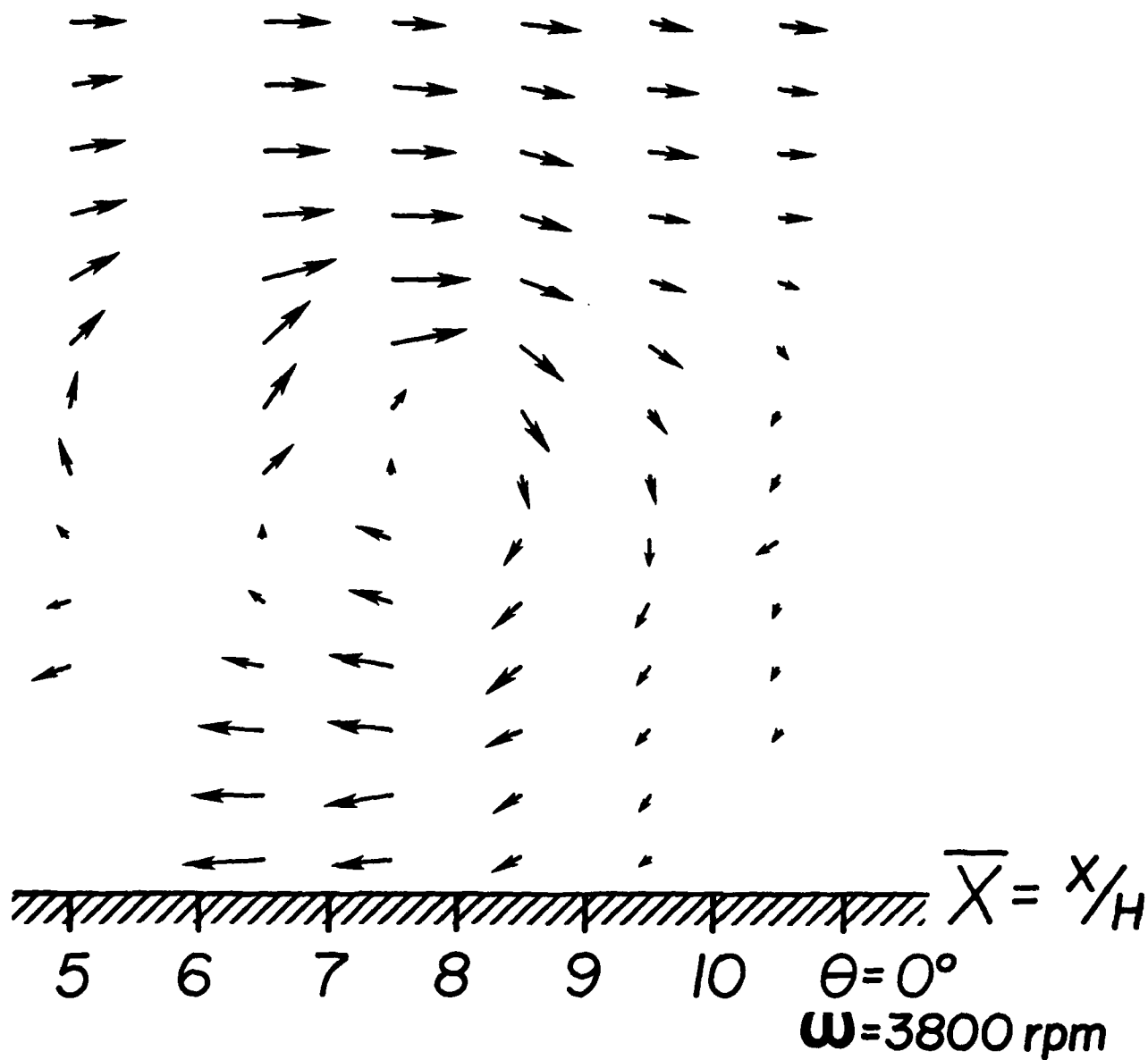


Figure 108b. Identification of a vortex structure in a reference frame moving at 11.5 m/sec.

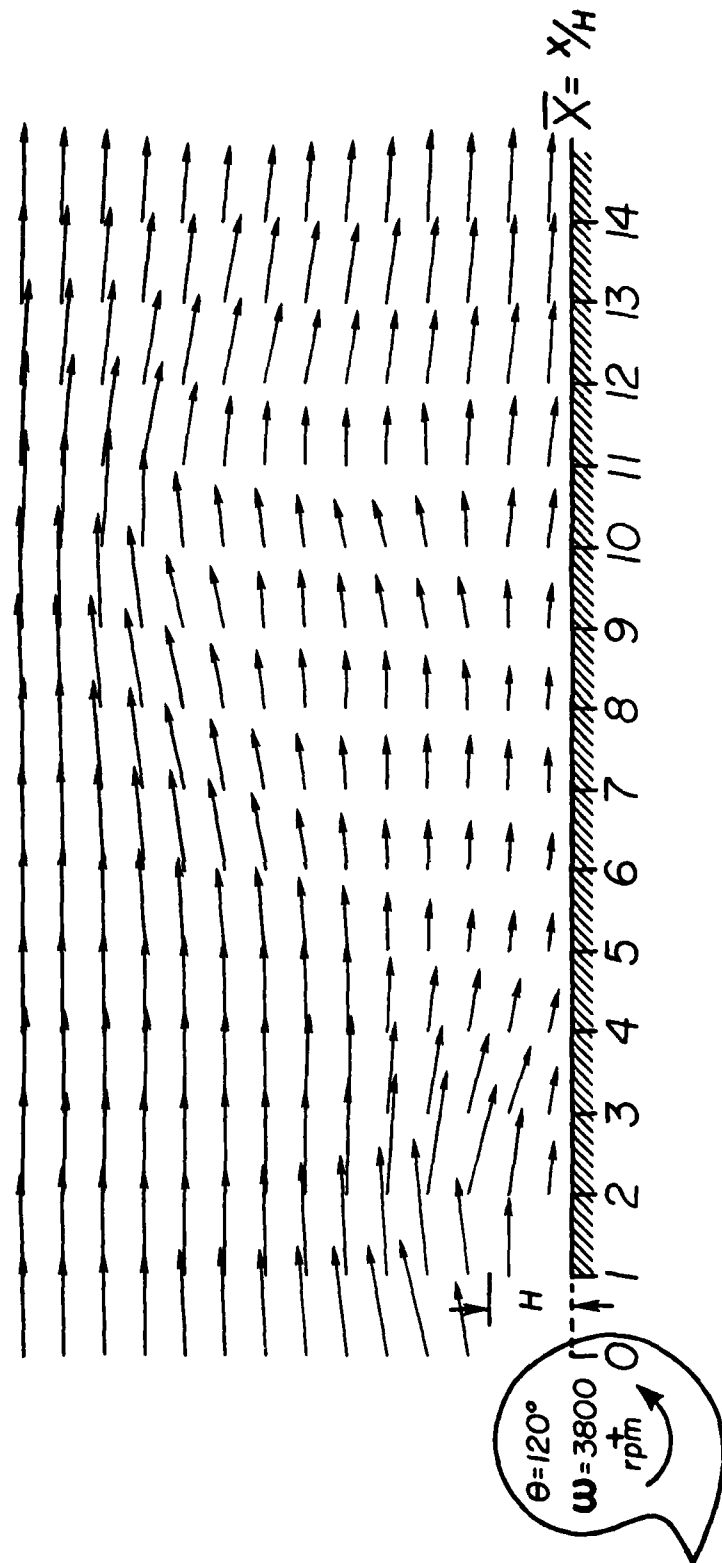


Figure 109a. Instantaneous velocity field with the rotor in the  $\theta = 120^\circ$  position.

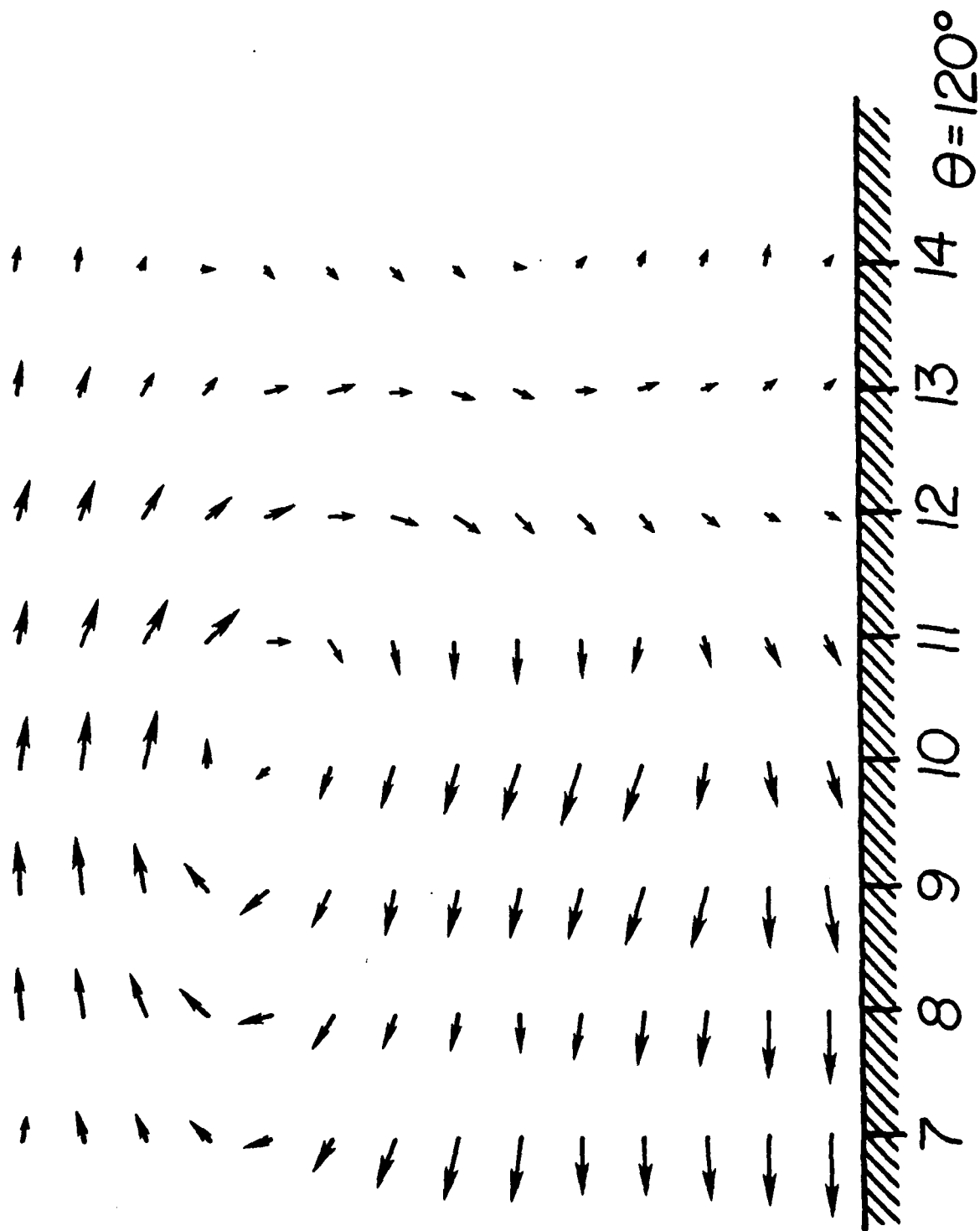


Figure 109b. Identification of a vortex structure in a reference frame moving at 11.8 m/sec.

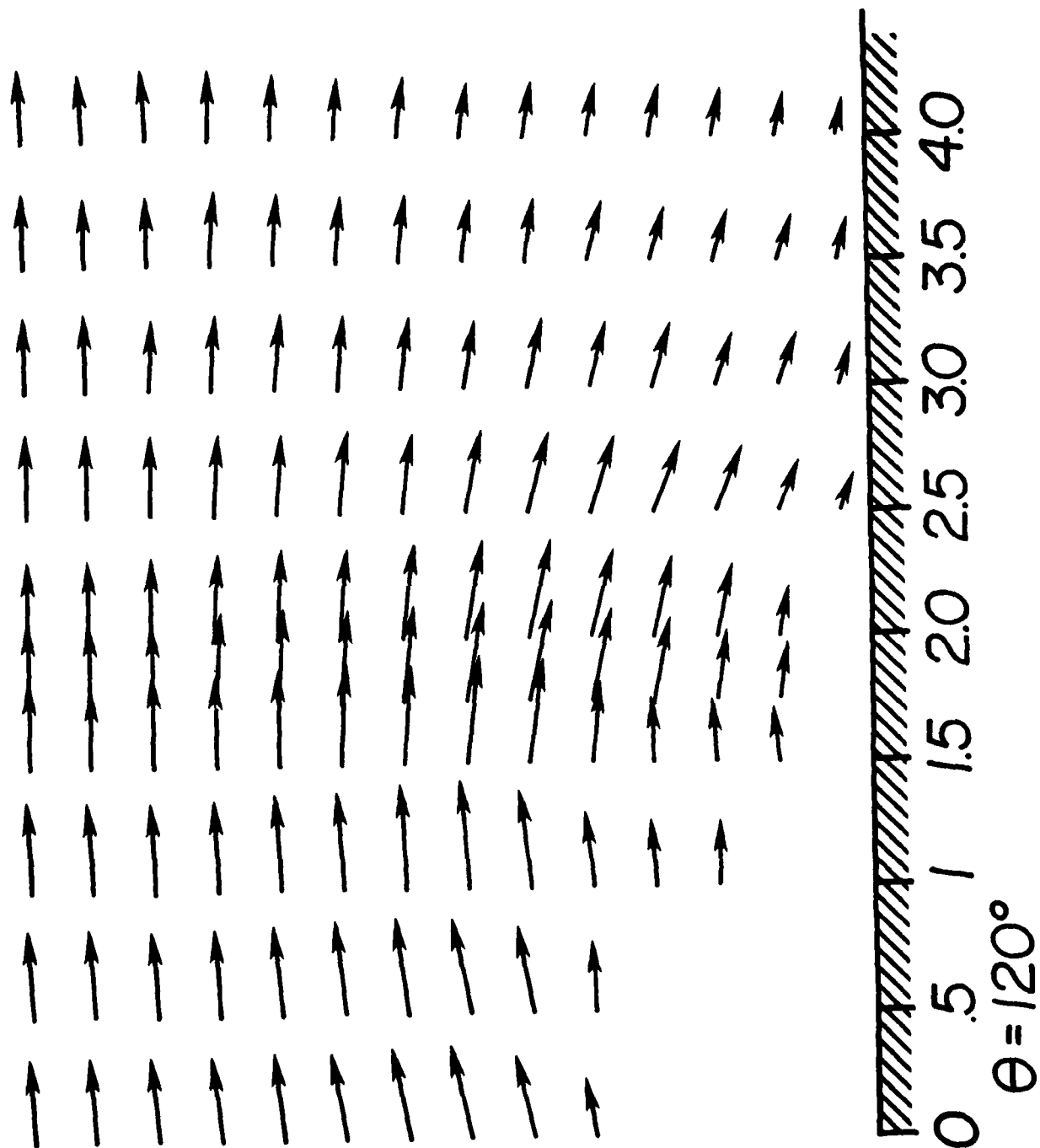


Figure 109c. More detail of the flow near the rotor with  $\theta = 120^\circ$ .

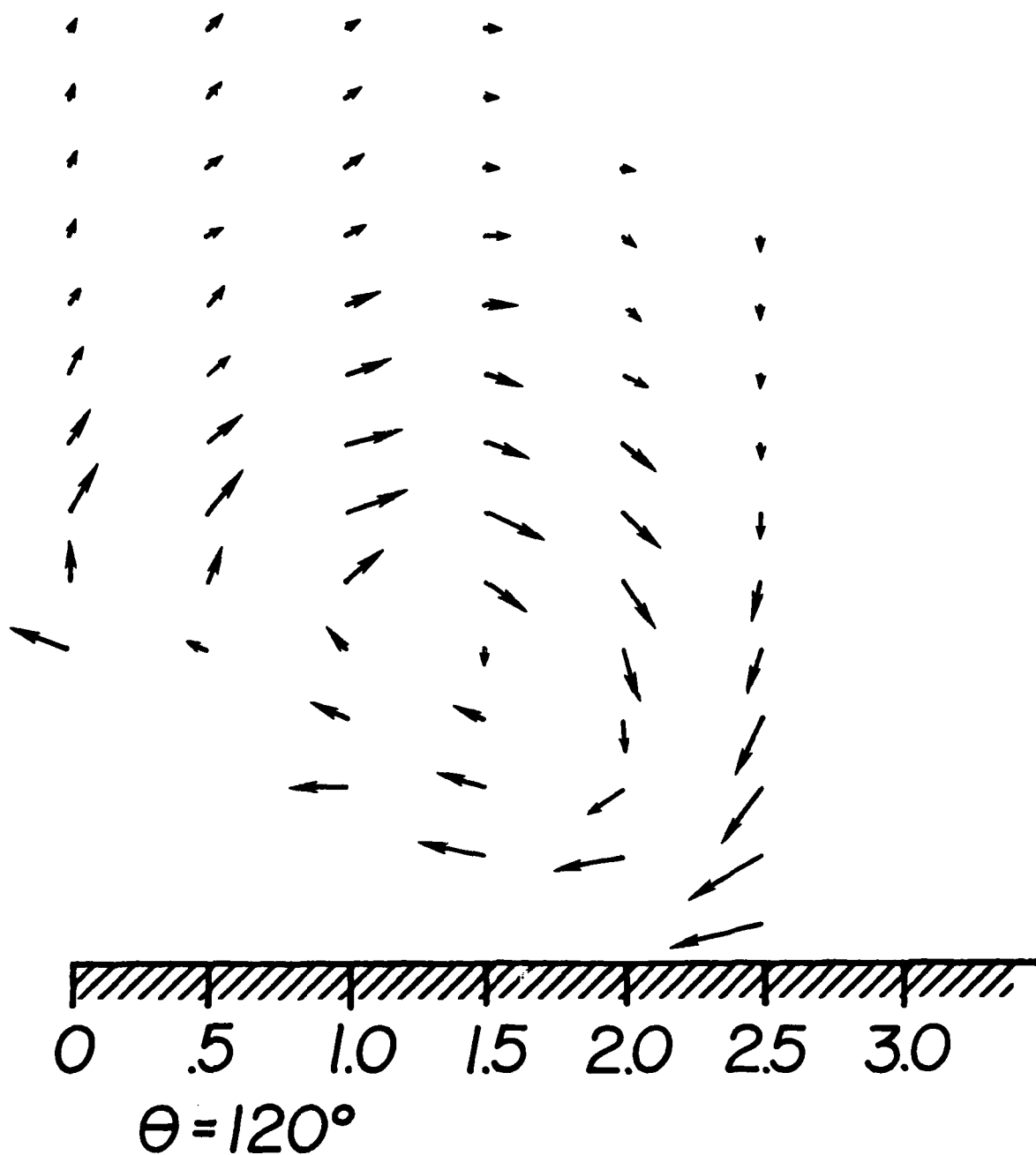


Figure 109d. Identification of a vortex structure in the flowfield of Figure 109c.

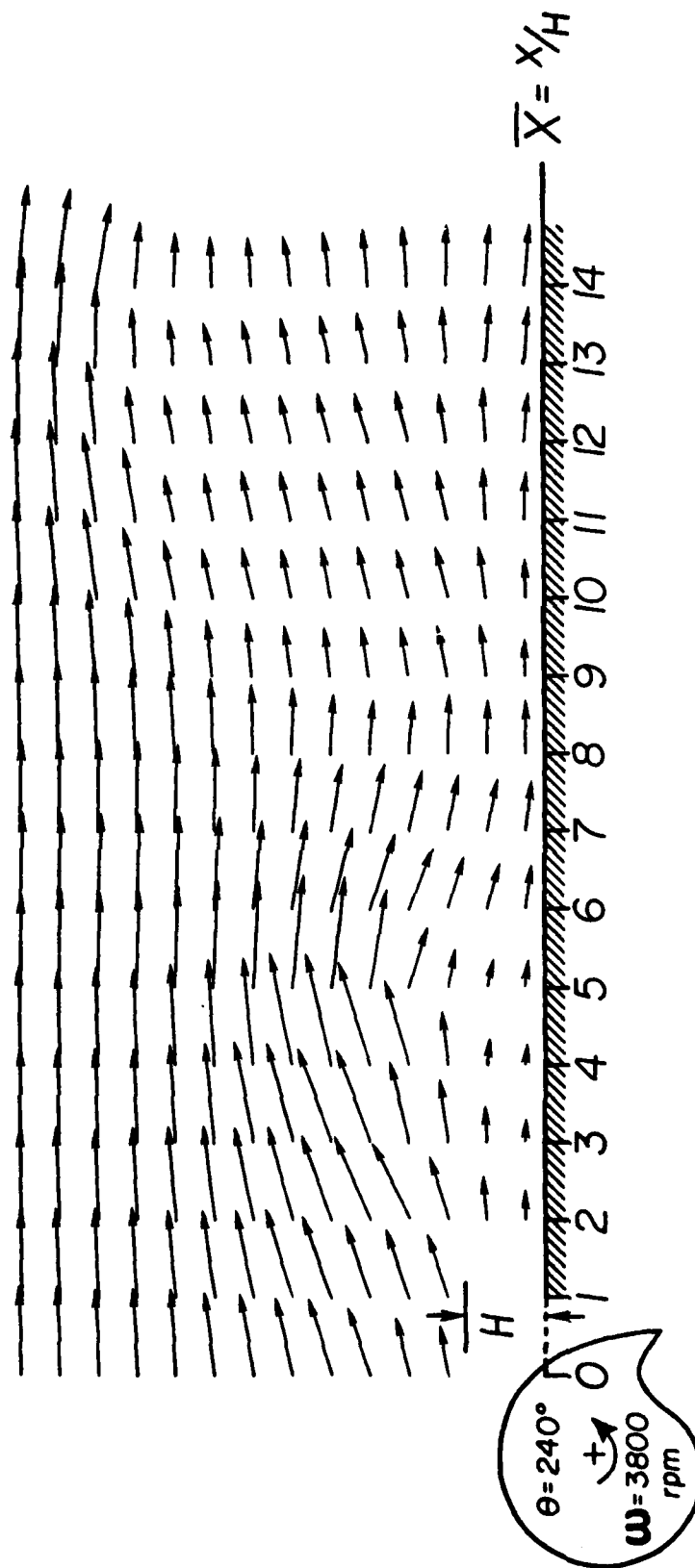


Figure 110a. Instantaneous velocity field with the rotor in the  $\theta = 240^\circ$  orientation.

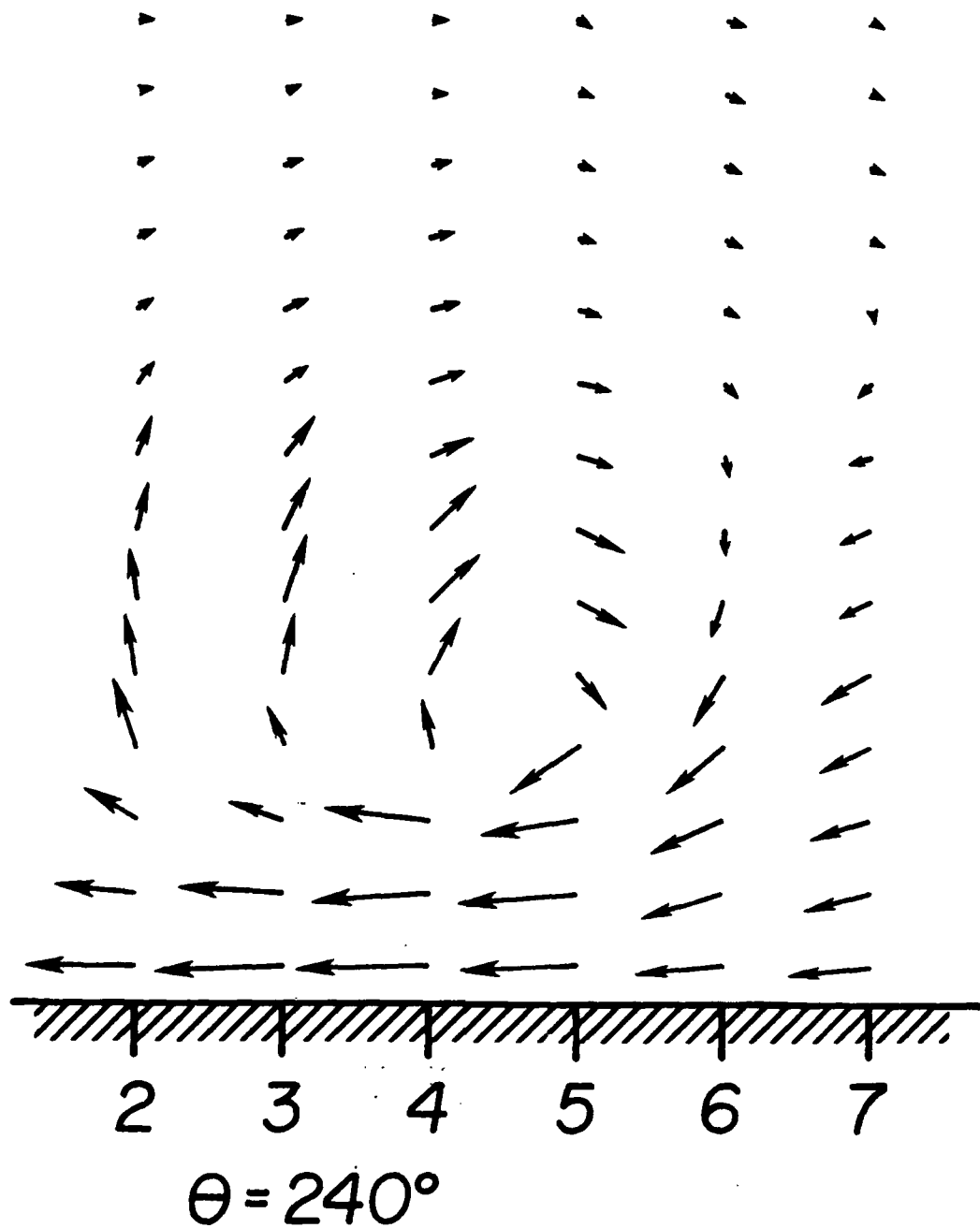


Figure 110b. Identification of a vortex structure in the flowfield of Figure 110a at  $\bar{x} = 4.5$ ,  $\bar{y} = 2.0$ .

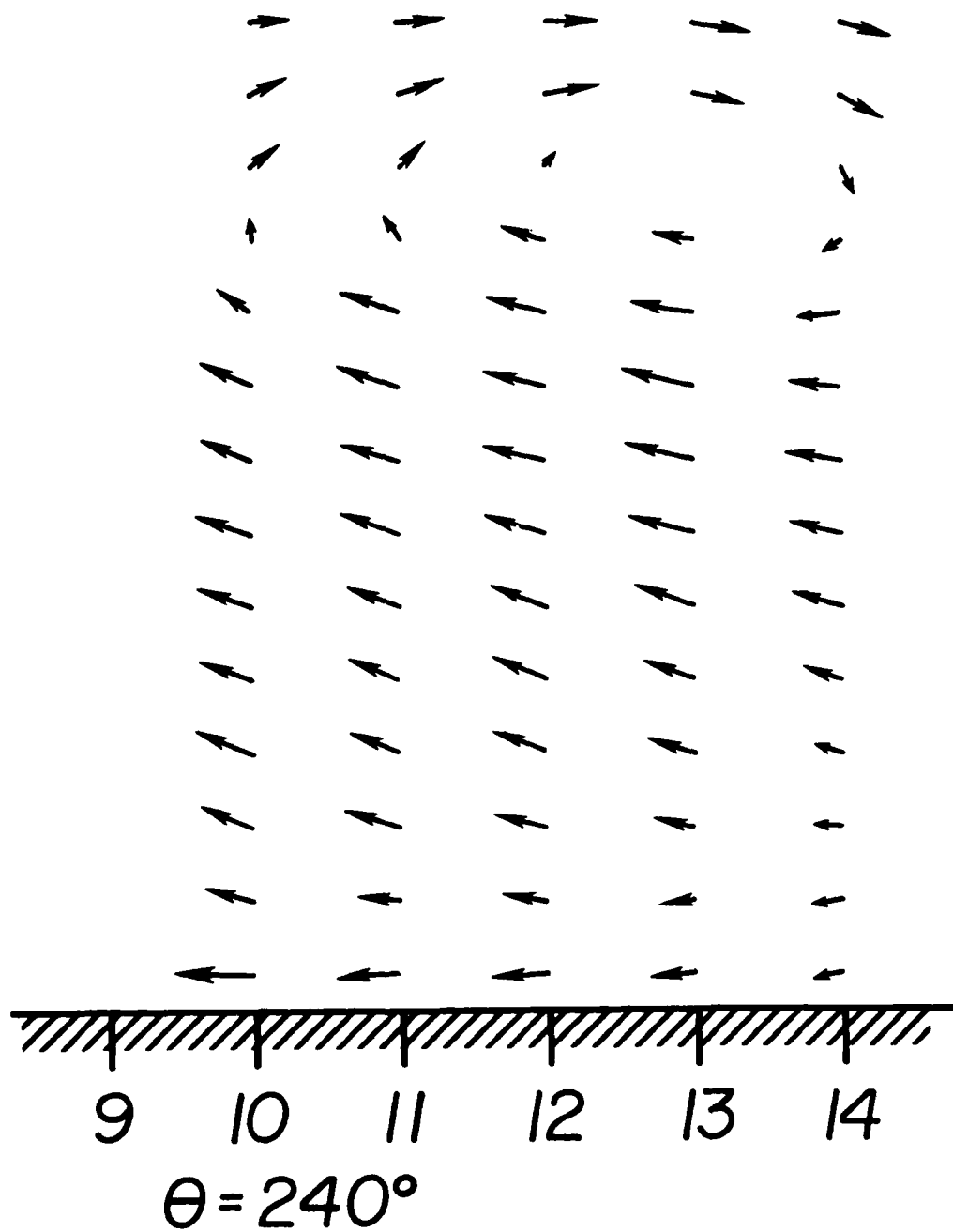


Figure 110c. Identification of a vortex structure in the flowfield of Figure 110a at  $\bar{x} = 13.0$ ,  $\bar{y} = 5.75$ .

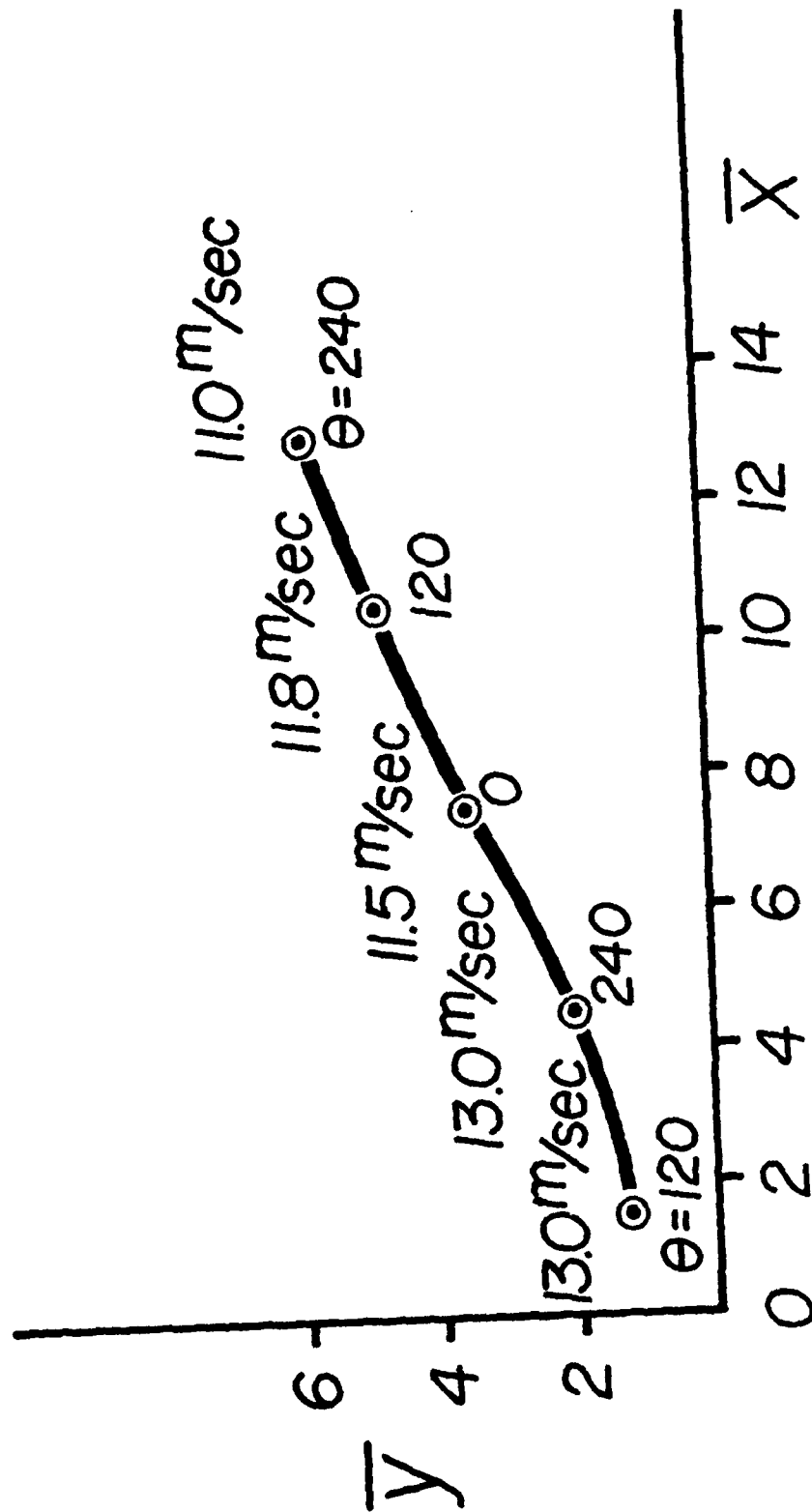


Figure 111. Trajectory of the vortex center as it moves downstream.

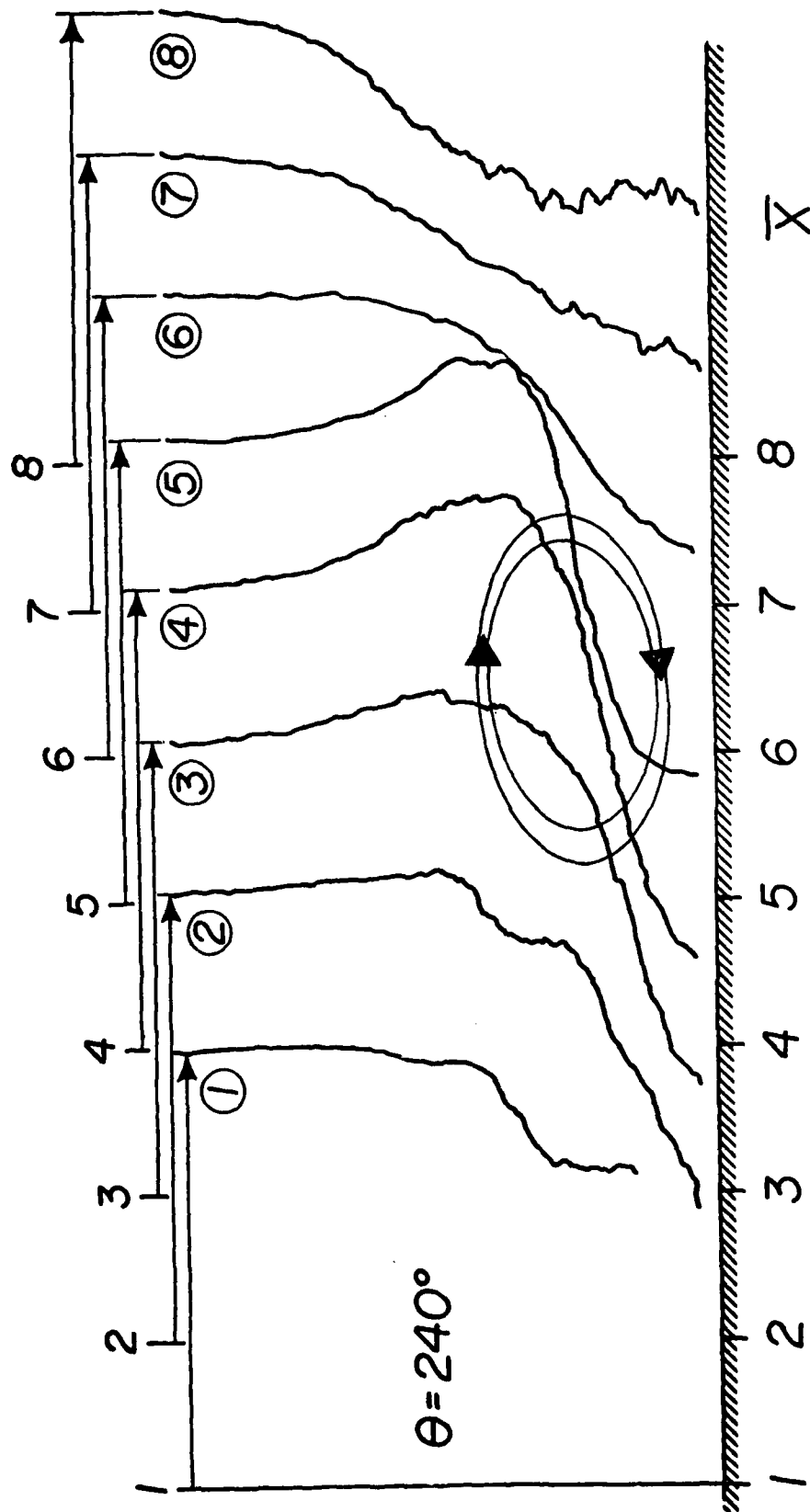


Figure 112. Influence of the vortex on the streamwise velocity profile.

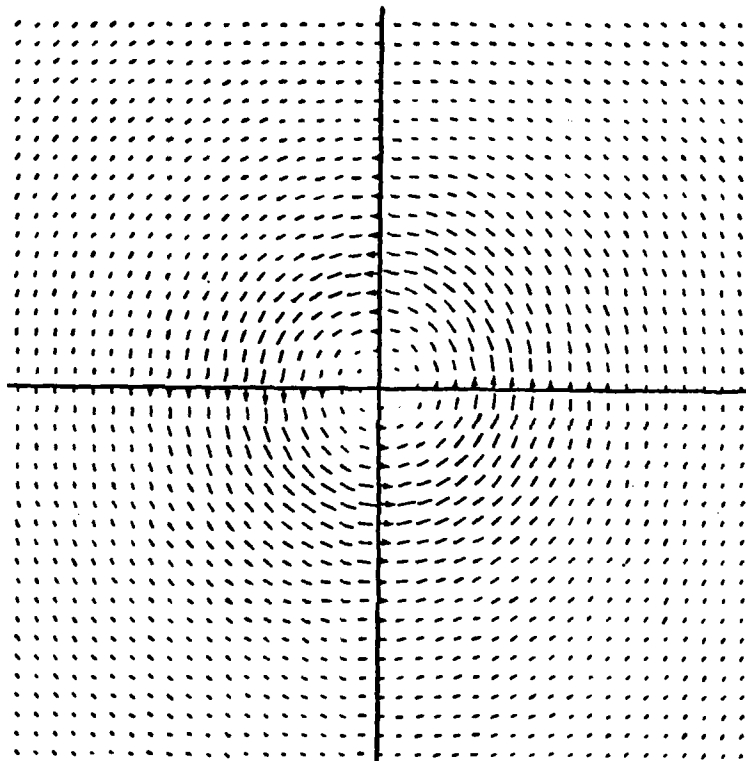


Figure 113a. Spatial vortex existing on the axis.

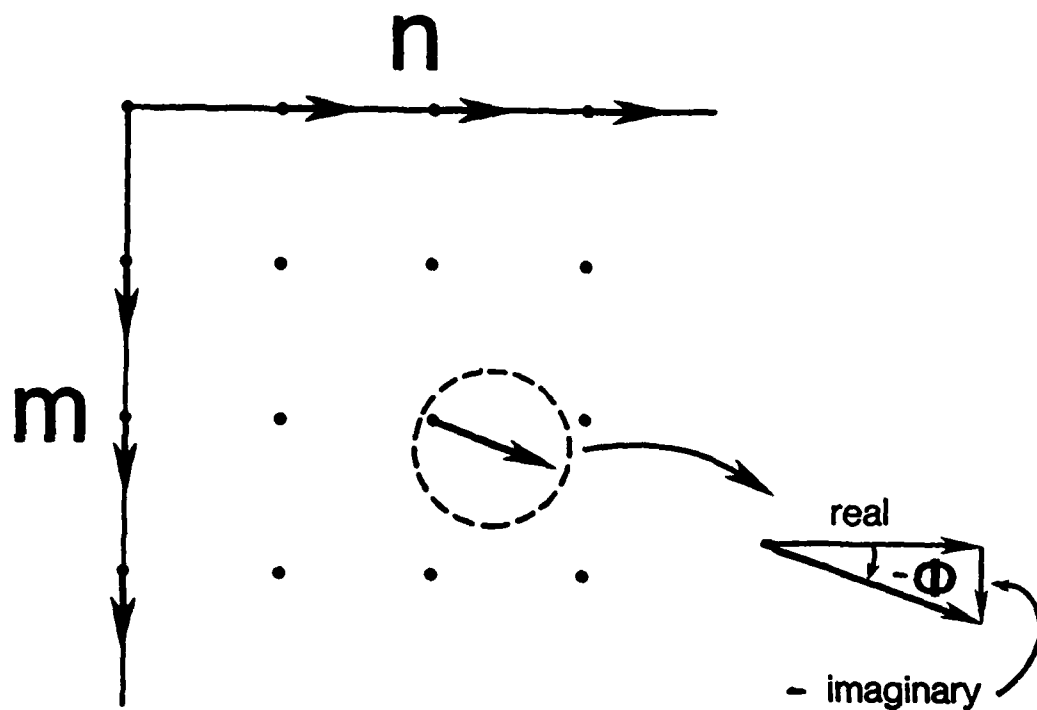


Figure 113b. Transformation of the vortex of Figure 113a.

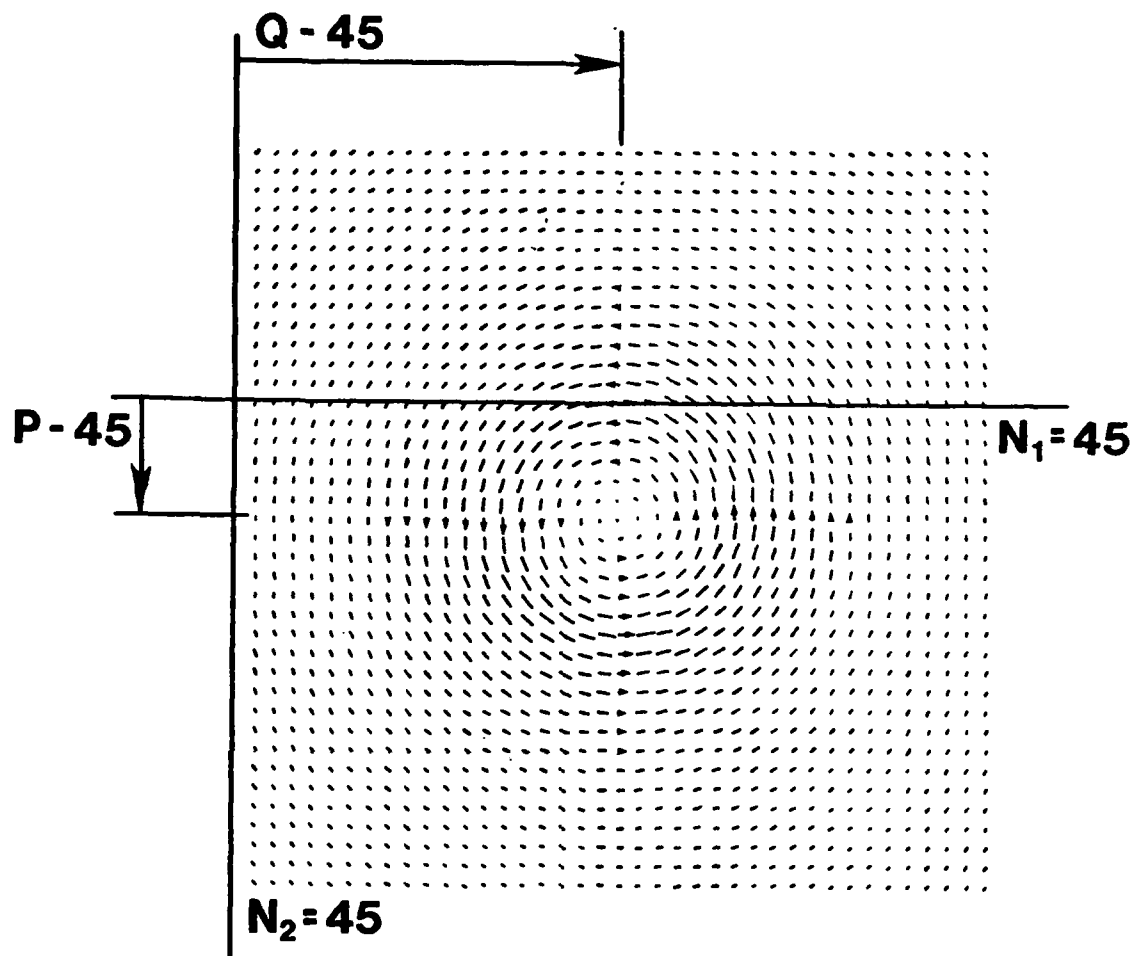


Figure 114a. Vortex shifted to an off axis location.  
Center shifted down by 50 units and right  
by 64 units from the upper left data point.

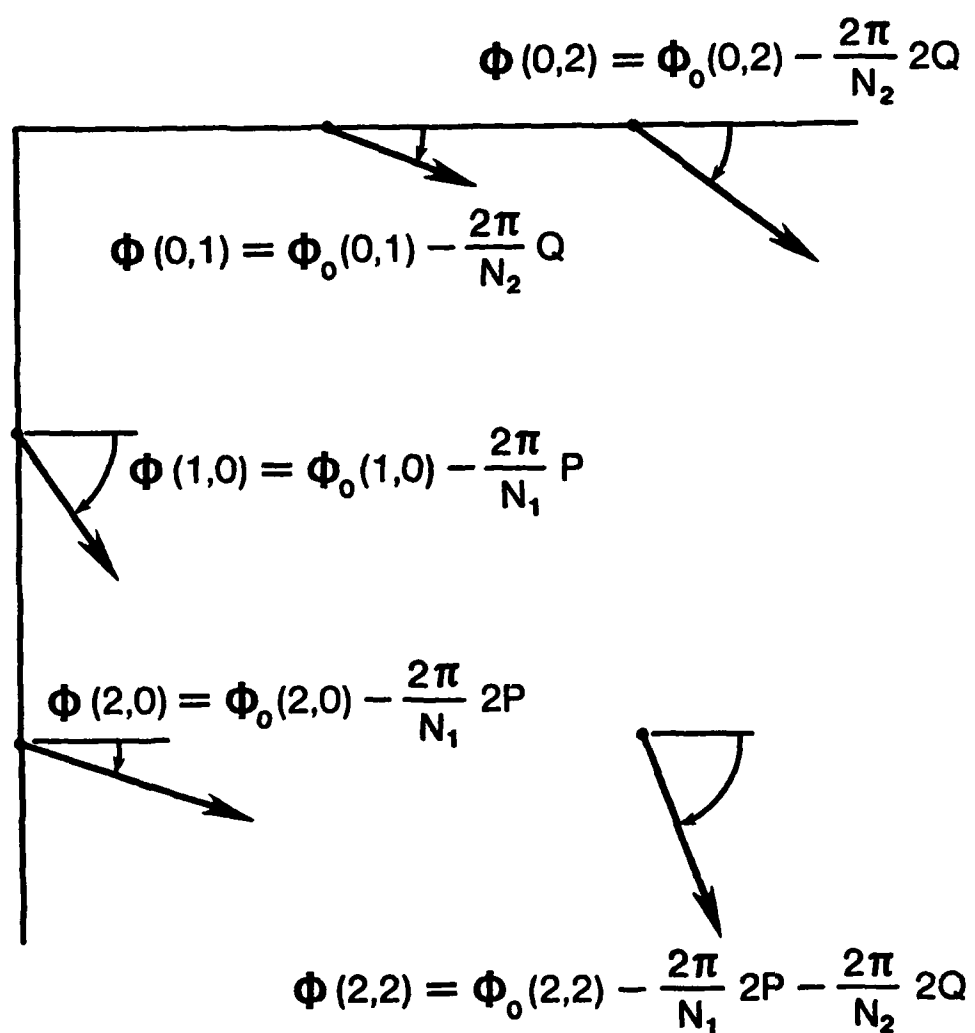


Figure 114b. Schematic of phase angle shift.

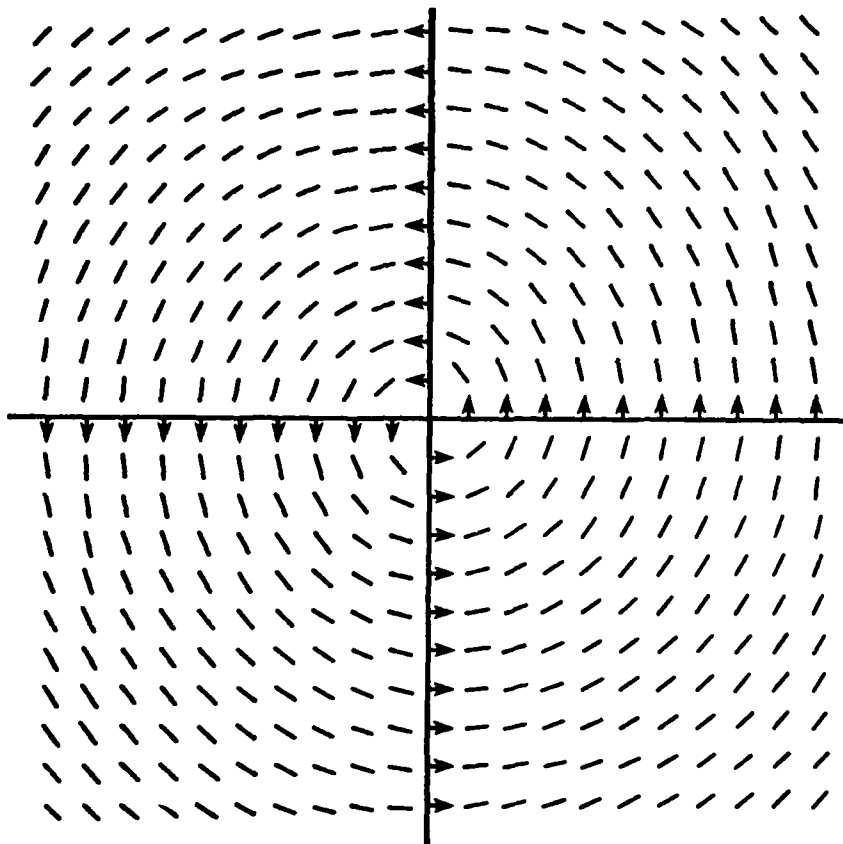


Figure 115. Rotational flow with a constant magnitude velocity.

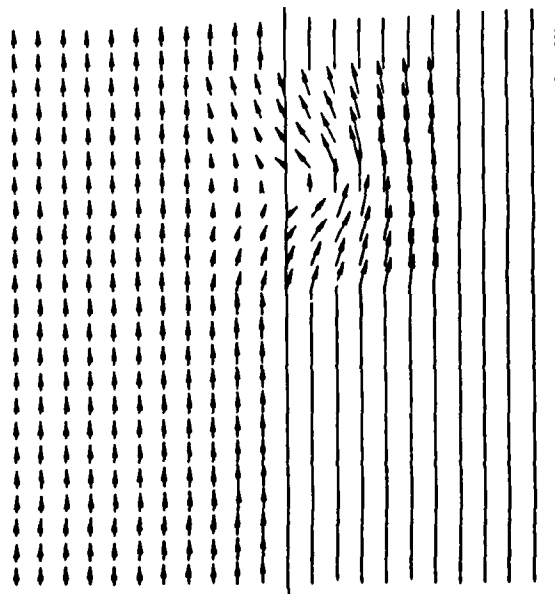


Figure 116a. Superimposed vortex on a parabolic translational flow.

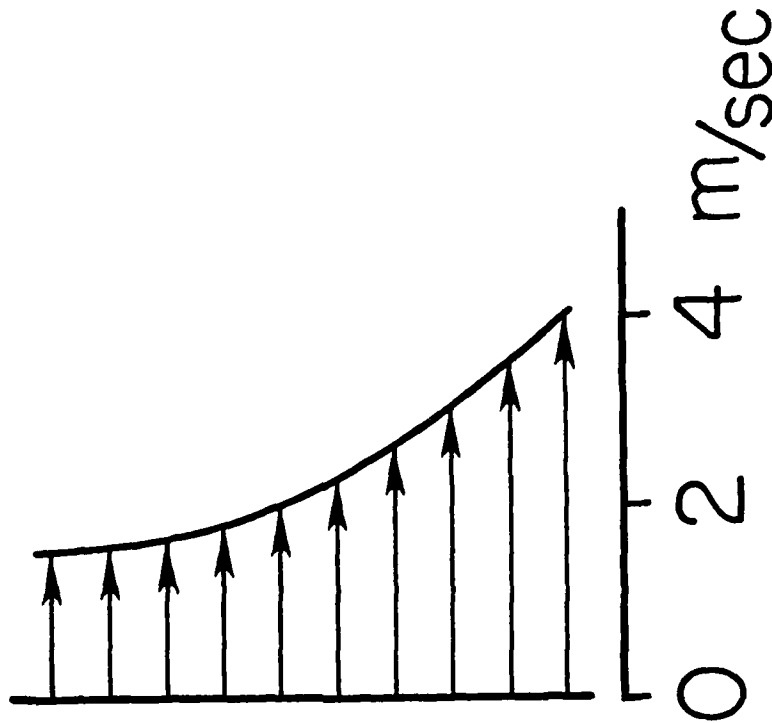


Figure 116b. Translational velocity component of the flowfield of Figure 5a.

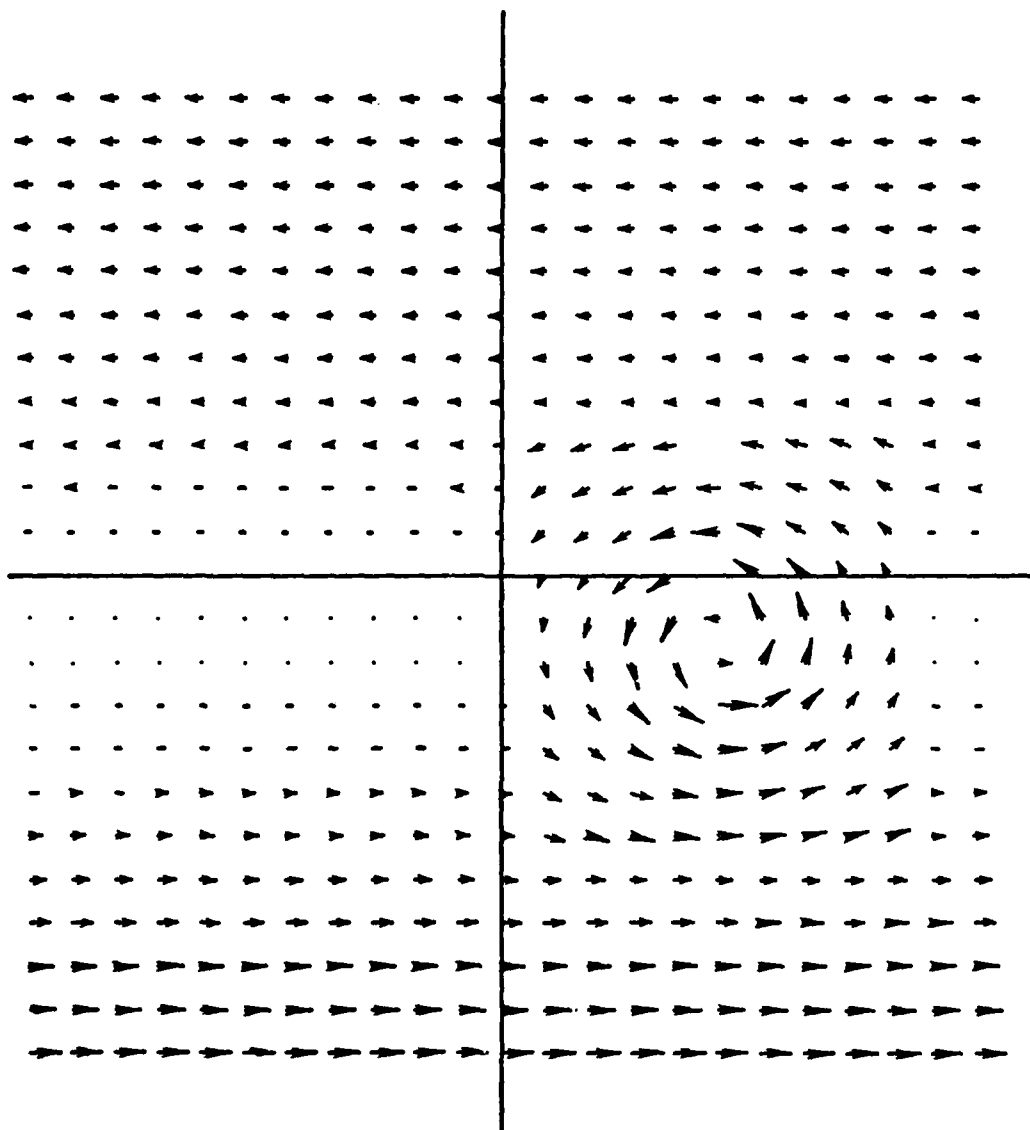


Figure 116c. Flowfield in the moving coordinate system.

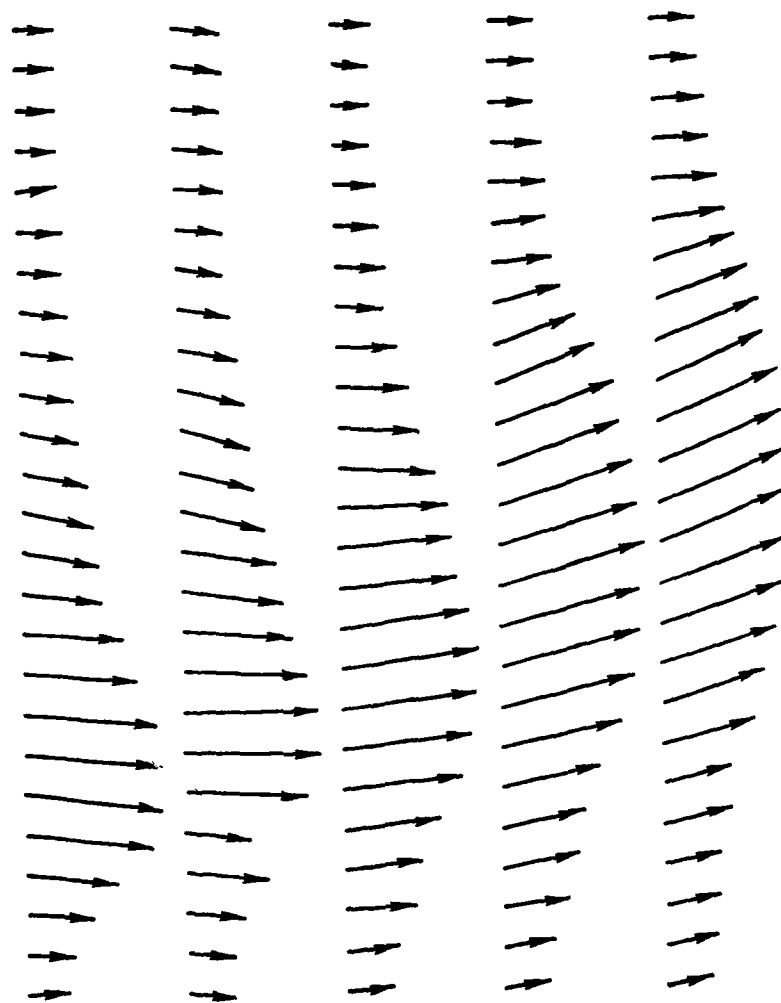


Figure 117. Instantaneous velocity structure of an oscillating jet.

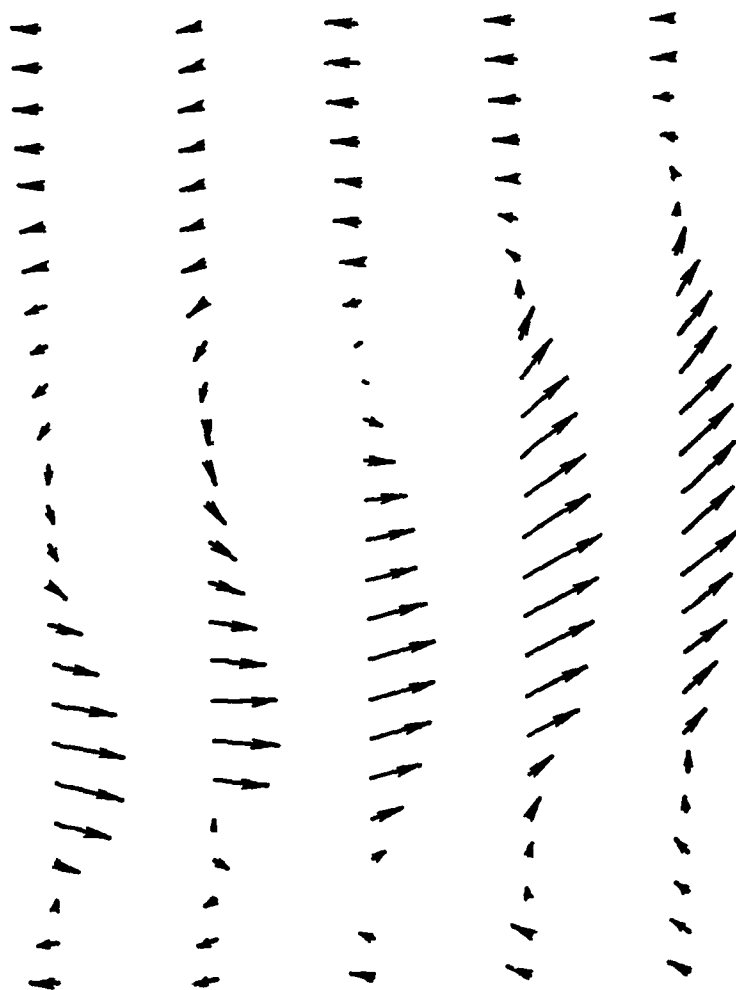


Figure 118. Flow structure in a reference frame moving with the velocity at the point identified as the vortex center.

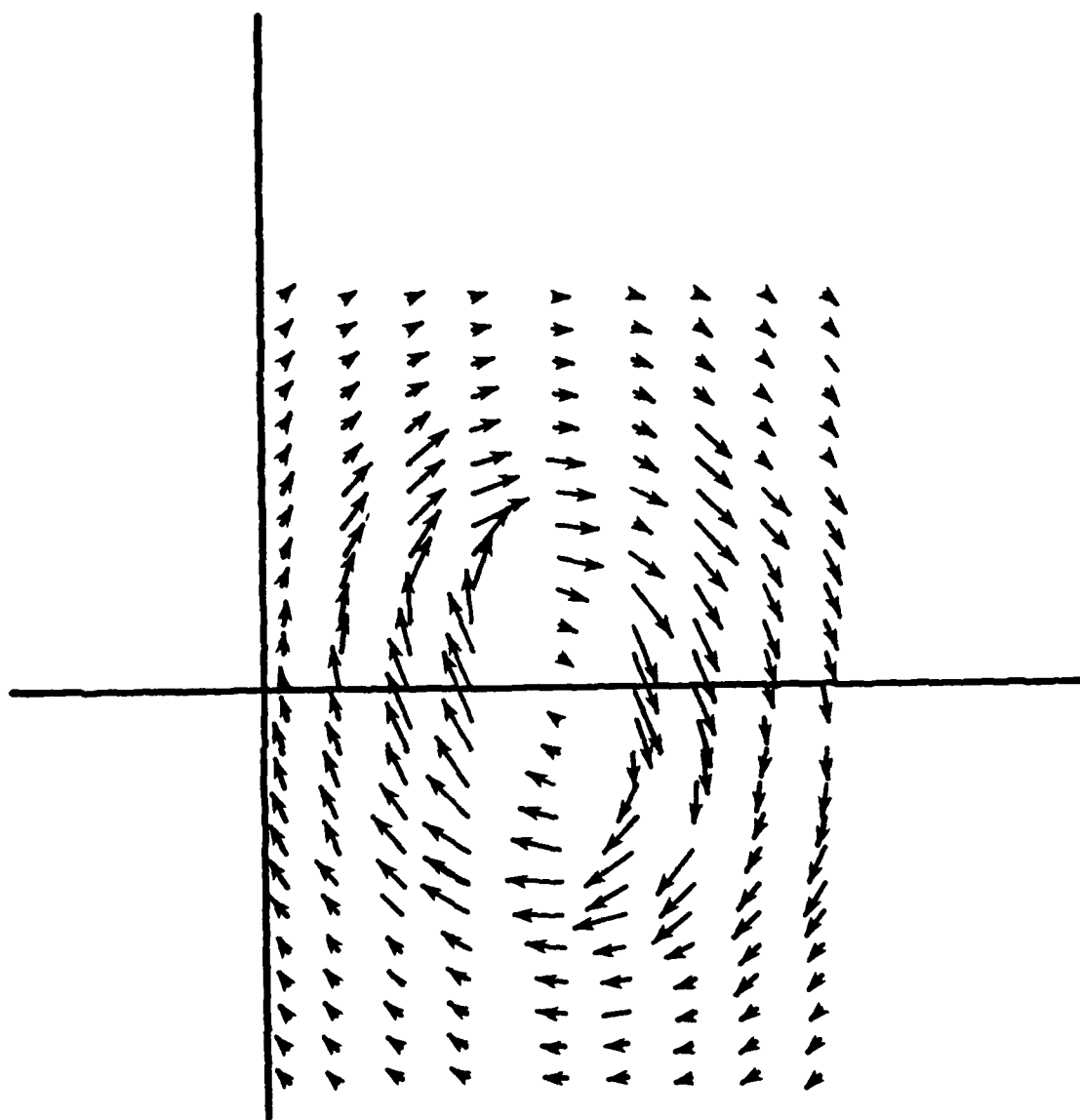


Figure 119. Generated velocity field containing two vortices.

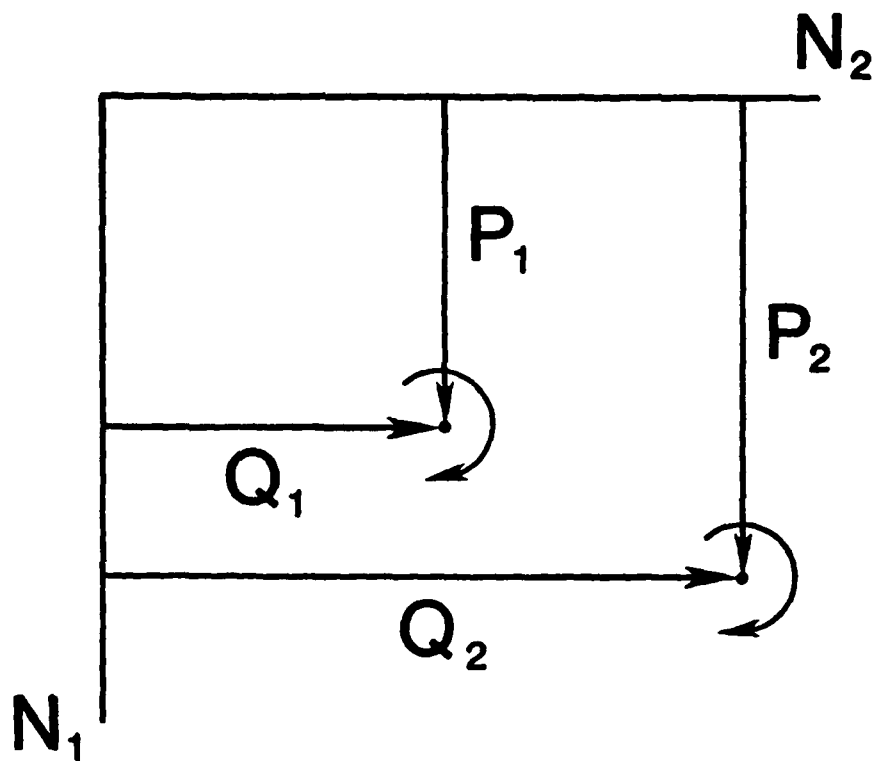


Figure 120a. Schematic of two vortices in the physical plane.

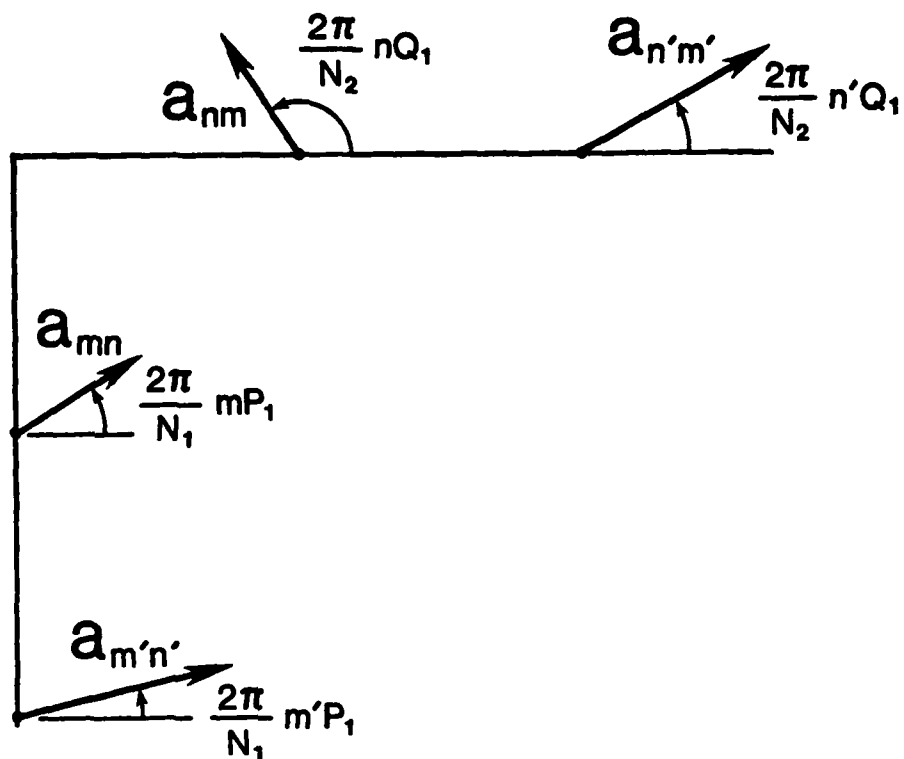


Figure 120b. Schematic of the transformed plane of vortex number 1 in Figure 120a showing magnitudes and phase angle changes due to shift of vortex center location.

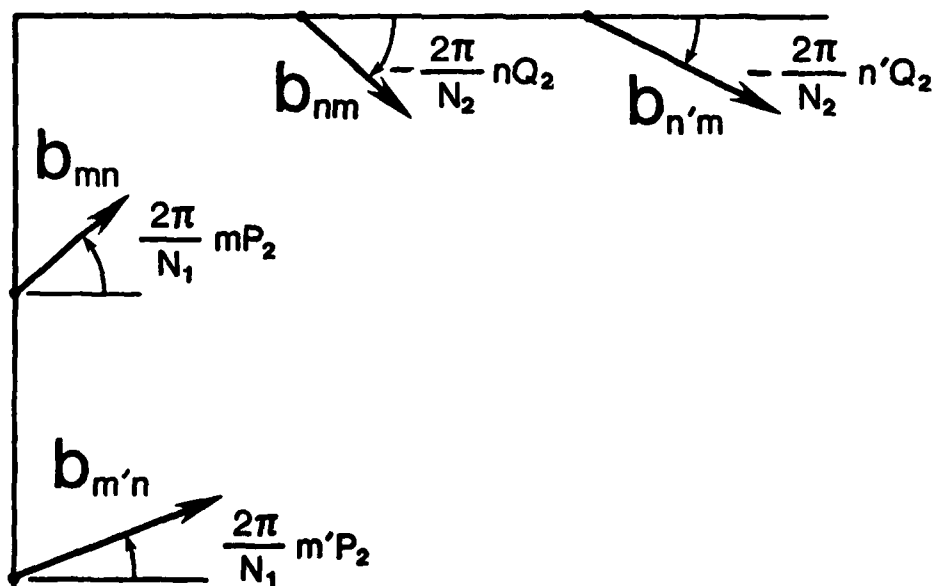


Figure 120c. Schematic of the transformed plane of vortex number 2 in Figure 120a, showing magnitudes and phase angle changes due to shift of vortex center location.

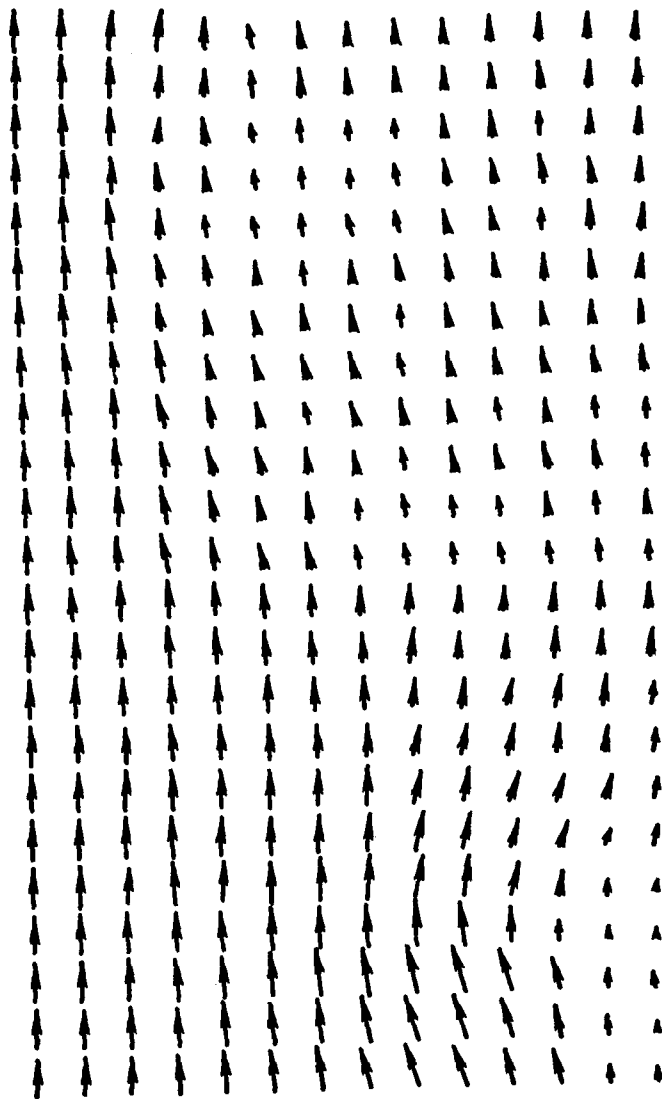


Figure 121. Instantaneous velocity field generated by the rotor.

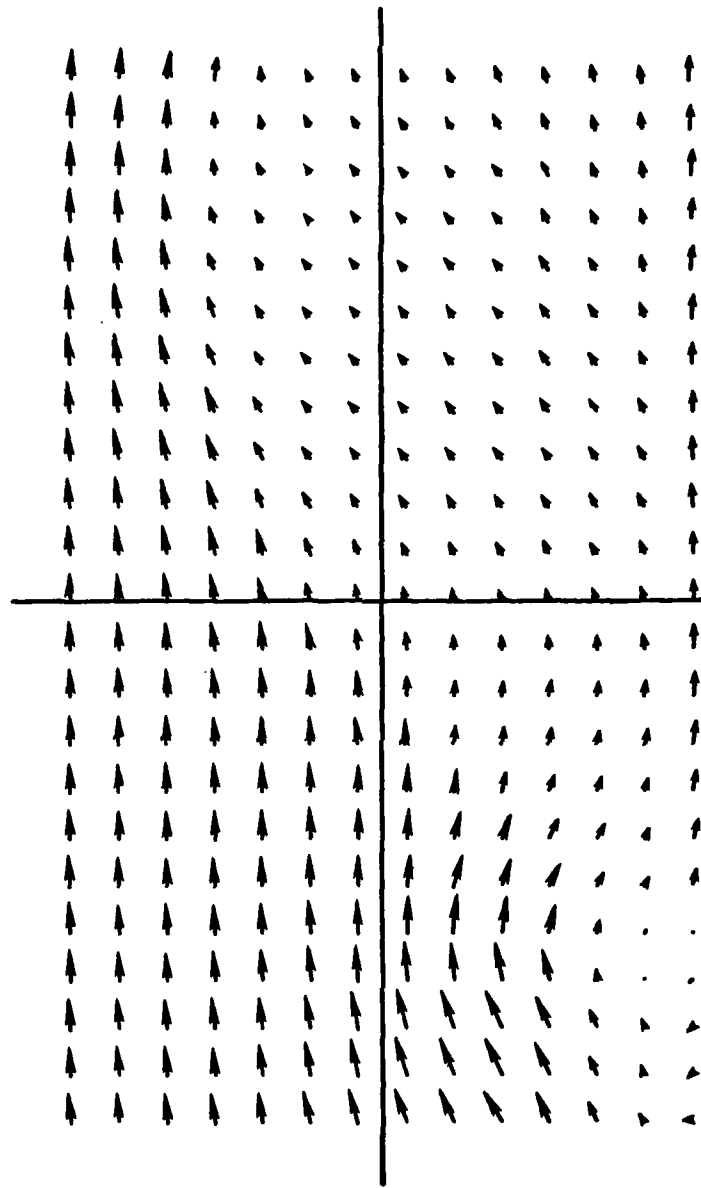


Figure 122a. The upstream vortex in a coordinate frame moving with its center.

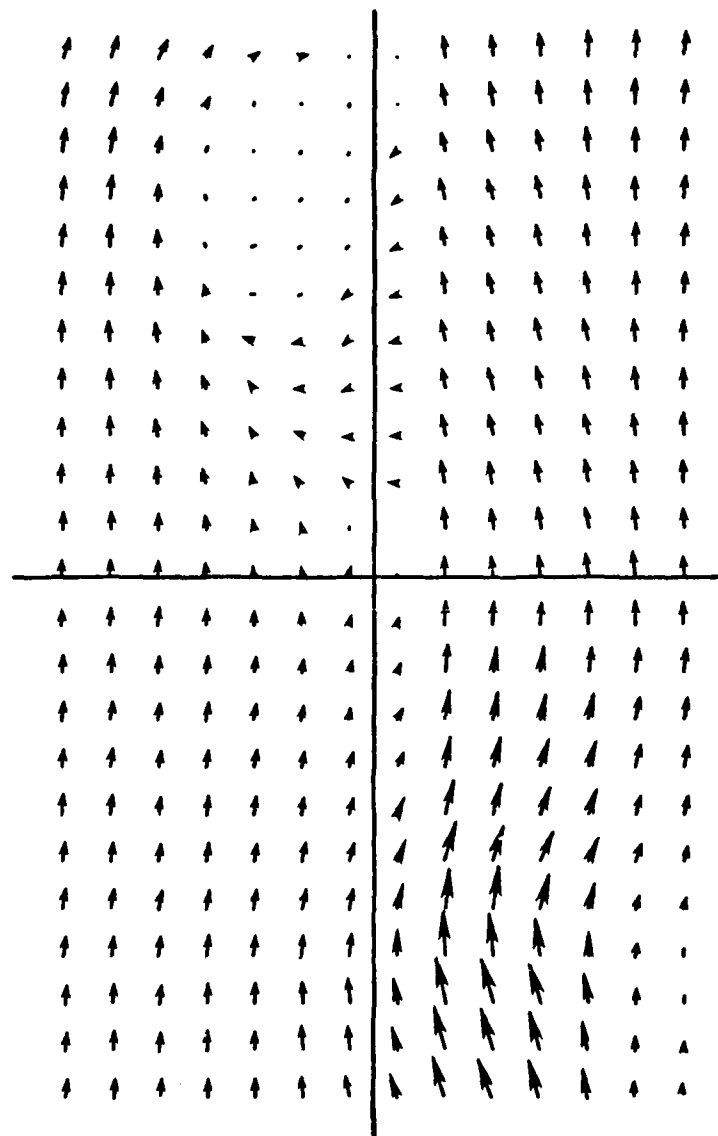


Figure 122b. The downstream vortex in a coordinate frame moving with its center.